

University of Nottingham
UK | CHINA | MALAYSIA

Investigating Placental Haemodynamics Using MRI

George Hutchinson

Thesis submitted to the University of Nottingham
for the degree of Doctor of Philosophy

July 2022

Abstract

Magnetic Resonance Imaging (MRI) has been proven to be a safe and powerful tool for investigating the small scale motion of blood as it moves throughout the human placenta in utero, using techniques such as Diffusion Weighted Imaging (DWI) which have been proven to be sensitive to placental haemodynamics and changes in placental insufficiency. However due to the complexity of the human placenta, and the sensitivity of DWI to flow effects interpreting the results of DWI in utero is challenging, as within a single voxel many haemodynamic features can combine, such as blood percolating across the intervillous space, turbulent blood supplied by the spiral arteries and the fetal circulation within the villous tree network. The direct effect of these processes combining is not obvious, and while DWI has been shown to be sensitive to placental dysfunction it is not always clear how changes in signal reflect changes in structure.

This thesis investigates the placental DWI response further, initially through the use of an Inverse Laplace Transform (ILT) based approach to fit the data and provide more understanding of the slow diffusive, and faster 'pseudodiffusive' components, where I found multiple components, which were altered in placental dysfunction. I then fitted the same data using a more popular Intra-Voxel Incoherent Motion IVIM model, and made the first comparisons between data fit with an ILT based approach, and an IVIM model, to provide more context to what IVIM parameters are measuring within the placental DWI data. While I found that the ILT provided more information about the faster incoherent motion of blood, the IVIM model still provides similar information through easier to fit and interpret parameter maps.

This thesis outlines the first implementation of Phase Contrast Angiography (PCA) for measurement of the velocity of blood within the placenta, which was used to provide better understanding of placental haemodynamics. Importantly I found that the speed of blood in placentas with insufficiency (namely Pre Eclampsia (PE) and Fetal Growth Restriction (FGR)) was significantly faster than in those without. These measurements were also used to provide more context to DWI measures as the bulk flow of blood throughout the organ is also important for ensuring proper development and function of the placenta. This thesis also outlines the first measurements of the poorly understood venous drainage system using MRI, which has seen little attention but must also be important for sustaining the placental environment.

The presence of 'rebounds' in placental Pulse Gradient Spin Echo (PGSE) data, where voxels which begin decaying (as in normal DWI) begin to regain a proportion of the initial signal intensity. Rebounds have theoretically been shown to be possible but have yet to be reported in experimental data, however I believe the rebounds presented here are not of the same form as those previously described, and instead were due to flow effects within the placenta. Here I introduced a method for identifying these voxels, and providing quantitative information about the underlying flow.

Finally, as all the results presented here are expected to depend on the exact properties of the PGSE sequence used, I investigated how the response of the placental DWI results presented here could vary with diffusion time (Δ). This work could only be carried out in an imaging phantom due to the COVID-19 pandemic, and while it showed promise and outlined a method to combine diffusion encoded, and flow encoded measurements into a single set of imaging gradients to better investigate the placental environment, the work needs to be repeated in utero.

Acknowledgements

First I would like to express my gratitude and thanks to my supervisor Professor Penny Gowland for her continuous support during my doctoral studies. Her insight and dedication were invaluable to me, and I will always be grateful for everything she has done to support and guide me, especially considering the extra challenges of a global pandemic.

I would like to thank the EPSRC-MRC Oxford Nottingham Biomedical Imaging Centre for Doctoral Training for funding my studies, and giving me the opportunity to undertake them.

I would also like to extend my thanks others at the University of Nottingham, Dr Neele Dellschaft, Dr Lopa Leach, Dr Nia Jones, and Dr Simon Shah for all contributing to improving my research work, especially for their patience in teaching a physicist about placental biology.

I would also like to thank all of those at the Sir Peter Mansfield Imaging Centre for making my studies so enjoyable, from lunch time quizzes, to Christmas bar crawls, rounders matches, and endless cups of tea in the tea room. There are too many people to name who contributed to making the centre such a welcoming environment, but I would like to thank you all.

Finally I'd like to offer a huge thanks to my parents Rob and Jacky who have provided me with so much support over the years, and when I had to move home to finish writing my thesis during my COVID extension provided me somewhere to live, and endless food to fuel my thesis.

Contents

Abstract i

Acknowledgements iii

List of Tables ix

List of Figures x

1 Introduction 1

1.1 The Placenta 1

1.1.1 Background 1

1.1.2 Maternal Circulation 2

1.1.3 Fetal Circulation 4

1.1.4 Preeclampsia and Fetal Growth Restriction 5

1.2 Magnetic Resonance Imaging 6

1.2.1 Net Magnetisation 7

1.2.2 Chemical shift 9

1.2.3 Resonance 10

1.2.4 Off Resonance Effects 12

1.2.5 Free Induction Decay 13

1.2.6 Bloch Equations 14

1.2.7 Signal detection 19

1.2.8 Spatial Localisation 20

1.2.9 Parallel Imaging 24

1.2.10 Compressed Sensing 26

1.2.11 Motion Sensitising Gradients 27

1.2.12 Intra-Voxel Incoherent Motion 29

1.2.13 Image Artifacts . . . 32
1.2.13.1 Eddy Currents . . . 32
1.2.13.2 Motion Artifacts . . . 33
1.3 Imaging in Pregnancy . . . 34
1.3.1 Ultrasound . . . 34
1.3.2 MRI . . . 35
1.3.2.1 Fetal MRI safety . . . 35
1.3.2.2 Diffusion Weighted Imaging . . . 36
1.3.2.3 Arterial Spin Labelling . . . 37
1.3.2.4 Dynamic Contrast Enhanced . . . 37
1.3.2.5 Half-Fourier Acquisition Single-shot Turbo Spin-Echo . . . 38
1.4 Thesis Outline . . . 38
1.5 Bibliography . . . 39
2 Cohort and Data Collection 46
2.1 Cohort . . . 46
2.2 Data Collection . . . 47
2.2.1 Diffusion Weighted Imaging . . . 48
2.2.2 Phase Contrast Angiography . . . 48
2.2.3 Masking . . . 51
3 Fitting placental DWI data with an Inverse Laplace based approach 52
3.1 Introduction . . . 52
3.2 Theory . . . 54
3.2.1 Inverse Laplace Transform . . . 54
3.3 Methods . . . 56
3.3.1 Outline . . . 56
3.3.2 Setting up the Inverse Laplace Transform . . . 57
3.3.3 Testing the Inverse Laplace Transform . . . 57
3.3.4 Fitting placental data . . . 58

3.4 Results . . . 60
3.4.1 Simulated data . . . 60
3.4.2 Placental Data . . . 62
3.5 Discussion . . . 70
3.6 Conclusion . . . 73
3.7 Bibliography . . . 75

4 Fitting Placental DWI data using an IVIM model; and comparisons with the ILT based approach. 77

4.1 Introduction . . . 77
4.2 Theory . . . 79
4.2.1 Measuring blood flow with IVIM . . . 79
4.2.2 Kurtosis . . . 80
4.3 Methods . . . 80
4.3.1 Data collection . . . 80
4.3.2 Fitting . . . 81
4.3.3 Comparison to ILT . . . 82
4.4 Results . . . 83
4.5 Discussion . . . 92
4.5.1 IVIM vs ILT . . . 95
4.6 Conclusion . . . 97
4.7 Bibliography . . . 98

5 Phase Contrast Angiography in the Placenta. 101

5.1 Introduction . . . 101
5.2 Theory . . . 103
5.2.1 Phase Contrast Angiography . . . 103
5.3 Methods . . . 103
5.3.1 Placental data . . . 103
5.3.2 Magnitude Velocity . . . 103
5.3.3 Inflow and outflow . . . 104
5.3.4 Statistical tests . . . 106

5.4 Results . . . 106
5.5 Discussion . . . 115
5.6 Conclusion . . . 117
5.7 Bibliography . . . 117

6 Rebounding of PGSE data **121**

6.1 Introduction . . . 121
6.2 Theory . . . 123
6.2.1 The IVIM model . . . 123
6.2.2 The sinc model . . . 124
6.2.3 Rephased model . . . 128
6.3 Methods . . . 131
6.3.1 Isochromat simulations . . . 131
6.3.2 Synthetic data . . . 133
6.3.3 Placental data . . . 134
6.4 Results . . . 135
6.4.1 Isochromat simulations . . . 135
6.4.2 Synthetic data . . . 135
6.4.3 Placental results . . . 137
6.5 Discussion . . . 143
6.6 Conclusion . . . 146
6.7 Bibliography . . . 149

7 Effects of PGSE sequence on DWI data **151**

7.1 Introduction . . . 151
7.2 Methods . . . 152
7.2.1 Phantom . . . 152
7.2.2 Imaging . . . 154
7.2.2.1 Diffusion Encoding . . . 154
7.2.3 Flow Encoding . . . 155
7.2.4 Results . . . 156

7.3 Discussion 160
7.3.1 Conclusion 161
7.4 Bibliography 163
8 Summary and conclusions **164**
Appendices **169**
A List of Abbreviations **169**
B ILT of all participants **170**
C IVIM maps of all participants **178**
D PCA results from all participants **189**

List of Tables

2.1 Table of all participants 47

2.2 Table of Participants included in DWI and discarded volumes. . 50

2.3 Outlining the complete PCA data from each participant 51

3.1 Section boundaries the diffusograms were split into. 59

5.1 Mean velocity of inflow and outflow clusters, for HP and CP. . . 112

List of Figures

1.1 a) Schematic of the human placenta, figure originally from [5], b) the placenta split into the ROIs used in this thesis. 2

1.2 Example of proper vs improper spiral artery remodelling 3

1.3 Example of the placental cotyledon 4

1.4 Diagram of Zeeman energy levels 8

1.5 Magnetisation vectors for spins in an external magnetic field . . 10

1.6 Figure showing the recovery of M back to equilibrium 11

1.7 The recovery of M in the rotating reference frame 12

1.8 Detailing how off resonance effects alter the precession of M . . 13

1.9 Figure detailing the FID 13

1.10 Recovery of the M_{xy} and M_z components back to equilibrium . 15

1.11 Graph of how T_1 and T_2 vary by molecular size 16

1.12 The RF pulses needed to generate a spin echo 17

1.13 Detailing how a spin echo is formed 18

1.14 Pulse sequence diagram for spatial localisation 21

1.15 Pulse sequence diagram, and resulting k-space trajectory for EPI 23

1.16 Original image, and wrap around artifact caused by subsampling k-space 24

1.17 Figure outlining how SENSE works to speed up image acquisition 25

1.18 Example PGSE sequence 28

1.19 Phase change for spins in an external magnetic field gradient . . 28

1.20 A randomly orientated capillary network 30

1.21 Example plot detailing the IVIM response 31

1.22 Example molecular displacement for pure Gaussian diffusion, and diffusion with positive kurtosis 31
1.23 How eddy currents affect the PGSE sequence 33

2.1 A single slice of a placenta throughout all b-values 49

3.1 Regularisation of the ILT through an L curve 56
3.2 Flow chart detailing how the placental data was fit using an ILT based approach 58
3.3 Diffusograms from simulated bi-exponential and tri-exponential data 61
3.4 A diffusogram from a placental voxel 62
3.5 A diffusogram that demonstrates all of the typical features in the placental data 63
3.6 Mean individual diffusograms 64
3.7 Mean diffusograms 66
3.8 Mean normalised weighting of each participant at the slowest measured diffusion coefficient 67
3.9 Fraction of voxels with a peak at each diffusion coefficient . . . 67
3.10 Fraction maps from 4 HP and 4 CP 68
3.11 Mean slow, medium, and fast fractions from each participant . . 69

4.1 Example diffusogram produced using the ILT approach 82
4.2 Parameter maps from the IVIM fit 86
4.3 Mean IVIM values from each participant 88
4.4 Standard deviation of k in each participant 89
4.5 D^* histograms 89
4.6 Comparison between ILT and IVIM fit parameters 91

5.1 Outlining how the basal plate mask was transformed to determine the angle of travel of voxels near the basal plate 107
5.2 Velocity maps from a single HP and CP 108

5.3 Mean speed from each participant 108
5.4 f_{IVIM} values from the fastest voxels 110
5.5 Bar chart comparing the mean f_{IVIM} from the fastest, and slower voxels 111
5.6 Comparing the speed of voxels depending on their angle of travel 112
5.7 Example of venous return and clustering 113
5.8 Plots of inflow and outflow clusters 114

6.1 Example of rebounding voxels 122
6.2 Example capillary network and PGSE gradient lobes 124
6.3 How c varies with b value for the gradients used in this experiment 125
6.4 A representation of isotropically distributed velocity vectors, at a constant speed $|v|$ 126
6.5 Diagram showing how Le Bihans sinc refocusing causes rebounds 127
6.6 Detailing the environment needed for rebounds due to the rephased model 128
6.7 Diagram of how the rephased model can cause rebounds 129
6.8 Comparison of the IVIM, sinc, and rephased models 130
6.9 How the rephased model fits the underlying data 131
6.10 An increasing initial signal voxel 135
6.11 Simulated data showing how increasing velocity causes rebounds 136
6.12 Phase histograms detailing how rebounds occur in the rephased model 137
6.13 A comparison of IVIM vs the rephased model for simulated data containing rebounds 138
6.14 Plot showing how v' from the rephased model varies with v_2 . . 139
6.15 4 rephased voxels and their fits 139
6.16 A single central slice from each participant with v' value overlaid for voxels where the rephased model was a significant improvement to the IVIM model 140

6.17 A bar chart of the fraction of voxels from each participant was best described by the sinc and or rephased model 141
6.18 Increasing initial intensity voxels in each participant 142
6.19 Figure detailing how increasing initial intensity voxels could be caused by local field offsets 147

7.1 Schematic of the imaging phantom, and an example PGSE gradient 153
7.2 Detailing how the b value and c value of the two imaging gradient sets varied 155
7.3 Sponge for $\Delta = 23ms$ across all b-values 156
7.4 Underlying data and IVIM fits from a single voxel from sponge 1 and 2 156
7.5 Mean f_{IVIM}, D and D^* from each sponge, from each session . . 157
7.6 Phase histograms from a single imaging session 158
7.7 How the apparent velocity of peak 1 and peak 2 vary with diffusion time 159

Chapter 1

Introduction

1.1 The Placenta

1.1.1 Background

The placenta is an organ that forms during pregnancy and facilitates the transfer of nutrients and waste products between the mother and the fetus while ensuring that the maternal and fetal circulations remain separated. The placenta relies on a steady flow of maternal blood into the organ, which undergoes exchange with the fetal blood pool to ensure the fetus is supplied with sufficient nutrition, and for the removal of waste products such as carbon dioxide [1]. Disruption in the placental system can cause serious complications such as Fetal Growth Restriction (FGR) and/or Pre-Eclampsia (PE) [2, 3], with the latter affecting between 4-5% of pregnancies world wide[4] and posing significant health risks to the mother and fetus with no known cure, other than premature delivery of the fetus.

In this chapter I outline of the basics of placental structure and function, including the flow environments that are of interest for MR measurements, and that are known or theorised to be altered in disease, and provide an overview of imaging methods used to investigate placental haemodynamics.

1.1.2 Maternal Circulation

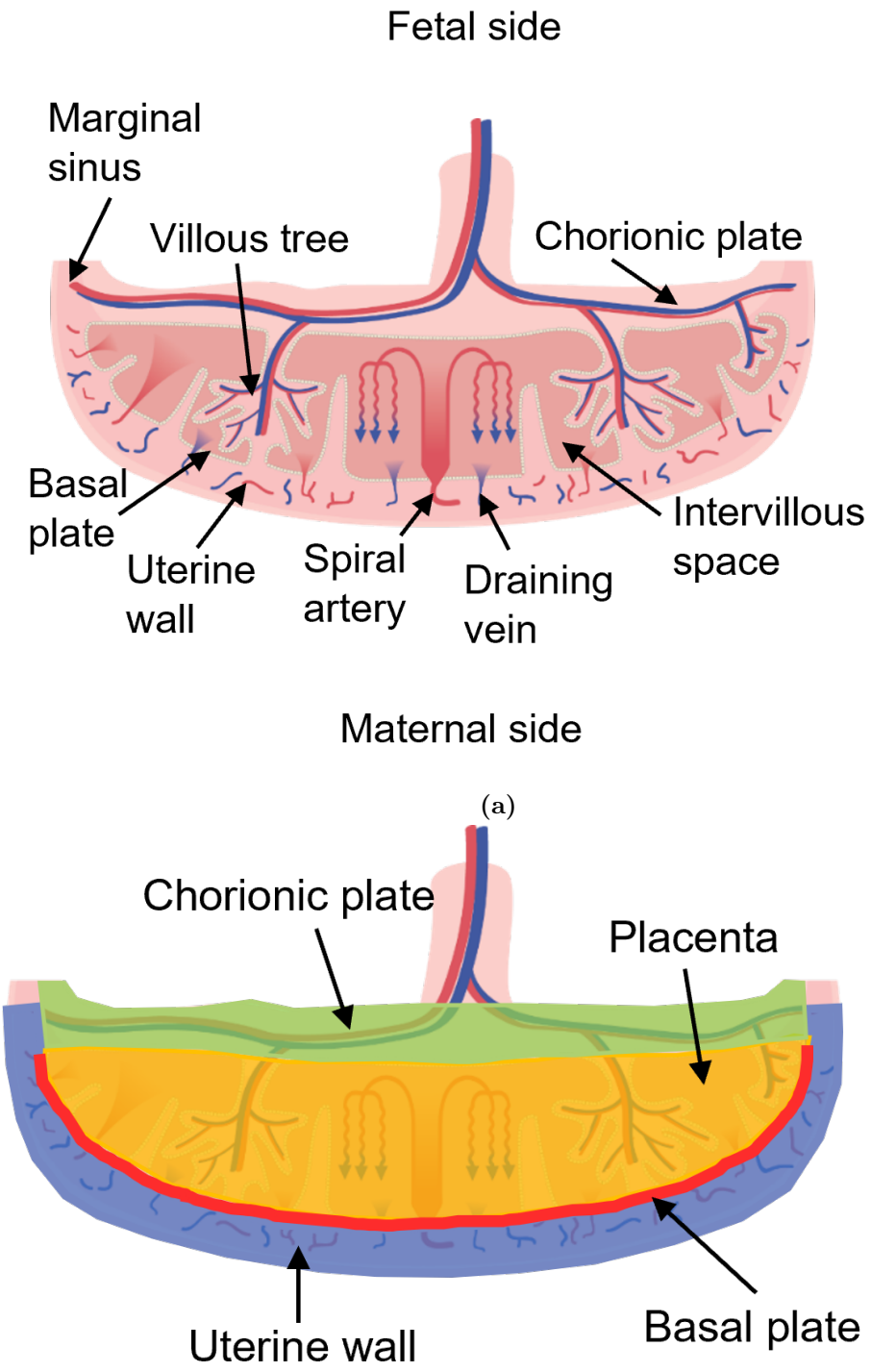


Figure 1.1: *a) Schematic of the human placenta, figure originally from [5], b) the placenta split into the ROIs used in this thesis.*

The path maternal blood takes can be seen in the schematic in **Figure 1.1a**, where the maternal side is on the bottom of the figure. Spiral arteries

supply blood through the uterine wall and basal plate, where it enters the placenta and travels across the width of the intervillous space, then returns to the basal plate and drains through draining veins. Spiral arteries regulate the supply of maternal blood into the placenta, and in early gestation spiral arteries have a terminal diameter of around 0.4-0.5mm, which are eroded by trophoblast cells that widen this diameter up to around 2.5mm[6], where the number of spiral arteries supplying blood to the placenta is not known with estimates ranging from 30-120 arteries [2, 7]. Spiral artery erosion has theoretically been calculated to slow the flow of maternal blood from around 1 m/s for a non-eroded artery, to around 10 cm/s near the terminal end of the spiral artery, which would continue to slow as it travels into the intervillous space[2]. This erosion allows the supply of high volume, low resistance flow into the placenta, which at term is around 600-700 ml/min of blood [7].

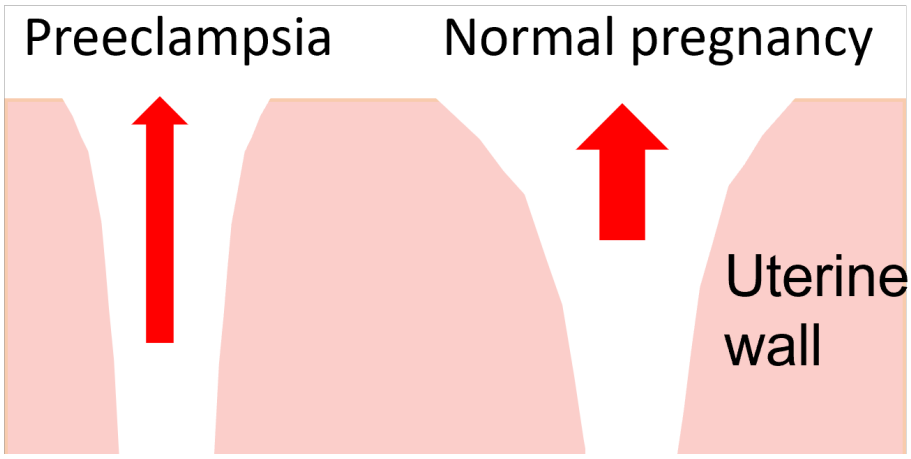


Figure 1.2: *An example of improper vs improper spiral artery remodelling, where the red arrow represents the direction of blood flow. In the left hand artery the path for blood to flow through is narrower, leading to increased flow velocity. In the right hand artery trophoblast cells erode the terminal end of the spiral artery, dampening blood flow providing slower, more turbulent flow into the placenta.*

1.1.3 Fetal Circulation

Fetal circulation comes from the top of **Figure 1.1a**, where fetal blood is supplied to the placenta through the umbilical cord which contains one vein and two arteries. As the fetal flow is a closed loop ultrasound measurements of the umbilical vein can serve as a measure of total fetal blood volume supplied to the placenta, results tend to vary depending on the exact measurement site and study design but at 40 weeks Gestational Age (GA) this flow is thought to be 64mL/min/kg of fetal weight[8]. This blood travels through arteries and veins in the chorionic plate, where it is supplied to fetal villous trees which bathe in the maternal circulation within the intervillous space. As fetal blood is sequestered in the villous trees, the exchange between the maternal and fetal blood pools occurs without direct mixing. Some of these villous trees will extend across the placenta and will anchor to the basal plate, adding to the structural stability of the placenta, with others freely suspended in the maternal blood [7]. These villous trees are within placental cotyledons, shown in **Figure 1.3a** and **1.3b** which are shown from side on, and top down (from the maternal side) views. The number of placental cotyledons varies, with one study reporting between 3 and 37 cotyledons per placenta[9], but typically this number is expected to be between 15-28 cotyledons[7].

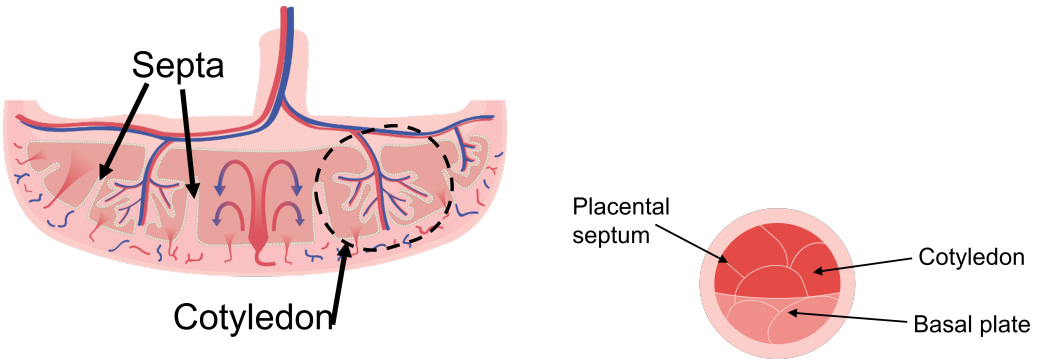


Figure 1.3: *a) A side on schematic of the placenta, with a cotyledon highlighted, and the septa from another cotyledon labelled. b) A top down view from the maternal side of the placenta, with the basal plate partially peeled back to show the cotyledons.*

1.1.4 Preeclampsia and Fetal Growth Restriction

PE typically develops after 20 weeks of pregnancy, and while the exact cause is unknown risk factors include diabetes, high blood pressure, autoimmune conditions, having previous pregnancies afflicted with PE, obesity, multiple gestation, and first pregnancy. PE is defined as new onset high blood pressure after 20 weeks of pregnancy and the presence of protein in urine after 20 weeks. PE has serious short term and long term health implications for the mother, where in the short term PE can lead to liver damage, kidney injury, stroke, and severe cases can lead to eclampsia which is indicated by maternal seizures. Worldwide PE affects approximately 4.6% of pregnancies, and eclampsia 1.4% [10], which combined are estimated to cause over 70 000 maternal deaths, and 500 000 fetal deaths annually worldwide[11], with accurate reporting difficult as most deaths occur in low or middle income countries. There is no cure for PE, with the condition only subsiding after delivery of the fetus, meaning treatment typically focuses around treating symptoms such as managing high blood pressure with medical or lifestyle interventions. Typically the mother is closely monitored and labour is induced between the 37^{th} to 38^{th} week of pregnancy, and after delivery both mother and fetus are closely monitored as complications can still arise a few days after birth[12]. PE can also cause FGR, but it is not the only risk factor as other placental insufficiencies due to either maternal causes such as anemia, maternal weight (either high or low BMI), substance use, and diabetes or fetal factors including infection, and multiple gestation. FGR is defined as a fetus which does not reach its expected size, and is caused by failure to provide sufficient oxygen and nutrition to the fetus. While most fetuses are still delivered normally, in the UK FGR is the most significant risk factor for stillbirth[13] and is associated with neonatal and perinatal morbidities[14]. Treatment can involve addressing maternal factors where possible (e.g. cessation of smoking during pregnancy or maintaining a healthy diet), and close monitoring of the fetus after delivery. In PE and FGR

it is reported that there is insufficient spiral artery erosion relative to those observed in a healthy pregnancy (**Figure 1.2**). This would result in faster flowing jets of blood to enter the placenta, instead of the slower, turbulent stream of blood that spiral artery erosion is thought to provide [2]. While the same volume of blood is supplied to the placenta, the pulsatile flow from improper spiral artery remodelling is thought to disrupt placental perfusion causing damage to the placenta through hypoxia, and the force of the jets could damage the fetal villous trees that are near to, or anchored to the basal plate [2, 3]. These effects can also impair the function of the villous trees through mechanisms including oxidative stress, infarction, inflammation, and high maternal blood pressure, which cause either damage to the villous trees, or affect the balance between maternal and fetal exchange[3].

1.2 Magnetic Resonance Imaging

Magnetic resonance imaging provides unique opportunities to study the structure of the placenta, and the maternal and fetal flows described here. Diffusion Weighted Imaging (DWI) has already been shown to be a marker of placental dysfunction[5, 15, 16, 16–20], where the small scale motion of blood is altered, typically around the periphery of PE placentas. In this thesis I aim to investigate the DWI signal further, by using a data-driven fitting approach and comparing with a more standard analysis pipeline for placental DWI, which I combine with measures of bulk flow of blood (Phase Contrast Angiography, PCA) to provide better understanding of the placental environment. In this section I outline the principles of MRI, starting from an explanation of the Nuclear Magnetic Resonance (NMR) phenomenon which is the basis of MRI, and discuss safety concerns present when scanning pregnant women.

1.2.1 Net Magnetisation

The magnitude of the spin angular momentum of a nucleus is given by

$$|L| = \hbar\sqrt{I(I+1)} \tag{1.1}$$

where all nuclei posses a nuclear spin I which describes the spin angular momentum of a nucleus and is discretised into integer, or half integer values. Any nucleus with non-zero I can be detected with NMR, as I gives rise to a nuclear magnetic moment

$$\boldsymbol{\mu} = \gamma \mathbf{I} \tag{1.2}$$

where γ is the gyromagnetic ratio which is different for each atomic species, has units MHz/T and describes how nuclear spin interacts with an applied external field. As I is quantised, so is the angular momentum, where for a magnetic field applied in the z direction

$$\mu_z = \gamma \hbar m_I \tag{1.3}$$

where

$$m_I = -I, -I+1, \ldots, I. \tag{1.4}$$

A nuclear spin will posses an energy E depending on its orientation to a magnetic field $\boldsymbol{B}$ of

$$E = -\boldsymbol{\mu} \cdot \boldsymbol{B} \tag{1.5}$$

where for a magnetic field applied along a single axis B_0

$$E = -\gamma \hbar m_I B_0 \tag{1.6}$$

this results in a finite number of energy states, depending on the nuclear spin I. For a hydrogen nucleus, $I = \frac{1}{2}$, this corresponds to two spin states $m_I = -\frac{1}{2}$ and $\frac{1}{2}$, and therefore two energy states $E = \pm\gamma\hbar\frac{1}{2}B_0$ which are shown in

Figure 1.4. From **Equation 1.6** for the spin $I = \frac{1}{2}$ system the high energy

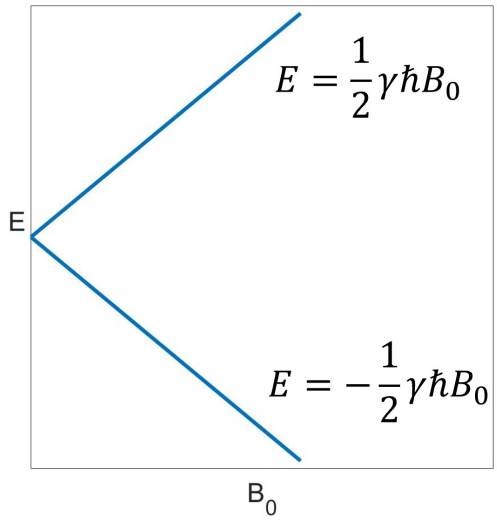


Figure 1.4: *Diagram showing how the two energy levels of a spin $\frac{1}{2}$ nucleus vary in the presence of a background field B_0, applied in one direction.*

state ($m_I = -\frac{1}{2}$) occurs when the magnetic moment is aligned anti-parallel to the magnetic field, and the low energy state ($m_I = \frac{1}{2}$) corresponds to the magnetic moment aligned parallel. The difference in energy between these two states

$$\Delta E = \gamma\hbar B_0 \tag{1.7}$$

is known as the Zeeman equation, when if combined with Planck's equation

$$\Delta E = hv \tag{1.8}$$

this describes how the energy of a system can change by either the emission or absorption of a photon of frequency v, where h is Planck's constant and gives the Larmor equation

$$\omega_0 = \gamma B_0. \tag{1.9}$$

The Larmor equation describes how transitions in energy states can be induced by application of electromagnetic radiation of angular frequency ω_0, for a nucleus of gyromagnetic ratio γ, in a static background field B_0. At absolute zero spins would be in the low energy state, but due to random collisions of

molecules due to thermal effects at higher temperatures spins can occupy the higher energy state, where an equilibrium ratio between high and low energy spins can be described using a Boltzmann distribution where the ratio of the number of high energy spins $N_{-\frac{1}{2}}$ and low energy spins $N_{\frac{1}{2}}$

$$\frac{N_{\frac{1}{2}}}{N_{-\frac{1}{2}}} = e^{-\frac{\Delta E}{k_b T}} = e^{-\frac{\gamma \hbar B_0}{k_b T}} \tag{1.10}$$

where k_b is the Boltzmann constant and T is the temperature in Kelvin. Providing $k_b T \gg \gamma \hbar B_0$

$$\frac{N_{\frac{1}{2}}}{N_{-\frac{1}{2}}} \approx 1 - \frac{\gamma \hbar B_0}{k_b T} \tag{1.11}$$

and this difference in populations provides a net magnetisation vector

$$M_0 \approx \frac{\gamma^2 \hbar^2 N_s B_0}{4 k_b T}. \tag{1.12}$$

While in quantum mechanical terms spins do not have to exist in a single parallel or anti parallel state, and are instead some linear combination of the two states this interpretation is not required for the work in this thesis, and a classical explanation of NMR will be considered starting from this net magnetisation M_0.

As spins posses angular momentum, spins are aligned either parallel or anti-parallel to the B_0 field and precess around it, shown by the red arrows in **Figure 1.5a**, with more spins aligned in the lower energy parallel state which provides a net magnetisation along the direction of the field (**Figure 1.5b**).

1.2.2 Chemical shift

The exact rate of precession of magnetisation depends on the field experienced by a spin, and while B_0 is ideally constant over all spins, the local field experienced B_{loc} can vary as nuclei are shielded from the B_0 field. Shielding occurs as the Larmor precession of atomic electrons' in the B_0 field induce a field B_{ind}

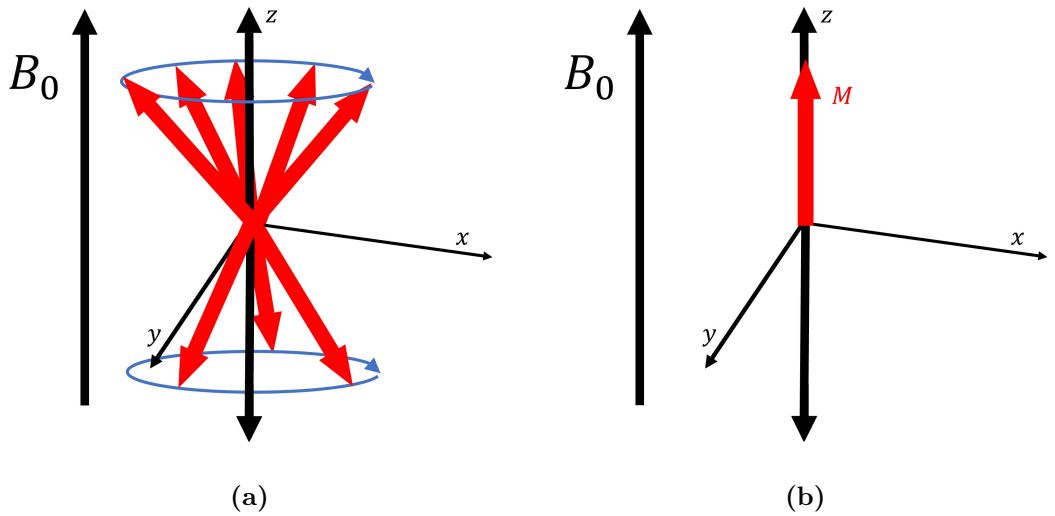


Figure 1.5: *a) Magnetisation vectors from individual spins, where more favour the low energy state parallel to B_0, these vectors when summed provide the bulk magnetisation $\boldsymbol{M}$ in b).*

that opposes B_0 and reduces the field experienced by the nucleus

$$B_{loc} = B_0 - B_{ind} \tag{1.13}$$

Additional shielding or deshielding can occur as electronegative atoms can draw electrons towards themselves, which reduces the electron density of neighbouring nuclei providing a negative shielding constant. As nuclei experience different local fields depending on their environments their Larmor frequency will be offset by an amount known as the chemical shift, which is defined as the relative difference in the frequency of a spin under investigation $v_{measured}$, and the frequency of some reference compound v_{ref}

$$\delta = \frac{v_{measured} - v_{ref}}{v_{ref}}. \tag{1.14}$$

1.2.3 Resonance

A magnetic moment ($\boldsymbol{M}$) within a magnetic field ($\boldsymbol{B_0}$) experiences a torque

$$\boldsymbol{\tau} = \gamma \boldsymbol{M} \times \boldsymbol{B_0} \tag{1.15}$$

which is acts perpendicular to the angular momentum $\boldsymbol{L}$, causing $\boldsymbol{M}$ to precess around the direction of the magnetic field. In MRI the net magnetisation vector $\boldsymbol{M}$ is intentionally tipped out of alignment with the B_0 field, using a time varying field perpendicular to B_0 that oscillates at ω_0 and is applied by using a radio frequency pulse to generate a time varying field composed of two components, one oscillating clockwise and one oscillating anti-clockwise. We only consider the component of $B_1(t)$ that oscillates in the direction of ω_0

$$\boldsymbol{B_1}(t) = B_1 cos\omega_0 t\mathbf{i} - B_1 sin\omega_0 t\mathbf{j} \tag{1.16}$$

where **i** and **j** represent unit vectors in the x and y axis since the other component is very off resonance to the spins and has no significant effect on the dynamics of the magnetisation. This field provides a torque that causes $\boldsymbol{M}$ to oscillate around B_1 and can be used to tip $\boldsymbol{M}$ into the xy plane. After this $\boldsymbol{B_1}$ field is switched off $\boldsymbol{M}$ precesses around the static field B_0, but also recovers back to equilibrium, as shown in **Figure 1.6**. Because of this precession it is

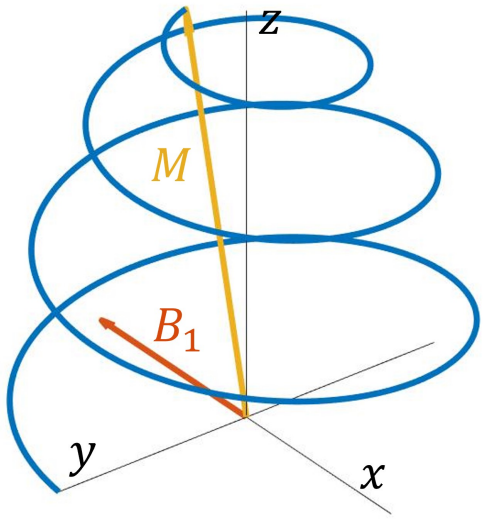


Figure 1.6: *Figure showing the recovery of M after the field marked B_1 is switched off in the laboratory reference frame where the blue line represents the path of the M.*

easier to describe the effects of RF pulses on M using the rotating reference frame, where the xy plane in **Figure 1.7** can now be seen to be rotating about

the z axis at the Larmor frequency, transforming into coordinates x', y', and z'. In this rotating frame the B_1 field tips M into the the xy plane by an angle defined as the flip angle

$$\alpha = \gamma B_1 t \tag{1.17}$$

depending on the magnitude of the B_1 field, and the duration it is applied for (t).

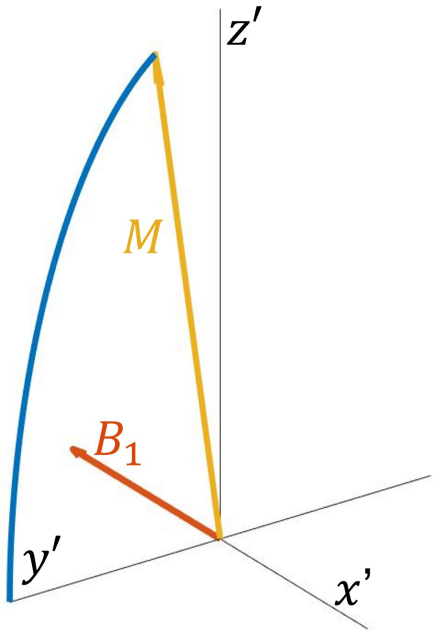


Figure 1.7: *Figure showing the recovery of M after the field marked B_1 is switched off in the rotating frame, where the blue line represents the path of the M.*

1.2.4 Off Resonance Effects

If B_1 is applied at some frequency ω_1 where $\omega_1 \neq \omega_0$ then in the rotating frame (which is rotating at ω_1) there will be a component $(B_{z'})$ of the B_0 field

$$B_{z'} = \frac{f_0 - f_1}{\gamma} \tag{1.18}$$

which remains and contributes to the applied B_1 field. This creates an effective field B_{eff} which M will now precess around, shown in **Figure 1.8**, instead of just precessing around B_1.

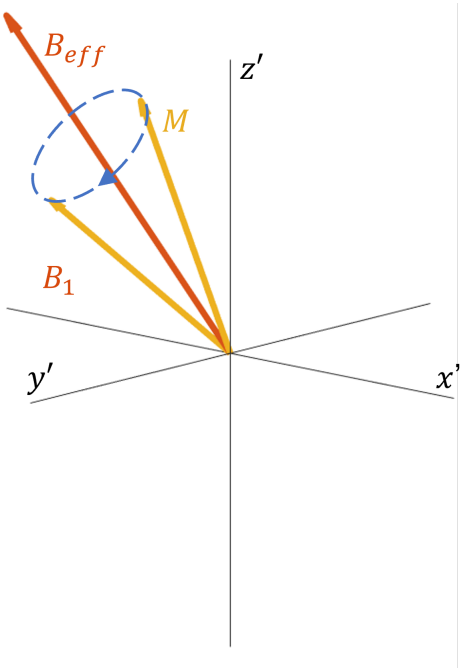


Figure 1.8: *Figure showing the recovery of M after the field marked B_1 is switched off, where the blue line represents the path of the M.*

1.2.5 Free Induction Decay

The net magnetisation in the xy plane can be detected using a receiver coil, as $\boldsymbol{M}$ precesses it induces a voltage that can be measured. For a 90° pulse that rotates the magnetisation into the xy plane, the Free Induction Decay (FID) can be measured (**Figure 1.9**) where the signal

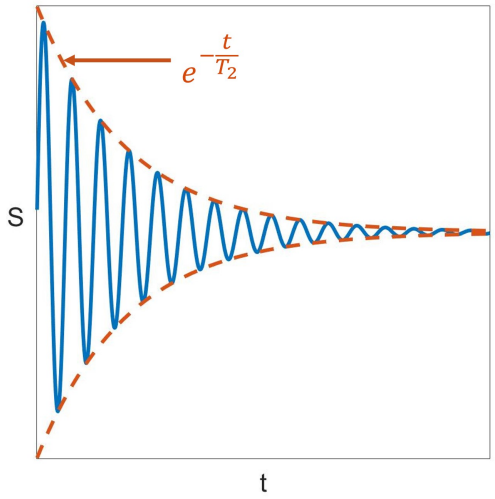


Figure 1.9: *Figure showing the FID*

$$S = sin(\omega_0 t) e^{-\frac{t}{T_{2^*}}}. \tag{1.19}$$

oscillates at the Larmor frequency, and decays at a rate T_2 as defined next by the Bloch equations.

1.2.6 Bloch Equations

The rotation of M in a time varying field can be described by the Bloch equations, which consider the recovery of M as

$$\frac{d\boldsymbol{M}}{dt} = \gamma \boldsymbol{M} \times \boldsymbol{B}. \tag{1.20}$$

Bloch in 1964 extended this equation to include a phenomenological description of the rate at which the magnetisation returns to equilibrium following perturbation by an RF pulse. The longitudinal recovery (along z) occurs at a rate T_1 and is described by

$$\frac{dM_z(t)}{dt} = \frac{M_z(t) - M_0}{T_1} \tag{1.21}$$

and the transverse components (xy) returns to equilibrium at a rate T2 described by

$$\frac{dM_x(t)}{dt} = \frac{M_x(t)}{T_2} \tag{1.22}$$

$$\frac{dM_y(t)}{dt} = \frac{M_y(t)}{T_2} \tag{1.23}$$

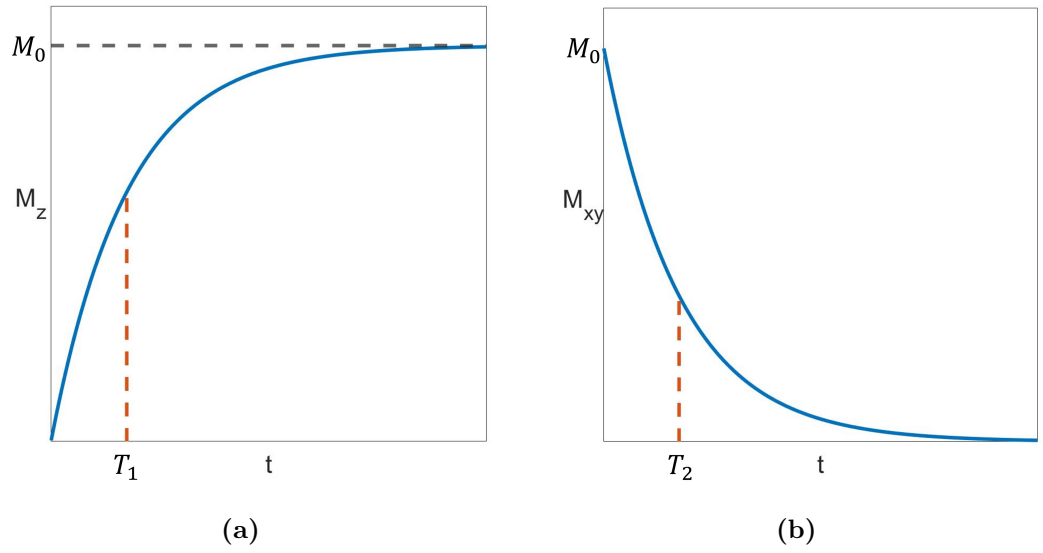
Following a 90° pulse which tips the magnetisation into the xy plane, the solution to $M_z(t)$ is

$$M_z(t) = M_0(1 - e^{-\frac{t}{T_1}}) \tag{1.24}$$

where $M_z(0)$ is the initial M_z magnetisation before recovery. By combining the xy transverse terms

$$M_{xy}(t) = M_{xy}(0) e^{-\frac{t}{T_2}}. \tag{1.25}$$

For a 90° pulse the magnetisation M_z and M_{xy} vary over time as shown in **Figure 1.10a** & **1.10b**, where T_1 defines the time taken for M_z to recover (1-$\frac{1}{e}$) of the initial signal, and T_2 the time taken for signal to decay to $\frac{1}{e}$ of its initial value.



(a) **(b)**

Figure 1.10: *a) Recovery of the M_z component back to equilibrium, where the relaxation time T_1 is labelled. b) Recovery of the M_{xy} component back to equilibrium, where the relaxation time T_2 is labelled.*

T_1 and T_2 relaxation are largely driven by dipole interactions between spins. T_1 relaxation is most efficient when molecules are free to tumble at the Larmor frequency, which induces fields that cause fast T_1 relaxation in neighbouring molecules. If molecules are bound in solids and tumble too slowly, or are free in water and tumble too quickly the induced field is not optimal for T_1 relaxation and these materials will have higher T_1.

Any process that causes T_1 will also have an impact on T_2, as recovery of the longitudinal component will diminish the transverse component of the magnetisation. T_2 is also enhanced by low frequency dipole dipole interactions as spins that are rotating more slowly (e.g. due to hydrogen bonding) will experience a more stable (slower varying) local magnetic field, which either adds or subtracts from B_0 causing nearby spins to precess at an altered ω_0. This causes spins to no longer precess at the same rate, as some precess faster

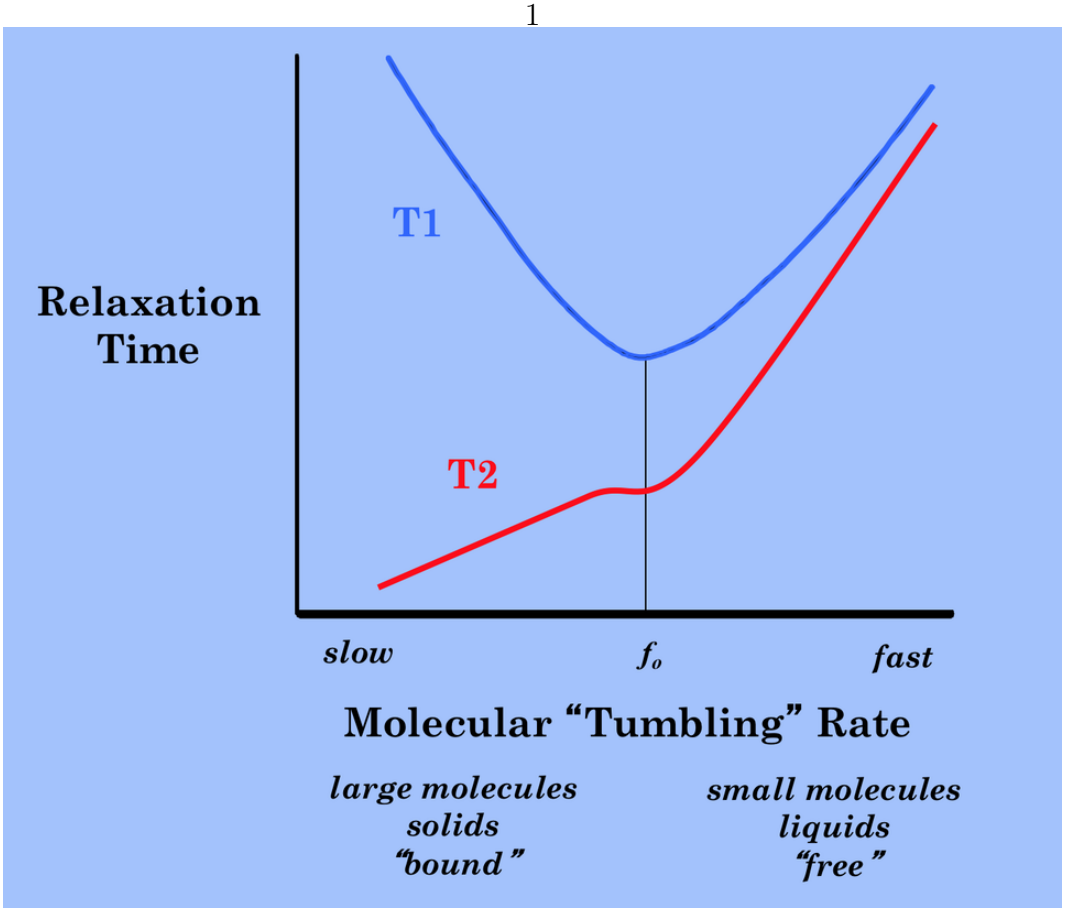


Figure 1.11: *Graph of how T_1 and T_2 relaxation time vary by molecular size. Figure Courtesy of Allen D. Elster, MRIquestions.com.*

and some slower than the average which diminishes the net xy projection of M. This signal decay can be recovered in the form of a spin echo, if following the 90° pulse which tips the magnetisation into the xy plane a 180° pulse is added after a time $\frac{TE}{2}$ as shown in **Figure 1.12**. This echo forms as the initial 90° pulse tips M into the xy plane (**Figure 1.13a**), where T_2 decay causes signal loss as spins precess at different rates and fan out, with some precessing faster and some slower (**Figure 1.13b**) as local magnetic fields may be different for each spin. By following this with a 180° pulse after a time $\frac{TE}{2}$ the magnetisation vectors of each spin are flipped (**Figure 1.13c**), now the spins that were precessing faster and have travelled the furthest away from the x-axis are now travelling back towards it, and begin to catch up with the slow precessing spins. This causes an echo at the echo time TE as M recovers,

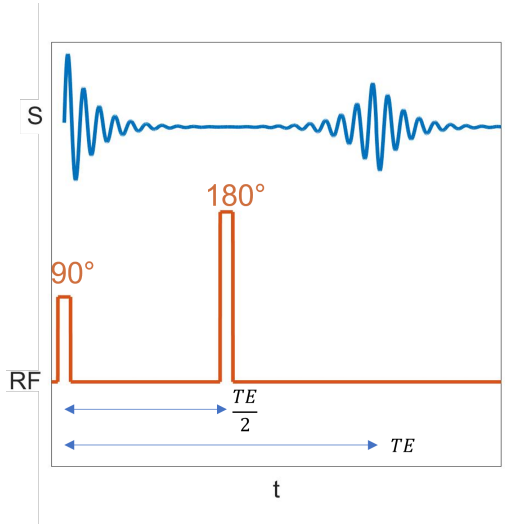


Figure 1.12: *The RF pulses needed to generate a spin echo, and resulting signal with Echo time TE labelled.*

and in the absence of any further gradients decays again.

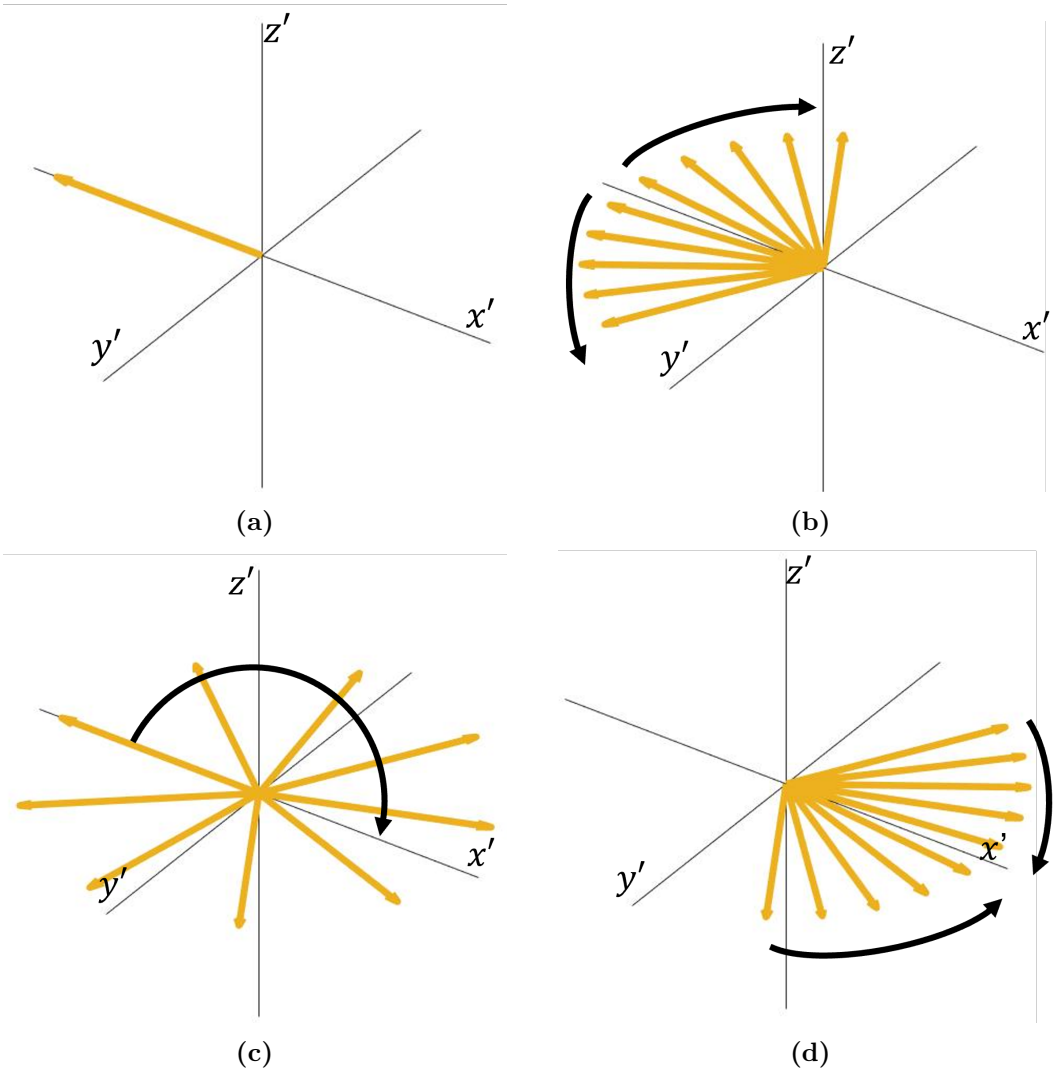


Figure 1.13: *How a spin echo is formed ignoring T_1 contributions in the rotating frame. a) Following a 90° pulse about y' spins are tipped into the $x'y'$ plane, where they begin to fan out in b) with some spins travelling faster and others slower depending on the local field experienced. At c) a 180° inversion pulse is applied which flips the magnetisation, and now causes spins to travel back together in d) forming an echo.*

In practice the echo produced will not match the initial FID intensity as spins will experience time varying inhomogeneity in the local field, which cannot be rephased. The observed rate of transverse decay is further reduced due to variations in the local field caused by inhomogeneities in the B_0 field, or due to susceptibility differences within the tissue being imaged (which are recovered by the 180° pulse), and in this case the rate of transverse decay of the original FID is known as T_{2^*} where

$$\frac{1}{T_{2^*}} = \frac{1}{T_2} + \frac{1}{T_{2_i}} \tag{1.26}$$

and is the sum of contributions from the 'true' T_2, and T_{2_i} which is due to field inhomogeneities. When the spin echo in **Figure 1.13** is formed effects due to local field inhomogeneities T_{2_i} are refocused, as they are constant. Effects due to T_2 interactions however are time varying, and as such can not be refocused by the gradients as spins will experience different effects while the spins 'fan out' and 'fan back together' in **Figure 1.13** meaning the echo formed will not recover the full magnetisation vector M.

1.2.7 Signal detection

The signal detected in MRI is due to the precession of the magnetisation vector M which induces a current in two coils positioned in quadrature. One coil is called I (for in phase) and the second Q (for in quadrature), where theoretically the two signals should be identical copies, with a 90° phase shift between them, but noise in detection causes differences in signal. Signal is considered to be a complex conjugate, where I provides the 'real' information and Q is 'imaginary', but the distinction between the two channels is arbitrary. This allows the magnitude of the two signals, the real component, the imaginary component, and the phase difference between the two signals to be recorded. These signals contain information about all spins in the imaging sample, to

produce 2D or 3D images one needs to determine the locations of spins within the sample.

1.2.8 Spatial Localisation

To produce 2D or 3D imaging data spins need to be spatially encoded so it is possible to tell where in the body signals originate from. In MRI one method is to only excite a slab of spins (referred to as a slice), by adding a field gradient G_z which adds a field offset depending on the position z meaning the Larmor frequency is now spatially dependent

$$\omega_0 = \gamma(B_0 + G_z z). \tag{1.27}$$

If G_z is applied in the z direction, each slice then covers a range of frequencies

$$\Delta f = \frac{\gamma}{2\pi} G_z z \tag{1.28}$$

and a slice selection encoding gradient can be used to excite only spins in a slice of thickness

$$\Delta z = \frac{2\pi \Delta f}{\gamma G_z} \tag{1.29}$$

where the slice thickness is usually controlled by altering G_z. The slice selection module is shown in **Figure 1.14**, and is applied during RF excitation pulses to only excite the desired nuclei. While it is now possible to select a slice in z the information about the x and y locations of the spins needs to be determined. This is done by a mixture of frequency and phase encoding, as MR image data is a combination of signal amplitudes A, fundamental frequencies ω, and phase shifts ϕ from all spins in an entire slice. For one dimension (x, for example) spins can be frequency encoded by applying a field gradient across the image which causes ω to vary with position in the x axis

$$\omega(x) = \gamma(B_0 + G_x x). \tag{1.30}$$

Now the x position of any given spin is stored in its frequency of oscillation, which can be determined by moving from the time domain, to the frequency domain by taking the 1D Fourier transform of the signal

$$S(\omega) = \int_{-\infty}^{\infty} s(t) e^{-i\omega t} dt \tag{1.31}$$

which produces a histogram of frequencies present in the signal or projection along the x axis. To determine the y location phase encoding is used, where unlike in frequency encoding, a constant gradient is not required. Instead by applying a gradient G_y for a short period of time τ before collecting the signal, the Larmor frequency as measured at collection is still $\omega_0 = \gamma B_0$, but there is now a positionally dependent phase shift of

$$\phi(y) = \gamma \tau G_y y \tag{1.32}$$

relative to a spin at $y = 0$. By combining these techniques and using a slice

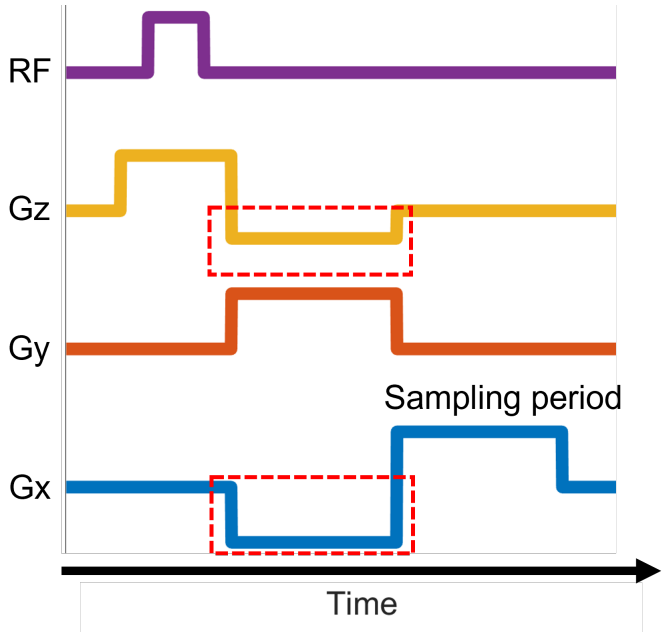


Figure 1.14: *Detailing how the G_z slice select, G_y phase encoding, and G_x frequency encoding gradients combine to allow for spatial localisation of spins in MRI. Gradients marked with the red dashed lines are required to ensure dephasing caused by the imaging gradients is removed by the centre of the sampling period.*

selection gradient, while a gradient G_x is applied, after a short G_y gradient

one can capture frequency and phase dependent information which contains the spatial location of spins. The signal $S(t)$ is therefore affected by frequency and phase encoded oscillations

$$S(t) = \int\int\int \rho(x,y) e^{-i\omega_0 t + i\gamma G_x x t + i\gamma G_y y t'} dx dy dt' \tag{1.33}$$

where the Larmor frequency term $e^{-i\omega_0 t}$ represents the oscillation of the spins, and is filtered out, and $\rho(x,y)$ represents the spin density. In the frequency domain (also known as k-space) k_x and k_y can be defined as

$$k_x = \gamma G_x t_x \tag{1.34}$$

and

$$k_y = \gamma G_y t_y \tag{1.35}$$

meaning **Equation 1.33** can be written in terms of k_x and k_y

$$S(k_x, k_y) = \int\int \rho(x,y) e^{-i[k_x + k_y]} dx dy \tag{1.36}$$

where now a 2D Fourier transform can recover $\rho(x,y)$

$$\rho(x,y) = \int\int S(k_x, k_y) e^{-i[k_x + k_y]} dk_x dk_y. \tag{1.37}$$

To produce the density $\rho(x,y)$ the signal $S(k_x, k_y)$ is sampled across k-space. In this thesis all data were sampled using Echo Planar Imaging (EPI), with an example shown in **Figure 1.15**. By applying gradient slice selection G_z, then travelling to the edge of k-space using the frequency encoding (G_x) and phase encoding (G_y) gradients, then traversing across k_x, and up k_y sampling the signal to collect a map of k-space.

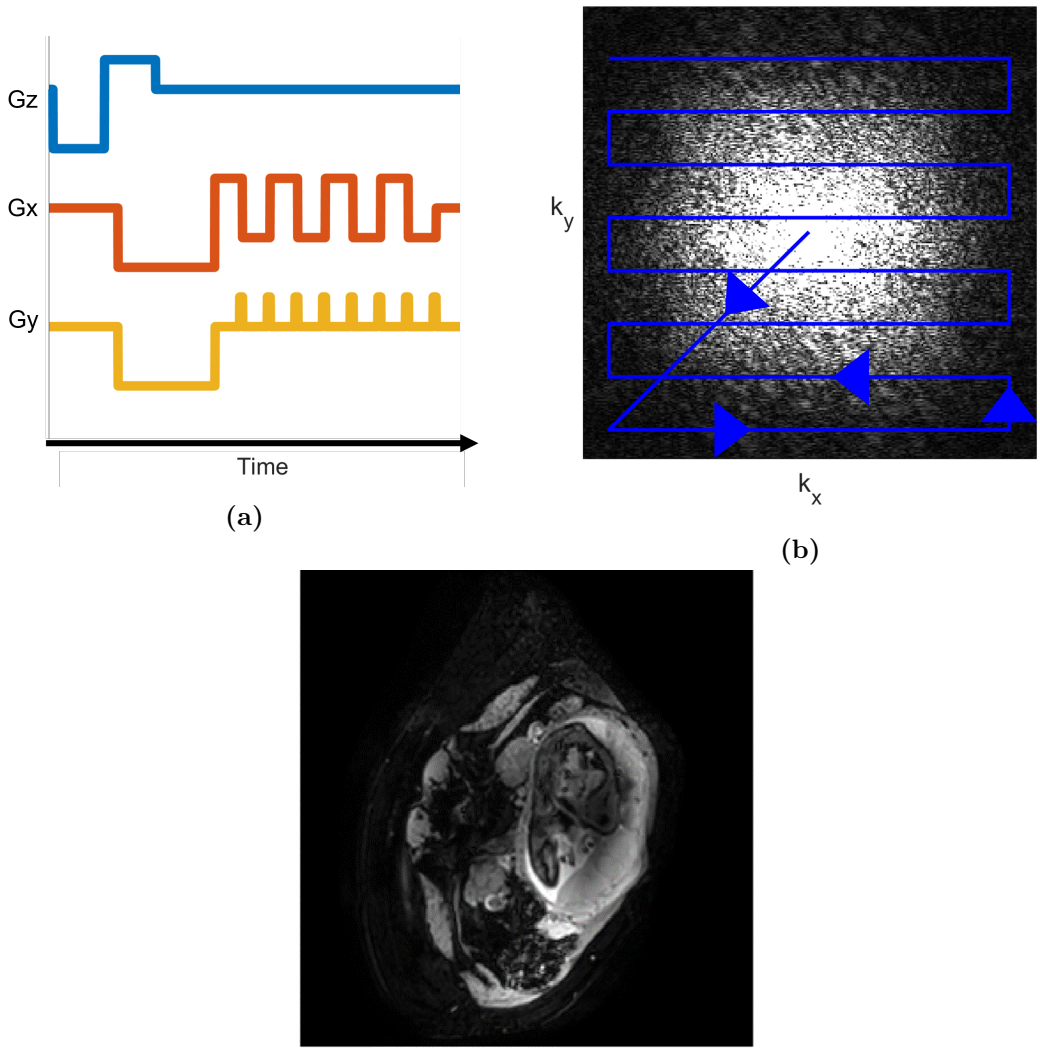
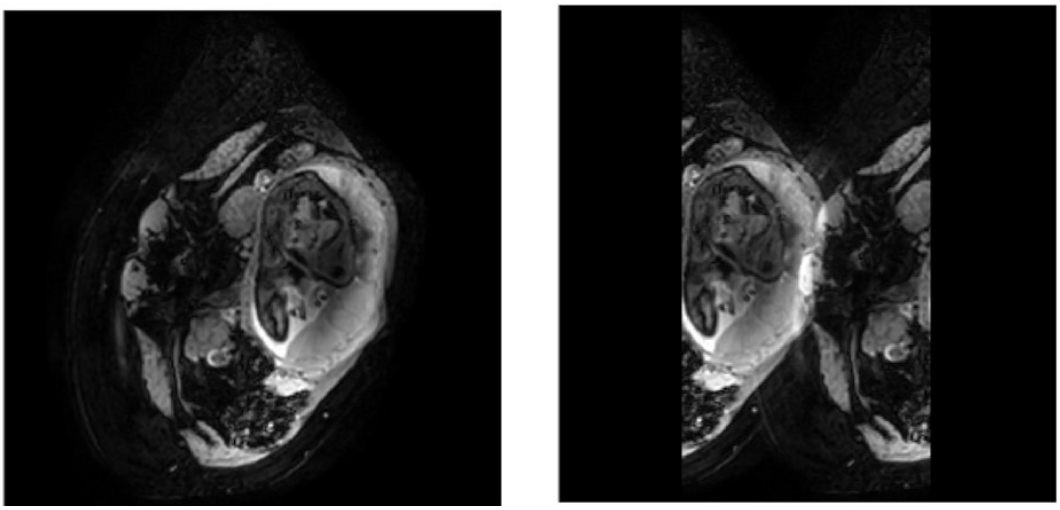


Figure 1.15: *a) Example gradients G_z G_x and G_y that enable a single slice of k-space to be sampled using EPI. b) The path the gradients in a) take through k-space. c) An example 2D imaging slice produced using EPI.*

1.2.9 Parallel Imaging

To increase sensitivity and reduce the number of k-space samples that need to be acquired parallel imaging can be used, where the position of receive coils can be used to provide spatial information about the MR signal. By sampling fewer lines of k-space imaging time is greatly reduced, but this results in a reduced Field Of View (FOV) and causes aliasing as shown in **Figure 1.16** as less spatial frequencies are collected. SENSitivity Encoding (SENSE) is a

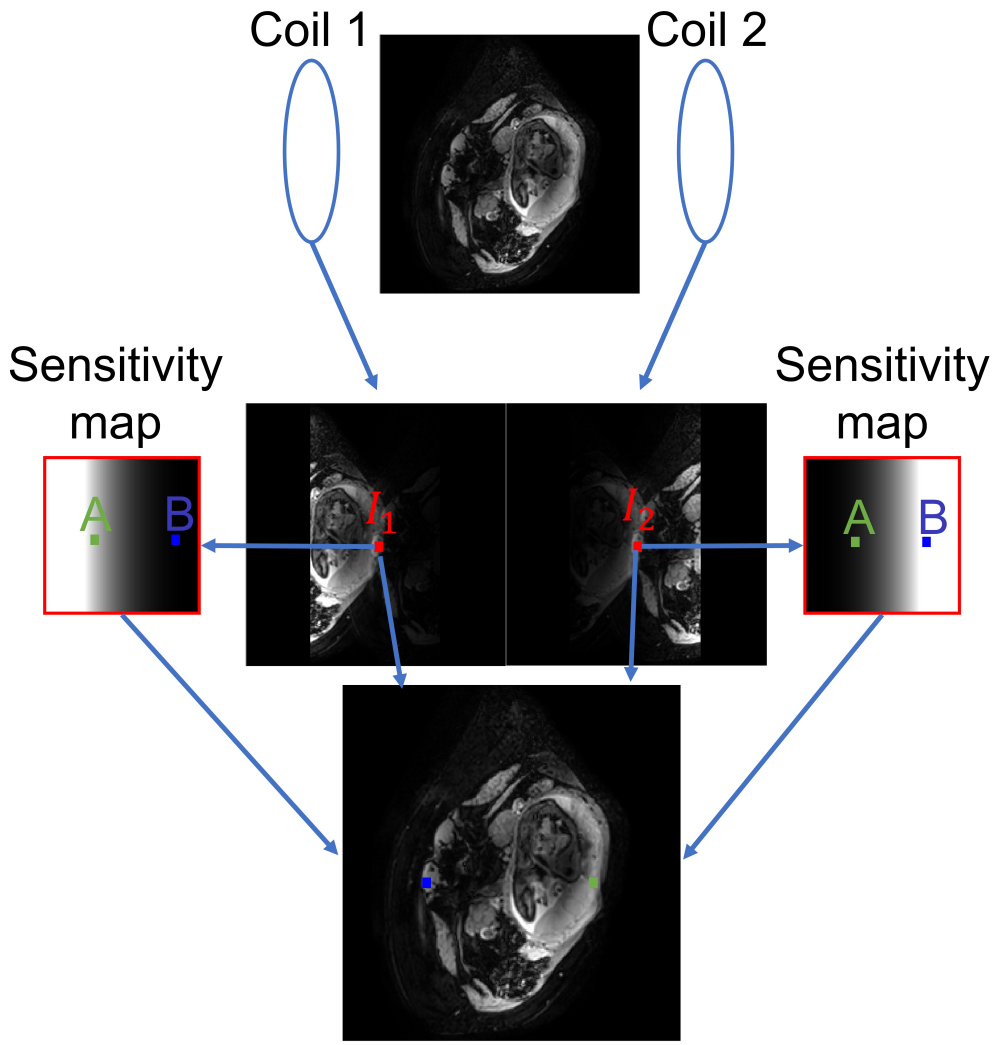


(a) **(b)**

Figure 1.16: *a) Original MR image of size 256x256 voxels, reconstructed by sampling every line of k-space. b) MR image produced from sampling K_x 128 times, skipping every other line of k-space (a SENSE factor of 2).*

parallel imaging method that can 'unfold' the aliased image to generate the image in **Figure 1.16a**, starting with **Figure 1.16b**. SENSE relies on the fact that signals will have higher intensity the closer they are to an imaging coil, for example the two coils in **Figure 1.17a**. Coil sensitivity maps are produced prior to imaging, which describe the strength of signal received at different positions relative to the coil for the full FOV. Next the desired pulse sequences can be used, where for the example in **Figure 1.16b** imaging has been accelerated by reducing the number of k-space points sampled by a factor of 2. From **Figure 1.17** each coil with produce an image which contains aliasing, so a single voxel will have signal contributions from two spatial locations within the final image. For the same point measured from coil 1 with intensity

I_1, and from coil 2 with intensity I_2, both are a linear combination of signal from two separate spatial locations A and B in the full FOV image. As the coil sensitivity maps at A and B ($Smap_{1a,1b}$ and $Smap_{2a,2b}$) are already known, the image can be unwrapped and the intensities at A and B in the full FOV image can be calculated by solving two simultaneous equations



(a)

Figure 1.17: *Example figure outlining how SENSE can be used for two coils; where one is on each side of the imaging target to unfold the aliased image, based on coil sensitivity maps.*

$$I_1 = Smap_{1a} \cdot A + Smap_{1b} \cdot B \tag{1.38}$$

$$I_2 = Smap_{2a} \cdot A + Smap_{2b} \cdot B \tag{1.39}$$

1.2.10 Compressed Sensing

Another method to increase the speed of data acquisition is to undersample k-space in a pseudorandom manner, provided the data are sparse, or can be transformed into a relatively sparse form. Sampling cannot be too random, as it is important to ensure sufficient sampling of the centre of k-space which contains the low spatial frequency information, which corresponds to the general shape of the image, the brightness, and contrast which are vital to image reconstruction. At the same time if sampling is too coherent skipped regions of k-space would produce aliasing effects, causing wrap around artifacts. If sampling is appropriately pseudorandom the reconstructed image will still resemble the imaging target, but will have noise present due to the undersampling, which is smoothed across the entire image. The noise present in this image is of low intensity and can be filtered out of the background voxels via thresholding, as the reconstructed image is sparse. By carrying out an inverse Fourier transform to convert this thresholded image back into k-space it should be similar to the initial k-space sampling, but as noise components have been thresholded out differences in the two k-spaces are likely to be due to noise and can be removed, and similarities are likely due to image data and can be kept. This process of image reconstruction, thresholding, taking an inverse Fourier transform, and comparing back to the initial k-space sampling can be repeated until the solution converges. This allows for faster imaging by subsampling k-space, while still providing excellent image quality.

1.2.11 Motion Sensitising Gradients

Throughout the experimental chapters of this thesis I used motion sensitising gradients to measure the movement of blood throughout the placenta. In MRI motion can be encoded using a Pulse Gradient Spin Echo (PGSE) sequence which uses magnetic field gradients to cause spins to accumulate phase depending on their position. This process is similar to the spin echo (**Section 1.2.6**) where signal decay is caused by differences in precession of spins based on local field, which are time varying and cannot be recovered following the 180° inversion. If instead one applies an external field gradient across the ensemble of spins being imaged, this will also cause spins to precess at different rates, depending on their position within the gradient, and for a magnetic field gradient applied in the x direction, will acquire a phase

$$\phi(t) = \gamma \int_0^t G(t)x(t)dt. \tag{1.40}$$

In PGSE two gradients are used either side of the 180° inversion pulse (**Figure 1.18**), which means providing the spin is stationary ($x(t) = x_0$) any phase acquired during the first gradient lobe will be 'undone' by the second (provided the two gradient lobes have the same area), as shown in **Figure 1.19a** causing no net phase change. If the spin is moving during the gradients however it will experience a different field during the second lobe, for example **Figure 1.19b** where a spin is moving in the positive gradient direction. As the spin is experiencing stronger gradients over time, the second gradient lobe will 'undo' more phase than the first gradient adds, causing a net offset $\Delta\phi$ which is proportional to the velocity the spin was travelling at

$$\Delta\phi = \gamma\Delta\delta G v. \tag{1.41}$$

and forms the basis of Phase Contrast Angiography (PCA) as a measure of net velocity within a voxel. A PGSE sequence is also sensitive to diffusion,

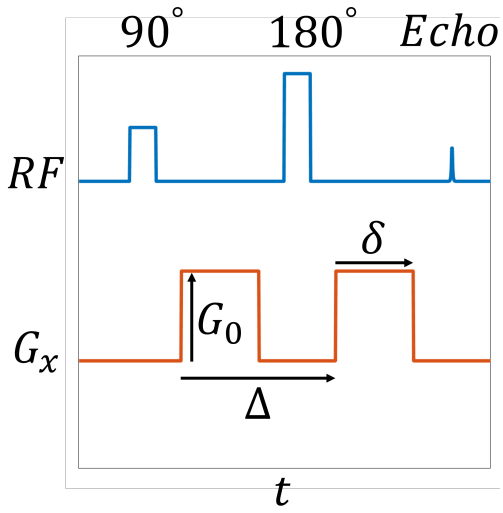


Figure 1.18: *Example PGSE sequence*

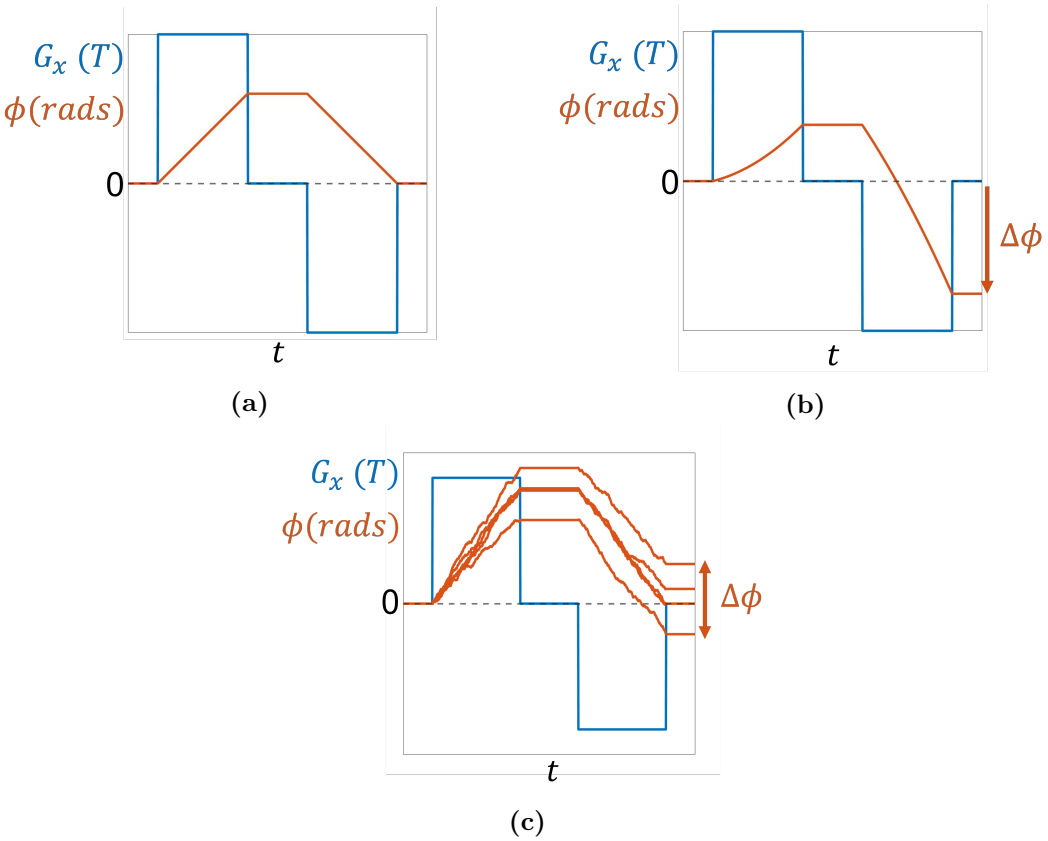


Figure 1.19: *For each figure the applied PGSE gradients are in blue, and the phase of individual spins are plotted in orange. For a) a stationary spin, b) a spin moving at a constant velocity v, c) for multiple spins randomly diffusing.*

as the random motion of spins during the first gradient lobe is unlikely to be repeated in the second, causing a random phase change in each spin (**Figure 1.19c**). These phase changes cause dephasing which reduces the size of the bulk magnetisation M_{xy}, reducing the size of the spin echo, and therefore the

magnitude of the detected signal. For diffusion the resulting signal from a PGSE is

$$S(b) = S_0 e^{-bD} \tag{1.42}$$

where S_0 is the signal from a PGSE of zero gradient strength, and D is the diffusion coefficient of the spin population (assuming Gaussian diffusion). The b value can be defined for an arbitrary waveform

$$b = (2\pi)^2 \int_0^{TE} \boldsymbol{k}(t) \cdot \boldsymbol{k}(t) dt \tag{1.43}$$

where

$$\boldsymbol{k}(t) = \frac{\gamma}{2\pi} \int_0^t \boldsymbol{G}(t') dt'. \tag{1.44}$$

The b-value describes the sensitivity to motion of a particular gradient sequence, and for a PGSE is defined

$$b = \gamma^2 G^2 \delta^2 (\Delta - \frac{\delta}{3}) \tag{1.45}$$

where the b-value has units s/mm^2, and Δ, δ, and G match those defined in **Figure 1.18**.

1.2.12 Intra-Voxel Incoherent Motion

In practice for a PGSE non-diffusive processes can also contribute to the signal decay [21]. Pseudorandom motion caused by blood in capillary networks (**Figure 1.20**), turbulent blood, or in the placenta blood that is percolating through the intervillous space can mimic a diffusive process. These processes can be described in terms of classical diffusion as there is still a characteristic length between collisions l, with molecules moving at a speed v which describes the pseudodiffusion coefficient

$$D^* = \frac{lv}{6}. \tag{1.46}$$

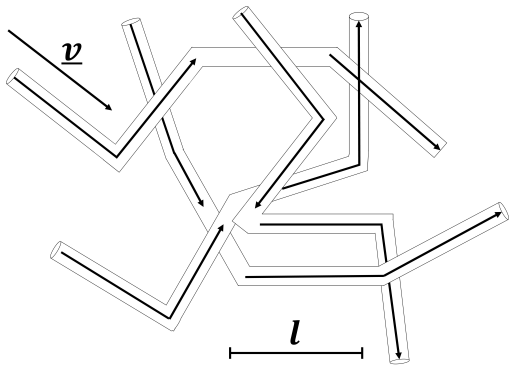


Figure 1.20: *A randomly orientated capillary network, with average segment length l, where blood is flowing through the network at speed v.*

where D^* diffuses faster than D. In Intra-Voxel Incoherent Motion (IVIM) the signal decay in a voxel is described by the contribution from each diffusing spin

$$S(b) = \sum_{n=1}^{N} e^{-bD_n}. \tag{1.47}$$

where it is assumed there are only two types of motion, regular diffusion at a rate D and pseudodiffusion at a rate D^* meaning the IVIM signal from a voxel can be described

$$S(b) = S_0[(1 - f_{IVIM})e^{-bD} + f_{ivim}e^{-bD^*}]. \tag{1.48}$$

The IVIM fraction f_{IVIM} describes the proportion of the signal decay from a voxel which is due to the faster pseudodiffusion. In practice the slower diffusion coefficient D is not strictly due to diffusion, and is often referred to as the apparent diffusion coefficient as it is likely the combination of the true diffusion coefficient, and other processes depending on the exact cellular environment such as exchange or restricted diffusion. A voxel showing high f_{IVIM} is shown in red in **Figure 4.3a**, which shows very fast decay over low b-value compared to pure water diffusion ($3.0\text{x}10^{-3}\text{mm}^2/\text{s}$) and diffusion due to water in blood ($1.5\text{x}10^{-3}\text{mm}^2/\text{s}$ [22]). The diffusion coefficient D describes the slow water diffusion, which can have a kurtosis effect (blue in **Figure 4.3a**) as water diffusion in tissue can be constrained by interactions with membranes or

the cellular environment which is more noticeable at higher b-value. Kurtosis

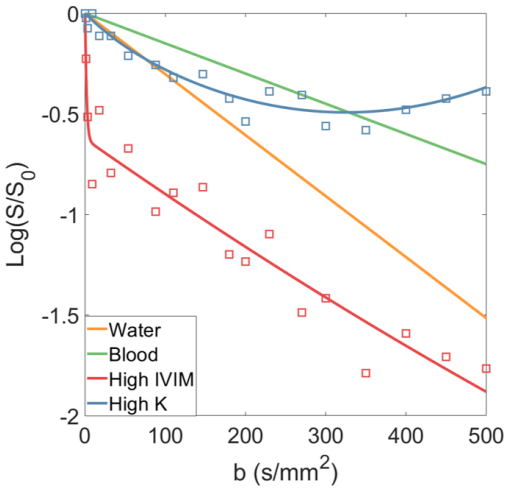


Figure 1.21: *A plot comparing how the DWI signal from a range of processes varies. Pure diffusion due to water (green, $D = 3.0x\ 10^{-3} mm^2/s$) and water in blood (yellow, $D = 1.5x\ 10^{-3} mm^2/s$ [22]) produce a mono-exponential decay described by* ***Equation 1.45****. A voxel showing high IVIM was taken from within a placenta, and the fit and underlying data is shown in red, and a voxel showing high kurtosis is shown in blue with the fit and underlying data.*

describes restricted diffusion where the molecular displacement, which limits the length scale that slow D can occur over, is skewed as in **Figure 1.22**. Additionally f_{IVIM} is linked to perfusion as

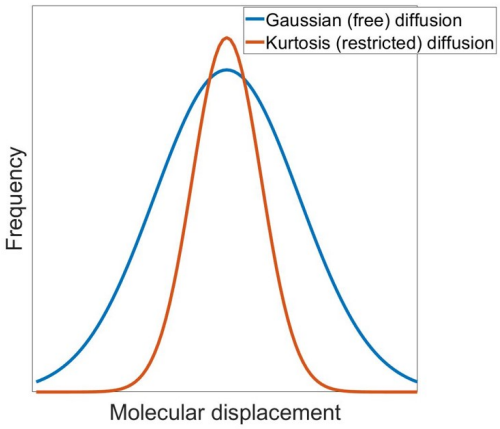


Figure 1.22: *Example of molecular displacement after some time t for pure Gaussian diffusion (blue), and for restricted diffusion (orange) which has positive kurtosis.*

$$f_{IVIM} = \frac{V_{IVIM}}{V_{voxel}} \tag{1.49}$$

where V_{IVIM} is the volume of blood that is moving incoherently, V_{voxel} is the total volume of NMR visibile water. It is possible to link these parameters to perfusion as the Mean Transit Time (MTT) is defined as

$$MTT = \frac{L}{v} \tag{1.50}$$

which describes how long it takes blood to clear a voxel, as L is the total capillary length, and v is the speed of blood within the network. Combining **Equation 1.46** and **Equation 1.50**

$$MTT = \frac{Ll}{6D^*} \tag{1.51}$$

describes the mean transit time in terms of D^*, allowing for a definition of blood flow purely in IVIM terms as flow within a voxel [23]

$$F = \frac{V_{IVIM}}{MTT} = \frac{6V_{voxel}}{Ll} f_{IVIM} D^* \tag{1.52}$$

which provided V_{voxel}, L, and l are constant implies that

$$F \propto f_{IVIM} D^* \tag{1.53}$$

and therefore the product $f_{IVIM}D^*$ can be considered an analogue of perfusion[24].

1.2.13 Image Artifacts

1.2.13.1 Eddy Currents

DWI often relies on rapidly switching strong magnetic field gradients, which can induce eddy currents in parts of the MRI scanner (for example RF coils, shielding, or any conductive material). Eddy currents are small loops of current in various conducting materials of the system that are induced by changing magnetic fields, and cause issues as the applied gradients will be altered as

shown in **Figure 1.23**, which can have lingering effects after the gradients are turned off. Eddy currents can cause a wide range of image artifacts including shears, dilations, and shifting of the image, and can cause errors in DWI data as applied gradients are not of the expected form. Eddy currents can be limited

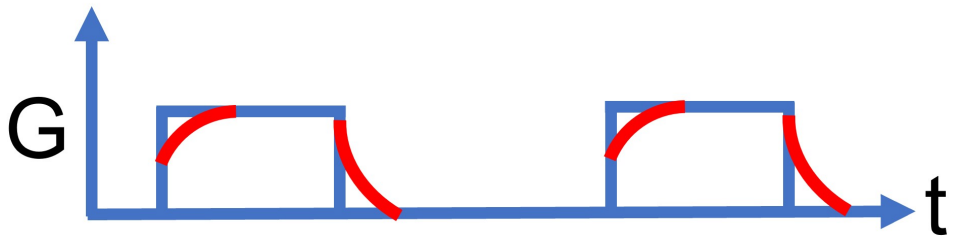


Figure 1.23: *An example bipolar PGSE sequence, where the planned sequence is in blue, but the gradients experienced by the alterations to the effective gradient by eddy currents are shown in red.*

by designing scanner hardware to break up current loops or through actively shielded gradients, which use another set of coils to generate gradients which work to cancel out the effects of the imaging gradients outside of the magnet bore, preventing eddy currents being induced in scanner hardware. Gradients can also be designed with pre-emphasis which aim to account for eddy currents by altering the shape of the applied field gradient so that after eddy currents are induced the desired pulse is still applied.

1.2.13.2 Motion Artifacts

For placental imaging motion artifacts are of significant concern, due to maternal breathing, fetal motion, and uterine and placental contractions. Maternal breathing can cause ghosting which is most prominent in the phase encode direction, as there is a larger time gap between sampling in the phase encode than the frequency encode direction. To limit the effects of maternal breathing images can be respiratory gated, using respiratory bellows which measure the participants breathing during the scan. By only then acquiring images while the participant is near the end of expiration the motion due to breathing is

minimised, at the cost of increased scan duration. To reduce the effects of other maternal and fetal motion faster readout sequences such as EPI can be used, which if combined with parallel imaging can provide fast acquisition, which minimises the effects of motion artifacts in the image. Image registration can also be used to account for placental motion, for example in DWI placental motion between b-values could corrupt data, as the voxel being examined for the first few b-values is now in a different position in the image. Registration can be either rigid (assuming the placenta only moves and does not deform) or non rigid (assuming the placenta will move and deform), and morphs the post-movement placental images to match the pre-movement images. In the placenta this is a difficult problem to solve, as movement can be caused by placental contractions, maternal motion, and fetal motion which can all not just move the placenta through space but also deform it.

1.3 Imaging in Pregnancy

The main imaging modalities for investigating either fetal or placental well-being for clinical or research purposes are ultrasound and MRI, as both use non-ionising radiation and pose no risk to the mother or fetus providing safety precautions are taken.

1.3.1 Ultrasound

Ultrasound is a non-ionising imaging method, that uses sound waves which can provide information about structures and flows from within the placenta. Doppler ultrasound is useful clinically for guiding care [25] by measuring the pulsatility and resistance of flow in the umbilical cord, where abnormalities are associated with an increased risk of the fetus being Small for Gestational Age (SGA), requiring neonatal care, or for the mother to develop PE. While this information is clinically relevant it can not be used to investigate changes in placental structure or maternal haemodynamics as it lacks the ability to pro-

vide microstructural or perfusion measures from within the placenta. 3D power Doppler ultrasound however can provide perfusion information from within the placenta, specifically by measuring Vascularisation Index (VI, measures overall perfusion), Vascular Flow Index (VFI, measures the blood velocity), and Flow Index (FI, a measure of overall blood flow). Previous work[26–29] has shown that 3D power Doppler could be useful for measuring or identifying differences between healthy placentas, and those with FGR, with FGR placentas showing significantly reduced VI and VFI, but these measures come with a high degree of variability. FI on the other hand is less variable between placentas, but can only detect differences between severe FGR and healthy placentas, meaning while the consistency is better the sensitivity is lower. 3D power Doppler is also still unable to make measurements about oxygenation or tissue microstructure which may contain vital information for measuring differences between healthy and compromised pregnancies, and be directly related to the causes of placental disease.

1.3.2 MRI

MRI has become an increasingly popular technique for investigating the placenta, and can be used to investigate placental structure, microstructure, perfusion, flow, diffusivity, and oxygenation. Here I outline safety concerns when undergoing MRI on a pregnant person, and MRI sequences of interest to investigate the placenta.

1.3.2.1 Fetal MRI safety

There are a number of safety concerns for both the mother and fetus which are different from normal human adult scanning. For the fetus energy deposition due to Specific Absorption Rate (SAR, units W/kg), which describes the rate of energy absorption of a human when exposed to RF fields, is a significant concern. This energy absorption causes heating which is known to be

teratogenic[30], causing early aging in the fetus. Dissipation of heat is more complex for the fetus, which relies on conduction and convection through the uterine wall for cooling, but modelling suggests a SAR of 2W/kg over 6 minutes to be safe, but extending up to 7.5 minutes could cause a significant level of heating to the fetus[31]. To limit the amount of heating it is recommended to spread high SAR sequences out between lower SAR sequences to allow for cooling. Additionally it has been shown through modelling that placing mothers in the left lateral position, instead of supine on the bed can significantly reduce fetal SAR[32]. For second and third trimester pregnancies at 3T current recommendations include using scanners in normal operating mode to limit whole body Specific Absorption Rate (SAR) $\leq$ 2 W/kg [33]. Observational studies have shown no adverse outcomes to fetuses scanned across all three trimesters at both 1.5 and 3T [33, 34], which are all considered safe in the UK. Acoustic noise is also a concern for the fetus, due to the noise itself, but also vibrations in the bed being transferred to the fetus. Current modelling indicates that the fluid in the mothers abdomen significantly dampens the acoustic noise, and while low frequency sounds can penetrate the fetal head there is no evidence of hearing loss due to MRI exposure during pregnancy [34–36]. To reduce mechanical vibrations it is recommended that the mother lies on a thick bedding to dampen any mechanical oscillations. For the mother there is a risk of aortocaval compression when laying supine, due to the weight of the fetus, to avoid this it is again recommended participants lay at a 15° degree angle in the left lateral position.

1.3.2.2 Diffusion Weighted Imaging

In the placenta Diffusion Weighted Imaging (DWI) has proved a popular technique to investigate the small scale movement of blood throughout the IVS[5, 15, 16, 16–20], providing information about diffusivity, microstructure, perfusion, and transfer between the maternal and fetal blood pools. In the placenta DWI data is typically considered to be described by the sum of ex-

ponential decays such as in the IVIM model, where one component is due to the slow self diffusion of water in blood, and the second is due to the faster incoherent motion of blood throughout the IVS. However due to the complexity of the underlying placental structure and the relationship between the flow, structure and IVIM signal, results can be difficult to interpret.

1.3.2.3 Arterial Spin Labelling

Arterial Spin Labelling (ASL) has also shown promise for measuring placental perfusion. In ASL blood is magnetically 'tagged' using an RF inversion pulse which then acts as a tracer, where by waiting for this blood to enter the target imaging slice, and then acquiring an image perfusion can be measured within the target slice. In the placenta pulsed ASL techniques have been used, such as flow sensitive alternating inversion recovery (FAIR)[37], velocity selective ASL (VSASL)[38–40] and a hybrid pseudocontinous ASL (pCASL) approach[41]. A strength of ASL is the ability provide dynamic information about placental perfusion by altering the time between tagging blood, and imaging the target slice. A comparison between FAIR ASL and IVIM was carried out in [37] found that IVIM provided more sensitivity to placental perfusion, but ASL was better at detecting reduced perfusion in the basal plate. ASL was also thought to be a more effective clinical measure as acquisition and analysis are faster than IVIM, but may be more sensitive to gross movement during readout.

1.3.2.4 Dynamic Contrast Enhanced

Dynamic Contrast Enhanced (DCE) MRI has also been used in the placenta as a measure of perfusion. Gadolinium causes shortening of T_1, and after an intravenous injection gadolinium will travel through the maternal circulatory system into the placenta, where changes in T_1 can be tracked to determine placental blood flow, the fraction of maternal blood in the placenta, and the MTT of blood. While DCE has been shown to be a useful measure of placental

perfusion[42] safety concerns around Gadolinium mean it is only used when the benefits to the mother outweigh the potential risks to the fetus, and is not routinely used in human research as it is possible that gadolinium crosses to the fetus [43] and there is evidence of contraindication [36].

1.3.2.5 Half-Fourier Acquisition Single-shot Turbo Spin-Echo

Half-Fourier Acquisition Single-shot Turbo Spin-Echo (HASTE) produces a T2 weighted image which is resilient to motion due to the rapid acquisition. In the placenta T2 is known to be sensitive to underlying tissue properties, blood oxygenation and macro-molecular properties[44], and is strongly correlated to the impedance of flow in the uterine arteries[45]. HASTE can be used by qualitative visual assessment, where SGA fetuses had placentas showing a two-tone pattern inside the placental parenchyma, and reduced signal intensity[46]. Quantitatively by repeating HASTE of increasing TE and calculating the T2 values of each voxel histograms of whole placental T2 show reduced mean T2, higher skewness, and higher kurtosis in placentas with less favourable outcomes [47]. This analysis shows promise as a marker of placental insufficiency, and may be more clinically relevant than ASL or IVIM as it is a simpler sequence to implement and analyse. However visual inspection is not quantitative, meaning results may depend on the observer and not be as robust as ASL or IVIM, and does not provide direct measures of perfusion or percolation of blood throughout the IVS.

1.4 Thesis Outline

The goal of this thesis was to provide new insight into the haemodynamics of the human placenta in utero by combining measurements of small scale movements from DWI, and larger scale bulk flows measured with PCA throughout the organ in both healthy placentas, and those compromised by PE/FGR. In **Chapter 2** I outline the cohort used in this thesis, and the data collec-

tion and prepossessing steps. In **Chapter 3** I introduce an Inverse Laplace Transform (ILT) based approach for fitting placental DWI data, which I used to provide better understanding of the underlying DWI signal of the healthy placenta, and changes in a PE/FGR cohort. In **Chapter 4** I then used this understanding to inform a more standard IVIM based approach and make the first comparisons between an ILT approach and an IVIM approach, and used both to better understand placental haemodynamics. **Chapter 5** contains the first measurements of bulk flow through the IVS using PCA, which I used to investigate both arterial input, and the poorly understood venous drainage system. In **Chapter 6** I investigated the 'rebounding' of signal I observed in placental PGSE data, which could be a potential marker of flow through the IVS, and provided a method to characterise these voxels.**Chapter 7** explores how altering the PGSE properties alters the DWI signal in a porous phantom, as this work could not be done in human volunteers due to the COVID-19 epidemic. **Chapter 8** summarises the main findings of this thesis, and concludes the work.

1.5 Bibliography

[1] T. McNanley and J. Woods, "Placental physiology [internet]. glob libr women's med. 2008." :http://www.glowm.com/index.html?p=glowm.cml/section_view&articleid=195, 2022.

[2] G. Burton, A. Woods, E. Jauniaux, and J. Kingdom, "Rheological and physiological consequences of conversion of the maternal spiral arteries for uteroplacental blood flow during human pregnancy," *Placenta*, vol. 30, no. 6, pp. 473–482, 2009.

[3] J. Kingdom, B. Huppertz, G. Seaward, and P. Kaufmann, "Development of the placental villous tree and its consequences for fetal growth," *Eur J Obstet Gynecol Reprod Biol*, vol. 92, no. 1, pp. 35–43, 2000.

[4] A. Edgardo, C. Cristina, L. Ana, C. Doris, and S. Lale, "Global and regional estimates of preeclampsia and eclampsia: a systematic review," *Eur J Obstet Gynecol Reprod Biol*, vol. 170, no. 1, pp. 1–7, 2013.

[5] N. Dellschaft, G. Hutchinson, S. Shah, N. Jones, C. Bradley, L. Leach, C. Platt, R. Bowtell, and P. Gowland, "The haemodynamics of the human placenta in utero," *PLOS Biology*, vol. 18(5), p. e3000676, 2020.

[6] J. Harris and E. Ramsey, "The morphology of human uteroplacental vasculature," *Contrib Embryol.*, vol. 38, pp. 43–58, 1966.

[7] Y. Wang and S. Zhao, *Vascular Biology of the Placenta*. San Rafael (CA): Morgan Claypool Life Sciences, 2010.

[8] G. Acharya, S. Sonesson, K. Flo, J. Rasanen, and A. Odibo, "Hemodynamic aspects of normal human feto-placental (umbilical) circulation," *Acta Obstet Gynecol Scand*, vol. 95, no. 6, pp. 672–82, 2016.

[9] "Maternal cotyledons at birth predict blood pressure in childhood," *Placenta*, vol. 34, no. 8, pp. 672–675, 2013.

[10] E. Abalos, C. Cuesta, A. Grosso, D. Chou, and L. Say, "Global and regional estimates of preeclampsia and eclampsia: a systematic review," *Eur J Obstet Gynecol Reprod Biol*, vol. 179, no. 1, pp. 1–7, 2013.

[11] S. Rana, E. Lemoine, J. P. Granger, and S. A. Karumanchi, "Preeclampsia," *Circulation Research*, vol. 124, no. 7, pp. 1094–1112, 2019.

[12] N. guideline [NG133], *Hypertension in pregnancy: diagnosis and management*. https://www.nice.org.uk/guidance/ng133, 2019.

[13] J. Gardosi, V. Madurasinghe, M. Williams, A. Malik, and A. Francis, "Maternal and fetal risk factors for stillbirth: population based study," *BMJ*, vol. 346, 2013.

[14] A. Malhotra, B. J. Allison, M. Castillo-Melendez, G. Jenkin, G. R. Polglase, and S. L. Miller, "Neonatal morbidities of fetal growth restriction: Pathophysiology and impact," *Frontiers in Endocrinology*, vol. 10, 2019.

[15] R. Moore, O. Stephen, T. Damian, R. Duckett, P. Baker, W. Dunn, I. Johnson, and P. Gowland, "Spiral artery blood volume in normal pregnancies and those compromised by pre-eclampsia," *Neuroimage*, vol. 21, pp. 376–380, 2008.

[16] P. Slator, H. J, L. McCabe, A. Gomes, A. Price, E. Panagiotaki, M. Rutherford, J. Hajnal, and D. Alexander, "Placenta microstructure and microcirculation imaging with diffusion mri," *Magnetic Resonance in Medicine*, vol. 80, no. 2, pp. 756–766, 2018.

[17] R. Moore, B. Strachan, D. Tyler, K. Duncan, P. Baker, B. Worthington, I. Johnson, and P. Gowland, "In utero perfusing fraction maps in normal and growth restricted pregnancy measured using ivim echo-planar mri," *Placenta*, vol. 21, no. 7, pp. 726–32, 2000.

[18] B. Kristi, N. Ditte, H. Caroline, S. Marianne, P. Astrid, B. Jens, A. David, and S. Anne, "Placental diffusion-weighted mri in normal pregnancies and those complicated by placental dysfunction due to vascular malperfusion," *Placenta*, vol. 91, pp. 52–58, 2020.

[19] S. Sohlberg, A. Mulic-Lutvica, M. Olovsson, J. Weis, O. Axelsson, J. Wikström, and A.-K. Wikström, "Magnetic resonance imaging-estimated placental perfusion in fetal growth assessment," *Ultrasound in Obstetrics & Gynecology*, vol. 46, no. 6, pp. 700–705, 2015.

[20] S. Sohlberg, A. Mulic-Lutvica, P. Lindgren, F. Ortiz-Nieto, A. K. Wikström, and J. Wikström, "Placental perfusion in normal pregnancy and early and late preeclampsia: A magnetic resonance imaging study," *Placenta*, vol. 35, no. 3, pp. 202–206, 2014.

[21] D. L. Bihan, "What can we see with ivim mri?," *Neuroimage*, vol. 187, pp. 56–67, 2019.

[22] C. Funck, F. B. Laun, and A. Wetscherek, "Characterization of the diffusion coefficient of blood," *Magn Reson Med*, vol. 79, no. 5, pp. 2752–2758, 2018.

[23] D. Le Bihan and R. Turner, "The capillary network: a link between ivim and classical perfusion," *Magn Reson Med*, vol. 27, no. 1, pp. 171–178, 1992.

[24] D. Le Bihan and R. Turner, "The capillary network: a link between ivim and classical perfusion," *Magn Reson Med*, vol. 27, no. 1, pp. 171–178, 1992.

[25] I. Derwig, D. Lythgoe, G. Barker, L. Poon, P. Gowland, and R. Yeung, "Association of placental perfusion, as assessed by magnetic resonance imaging and uterine artery doppler ultrasound, and its relationship to pregnancy outcome," *Placenta*, vol. 34, no. 10, pp. 885–91, 2013.

[26] C. Guiot, P. Gaglioti, M. Oberto, E. Piccoli, R. Rosato, and T. Todros, "Is three-dimensional power doppler ultrasound useful in the assessment of placental perfusion in normal and growth-restricted pregnancies?," *Ultrasound Obstet Gynecol*, vol. 31, no. 2, pp. 171–6, 2008.

[27] J. Noguchi, K. Hata, H. Tanaka, and T. Hata, "Placental vascular sonobiopsy using three-dimensional power doppler ultrasound in normal and growth restricted fetuses," *Placenta*, vol. 30, no. 5, pp. 391–397, 2009.

[28] C. Guiot, P. Gaglioti, M. Oberto, E. Piccoli, R. Rosato, and T. Todros, "Is three-dimensional power doppler ultrasound useful in the assessment of placental perfusion in normal and growth-restricted pregnancies?," *Ultrasound Obstet Gynecol.*, vol. 31, no. 2, pp. 171–176, 2008.

[29] M. Pomorski, M. Zimmer, J. Florjanski, J. Michniewicz, A. Wiatrowski, T. Fuchs, and E. Milnerowicz-Nabzdyk, "Comparative analysis of placental vasculature and placental volume in normal and iugr pregnancies with the use of three-dimensional power doppler," *Arch Gynecol Obstet*, vol. 285, no. 2, pp. 331–337, 2012.

[30] L. Konkel, "Taking the heat: Potential fetal health effects of hot temperatures," *Environmental Health Perspectives*, vol. 127, no. 10, p. 102002, 2019.

[31] J. Hand, Y. Li, and J. Hajnal, "Numerical study of rf exposure and the resulting temperature rise in the foetus during a magnetic resonance procedure," *Phys Med Biol*, vol. 55, no. 4, pp. 913–930, 2010.

[32] T. E. Abaci, F. Yetisir, E. Adalsteinsson, B. Gagoski, B. Guerin, P. E. Grant, and L. L. Wald, "Individual variation in simulated fetal sar assessed in multiple body models," *MRM*, vol. 83, no. 4, pp. 1418–1428, 2020.

[33] M. Jabehdar, A. Kapadia, and G. Liu, "Canadian association of radiologists recommendations for the safe use of mri during pregnancy," *Canadian Association of Radiologists Journal*, vol. 73, no. 1, pp. 56–67, 2022.

[34] L. Andre, J. Monique, R. M. Danielle, E. James, A. T. Danielle, and M. M. Robert, "The safety of maternal and fetal mri at 3 t," *American Journal of Roentgenology*, vol. 213, no. 5, pp. 1170–1173, 2019.

[35] C. Jaimes, J. Delgado, M. Cunnane, H. Hedrick, N. Adzick, M. Gee, and T. Victoria, "Does 3-t fetal mri induce adverse acoustic effects in the neonate? a preliminary study comparing postnatal auditory test performance of fetuses scanned at 1.5 and 3 t," *Pediatr Radiol*, vol. 49, no. 1, pp. 37–45, 2019.

[36] M. P. Jabehdar, A. Kapadia, and G. Liu, "Recommendations for the

safe use of mri during pregnancy," *Canadian Association of Radiologists Journal*, vol. 364, no. 73, p. 1, 2022.

[37] I. Derwig, D. Lythgoe, G. Barker, L. Poon, P. Gowland, R. Yeung, F. Zelaya, and K. Nicolaides, "Association of placental perfusion, as assessed by magnetic resonance imaging and uterine artery doppler ultrasound, and its relationship to pregnancy outcome," *Placenta*, vol. 34, no. 10, pp. 885–891, 2013.

[38] P. Gowland, S. Francis, K. Duncan, A. Freeman, B. Issa, R. Moore, R. Bowtell, P. Baker, I. Johnson, and B. Worthington, "In vivo perfusion measurements in the human placenta using echo planar imaging at 0.5 t," *Magn Reson Med.*, vol. 40, no. 3, pp. 467–473, 1998.

[39] Z. Zun and C. Limperopoulos, "Placental perfusion imaging using velocity-selective arterial spin labeling," *Magn Reson Med*, vol. 80, no. 3, pp. 1036–1047, 2018.

[40] A. Harteveld, J. Hutter, S. Franklin, L. Jackson, M. Rutherford, J. Hajnal, M. van Osch, C. Bos, and E. De Vita, "Systematic evaluation of velocity-selective arterial spin labeling settings for placental perfusion measurement," *Magn Reson Med*, vol. 84, no. 4, pp. 1828–1843, 2020.

[41] X. Shao, D. Liu, T. Martin, T. Chanlaw, S. Devaskar, C. Janzen, A. Murphy, D. Margolis, K. Sung, and D. Wang, "Measuring human placental blood flow with multidelay 3d grase pseudocontinuous arterial spin labeling at 3t," *Magn Reson Imaging*, vol. 47, no. 6, pp. 1667–2676, 2017.

[42] B. Deloison, C. Arthuis, G. Benchimol, and et al, "Human placental perfusion measured using dynamic contrast enhancement mri," *PLoS One*, vol. 16, no. 9, 2021.

[43] Z. Novak, A. Thurmond, P. Ross, M. Jones, K. Thornburg, and K. RW,

"Gadolinium-dtpa transplacental transfer and distribution in fetal tissue in rabbits," *Invest Radiol*, vol. 28, no. 9, pp. 828–830, 1993.

[44] P. A. Gowland, A. Freeman, B. Issa, P. Boulby, K. R. Duncan, R. J. Moore, P. N. Baker, R. W. Bowtell, I. R. Johnson, and B. S. Worthington, "In vivo relaxation time measurements in the human placenta using echo planar imaging at 0.5 t," *Magn Reson Imaging*, vol. 16, no. 3, pp. 241–247, 1998.

[45] I. Derwig, G. J. Barker, L. Poon, F. Zelaya, P. A. Gowland, D. J. Lythgoe, and K. Nicolaides, "Association of placental t2 relaxation times and uterine artery doppler ultrasound measures of placental blood flow," *Placenta*, vol. 34, no. 6, pp. 474–9., 2013.

[46] Y. Himoto, A. Kido, H. Mogami, Y. Moribata, S. Minamiguchi, F. Shitano, K. Kiguchi, Y. Kurata, I. Konishi, and K. Togashi, "Placental function assessed visually using half-fourier acquisition single-shot turbo spin-echo (haste) magnetic resonance imaging," *Placenta*, vol. Epub, pp. 55–60, 2016.

[47] Y. Himoto, K. Fujimoto, A. Kido, S. Otani, Y. Matsumoto, H. Mogami, K. Nakao, Y. Kurata, Y. Moribata, Y. Chigusa, S. Minamiguchi, M. Mandai, and Y. Nakamoto, "Risk stratification for pregnancies diagnosed with fetal growth restriction based on placental mri," *J Magn Reson Imaging*, vol. 56, no. 6, pp. 1650–1658, 2022.

Chapter 2

Cohort and Data Collection

In this thesis 23 pregnant participants were scanned, where 14 were classified as a healthy pregnancy (HP) and 9 were compromised placentas (CP) with some placental dysfunction (either preeclampsia (PE) or fetal growth restriction (FGR), or both). In this chapter I outline the selection criteria for the cohort, data collection, and preprocessing steps for the Diffusion Weighted Imaging (DWI) and Phase Contrast Angiography (PCA) data set.

2.1 Cohort

PE was defined as blood pressure $>$ 140/90 mmHg on two separate occasions $>$ 4 hours apart, and proteinuria of $>$30 mmg/mmol on protein-creatinine ratio or 300mg in a 24 hour urine collection. FGR was defined as women expecting a growth restricted baby, below the 10th centile for birth weight. All participants scanned were between the ages of 18-45 years, with BMI $<$ 30 kg/m^2, and singleton pregnancy. There were no significant differences between the ages or GA of participants in either the DWI group (for age p = 0.80, for GA p = 0.54) or PCA group (for age p = 0.27, for GA p = 0.66) at the time of scanning.

Participant ID	PE/FGR	Gestational Age (weeks)
HP01		$33+4$
HP02		$32+5$
HP03		$28+6$
HP04		$33+1$
HP05		$31+2$
HP06		$30+3$
HP07		$31+3$
HP08		$32+5$
HP09		$32+0$
HP10		$28+1$
HP11		$28+0$
HP12		$30+2$
HP13		$36+5$
HP14		$29+2$
CP01	PE	$31+0$
CP02	PE & FGR	$32+1$
CP03	PE & FGR	$31+5$
CP04	PE & FGR	$35+5$
CP05	PE & FGR	$28+5$
CP06	FGR	$28+4$
CP07	FGR	$34+2$
CP08	FGR	$28+2$
CP09	PE	$32+6$

Table 2.1: A list of all participants and their GA. For CP they are listed with either Pre-eclampsic, fetal growth restriction, or both.

2.2 Data Collection

All data were collected on a Philips 3T Ingenia scanner in normal operating mode with whole body average SAR < 2.0 W/Kg. Data were collected using posterior receive arrays that are built into the scanner bed, along with an anterior abdominal array. Both the DWI and PCA had a voxel size of 2.5x2.5x6 mm^3, and either 3, 5, or 6 slices (number of slices was increased part way through the study), but were consistent between the DWI and PCA of each participant, with Field Of View (FOV) 400x400x66 mm^3.

2.2.1 Diffusion Weighted Imaging

DWI data was collected using respiratory gated Pulse Gradient Spin Echo Echo Planar Imaging (PGSE EPI), for 19 b-values (0, 1, 3, 9, 18, 32, 54, 88, 110, 147, 180, 200, 230, 270, 300, 350, 400, 450, 500 s/mm^2), an example of a single slice through a participant at all b-values is shown in **Figure 2.1**. The PGSE had lobe length δ = 16ms, time between lobes Δ = 31ms, echo time (TE) = 61.4ms, minimum repetition time (TR) = 1800ms, and fat supression set to minimum with the b-value changed by increasing the gradient amplitudes. Gradients were repeated in three orthogonal directions, off of the scanner x,y,z direction to combine the strength of the applied gradients and achieve higher b-values, which were averaged to produce a single set of images corresponding to an NSA = 1. The total scan time without accounting for respiratory gating was 2 minutes 51 seconds. Volumes were removed if significant ($>$ 5mm displacement) was observed from a placental mask drawn on the b = 0 s/mm^2 volume, and if more than 8 volumes were discarded across the entire scan the participant was removed from further analysis, with the full list of removed volumes for each participant shown in **Figure 2.2**. This left 13 HP and 9 CP with sufficient DWI data for further analysis. Some regions of the placenta had very low initial signal which would provide meaningless fits, so to remove these an area of low but non zero signal was taken from within the participant as a noise floor, and any voxel with b = 0 s/mm^2 signal intensity less than 5 times this were removed from fitting. If a placental slice was near to the periphery of the placenta it would likely have flow patterns that were not representative of the rest of the organ, so these slices were discounted from analysis (only occurred in CP 08, slice 1).

2.2.2 Phase Contrast Angiography

PCA was collected using respiratory gated PGSE, using gradients of lobe length δ = 3.1ms, time between lobes Δ = 34ms, minimum repitition time

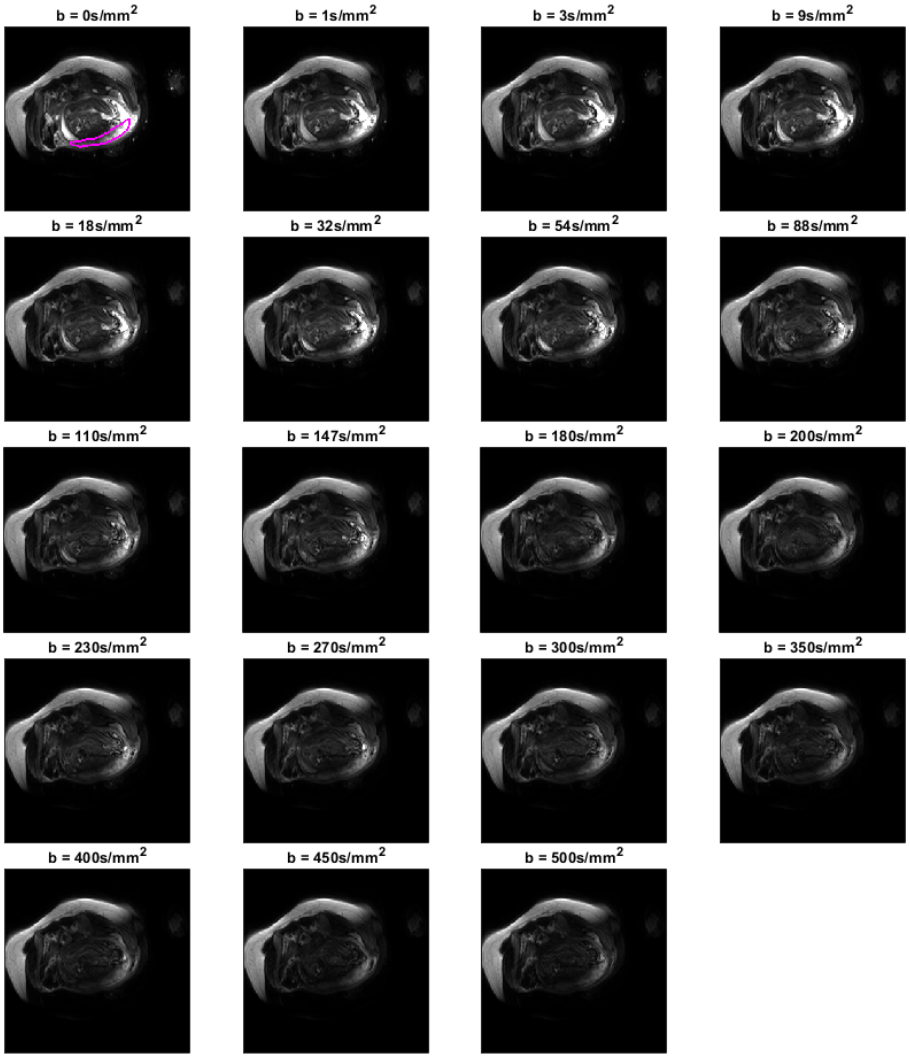


Figure 2.1: *A single slice through HP07 over all b-values, with the placenta outlined in magenta on the b = 0 s/mm^2 slice.*

(TR) = 1800ms, and fat supression set to minimum with scans repeated twice, once for a gradient amplitude G = 0 mT/m and again for G = 21mT/m to produce an encoded and non-encoded data set. These gradients were repeated 3 times on the scanner x,y,z axis, to produce velocity encoded scans in the x,y, and z direction, which took 27 seconds, not accounting for time added due to respiratory gating.This process was repeated 3 times, to produce 3 volumes of 3D velocity encoded data. Phase maps were produced by dividing the phase data from the encoded data set, by the non-encoded to account for any background phase variations not due to the encoding gradients. Global phase

Participant ID	Sufficient DWI	Discarded b-values
HP01	Y	
HP02	Y	
HP03	Y	
HP04	Y	270, 350, 400
HP05	Y	147
HP06	Y	110, 147, 180, 450
HP07	Y	
HP08	Y	110, 230, 450
HP09	Y	
HP10	Y	88, 200
HP11	Y	3, 230
HP12	N	
HP13	Y	9, 350
HP14	Y	32 88
CP01	Y	
CP02	Y	400, 450, 500
CP03	Y	147, 500
CP04	Y	
CP05	Y	
CP06	Y	
CP07	Y	180, 200, 230
CP08	Y	1, 32, 300, 450, 500
CP09	Y	88

Table 2.2: A table of all participants detailing which participants had sufficient DWI data, and the volumes which were discarded from analysis.

variations due to respiration of minor maternal or fetal motion were removed using a high-pass Butterworth spatial filter (6mm), and individual phase maps were then inspected, and any corrupted by gross maternal or fetal motion were discarded from analysis. This left 12 HP and 9 CP with at least one slice of 3D velocity information that could be used for further analysis, with the total number of slices with 3D velocity data for each participant outlined in **Table 2.3**. For these slices the processed velocity and speed maps are present in **Appendix D**.For participants were there was good alignment between the PCA and DWI data sets these measures were combined for further analysis, and the participants with good alignment between scans were also outlined in **Table 2.3**.

2.2.3 Masking

For both the DWI and PCA data images were masked into four regions of interest (uterine wall, basal plate, placenta, and chorionic plate), as shown in **Figure 1.1b**. For DWI masks were drawn by hand on the b = 0 s/mm^2 volume, and for PCA masks were drawn on the non flow-encoded images. The exact results in these sections will depend on how the data were masked, especially near the maternal side of the placenta where sometimes regions of basal plate may extend into the placental ROI, the effects of this were discussed in the relevant chapters.

Participant ID	Sufficient PCA	Slices imaged per volume	Slices with 3D Velocity data	Good alignment between DWI & PCA
HP01	Y	3	3/9	N
HP02	Y	3	2/9	N
HP03	N	3	0/9	No 3D velocity
HP04	Y	5	3/15	N
HP05	Y	6	3/18	Y
HP06	Y	6	10/18	Y
HP07	Y	6	6/18	Y
HP08	Y	6	2/18	Y
HP09	Y	6	1/18	Y
HP10	Y	6	7/18	N
HP11	Y	6	4/18	Y
HP12	Y	6	1/18	No DWI
HP13	Y	6	3/18	N
HP14	N	6	0/18	No 3D velocity
CP01	Y	5	4/15	Y
CP02	Y	5	1/15	N
CP03	Y	5	6/15	N
CP04	Y	6	3/18	Y
CP05	Y	6	6/18	Y
CP06	Y	6	2/18	Y
CP07	Y	6	4/18	N
CP08	Y	6	1/18	N
CP09	Y	6	3/18	Y

Table 2.3: All participants listed with their total slices of 3D velocity data processed from PCA maps, and if their PCA and DWI could be combined for further analysis.

Chapter 3

Fitting placental DWI data with an Inverse Laplace based approach

3.1 Introduction

Placental Diffusion Weighted Imaging (DWI) data is usually fitted to an Intra-Voxel Incoherent Motion (IVIM) model [1], which assumes that the signal is dominated by two motion components (**Equation 1.48**), with the first describing the slow self diffusion of water in blood, and the second describing the faster incoherent motion of blood as it travels turbulently through the uterine wall or percolates throughout the intervillous space (IVS). When using an IVIM model a number of assumptions have to be made about the data, such as that there are only two motion components in each voxel, and where is the boundary between the fast and slow components. In practice there is little evidence that the underlying structure reflects two components, and it is not clear how faster incoherent terms are affected by the placental environment, where turbulent flows, blood percolating across the intervillous space, flow across the organ, and fetal flows (which can combine within a single voxel) effect the signal.

An Inverse Laplace Transform (ILT) based approach to fitting this data is less biased by the choice of model or parameters, as instead of fitting data for a predetermined number of components, it is instead fitted to a distribution of diffusion coefficients. These are known as diffusograms[2] which describe the relative weighting (in arbitrary units) different values of diffusion coefficient contribute to the signal decay, over a continuous distribution of coefficients. ILT techniques are commonly used in relaxometry experiments when little or no a priori knowledge is available about the tissue or sample being imaged [3]. ILT techniques have also been successfully applied in diffusivity experiments, to investigate the number of diffusion components in cat brain[4], and investigate the number of components and potential changes in healthy vs ischemic rat brain[5]. The only previous work in the placenta [6] has focused on combined relaxometry/diffusivity measures to produce 2D spectra combining diffusion coefficients and relaxometry ($T2^*$) information to investigate structural changes between healthy and Pre-Eclampsic (PE) placentas. It was found that there were multiple diffusive components, and diffusivity changes in both the slow water self diffusion term, and in faster incoherent components in pre-eclampsic placentas. However, most diffusion experiments in the placenta involve just diffusivity, and not combined relaxometry/diffusivity, and 1D diffusograms have not yet been investigated in the placenta.

Here I implement an ILT based technique to investigate the diffusograms from 12 Healthy Placentas (HP) and 9 Compromised placentas (CP). These diffusograms were investigated to look for common features in both HP and CP, and differences to better understand the placental environment in health and disease. The differences between and within HP and CP were compared across 4 regions of interest (ROIs), (uterine wall, basal plate, placenta, and chorionic plate) to better understand placental structure and haemodynamics in HP and CP, and how this effects the DWI signal.

3.2 Theory

3.2.1 Inverse Laplace Transform

For an unknown number of diffusion coefficients **Equation 1.47** can be expanded to a 1D continuum

$$S(b) = \int_0^\infty p(D)e^{-bD}\,dD \tag{3.1}$$

where $p(D)$ are the weights that produce the diffusogram and describe what proportion of the signal decay each diffusion coefficient D contributes[7]. **Equation 3.1** is the forward Laplace transform, and so solving for $p(D)$ can be done using an ILT. This can be done numerically by approximating the 1D continuum **Equation 3.1** in discrete terms

$$S(b_i) = \sum_{j=0}^{K} p(D_j)e^{b_i D_j} \tag{3.2}$$

which states that the signal at point $S(b_i)$ can be calculated by summing the contribution of K diffusion coefficients. For all b values this can be rewritten in matrix form as

$$S(b) = Ap(D) \tag{3.3}$$

where the matrix

$$[A]_{ij} = e^{-b_i D_j} \tag{3.4}$$

. The weights $p(D)$ are therefore a 1xK array that transform the matrix A to fit to the signal S. To solve the ILT the minimisation

$$\min_{\mathbb{R}} ||Ap(D) - S(b)||_2^2 \tag{3.5}$$

is computed by finding the optimal $p(D)$, which is an ill-posed problem that requires regularisation. One such method is Tikhonov regularisation [8], by

adding a penalty term to **Equation 3.5** to give

$$\min_{\mathbb{R}} \; ||Ap(D) - S(b)||_2^2 + \lambda^2 ||p(D)||_2^2 \tag{3.6}$$

which penalises the size of $p(D)$. An advantage of Tikhonov regularisation is estimation of the regularisation term λ can be done through the use of the L-curve method, which has previously been used for producing diffusograms [4, 8, 9] and is advantageous as it does not require any knowledge or assumptions about the underlying noise in the signal, which can be complicated in placental DWI. The L-curve involves repeatedly fitting data with the ILT for varying values of λ, plotting the size of the solutions ($||p(D)||_2^2$) against the least squares fit of the solutions to the data ($||Ap(D) - S(b)||_2^2$). These plots resemble an 'L' (**Figure 3.1a**), and the corner of the L provides the λ value which gives a good combination of small solution size and good least squares fit. Appropriate regularisation is required as if the solution is under-regularised (i.e. λ is too small) the ILT will fit to noise in the signal, providing a smaller least squares fit but a large solution meaning the diffusogram would not accurately describe the underlying data (**Figure 3.1b**). If λ is too large the solution is over-regularised, providing a smaller solution but larger least squares fit, producing a diffusogram which is very smooth and loses detail present in the underlying data (**Figure 3.1c**). By taking the value of λ from the corner of the L curve (**Figure 3.1d**) it is possible to find a balance between solution size and least squares fit to accurately describe the underlying data.

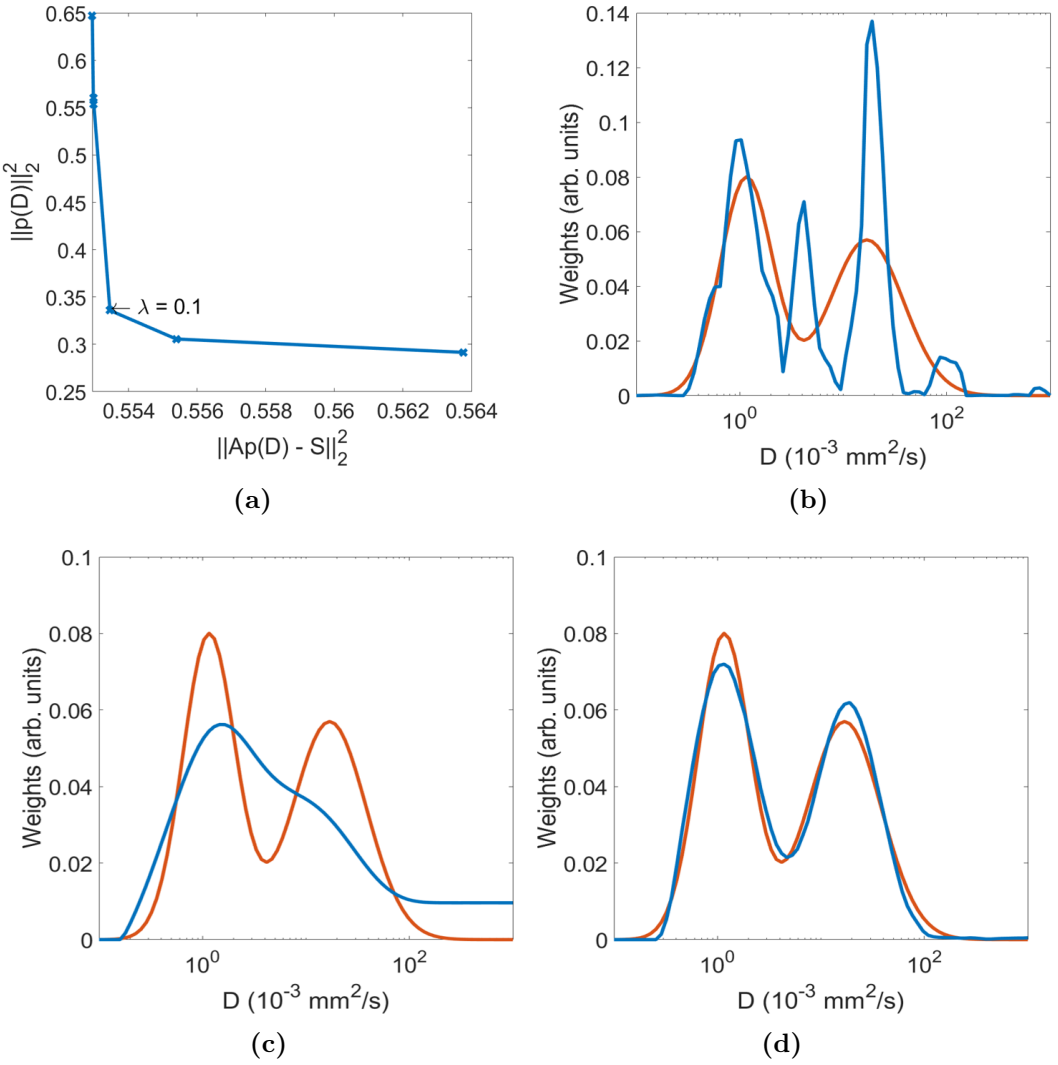


Figure 3.1: *For data simulated using* ***Equation 3.2*** *using the distribution $p(D)$ shown in orange in* ***a, b,*** *and* ***c****. The simulated data was fitted using an ILT approach to produce diffusograms shown in blue for a) $\lambda = 0.001$ which is under regulated, b) $\lambda = 1$ which is over regulated, and c) $\lambda = 0.1$, which is the value found by the L curve. d) Shows the L curve produced by plotting the solution size against the sum of squares for $\lambda = [0.0001\ 0.001\ 0.01\ 0.1\ 0.5\ 1]$. The corner value $\lambda = 0.1$ is labelled.*

3.3 Methods

3.3.1 Outline

Here I outline the implementation of the ILT, and the L curve for calculating the regularisation term λ, which were both tested on simulated data. Then I describe the implementation of the ILT in the placental DWI data, and how the resulting ILT data was processed, with data collection and preprocessing outlined in **Section 2.2.1**.

3.3.2 Setting up the Inverse Laplace Transform

The ILT was computed using an edited version of the MATLAB function *rilt* [10] which was adapted to take DWI data (**Equation 3.2**), and include Tikhonov regularisation. The minimisation shown in **Equation 3.6** was solved using inbuilt MATLAB function *fminsearch* which uses a simplex method [11] to determine optimum $p(D)$. This minimisation was repeated for a maximum of 1000 searches until it converged at a single solution using the previous solution as an initial guess to see if any improvement could be found. If the solution did not converge then the last $p(D)$ computed was taken as the solution. The matrix A was constrained by the chosen b values (**Section2.2.1**), and diffusion coefficients which were set between 10^{-1} and 10^{3} $\times 10^{-3}$ mm^2/s, which was around the limits of what could be feasibly detected in the placenta and matched previous work [6]. While the final diffusograms contained 80 diffusion coefficients evenly distributed in log-space it was computationally faster to carry out multiple repeats of increasing number of diffusion coefficients, using the previous solution as an initial guess for the next iteration as outlined in **Figure 3.2**. In the ILTs used here the transform was repeated 5 times, once each for 10, 20, 40, 60, and 80 diffusion coefficients where for the first fit no initial guess for $p(D)$ was given but for subsequent fits the previous $p(D)$ would be interpolated to span the new number of diffusion coefficients, and used as an initial estimate.

3.3.3 Testing the Inverse Laplace Transform

The ILT was initially tested using simulated data using **Equation 3.2** to create a bi-exponential and a tri-exponential data set. Weights $p(D)$ were constructed for 1500 spins randomly, and evenly distributed around three diffusion coefficients $D_1 = 3\times10^{-3}$ mm^2/s (the self diffusion of water in blood [12]), $D_2 = 300\times10^{-3}$ mm^2/s (100x the self diffusion of water in blood, similar to fast components observed in the placenta), and $D_3 = 30\times10^{-3}$ mm^2/s (10x

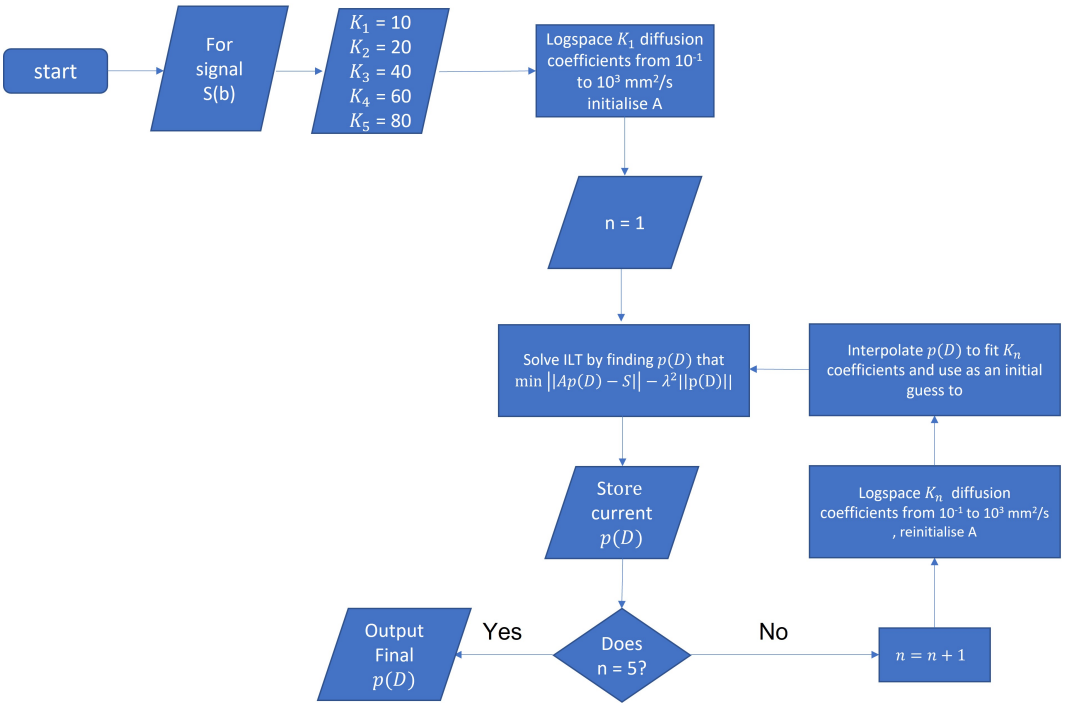


Figure 3.2: *Flow chart detailing how the code was executed for 5 repeats of increasing number of diffusion coefficients.*

the self diffusion of water in blood, within normal range in the placenta). The bi-exponential data contained 1000 total spins, evenly distributed around D_1 and D_2, and the tri-exponential data set contained 1500 total spins evenly distributed around D_1, D_2, and D_3. After calculating the signal $S(b)$ at each b value random Gaussian distributed noise was added to the signal of mean $\mu = 0$, and standard deviation $\sigma = 5\%$ of S_0. 19 b-values were simulated (b = 0, 1, 3, 9, 18, 32, 54, 88, 110, 147, 180, 200, 230, 270, 300, 350, 400, 450, 500 s/mm^2) that matched those used in human participants. Data was then fitted using the ILT and λ was preset at 0.1, as was found optimum in **Figure 3.3** by using an L curve and finding the point of maximum curvature (defined as the point which had the biggest change in gradient between the previous point, and the next point).

3.3.4 Fitting placental data

In the placental data there were challenges associated with finding the optimal λ. Fitting every voxel for multiple values of λ and plotting an L curve was

not feasible due to the computational cost (a single placenta took approximately 14 hours to fit on a Ryzen 7 3700x, parallel processed to use 5 cores @4.2GHz). Another option would have been to regularise each participant to a different value of λ by randomly sampling voxels from a participant, plotting an L curve for each of these voxels and then using the calculated value of λ for that participant. An issue with those approaches would be that fitting different voxels or participants to different values of λ could make comparisons either within or between participants difficult. Instead a single value of λ was used for all participants, similar to [4], which was found by randomly sampling voxels from the first 5 participants who were scanned (3HP, 2CP). 10 voxels were randomly selected from each participant and fitted to an ILT over λ = [0.05 0.1 0.2 0.3 0.4 0.6 0.8 1], which were used to plot an L curve where the corner of the L was defined as the point of maximum curvature. The corner was taken as the optimum value of λ for each voxel, and the mean value of all of these optimum λ was taken and used to regularise all ILT fits.

The resulting diffusograms were split into the slow, medium, and fast sectione which was based on patterns observed in the data (**Table 3.1**), which is outlined further in **Section 3.4.2**, and was similar to [6]. The fraction that each section contributed to the signal decay was calculated by normalising the diffusogram from each voxel so the total weighted summed to 1 (i.e. $\sum p(D) = 1$), and then summing the normalised weight within each section to give the slow, medium, and fast fractions.

Section	D_{lower}	D_{upper}
Slow	$\geq 0.1\times10^{-3}$ mm^2/s	$<21\times10^{-3}$ mm^2/s
Medium	$>21\times10^{-3}$ mm^2/s	$<558\times10^{-3}$ mm^2/s
Fast	$>558\times10^{-3}$ mm^2/s	$\leq 1000\times10^{-3}$ mm^2/s

Table 3.1: Section boundaries the diffusograms were split into.

Individual mean diffusograms were produced by averaging the normalised diffusograms across all voxels within 4 ROI's (uterine wall, basal plate, pla-

centa and chorionic plate **Figure 1.1b**).

To further analyse the fits peaks were detected in the normalised diffusograms from every voxel, where any maxima above 0.01 was counted as a peak. These peak locations were then combined to produce a normalised histogram for each participant, which were then averaged to produce a single histogram of peak locations for all HP and CP. Histograms were normalised before averaging to ensure that a subject with a larger placenta did not provide more weighting in the final histogram than a smaller placenta.

Differences between mean parameter values between HP and CP were checked for significance with a Mann-Whitney U test. Differences within groups were initially investigated with a Friedman test, which if found significant differences within HP or CP a Wilcoxon rank sum test was used as a post-hoc test to identify which specific ROIs were different.

3.4 Results

3.4.1 Simulated data

The diffusograms from the bi-exponential and tri-exponential data are shown in **Figure 3.3** with diffusion coefficients marked to show the resolution of the diffusogram.

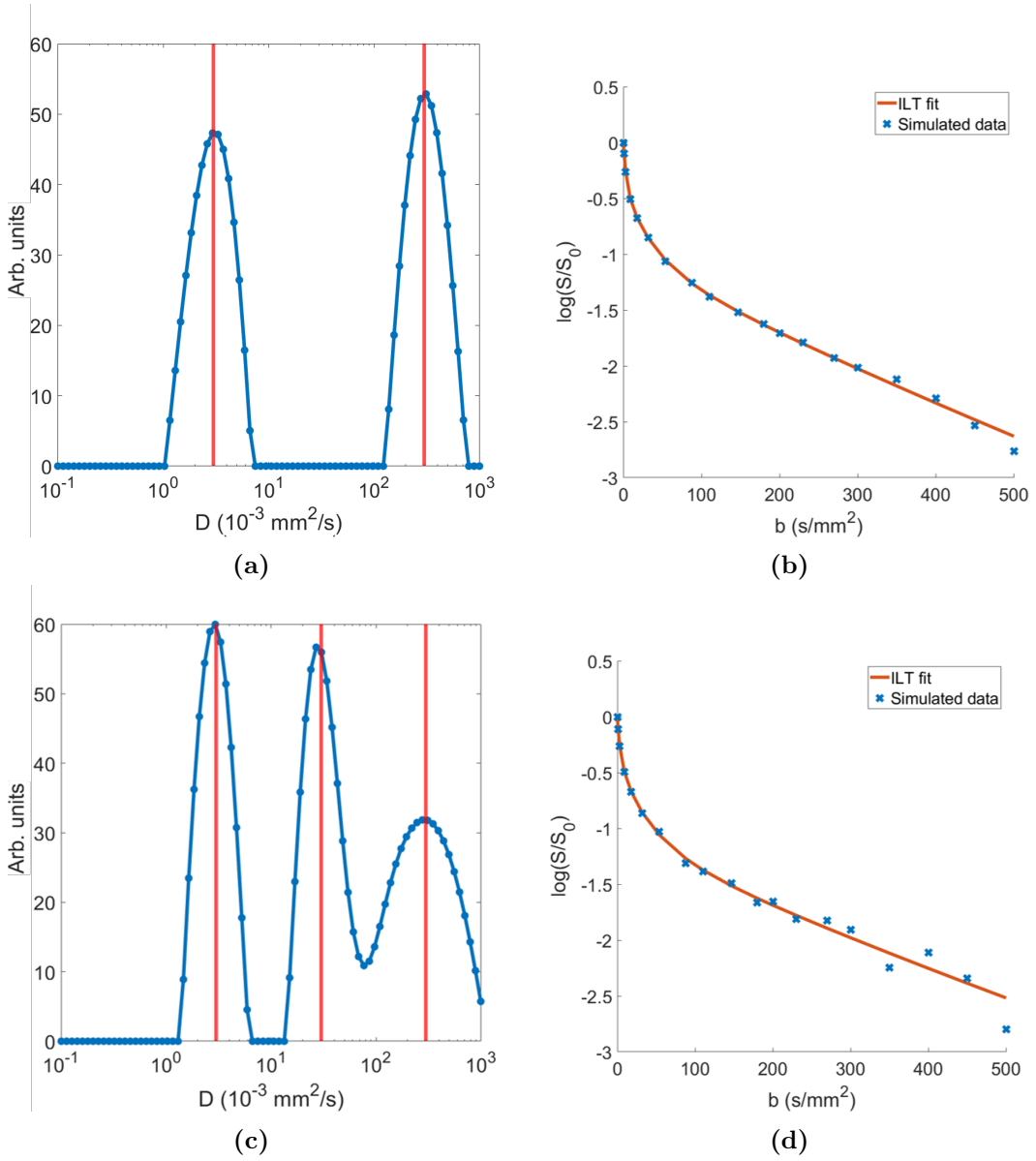
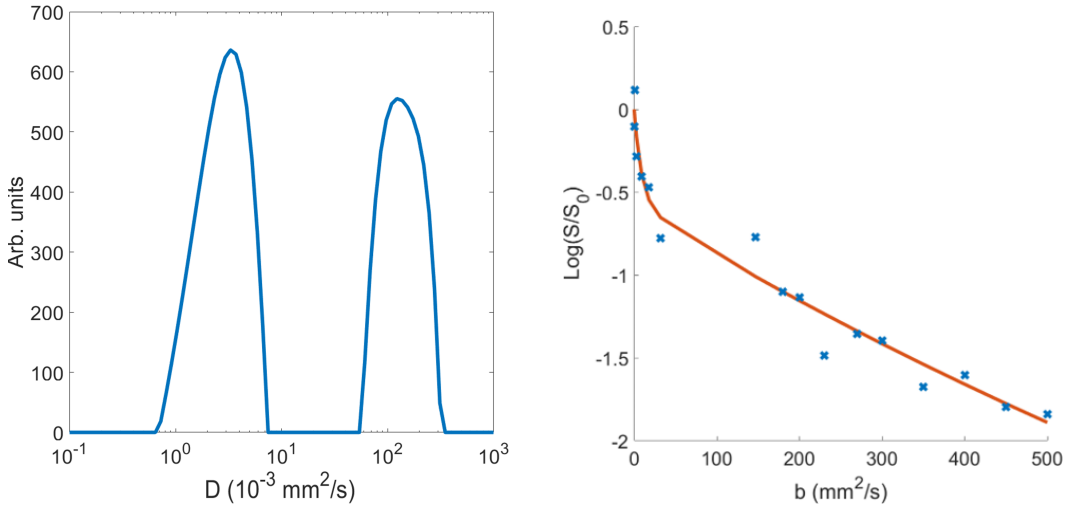


Figure 3.3: *Diffusograms produced by the ILT fit for a) bi-exponential and c) tri-exponential decay, with the simulated diffusion coefficients indicated in red. The underlying data, and fit produced by the diffusograms for the bi-exponential and tri-exponential fits are shown in b) and d).*

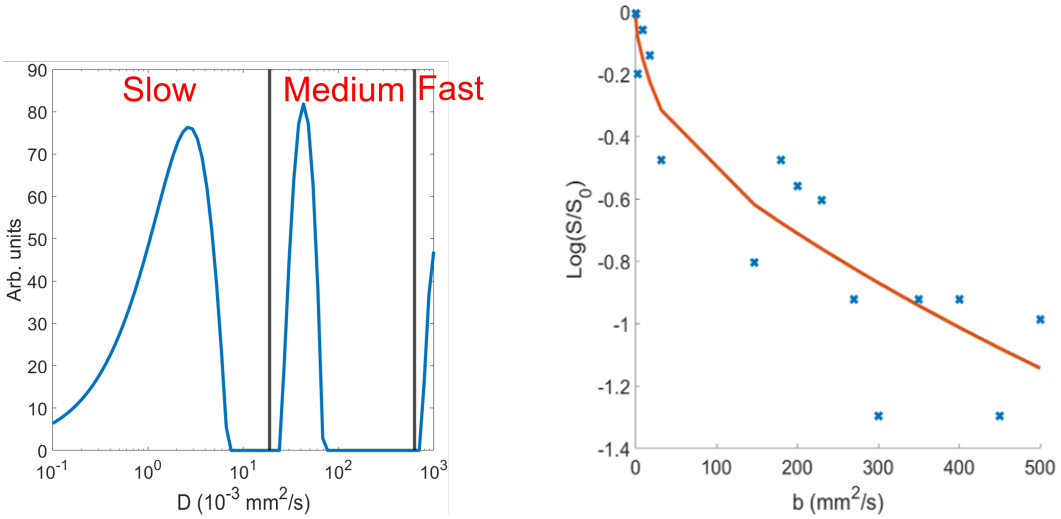
3.4.2 Placental Data

From the random sampling of placentas the best λ was found to be 0.2 ± 0.1, so all placental voxels were regularised with $\lambda = 0.2$. An example diffusogram from a single placental voxel which resembles a bi-exponential decay is shown in **Figure 3.4a**, and the fit produced by the diffusograms are in **Figure 3.4b**. Another diffusogram is shown in **Figure 3.5a** which is a single voxel which shows all the common features observed in the diffusograms, with the three sections (slow, medium, and fast) marked and labelled.



(a) **(b)**

Figure 3.4: *a) A diffusogram from a single placental voxel regularised with $\lambda = 0.2$, which showed apparent bi-exponential decay, and the raw data and fit produced by the diffusogram is shown in b).*



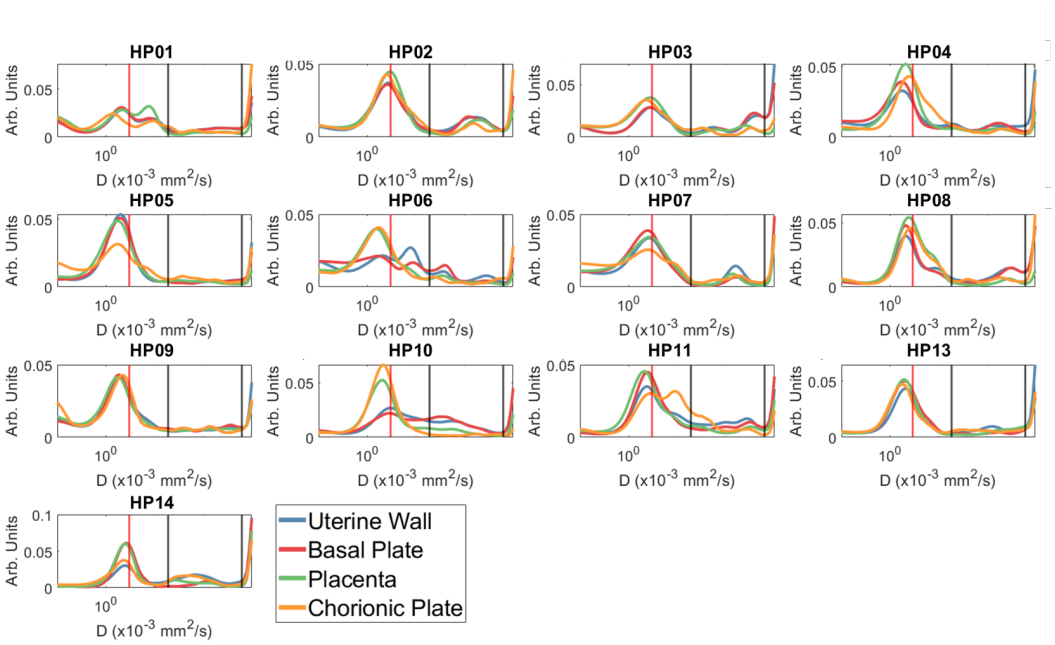
(a) **(b)**

Figure 3.5: *a) Diffusogram demonstrating the typical features observed across participants, with the boundaries between the slow, medium, and fast sections defined in 3.1 divided and labelled. The raw data and fit produced by the diffusogram is shown in b).*

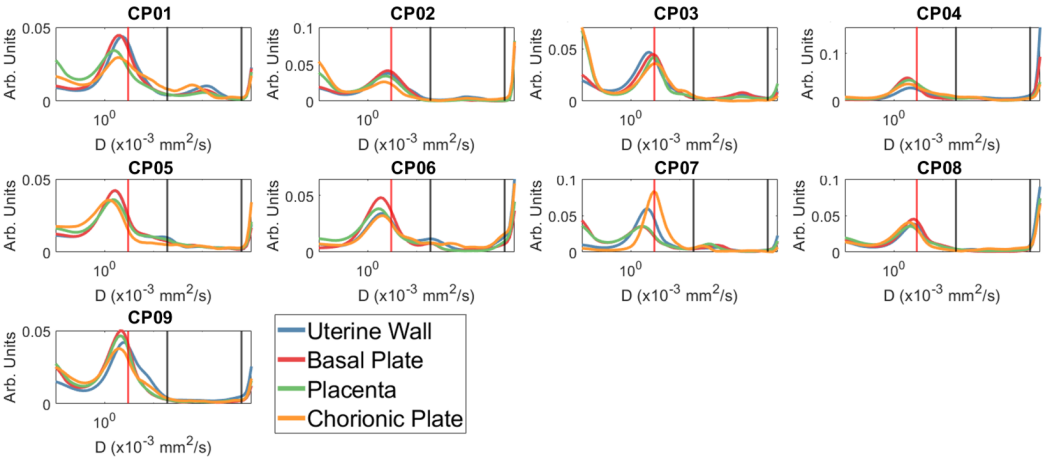
Diffusograms were then normalised so the weights from a single voxel in each participant summed to 1, and then averaged across the uterine wall, basal plate, placental and chorionic plate ROIs to produce 4 mean diffusograms for every participant (**Figure 3.6a** & **3.6b**). The mean diffusograms from each participant were then averaged again to produce a mean diffusogram for HP and CP for each ROI (**Figure 3.7a** & **3.7b**). The chosen separation between slow, medium, and fast sections are indicated by black vertical lines, and the self diffusion of water in blood is marked in red.

The normalised weights at 10^{-1} $\times 10^{-3}$ mm^2/s (the slowest D fit for) were averaged for each participant, containing all voxels from all ROIs, and are shown in **Figure 3.8**, where it was found that CP had significantly higher 10^{-1} $\times 10^{-3}$ mm^2/s weighting than HP ($p = 0.006$, Mann-Whitney U test).

The locations of peaks in the normalised diffusograms were taken from all voxels across the 4 ROIs, averaged across participants in the HP and CP group to show the proportion of HP or CP voxels that had a peak at any D (**Figure**



(a)



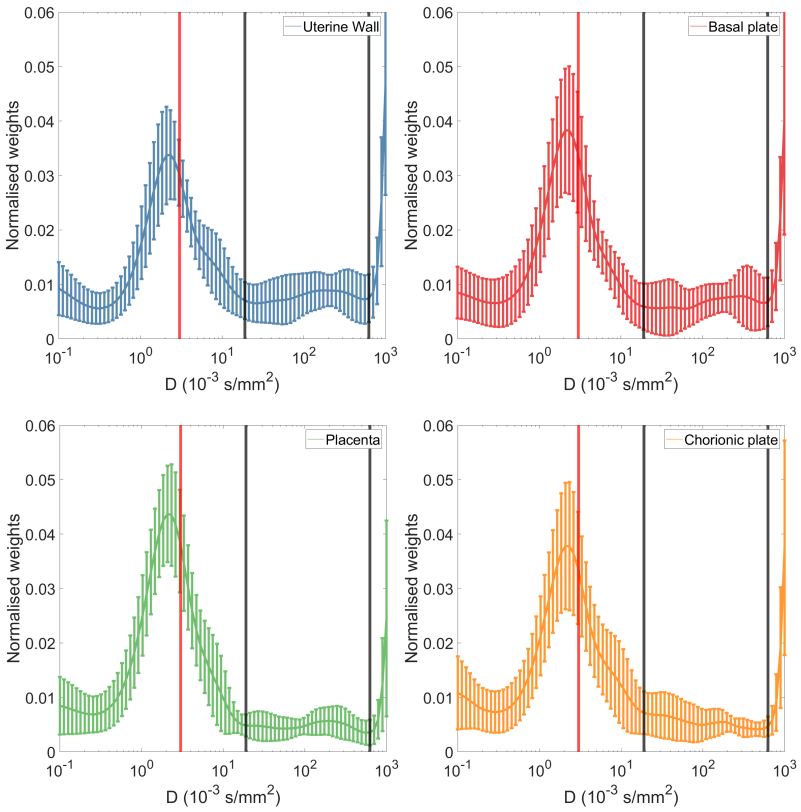
(b)

Figure 3.6: *Mean diffusograms of all a) HP, b) CP, the different ROIs are plotted in different colours, with black vertical lines representing the boundaries between sections and red vertical line shows the self-diffusion constant of water in blood, with error bars denoting standard deviation.*

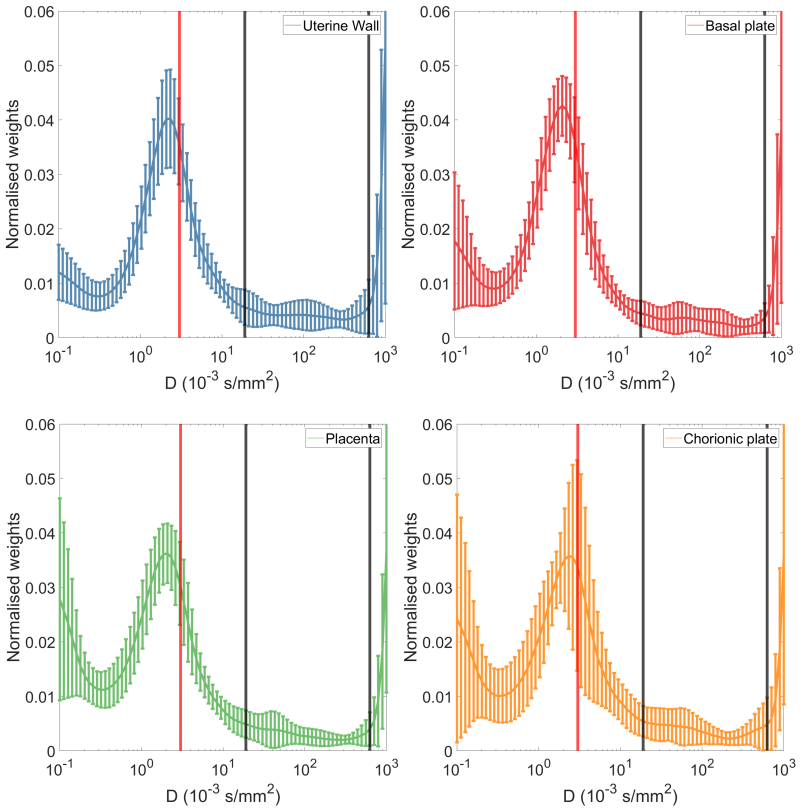
3.9).

Diffusogram fractions from a central slice, from the first 4 HP and CP are shown in **Figure 3.10** for all 3 sections, and all slices from all participants are availible in **Appendix B**. The mean diffusogram fraction for the slow, medium and fast sections for each participant, in each ROI are plotted in

Figure 3.11a, 3.11b & 3.11c. In HP there was significantly more slow fraction in the placenta than the uterine wall and basal plate ($p < 0.001$, $p = 0.01$ respectively, **Figure 3.11a**). For medium fraction there was significantly more in the uterine wall and basal plate vs the placenta ($p < 0.001$, $p = 0.01$, respectively), and for the fast fraction there was significantly more in the uterine wall and basal plate vs the placenta ($p = 0.002$, $p < 0.01$). Between HP and CP there was significantly less slow fraction in the uterine wall and basal plate of HP ($p = 0.02$, $p = 0.003$), and significantly more medium fraction in the uterine wall, basal plate, and placenta of HP ($p<0.001$, $p = 0.004$, and $p = 0.004$).



(a)



(b)

Figure 3.7: *Mean diffusograms of the entire a) HP and b) CP group. Diffusograms are normalised so each participant has equal weighting in the final average. Black vertical lines represent the boundaries between sections and red vertical line shows the self-diffusion constant of water in blood.*

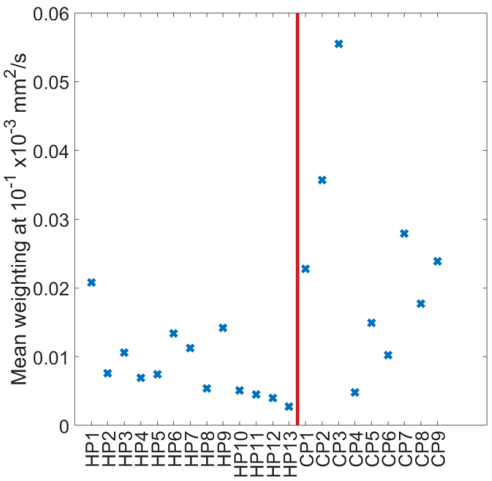


Figure 3.8: *Mean normalised weighting of each participant at the slowest measured diffusion coefficient.*

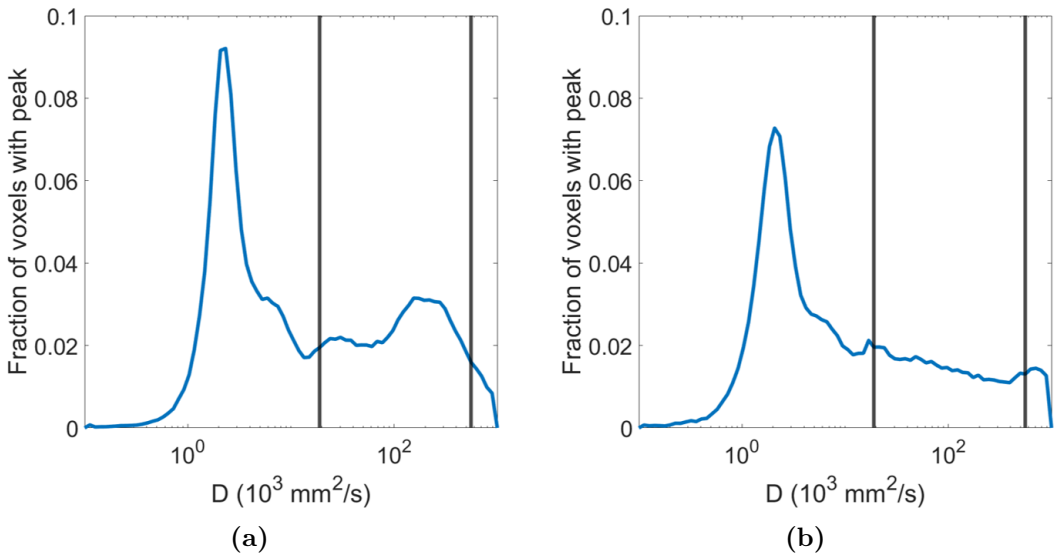
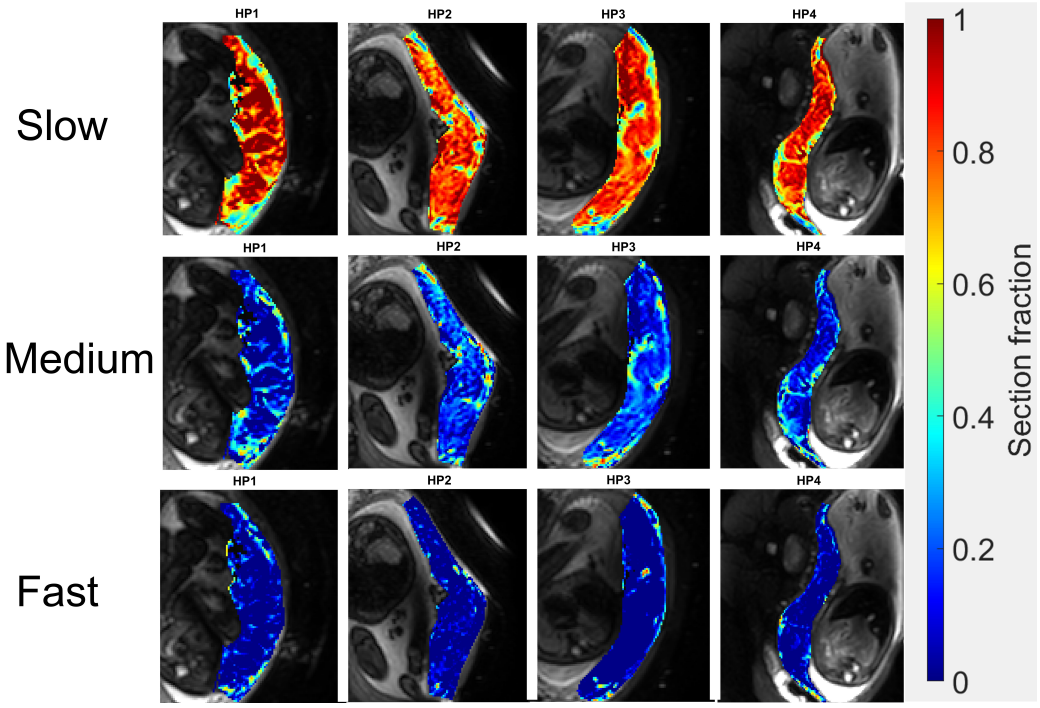
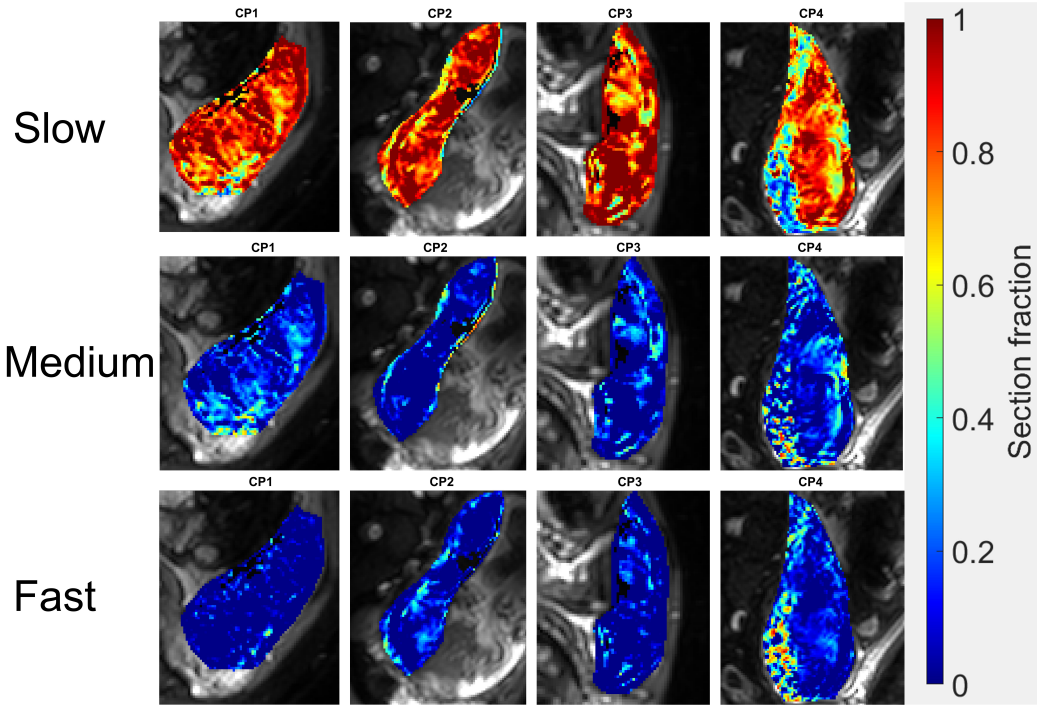


Figure 3.9: *Fraction of* ***a)*** *HP voxels, and* ***b)*** *CP voxels that have a peak at each diffusion coefficient, across the uterine wall, basal plate, placenta and chorionic plate ROIs. The boundaries between the slow and medium, and medium and fast sections are marked with black lines.*

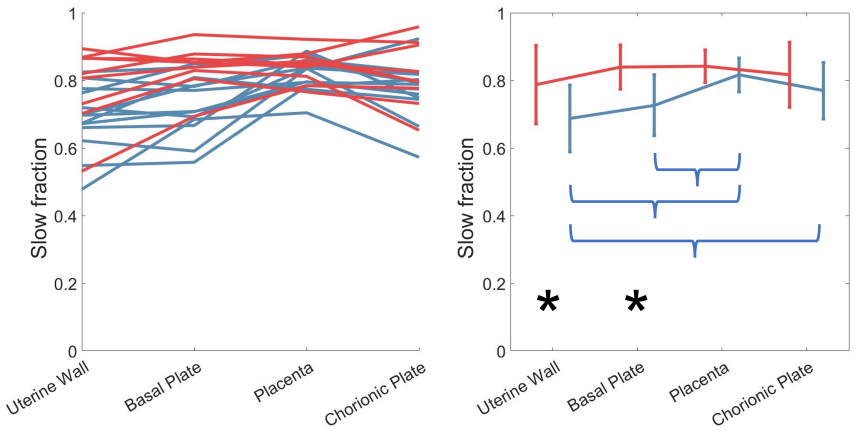


(a)

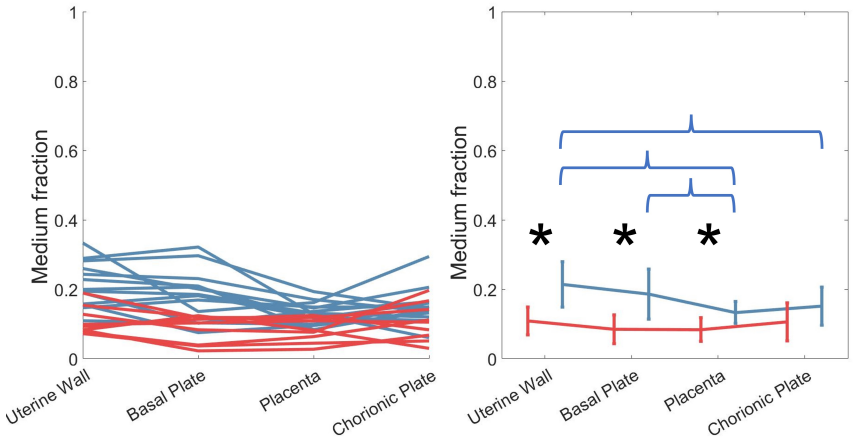


(b)

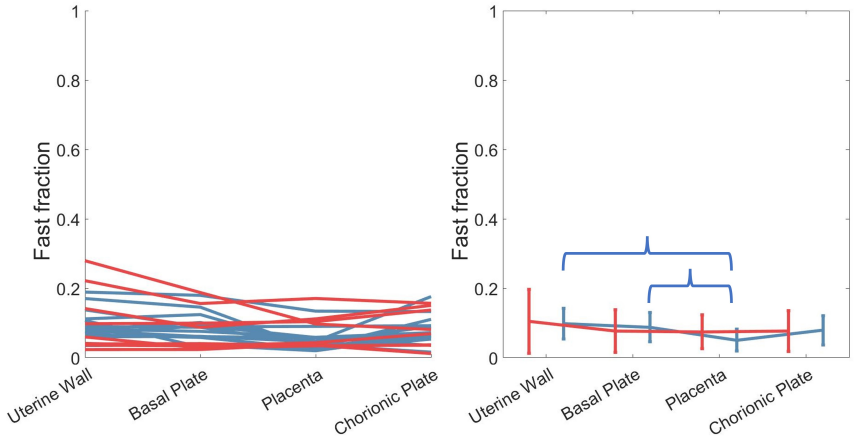
Figure 3.10: *Fraction maps of the first a) 4 HP, b) 4 CP.*



(a)



(b)



(c)

Figure 3.11: *a) slow, b) medium, and c) fast fraction from every participant, in each ROI with HP in blue, and CP in red. Left hand figure contains individual subjects connected with a line, and right hand contains only group averages, with errorbars showing the standard deviation. Significant differences between HP/CP are shown with an asterisk, and within participant groups with a curly brace.*

3.5 Discussion

For the simulated data the ILT was sensitive enough to detect the difference between two and three diffusion coefficients, shown in **Figure 3.3**, where the peaks in the diffusograms agreed well with the simulated coefficients. While the data was simulated with each component having equal weighting, the maximum fitted weightings often differed due to differences in peak widths, but sum of weights for each fitted peak were estimated to be approximately equal.

An example regularised diffusogram from a placental voxel, and the corresponding fit is shown in **Figure 3.4**. From investigating the diffusograms it became clear there were 4 key features that were commonly seen in voxels, and could all be seen in **Figure 3.5**. First was a non-zero weighting at 10^{-1} $\times 10^{-3}$mm^2/s, indicating the presence of a very slow component (slower than water diffusion) which has been previously reported when fitting placental DWI using a similar approach[6]. This was seen in both the individual diffusograms (**Figure 3.6**), and mean diffusograms in HP and CP groups (**Figure 3.7**) and was parameterised by comparing the average 10^{-1} $\times 10^{-3}$mm^2/s weighting from each participant (**Figure 3.8**), where the CP had significantly larger 10^{-1} $\times 10^{-3}$mm^2/s weighting. This could be due to restricted water diffusion or percolation which can cause the signals to increase slightly at high b values, causing a kurtosis component sometimes fitted in DWI [1] which is thought to be due to changes in cellular environment[13] and could be indicative of altered exchange between the maternal and fetal blood pools.

The second feature was a broad peak typically constrained between 0-21$\times 10^{-3}$mm^2/s (which is marked by the lowest black vertical line in the diffusogram), which was present in the mean diffusogram from every participant **Figure 3.6 & 3.7**. The mean apparent diffusion coefficient of this peak was slightly slower than the self-diffusion constant of water in blood (3×10^{-3}mm^2/s

at 37°C). It may be better defined in HP than CP as seen in **Figure 3.9**. Looking at the location of peaks within the diffusograms on average 95 ± 6% of voxels contained at least 1 peak within the slow section, meaning almost all voxels contain some slow water diffusion as expected.

The third feature was a peak in the medium section of the diffusogram, which was on a timescale to suggest it was caused by some incoherent motion of blood throughout the placenta. These peaks were at slightly different positions, and averaged out when looking at the mean diffusograms, in which for HP and CP no clear peaks could be seen in either the individual (**Figure 3.6**) or grouped diffusograms (**Figure 3.7**). However considering the peak locations **Figure 3.9** there were peaks present in the medium section of the HP group, and less in CP. In the medium section for HP an average of 60 ± 10 % of voxels contained at least one peak, compared with 35 ± 11 % in the CP. This indicates an absence of medium section incoherent movement in CP, which could be due to a reduction in incoherent flow, or if the incoherent flow of CP is much faster than observed in HP, or a combination of both, and which may be expected due to either a change in arterial input or placental structure.

The fourth feature was an increase in weights in the fast section of the diffusogram, implying there was some very fast decay over the early b-values, which has been previously reported [6], and was present on all individual mean diffusograms **Figure 3.6a & 3.6b** and the group mean diffusograms **Figure 3.7a & 3.7b**. This increase did not get detected by peak finding **Figure 3.9** as there were no maxima to detect and needs to be investigated with fraction maps, with the fast section chosen to contain this feature.

The fraction maps (**Figure 3.10**) showed that for both HP and CP the placenta is dominated by the slow fraction, which is due to the slower self diffusion of water in blood. In HP there was significantly more slow fraction

in the placental ROI than the uterine wall and basal plate (**Figure 3.11a**), due to an increase in medium and fast fraction in these ROIs, probably caused by the supply of fast turbulent blood to the placenta through the remodelled spiral arteries. In CP however there was significantly less medium fraction in the uterine wall, basal plate, and placenta relative to HP (**Figure 3.11b**). In the uterine wall and basal plate this was probably due to altered arterial input which would be explained by improper spiral artery remodelling, where instead of supplying slower turbulent blood, faster coherent blood is supplied which reduces the medium fraction, resulting in an increase in the slow fraction in these ROIs relative to HP. In the placenta the reduction in medium fraction was not accounted for by an increase in either the fast or slow fraction, meaning the reduction in medium fraction could be caused by a combination of both altered percolation through the IVS, reducing the amount of pseudodiffusive blood, and an increase in fast fraction as the remaining pseudodiffusive blood is travelling faster through the organ.

When comparing HP and CP these findings largely agree with previous work [6], that found three prominent fractions of the $T2^*/D$ spectra, where the placenta is dominated by slow diffusive blood, with more incoherently moving blood in the uterine wall vs the placenta. This work observed a decrease in medium fraction incoherent blood of CP, however there was also a decrease in the slow peak of CP, which I did not see here. This could be explained by the results shown here being a 1D diffusogram, whereas [14] investigated the effect of both $T2^*/D$ to produce more detailed information about this slow water peak.

The exact results presented in this chapter depends on the masking of data, and for example in **Figure 3.10b** CP 04 may have a region of basal plate which is within the placental ROI in the bottom left of the placenta, near the maternal side. Any participant where this happened would have had

an increase in medium and fast fraction within the placental ROI, and a reduction of the slow fraction. When averaging across the entire placental ROI this effect would be reduced as the placental ROI was so large, but it would still have lead to an overall increase in medium and fast fraction. This was unlikely to significantly affect the results presented here, as those occurrences were seemingly random across both participant groups (**Appendix B**, and groups were averaged together), but would have lead to an increase in variability within both the HP or CP group. In future it may be best to use fraction information to more accurately asses boundaries between the basal plate and placenta but it still may not be clear what is a region of placenta with medium and fast incoherent motion, and what is basal plate.

Future work should include investigating further what could cause this potential reduction in incoherent motion, including more histology or scanning of extra-corporeally perfused placentas which can then be investigated further. Additionally the numerical solution to the ILT could be optimised further with better minimisation searches to make fitting voxels this way less computationally expensive.

3.6 Conclusion

An ILT based approach provides a less biased method of fitting DWI data than IVIM, which is especially useful when the underlying tissue structure is complex or poorly understood. Here by fitting placental DWI data using an ILT based method it was possible to identify a number of key features in the placental DWI signal, such as a slow water diffusion peak which was found to be consistent between both HP and CP, as well as very slow components, where the CP had significantly more of this type of diffusion. Medium and fast incoherent motion was present in both HP and CP, but the medium fraction was found to be significantly reduced in CP, where in the uterine wall and basal

plate this was accounted for by an increase in slow fraction indicating a loss of incoherent motion. In the placental ROI however there were no significant differences between slow fraction, and fast fraction between HP and CP, so it was unclear whether the lack of medium fraction incoherent motion was due to either altered blood flow, structural changes, or both. These results help to investigate the complex placental DWI signal, and provide information about the underlying structural and haemodynamic processes in HP, and help identify where dysfunction can occur in CP.

3.7 Bibliography

[1] D. L. Bihan, "What can we see with ivim mri?," *Neuroimage*, vol. 187, pp. 56–67, 2019.

[2] J. Pfeuffer, S. Provencher, and R. Gruetter, "Water diffusion in rat brain in vivo as detected at very large b values is multicompartmental," *MAGMA*, vol. 8, no. 2, pp. 98–108, 1999.

[3] B. D and B. PJ, "Multidimensional correlation mri," *NMR in Biomedicine*, vol. 33, no. 12, p. e4226, 2020.

[4] I. Ronen, S. Moeller, K. Ugurbil, and D. Kim, "Analysis of the distribution of diffusion coefficients in cat brain at 9.4 t using the inverse laplace transformation," *Magnetic resonance imaging*, vol. 24, no. 1, pp. 61–68, 2005.

[5] J. Pfeuffer, S. W. Provencher, and R. Gruetter, "Water diffusion in rat brain in vivo as detected at very large b values is multicompartmental," *Magnetic Resonance Materials in Physics, Biology and Medicine*, vol. 8, no. 2, pp. 98–108, 1999.

[6] P. J. Slator, J. Hutter, M. Palombo, L. H. Jackson, A. Ho, E. Panagiotaki, L. C. Chappell, M. A. Rutherford, J. V. Hajnal, and D. C. Alexander, "Combined diffusion-relaxometry mri to identify dysfunction in the human placenta," *Journal of Cerebral Blood Flow metabolism*, vol. 37, no. 8, pp. 2987–3000, 2016.

[7] D. Yablonskiy, G. L. Bretthorst, and J. J. Ackerman, "Statistical model for diffusion attenuated mr signal," *Magn Reson Med*, vol. 50, no. 4, p. 664–669, 2003.

[8] C. Hansen, "Regularization tools, a matlab package for analysis and solution of discrete ill-posed problems," *Numerical Algorithms*, vol. 46, p. 189–194, 2007.

[9] C. Hansen, *Computational Inverse Problems in Electrocardiology*.

[10] I.-G. Marino, "rilt.m." https://www.mathworks.com/matlabcentral/fileexchange/6523-rilt, 2022.

[11] J. C. Lagarias, J. A. Reeds, M. H. Wright, and P. E. Wright, "Convergence properties of the nelder–mead simplex method in low dimensions," *SIAM Journal on Optimization*, vol. 9, no. 1, pp. 112–147, 1998.

[12] C. Funck, F. Laun, and A. Wetscherek, "Characterization of the diffusion coefficient of blood," *Magn Reson Med*, vol. 79, no. 5, pp. 2752–2758, 2018.

[13] J. Jensen, J. Helpern, A. Ramani, H. Lu, and t. . D. Kaczynski, K *Magn Reson Med*, vol. 53, no. 6, pp. 1432–1440, 2005.

[14] P. J. Slator, J. Hutter, L. McCabe, A. D. S. Gomes, A. N. Price, E. Panagiotaki, M. A. Rutherford, J. V. Hajnal, and D. C. Alexander, "Placenta microstructure and microcirculation imaging with diffusion mri," *Magnetic Resonance in Medicine*, vol. 80, no. 2, pp. 756–766, 2018.

Chapter 4

Fitting Placental DWI data using an IVIM model; and comparisons with the ILT based approach.

4.1 Introduction

A bi-exponential Intra-Voxel Incoherent Motion (IVIM) model is currently the most popular method for fitting placental Diffusion Weighted Imaging (DWI) data, with current studies tending to focus on how the IVIM fraction (f_{IVIM}) and slow diffusion coefficient (D) change either with placental dysfunction or Gestational Age (GA). Unlike in the Inverse Laplace Transform (ILT) approach presented in **Chapter 3**, with the IVIM model, data is fitted for only two distinct diffusion coefficients [1] where D is attributed to the slow self diffusion of water in blood, and pseudodiffusion (D^*) is due to faster incoherent processes. While parameters can vary with the exact sequence timings [2] there is general agreement that f_{IVIM} is lower in either Small for Gestational Age (SGA) [3], Fetal Growth Restriction (FGR) [4–6] or Pre-Eclampsic (PE) [7, 8] placentas compared with Healthy Placentas (HP), especially around the

edge of the placenta and in the basal plate, with one study also showing a reduction in D in CP[9]. Less attention is given to D^* with many studies not quoting their D^* values or discussing the range of fitted parameters used, as D^* can be noisy and difficult to estimate[10], however by concentrating more sampling over low b-values (0-50 s/mm^2) than higher b-values (>450 s/mm^2) more accurate estimates of D^* are possible [11]. In the placenta the incoherent motions that drive D^* are complex and not easy to predict and include various different motions such as turbulent blood in the spiral arteries, blood that percolates through the intervillous space, flow across the organ [12], and fetal blood within the villous trees, and it is not immediately obvious how these combine into a single term that affects the signal. As I showed by fitting data with an ILT based approach in **Chapter 3** there are many voxels where the decay is not described by a bi-exponential model, with broad, skewed slow peaks often combining with medium and fast incoherent blood giving rise to more complex signal decay than can be described by two components. While both approaches have been used to fit DWI data before a direct comparison between approaches has not. In practice it is feasible that by using two components that are constrained properly, where a single slow diffusive term describes the average slow component, and the medium and fast incoherent blood is now averaged into a single term D^*, maps can be produced that provide useful potential biomarkers to characterise the clinical problem.

Here I fitted the same placental DWI data from **Chapter 3** to an IVIM model, where I use the boundary between slow water diffusion, and faster incoherent motion defined by the ILT in **Chapter 3** to inform the fit. Then I compared parameter maps of HP and CP across 4 Regions Of Interest (ROI), (uterine wall, basal plate, placenta, and chorionic plate) to investigate differences in placental structure and haemodynamics both across the regions, and between HP and CP. These values were then compared back to literature, where I expected f_{IVIM} to be reduced in the uterine wall and basal plate of CP

relative to HP, and knew there may have been reduced D in CP relative to HP. I then compared these IVIM fits back to the ILT fits, to investigate similarities and differences between the two approaches, and discuss the advantage and disadvantages of both approaches for fitting DWI.

4.2 Theory

4.2.1 Measuring blood flow with IVIM

The IVIM model is outlined in **Chapter 1** and describes DWI data by a bi-exponential decay driven by D and D^*

$$S = S_0[(1 - f_{IVIM})e^{-bD} + f_{IVIM}e^{-bD^*}]. \tag{4.1}$$

The difficulty in estimating D^* in the placenta originates from **Equation 1.46**

$$D^* = \frac{lv}{6} \tag{4.2}$$

where l is the lengthscale of the incoherent motion and v is the velocity of blood. While it can be expected that there are regions of high D^* in the uterine wall as fast moving incoherent blood travels through the spiral arteries it is hard to predict how D^* would change, as the aforementioned flows of blood combine into a single term within a voxel. This uncertainty extends to **Equation 1.53** which states that blood flow (F) $\propto f_{IVIM}D^*$, provided the characteristic length l and total length of incoherent motion L remain constant. In practice it is hard to assume that in different regions of the placenta L and l will remain the same, as faster flowing turbulent blood supplied by spiral arteries must slow down and perfuse throughout the intervillous space, which both produce incoherent effects of different lengths. However I still think this product is a useful marker, as it could be used to distinguish voxels that show a high proportion of higher D^* blood (meaning either short length scales l or

high velocity v).

4.2.2 Kurtosis

As discussed in **Chapter 1** the DWI signal is often not described purely by exponential decays, as these rely on pure Gaussian diffusion. In tissue kurtosis can occur depending on the exact cellular environment[13], and changes in kurtosis could indicate changes in exchange between the maternal and fetal blood pools. There are a number of models that can empirically account for kurtosis, and one such model is outlined further in [13], by taking a Taylor expansion of $ln(b)$ from the slow diffusive term to give

$$ln(S(b)) = ln(S(0)) - bD + \frac{1}{6}b^2D^2K + O(b^3) \tag{4.3}$$

[14] where higher order terms are ignored, and K is a dimensionless constant that gives an approximate measure of amount of kurtosis in the diffusion signal. This can be added to the IVIM model to give

$$S(b) = S_0[(1 - f_{IVIM})e^{-bD+\frac{1}{6}b^2D^2K} + f_{IVIM}e^{-bD^*}]. \tag{4.4}$$

This particular model was chosen as it is a simple extension of the IVIM model that gives a quantitative measure of non-Gaussian diffusion.

4.3 Methods

4.3.1 Data collection

The data collection here is outlined in **Section 2.2.1**, and was the same as in **Chapter 3** where 19 b-values were collected (b = [0 1 3 9 18 32 54 88 110 147 180 200 230 270 300 350 400 450 500]). There were 13 healthy placentas (HP) and 9 compromised placentas (CP) with sufficient data for further analysis.

4.3.2 Fitting

The IVIM model (**Equation 4.3**) was fitted in a number of stages. Initially low b-value data (0-110 s/mm^2) was fitted to a mono-exponential decay to provide an initial estimate for S_0 and D^* as at low b-value D^* dominates the signal decay. D^* was always limited to be between 25-1000 $\times 10^{-3}$ mm^2/s, which was informed by the boundaries set in the ILT based fits in **Chapter 3** which were designed to split the faster incoherent components from the slow water diffusion component. The higher b-values (200-500 s/mm^2) were then fitted to a mono-exponential decay to provide an initial estimate of D, which makes a higher proportion of the signal decay at larger b-value, where D was constrained between 0-25 $\times 10^{-3}$ mm^2/s, again informed by the ILT.

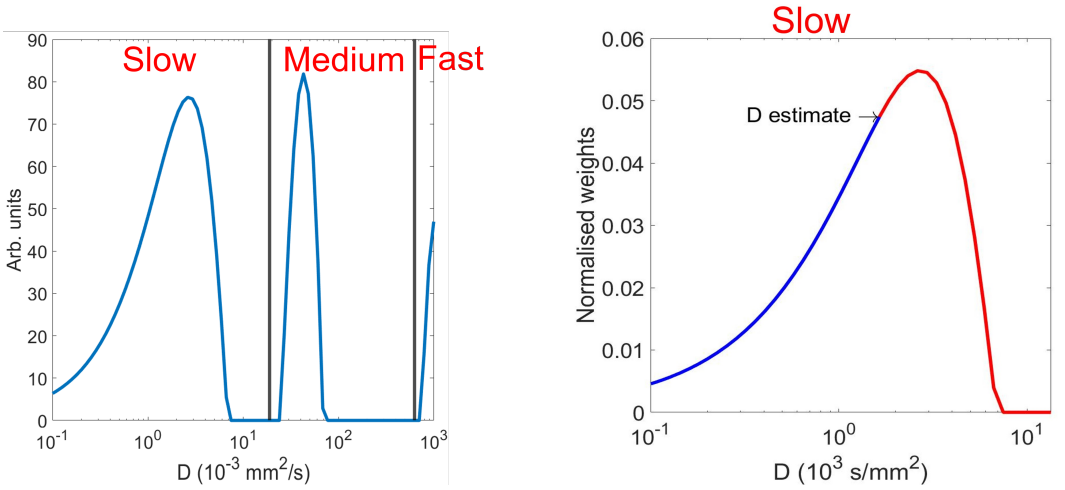
These initial estimates were then used to fit the data to the IVIM model without kurtosis (**Equation 4.1**), to provide a new set of estimates of S_0, D, D^* and an estimate of f_{IVIM}. Finally these estimates were used to fit voxels to the full IVIM model with added kurtosis (**Equation 4.4**) as it is generally recommended to fit to an IVIM model in stages to provide more accurate estimation of parameters [10]. For all fits f_{IVIM} was constrained to be between 0-1, and K from 0-10, which were biologically plausible values.

These fits were then used to produce parameter maps of f_{IVIM}, D, D^*, K and $f_{IVIM}D^*$. Average values of these parameters were computed for four different ROI's (uterine wall, basal plate, placenta, and chorionic plate, **Section 2.2.3**). Similar to **Chapter 3** differences between mean parameter values between HP and CP were checked for significance with a Mann-Whitney U test. Differences within groups were initially investigated with a Friedman test, which if found significant differences within either HP or CP a Wilcoxon rank sum test was used as a post-hoc test to identify which specific ROI's were different. As a high degree of variance was seen in the K maps the standard

deviation of the K across all ROIs was calculated.

4.3.3 Comparison to ILT

To compare this fit back to the ILT based approach, IVIM parameters were compared to the common features of the ILT diffusograms outlined in **Chapter 3** (shown again in **Figure 4.1a**). The medium and fast fractions (calculated by normalising the weights over the entire diffusogram to sum to 1, then summing the weights in the medium and fast sections respectively, to give a measure of the fraction of total signal decay comes from each section) are measures of the proportion of a voxel that contains medium, or fast moving incoherent blood so was compared to f_{IVIM} and $f_{IVIM}D^*$. K was compared to the ILT weight at the slowest diffusion coefficient fitted for ($10^{-1}\times$ 10^{-3} mm^2/s) using the ILT, in each ROI, for each participant.



(a) **(b)**

Figure 4.1: *a) An example diffusogram produced by the ILT based approach in **Chapter 2** with slow, medium and fast sections labelled. b) An example of how D is estimated from the ILT diffusogram. The slow compartment from a) is normalised so the weights sum to 1, then cumulatively summed to find the halfway point (0.50), which is taken as an estimate for D. The blue section highlights where the cumulative sum is < 0.50, and the red when it is > 0.50.*

Comparing D with an ILT measure was more complicated, as the peaks in the slow section tended to be skewed (**Figure 4.1a**) which could lead to a

significant over or underestimate of D. Instead to try to provide a more accurate estimate of D from the ILT I took the slow section from the diffusogram, and normalised the weights to sum to 1. Then by cumulatively summing these weights and finding the diffusion coefficient at the halfway point (when the cumulative sum was closest to 0.5) and taking this coefficient as D_{ILT} (**figure 4.1b**), which was directly compared with D from the IVIM fit.

4.4 Results

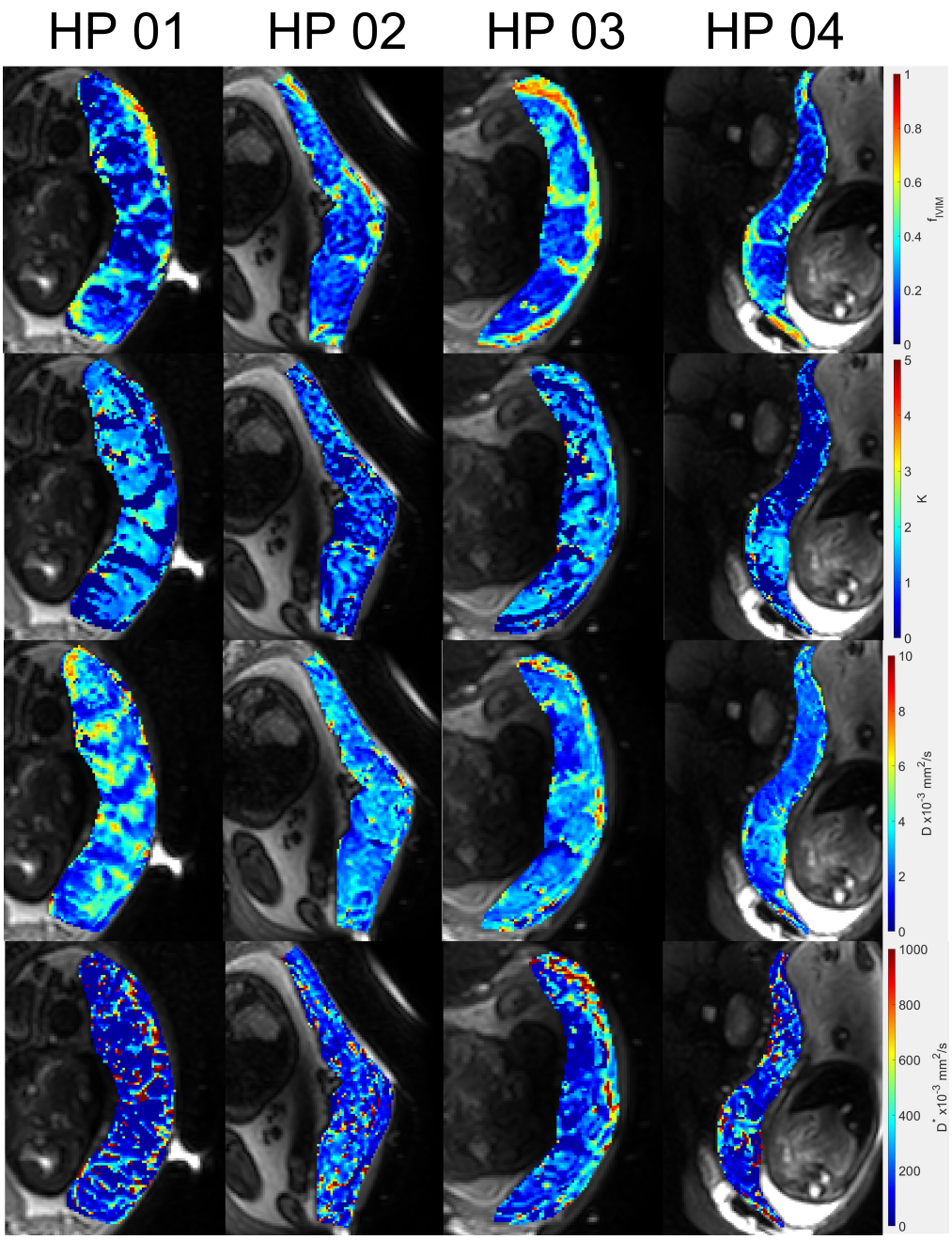
Parameter maps from the first four HP, and four CP chronologically scanned as part of the experiment are shown in **Figure 4.2** for f_{IVIM}, K, D, and D^*, and all slices from all participants are availible in **Appendix C**. Average values of the fitted parameters from each ROI were calculated for each participant, and resulting plots of f_{IVIM}, K, D, D^*, and $f_{IVIM}D^*$ are shown in **Figure 4.3**. Significant differences between HP and CP are indicated with an asterisk, and differences between ROIs are highlighted with a curly bracket. In **Figure 4.3a** CP had significantly lower f_{IVIM} in the basal plate and uterine wall ROI ($p = 0.03$ & $p = 0.003$) compared to HP, and within HP the uterine wall had higher f_{IVIM} than the placenta and chorionic plate ($p < 0.001$ & 0.02) and the basal plate had significantly higher f_{IVIM} than the placenta ($p = 0.01$). Both HP and CP had significantly reduced D in the placenta, relative to the uterine wall (**Figure 4.3c**, $p = 0.02$ & $p = 0.02$), where also in the placenta CP had significantly lower D than HP ($p = 0.009$). For $f_{IVIM}D^*$, in HP (**Figure 4.3e**) $f_{IVIM}D^*$ was higher in the uterine wall than the placenta ($p = 0.001$).

A plot of the standard deviation (σ) of K across the placenta for every participant is shown in **Figure 4.4**, where CP had significantly higher σ ($p = 0.03$).

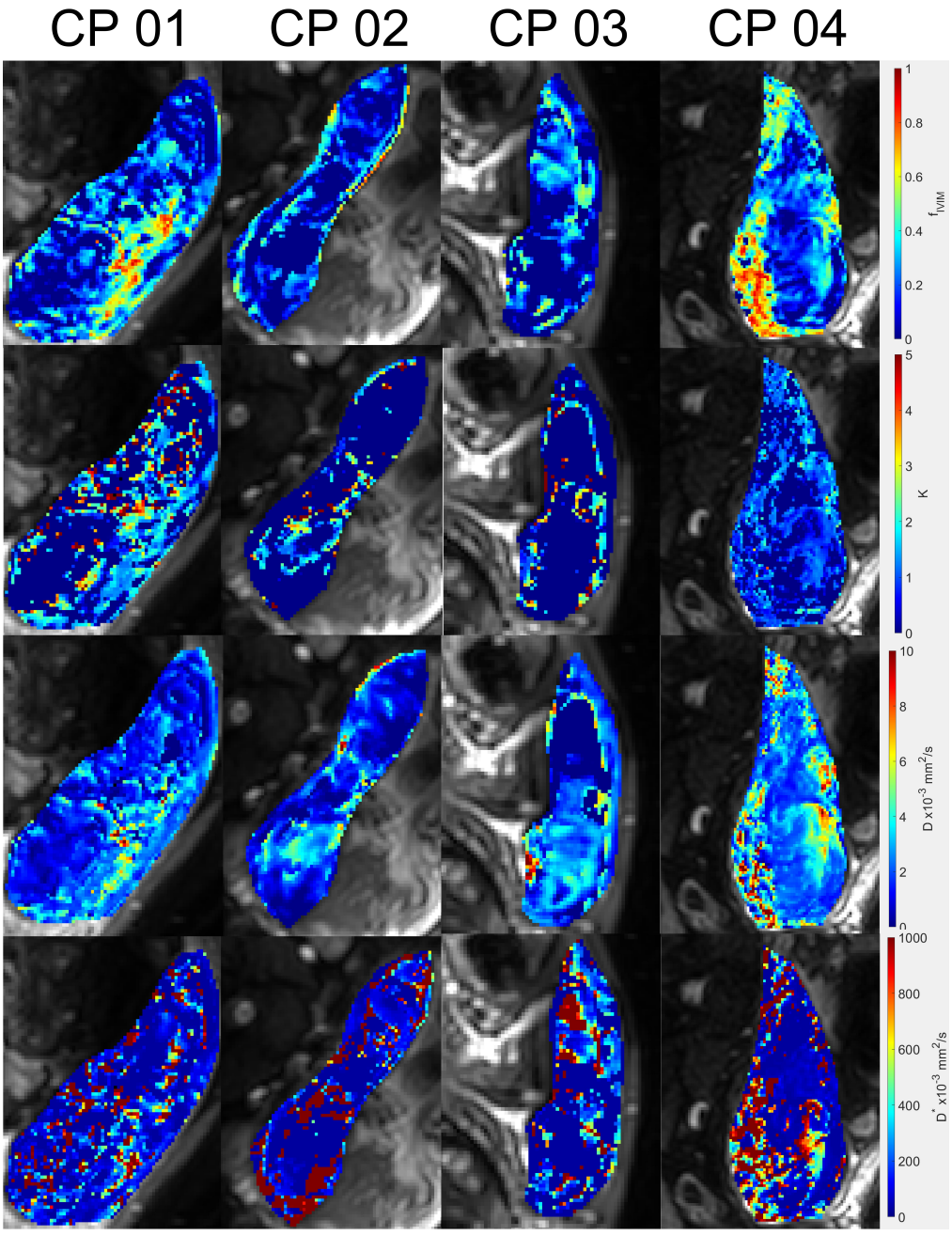
Figure 4.5a shows a histogram of D^* values across all ROIs, for all partic-

ipants. From this the f_{IVIM} from voxels corresponding to low D^* (25-30 $\times 10^{-3}$ mm^2/s), and high D^* (950-1000 $\times 10^{-3}$ mm^2/s) are plotted in histograms in **Figure 4.5b & 4.5c** respectively.

Figure 4.6 shows the comparisons between the IVIM parameters, and the ILT results from **Chapter 3**. The mean medium (**Figure 4.6a**), and fast (**Figure 4.6b**) fraction was plotted against mean f_{IVIM} from all ROIs, from all participants. There was a strong correlation between f_{IVIM} and medium fraction (adjusted $R^2 = 0.78$) and weak correlation between f_{IVIM} and fast fraction (adjusted $R^2 = 0.41$). In **Figures 4.6c & 4.6d** the mean medium and fast fraction was plotted against $f_{IVIM}D^*$ from all ROIs, from all participants where there was no correlation between medium fraction and $f_{IVIM}D^*$ (adjusted $R^2 = 0.17$), but a strong correlation (adjusted $R^2 = 0.91$) between fast fraction and $f_{IVIM}D^*$. Mean K was plotted against the 10^{-1} $\times 10^{-3}$ mm^2/s weighting from the ILT in **Figure 4.6e**, which showed no correlation (adjusted $R^2 = 0.03$). When the groups were split into HP and CP however, there was still no correlation in the CP group (adjusted $R^2 = 0.03$) but a weak correlation in the HP group (adjusted $R^2 = 0.43$). From the IVIM results the D was compared with the ILT in **Figure 4.1b** by finding the halfway point of the slow fraction, which was strongly correlated (adjusted $R^2 = 0.80$). Additionally D from the IVIM model was compared with the ILT by finding the mean position of the largest peak within the slow section, which was plotted against D in **Figure 4.6h** which showed a very weak correlation (adjusted $R^2 = 0.24$).

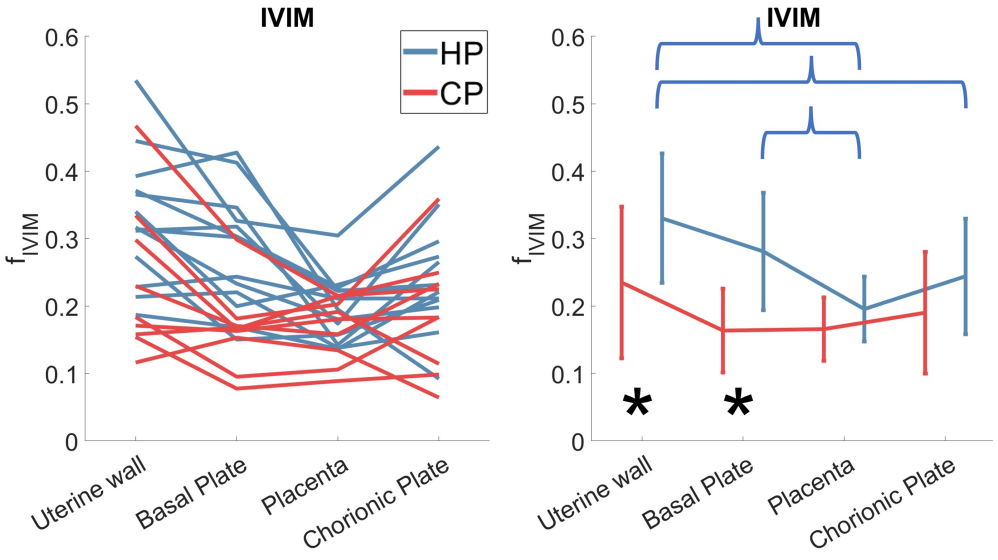

HP 01
HP 02
HP 03
HP 04
1
0.8
0.6
0.4
0.2
0
f_{IVIM}
5
4
3
2
1
0
K
10
8
6
4
2
0
D x10^{-3} mm^2/s
1000
800
600
400
200
0
D* x10^{-3} mm^2/s

(a)

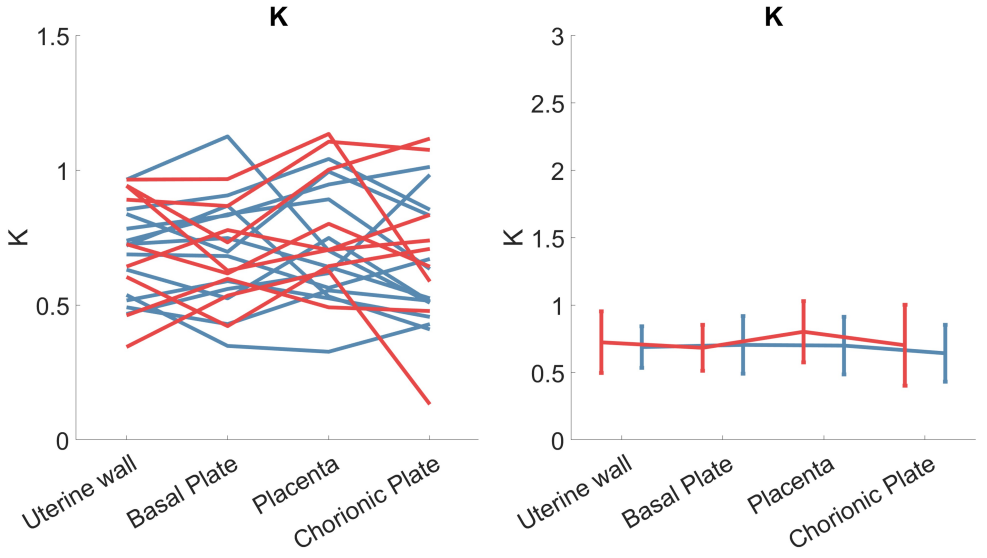


(b)

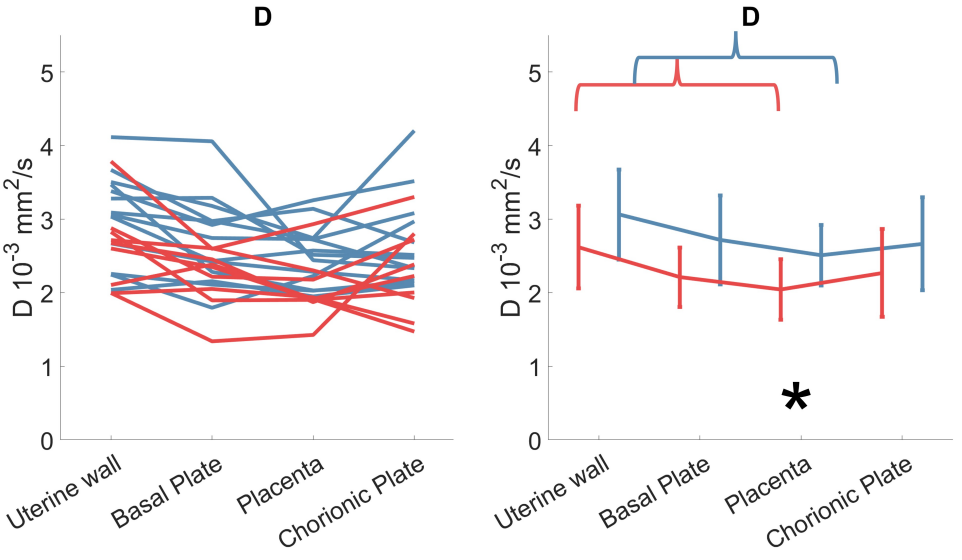
Figure 4.2: *Parameter maps from the IVIM fit for a central slice from the first 4 a) HP and b) CP scanned. From top to bottom parameter maps are f_{IVIM}, K, D, and D^*.*


IVIM
HP
CP
f_{IVIM}
0.6
0.5
0.4
0.3
0.2
0.1
0
Uterine wall
Basal Plate
Placenta
Chorionic Plate
IVIM
*
*

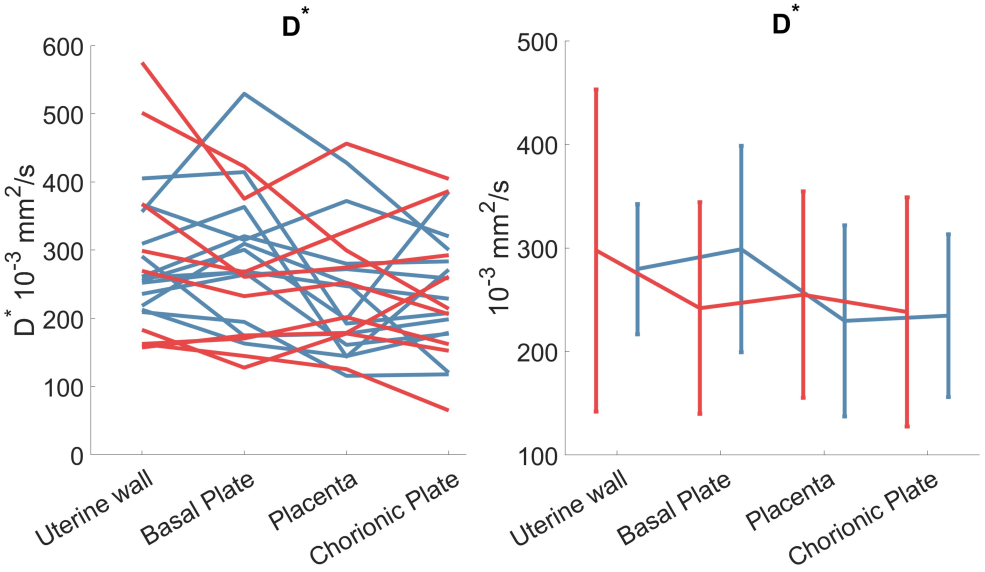
(a)


K
1.5
1
0.5
0
3
2.5
2
1.5
Uterine wall
Basal Plate
Placenta
Chorionic Plate

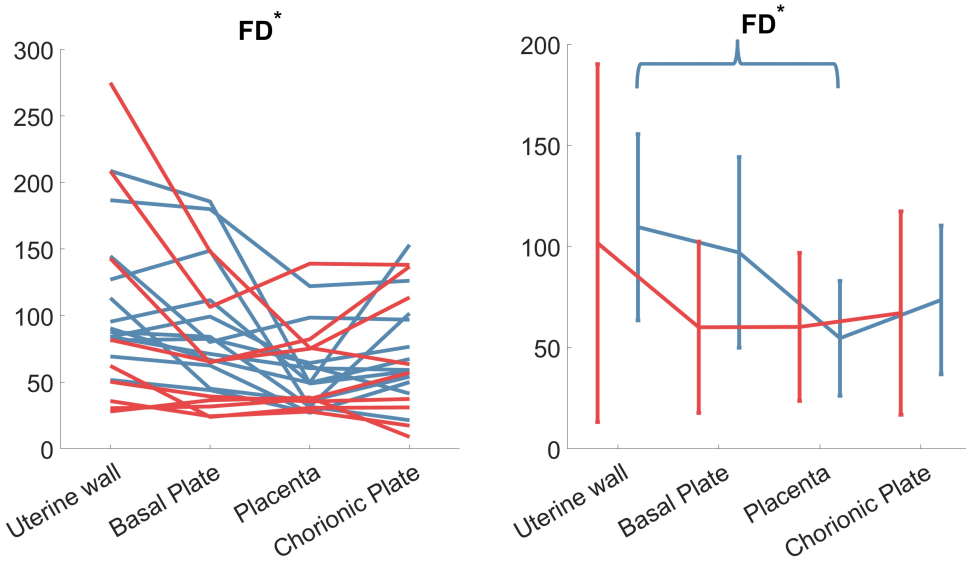
(b)


D
$D\ 10^{-3}\ mm^2/s$
5
4
3
2
1
0
Uterine wall
Basal Plate
Placenta
Chorionic Plate
*

(c)



(d)



(e)

Figure 4.3: *Mean values of a) f_{IVIM}, b) K, c) D, d) D^*, e) $f_{IVIM}D^*$ are shown twice, once where each participants values are connected by a line and the mean parameter value from each ROI is plotted, and again with the mean HP and CP values shown, with the errorbar showing the standard deviation. Curly brackets represent significant differences within either HP or CP, and asterisks represent significant differences between HP and CP.*

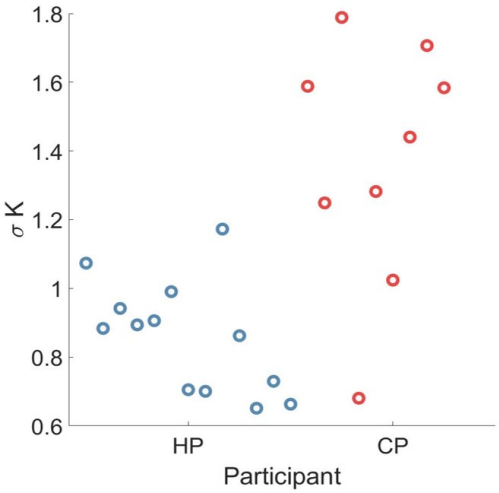


Figure 4.4: *Standard deviation of K across all 4 ROI's from each placenta, HP are plotted in blue and CP in red.*

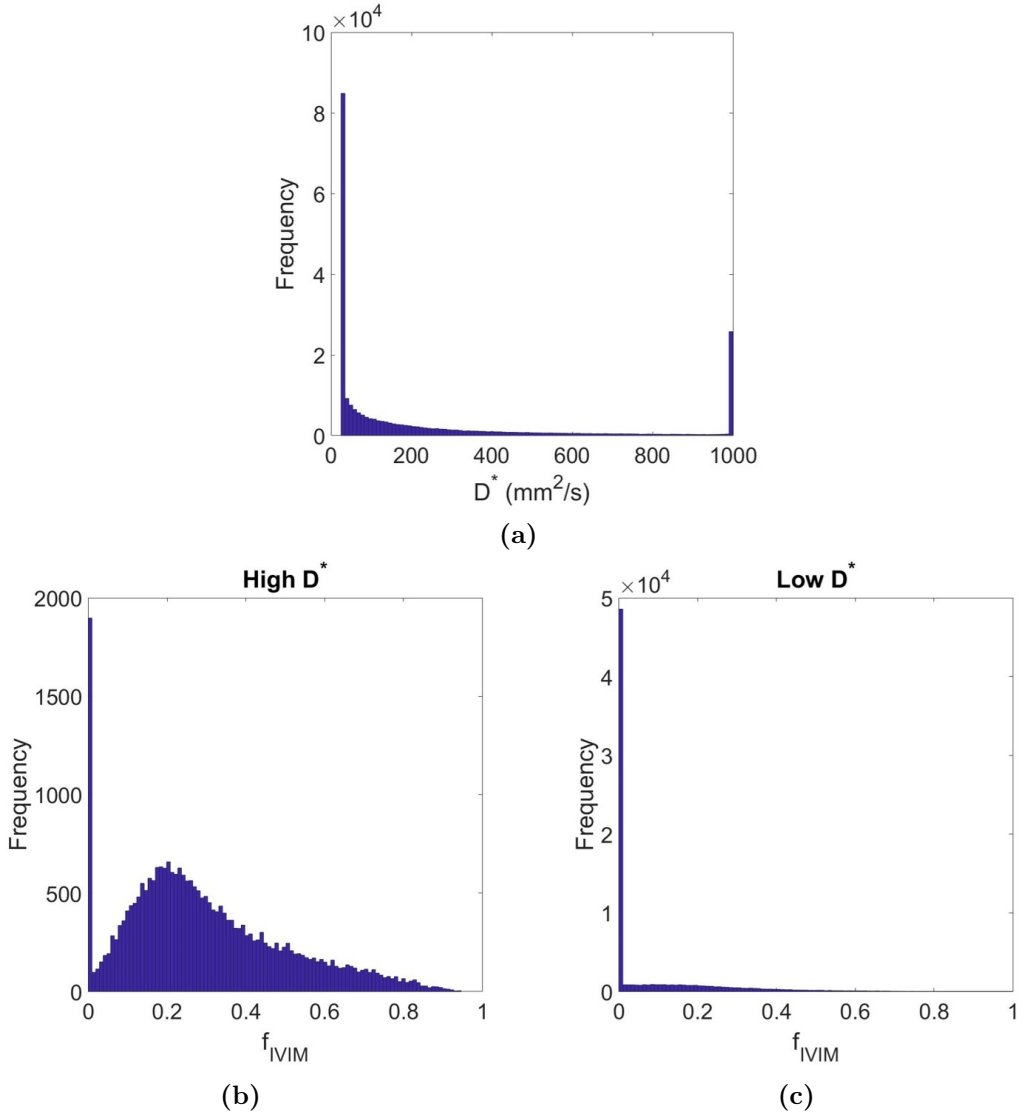
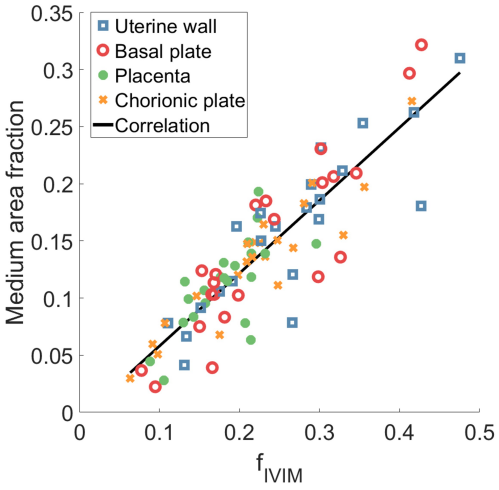
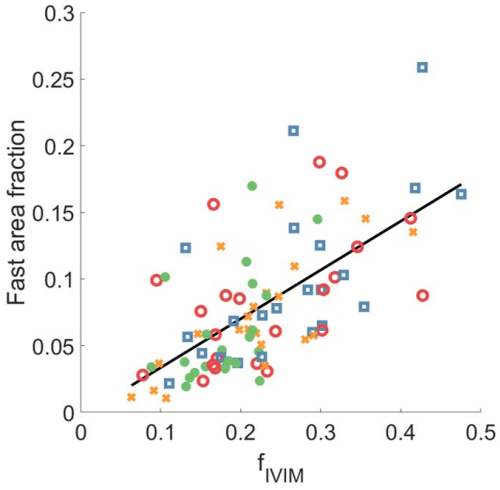


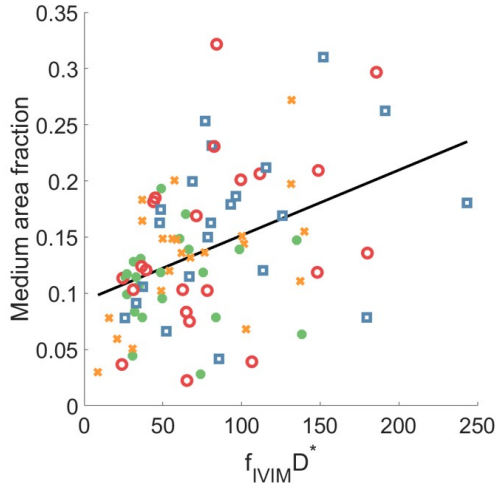
Figure 4.5: *a) D^* histograms from all voxels. f_{IVIM} histograms from only b) low D^* voxels (25-30 $\times 10^{-3}$ mm^2/s) and c) high D^* voxels (950-1000 $\times 10^{-3}$ mm^2/s)*


Uterine wall
Basal plate
Placenta
Chorionic plate
Correlation
Medium area fraction
f_{IVIM}

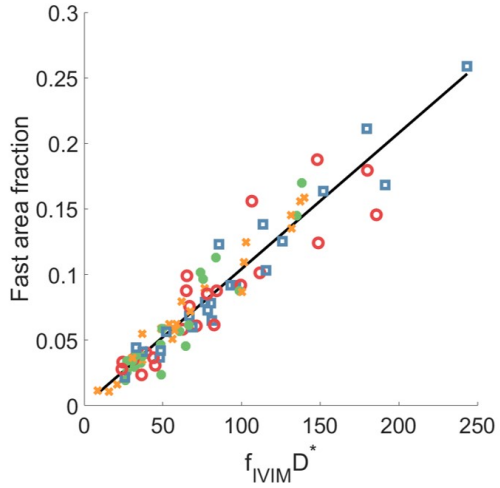
(a)


Fast area fraction
f_{IVIM}

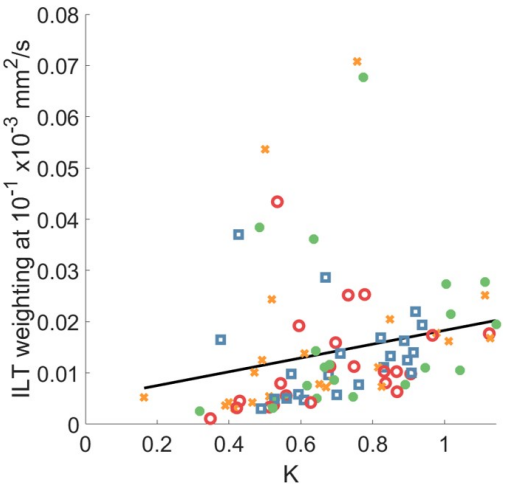
(b)


Medium area fraction
$f_{IVIM}D^*$

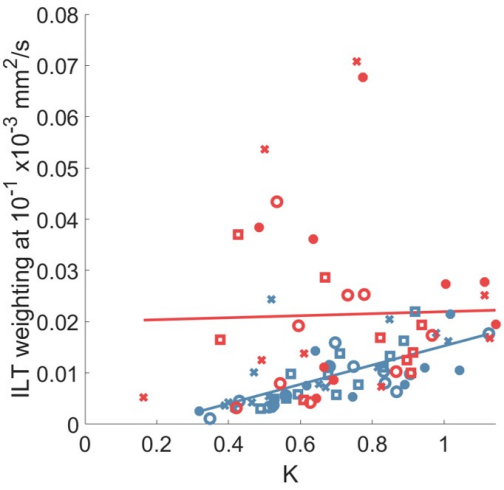
(c)


Fast area fraction
$f_{IVIM}D^*$

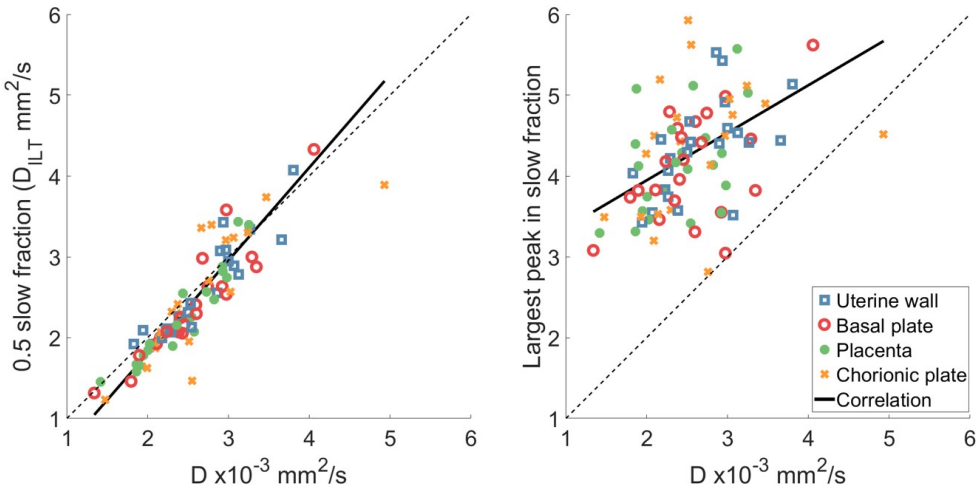
(d)


ILT weighting at 10^{-1} x10^{-3} mm^2/s
K

(e)


ILT weighting at 10^{-1} x10^{-3} mm^2/s
K

(f)



(g) **(h)**

Figure 4.6: *Figures comparing ILT measures with parameters from the IVIM fit, with the correlation between the parameters plotted as a solid black line. a) and b) show the relationship between f_{IVIM} and the medium and fast fractions, c) and d) show the relationship between $f_{IVIM}D^*$ and the medium and fast fractions. e) shows the relationship between the the ILT weight at the slowest diffusion coefficient fitted for using the ILT ($10^{-1} \times 10^{-3}$ mm^2/s) with f) showing the same results but HP are represented in blue, and CP in red, and the shapes of the individual points matches the ROIs from the previous figures. g) Shows the relationship between D from the IVIM fit, and D_{ILT} estimated from the ILT based fits, with the line D_{ILT} = D plotted as a black dashed line. h) Shows the average position of the largest peak within the slow fraction, and D from the IVIM fit.*

4.5 Discussion

The parameter maps (**Figures 4.2a 4.2b**) show the general features of the IVIM fit in the placenta. As expected from previous results in HP[3] there are regions of higher f_{IVIM} in the uterine wall and basal plate ROIs, significantly higher than in the placental ROI. This was probably due to the volume of incoherent blood that was supplied to the placenta through the uterine wall into the basal plate, which was then dampened upon entry. In CP however these patterns were not observed, the regions of higher f_{IVIM} in the uterine wall and basal plate were not present, which agrees with previous work [3, 7]. This was probably indicative of improper spiral artery remodelling causing jets of faster flowing coherently moving blood, as opposed to the slower turbulent stream that spiral artery remodelling is thought to provide[15].

The K maps in HP (**Figure 4.2a**) appeared to show regions of different structures, with regions of higher K having regions of low or no K interspersed between them. In CP however (**Figure 4.2b**) the K maps appear less well ordered, with regions of very high k dispersed around regions of zero K, and although no differences in mean K between HP and CP were observed (**Figure 4.3b**), CP had higher mean standard deviation of K within each participant (**Figure 4.4**). As K is caused by restricted diffusion in the cellular environment these sections of very high, and very low K in the CP could be due to regions of altered exchange between the maternal and fetal blood pools, causing increased variation in oxygenation across the placenta which has been observed before [16].

The diffusion coefficient D describes the slow self diffusion water of blood, which is not purely due to the self diffusion of water in blood (which is $\approx 3{\times}10^{-3}$ mm^2/s) but similar to K will vary depending on the exact cellular environment. In both HP and CP D was significantly reduced in the placental

ROI compared to the uterine wall **Figure 4.3c**, probably because the placental cellular environment is very different to that in the uterine wall. Here I also observed a reduction in D in the placental ROI of CP compared to HP, which has been reported before [9] and is probably caused by some change in exchange of oxygen between the two blood pools due to changes in villous tree structure.

D^* was quite varied as the exact value depends on both the length scale and the underlying velocity of the incoherent motion, which in the placenta is expected to vary greatly across the organ. The D^* fit produced a large number of voxels that were at either the lower (25 $\times 10^{-3}$ mm^2/s) or upper limit (1000 $\times 10^{-3}$ mm^2/s) permitted by the fit (**Figure 4.5a**). This does not necessarily mean that the D^* values were unreliable, as almost all voxels with low D^* and a significant proportion of voxels with high D^* also had very low f_{IVIM}. It is instead probable that these voxels were best described by a mono-exponential decay, but a limitation of the IVIM model is that every voxel is fitted to a bi-exponential decay. A significant proportion of the high D^* voxels however did contain a significant f_{IVIM}, indicating that $f_{IVIM}D^*$ may be a more appropriate method for analysing and understanding the faster incoherent terms within the placenta than D^* alone.

In HP there was significantly higher $f_{IVIM}D^*$ in the uterine wall than in the placenta (**Figure 4.3e**). The advantage of using $f_{IVIM}D^*$ over D^* was that voxels best described by mono-exponential decay (i.e. low f_{IVIM}) or low D^* (voxels without fast incoherent flow) would result in a lower value of $f_{IVIM}D^*$, mitigating some of the issues of using D^* alone. The uterine wall had higher $f_{IVIM}D^*$ than the placenta in HP, indicating a high volume of fast incoherent blood. Linking this back to flow it indicates that there was a drop in perfusion in the placenta vs the uterine wall, but in practice it is hard to make exact quantitative comparisons in terms of perfusion in different ROIs, as the relationship in **Equation 1.53** requires a constant V_{voxel}, L, and l.

This data has been fitted previously to an IVIM model without using the ILT to inform the fit [16], with a slightly different approach where D^* was fitted between 10-5000 $\times 10^{-3}$ mm^2/s and subtracted from the signal before fitting for D, which could range from between 0-10 $\times 10^{-3}$ mm^2/s. There was still agreement between the two fit approaches, with the key differences that here I observed a reduction in f_{IVIM} of CP relative to HP in the uterine wall, reduced D in the placental ROI of both HP and CP with respect to the uterine wall, and a reduction of D in the placental ROI of CP relative to HP which were not present in [16]. I believe the data presented here better reflects the underlying placental structure and haemodynamics, and is more appropriate for distinguishing slower self diffusion, and faster incoherent components. While the upper limit for D used here (25 $\times 10^{-3}$ mm^2/s) is fairly high for an IVIM fit, the diffusograms demonstrate that this slow component is quite broad and the exact value of D is likely to be some average of this component, and although values will rely on the exact sequence and timings used it agrees with previous work [17]. By having the boundary set lower in [16] I believe there was some mixing between the terms, which can be seen as [16] reports D to be lower than here, and because D is lower [16] also reports K to be higher, as K must be higher to account for the same amount of kurtosis in the signal (**Equation 4.4**).

Similar to **Chapter 3** the exact results here will depend on the masking of data, and if regions of basal plate extended into the placental ROI, for example participant CP 04 in **Figure 4.2b** this would alter the results. These regions would cause an increase in placental f_{IVIM}, and could cause an increase in D^* due to the faster flows present in the basal plate. It would be unlikely to change K however, as K was similar across all 4 ROIs. Ultimately as placental f_{IVIM}, D^*, and K did not change between HP and CP these results are probably not due to these effects, but it could have affected the variance

within the HP and CP group. The effect on D in the placental ROI however was unclear, and the change in placental D maybe could have been caused by either the HP or CP group containing more participants where the basal plate extended into the placental ROI. Maps from all participants are available in **Appendix C** and the effect appeared to be randomly distributed between the groups, indicating while the variance of D within a group may be increased, the effect on the mean is probably averaged out.

A limitation of this work is the number of comparisons made due to the number of ROIs and parameters to compare. While some values were expected to differ between health and disease as outlined in the introduction, some within group comparisons will need further investigation to ensure differences are not due to chance.

4.5.1 IVIM vs ILT

f_{IVIM} Was strongly correlated with medium fraction (**Figure 4.6a**), but weakly correlated with fast fraction (**Figure 4.6b**). This was probably because fast fraction corresponds to decay which occurred very quickly, over only 2-3 b-values, and for any voxel where there was a combination of fast and medium fraction these must be averaged into a single value of f_{IVIM} for an IVIM fit. It was therefore probable that D^* contained a disproportionate amount of the medium fraction, which decays over more b-values and provided a better sum of squares fit to the signal. This correlation is to be expected as the medium and fast fractions, and f_{IVIM} are both measures of the amount of incoherently moving blood within a voxel.

$f_{IVIM}D^*$ however, was strongly correlated with fast fraction (**Figure 4.6d**), but not correlated with medium fraction (**Figure 4.6c**). This is probably as both are measures of the proportion of very fast decay within a voxel, but

interestingly this relationship stays true in lower $f_{IVIM}D^*$ regions (for example in slower diffusing placental voxels) indicating that $f_{IVIM}D^*$ could be of potential interest in future placental DWI experiments.

Finding a predictor of K in the ILT based approach was challenging, as K causes an increase in signal at higher b-values, but the ILT could only consist of exponential decay terms. The hypothesis was that the ILT based approach could have added more very slow components, to try to provide a better sum of squares fit to the voxels with significant K present. The value of the normalised diffusogram at the slowest diffusion coefficient fitted for ($10^{-1}\times10^{-3}$ mm^2/s) plotted against mean K did not show any meaningful relationship (**Figure 4.6e**). However by splitting the data into HP and CP (**Figure 4.6f**) there was a weak correlation between the slowest diffusion coefficient fitted for and K, indicating there may have been some attempt by the ILT to try to account for K but the reason this correlation was lacking in CP is unclear.

The halfway point of the normalised slow section served as a good analogue for the D, with the two being strongly correlated (**Figure 4.6g**). This was a better technique than finding the largest peak in the slow section (**Figure 4.6h**), which had a weak correlation and over-predicted the D in almost all cases, indicating that the slow diffusion peak is on average negatively skewed. As a direct measure of D the halfway point did tend to underpredict D, which could be caused by the slow diffusion peak extending beyond the section boundary, meaning some of the peak was not factored in to calculating the halfway point, which would lead to an underestimate of D.

The findings between the two methods agree, both observed a decrease in the incoherent motion of CP in the basal plate and uterine wall of HP vs CP, and within HP less incoherent motion in the placental ROI relative to the basal plate and uterine wall. While the ILT based fit was more computationally ex-

pensive, it provided a less biased (relative to IVIM) approach that showed that the placental DWI signal is complicated with multiple incoherent components. However, an IVIM model (if constrained properly) provided parameter maps that contain similar information to the ILT based approach, but were easier to implement and compare, with similar sensitivity to compromised placentas. As IVIM parameters can vary depending on the exact imaging sequence and b-value selection, moving forward it may be that the best approach to understanding placental DWI is to employ a hybrid approach, where initial ILT fits are used to provide boundary conditions to an IVIM model.

While I have used information from the ILT approach to constrain the IVIM model, which may make the comparisons biased, the information has only been used to define the boundary between D and D^*, which is difficult to determine in placental DWI with no prior knowledge due to the complexity of the underlying structure and haemodynamics. Despite this the IVIM model can be used to distinguish between medium section and fast section decay (as f_{IVIM} is a better predictor for medium section incoherent motion, and $f_{IVIM}D^*$ is a better predictor for fast section incoherent motion) despite having no prior information about that boundary.

4.6 Conclusion

The work presented here showed good agreements to previous work that found reduction in f_{IVIM} in the basal plate and uterine wall of CP with respect to HP[3–8], and a reduction of f_{IVIM} in the placenta compared with the uterine wall and basal plate of HP. Average K does not change between or within HP and CP, but CP do show increased heterogeneity. In agreement with some studies, but not with others I found a reduction of D in CP relative to HP[9], and also I see a reduction of D in the uterine wall vs placenta. This

chapter also described the first direct comparison between data fit with an ILT technique, and an IVIM model, where I found good agreement between the fits. Ultimately placental DWI is a popular technique that can provide structural and haemodynamic information that is found to differ in placental dysfunction, and while an ILT based technique can provide deeper insights into the nature of data (which will depend on the exact sequence used), the IVIM model can be used to highlight similar information to describe placental haemodynamics, which can be seen to differ in CP.

4.7 Bibliography

[1] D. L. Bihan, "What can we see with ivim mri?," *Neuroimage*, vol. 187, pp. 56–67, 2019.

[2] D. Pyatigorskaya, Nand Le Bihan, O. Reynaud, and L. Ciobanu, "Relationship between the diffusion time and the diffusion mri signal observed at 17.2 tesla in the healthy rat brain cortex," *Magn Reson Med*, vol. 72, no. 2, pp. 492–500, 2014.

[3] I. Derwig, D. Lythgoe, G. Barker, L. Poon, P. Gowland, R. Yeung, F. Zelaya, and K. Nicolaides, "Association of placental perfusion, as assessed by magnetic resonance imaging and uterine artery doppler ultrasound, and its relationship to pregnancy outcome," *Placenta*, vol. 34, no. 10, pp. 885–891, 2013.

[4] R. Moore, B. Strachan, D. Tyler, K. Duncan, P. Baker, B. Worthington, I. Johnson, and P. Gowland, "In utero perfusing fraction maps in normal and growth restricted pregnancy measured using ivim echo-planar mri," *Placenta*, vol. 21, no. 7, pp. 726–32, 2000.

[5] S. Sohlberg, A. Mulic-Lutvica, P. Lindgren, F. Ortiz-Nieto, A. K. Wikström, and J. Wikström, "Placental perfusion in normal pregnancy and

early and late preeclampsia: A magnetic resonance imaging study," *Placenta*, vol. 35, no. 3, pp. 202–206, 2014.

[6] N. Siauve, G. Chalouhi, B. Deloison, M. Alison, O. Clement, Y. Ville, and L. Salomon, "Functional imaging of the human placenta with magnetic resonance," *Am J Obstet Gynecol*, vol. 213, no. 4, pp. 103–114, 2015.

[7] R. Moore, O. Stephen, T. Damian, R. Duckett, P. Baker, W. Dunn, I. Johnson, and P. Gowland, "Spiral artery blood volume in normal pregnancies and those compromised by pre-eclampsia," *Neuroimage*, vol. 21, pp. 376–380, 2008.

[8] S. Sohlberg, A. Mulic-Lutvica, M. Olovsson, J. Weis, O. Axelsson, J. Wikström, and A.-K. Wikström, "Magnetic resonance imaging-estimated placental perfusion in fetal growth assessment," *Ultrasound in Obstetrics & Gynecology*, vol. 46, no. 6, pp. 700–705, 2015.

[9] T. Lu, B. Song, H. Pu, K. Li, M. Huang, J. Mei, and S. Wang, "Prognosticators of intravoxel incoherent motion (ivim) mri for adverse maternal and neonatal clinical outcomes in patients with placenta accreta spectrum disorders," *Transl Androl Urol*, vol. 9, no. 2, pp. 258–266, 2020.

[10] O. Jalnefjord, M. Andersson, and M. Montelius, "Comparison of methods for estimation of the intravoxel incoherent motion (ivim) diffusion coefficient (d) and perfusion fraction (f)," *Magn Reson Mater Phy*, vol. 31, pp. 715–723, 2018.

[11] A. Lemke, B. Stieltjes, L. Schad, and F. Laun, "Toward an optimal distribution of b values for intravoxel incoherent motion imaging," *Magn Reson Imaging*, vol. 29, no. 6, pp. 766–776, 2011.

[12] T. McNanley and J. Woods, "Placental physiology [internet]. glob libr women's med. 2008." :http://www.glowm.com/index.html?p=glowm.cml/section_view&articleid=195, 2022.

[13] J. Jensen, J. Helpern, A. Ramani, H. Lu, and t. . D. Kaczynski, K *Magn Reson Med*, vol. 53, no. 6, pp. 1432–1440, 2005.

[14] D. Yablonskiy, G. Bretthorst, and J. Ackerman, "Statistical model for diffusion attenuated mr signal," *Magn Reson Med*, vol. 50, no. 4, pp. 664–669, 2003.

[15] G. Burton, A. Woods, E. Jauniaux, and J. Kingdom, "Rheological and physiological consequences of conversion of the maternal spiral arteries for uteroplacental blood flow during human pregnancy," *Placenta*, vol. 30, no. 6, pp. 473–482, 2009.

[16] N. Dellschaft, G. Hutchinson, S. Shah, N. Jones, C. Bradley, L. Leach, C. Platt, R. Bowtell, and P. Gowland, "The haemodynamics of the human placenta in utero," *PLOS Biology*, vol. 18(5), p. e3000676, 2020.

[17] P. Slator, J. Hutter, M. Palombo, L. Jackson, A. Ho, E. Panagiotaki, L. Chappell, M. Rutherford, J. Hajnal, and D. Alexander, "Combined diffusion-relaxometry mri to identify dysfunction in the human placenta," *Journal of Cerebral Blood Flow metabolism*, vol. 37, no. 8, pp. 2987–3000, 2016.

Chapter 5

Phase Contrast Angiography in the Placenta.

5.1 Introduction

The transfer of nutrients and waste products between the maternal and fetal blood pools will not just depend on the small scale motion of blood throughout the intervillous space, but will also depend on larger scale net flows[1] as blood that enters the placenta must traverse the placental width, before draining back across the organ and out through the venous drainage system. Placental dysfunction is thought to interrupt flow into the placenta, through improper spiral artery remodelling[2] causing faster flowing 'jets' of blood to enter into the placenta[3], instead of the slow, turbulent, low resistance flow spiral artery remodelling is thought to provide. These jets of blood are thought to impair exchange through altered transit times [3], increased oxidative stress[4] and the momentum of this blood could damage fetal villous tree structures [4]. Just as important as arterial input is venous drainage, which has seen some research in-vivo in primates [5] and ex-vivo in human placentas [6] but little attention in-vivo in humans, but must be occurring at the same rate as arterial input to sustain flow environments across the organ, and any impairment in this drainage could also impact exchange.

Today, MRI studies to investigate placental haemodynamics typically focus on perfusion and diffusion measures through the use of contrast free methods such as Arterial Spin Labelling (ASL) and Intra-Voxel Incoherent Motion (IVIM) techniques[7]. Ultrasound may also provide information about the velocity of blood in spiral arteries in the uterine wall[8, 9], and can provide perfusion and speed information[10] in the intervillous space (IVS). Phase Contrast Angiography (PCA) however is a contrast free MRI technique that uses phase encoding to provide three dimensional velocity information, and could prove an important tool to better understand the bulk flows of blood throughout the placenta. PCA is often used in cardiac imaging [11], where it can provide a range of quantitative measures about the flow of blood[12], from motion through valves up to more complex 4D flow reconstructions[13]. These bulk measurements of flow could help provide more context to the sub-voxel motion of blood measured using Diffusion Weighted Imaging (DWI), where incoherent motion is probably linked to the bulk flow of blood throughout the organ. As PCA provides magnitude, and directional information of the net velocity in each voxel it could also be used for more complex flow analysis, to investigate both the flow of blood into the placenta, and the poorly understood venous drainage system.

Here I aimed to use PCA data from both Healthy Placentas (HP) and Compromised Placentas (CP) to investigate the differences in the speed of blood throughout the uterine wall, basal plate, placenta, and chorionic plate. Then by combining these speed measures with IVIM parameters from **Chapter 3** I aimed to build a more complete picture of placental haemodynamics, and provide more context to $IVIM$ parameters in terms of bulk flow. Additionally I aimed to use the directional information about the flows measured using PCA to investigate flow into and out of the placenta.

5.2 Theory

5.2.1 Phase Contrast Angiography

PCA was carried out to produce 3D velocity maps [14], which were processed by Simon Shah. As outlined in **Equation 1.41** the phase difference as measured using Pulse Gradient Spin Echo (PGSE) is proportional to the velocity of a spin during the imaging gradients. As phase is wrapped from $-\pi$ to π the fastest measurable velocity for a particular gradient G, of lobe length δ and time between lobes Δ is known as the Veloctiy ENCoding (VENC) factor

$$VENC = \frac{\pi}{\gamma \Delta \delta G}. \tag{5.1}$$

By setting VENC too low aliasing will occur due to phase wrapping, but if VENC is too high then sensitivity will be lost.

5.3 Methods

5.3.1 Placental data

PCA phase data was processed as outlined in **Section 2.2.2** where 12 HP and 9 CP had at least 1 complete slice of 3D velocity data. Phase data was computed into velocity using **Equation 1.19b**, and scans were masked into 4 ROIs on the non-encoded image (uterine wall, basal plate, placenta, chorionic plate, **section 2.2.3**).

5.3.2 Magnitude Velocity

The magnitude of the 3D velocity data was calculated to determine the average speed of the contents of each voxel within the four ROIs. The speed data was then also used to provide more insight into the IVIM parameters from

Chapter 3 by selecting participants with good alignment between the DWI and PCA data sets leaving 6/12 HP and 5/6 CP for further analysis (judged by visual inspection, exact participants outlined in **Section 2.3**). Good alignment between data sets was required as sometimes fetal, placental, or maternal motion could have caused the placenta to have shifted meaning it was no longer possible to match IVIM components with velocity information. For the well aligned participants, the overlap between the PCA and DWI placental masks was taken and voxels were split into two categories depending on their speed, where mean f_{IVIM} from the fastest 20% of voxels was compared to mean f_{IVIM} from the remaining 80%.

5.3.3 Inflow and outflow

As PCA provides 3D velocity information this was used to investigate the inflow to, and outflow from the placenta. Inflow and outflow was defined by the direction of the velocity vector, considering only the in slice components v_x and v_y, relative to the basal plate mask.

Blood that has just entered, or is currently draining from the placenta is likely to be in close proximity to the basal plate, travelling roughly perpendicular to it, and correspond to the fastest voxels in the organ. To identify these voxels the basal plate mask was approximated as a series of straight lines, where the angle and position of these lines could then be compared to the direction of travel of nearby voxels. As the basal plate mask was often more than one pixel wide (**Figure 5.1a**) it was initially eroded down using inbuilt MATLAB functions to produce a single pixel wide skeleton of the original mask (**Figure 5.1b**). As these masks have to be fit into discrete voxels the masks often had jagged edges, which if joined together with a dot-to-dot approach would result in angles that are not truly representative of the placental shape.

Instead the skeleton mask was used to compute a convex hull (**Figure 5.1c**) using an inbuilt MATLAB function which forms the smallest polygon which contains all of the mask voxels. The edges of this polygon were stored (**Figure 5.1d**, where each colour represents a different edge), and the angle of each edge relative to the positive x-axis was calculated. To select only voxels near to the basal plate the distance of each placental voxel to its nearest convex hull edge was calculated, and only placental voxels within 4 voxels (10mm) of a convex hull edge were considered. This is outlined in **Figure 5.1e**, where placental voxels within 4 voxels of a convex hull edge were colour coded dependent on the nearest convex hull edge. As inflow and outflow probably correspond to the fastest moving voxels, only the fastest 20% of voxels were considered for further analysis (defined using the magnitude of the 3D velocity vector). The angle of travel of blood, relative to the basal plate could then be computed by measuring the angle between the velocity vector, and the normal to the nearest convex hull edge where 0° and 180° correspond to inflow and outflow (flow perpendicular to the basal plate), and 90° corresponds to flow parallel to the basal plate. The mean speed of these voxels was calculated at varying angles of travel (0-30°, 30-60°, 60-90°, 90-120°, 120-150°, and 150-180°) for each participant. Depending on the shape of the placenta, this process could fail to characterise the outline of the placenta when computing the convex hull, these participants were discarded from analysis leaving 11/12 HP and 6/9 CP.

Using this I attempted to better characterise regions of inflow and outflow by clustering neighbouring voxels together depending on their direction of travel. Clustering was implemented by identifying 'well aligned voxels', which correspond to θ = 0-45° for inflow, and θ = 135-180° for outflow, and 'less well aligned voxels' which could vary from θ = 45-60° for inflow and θ = 120-135° for outflow. Well aligned voxels were clustered with any other well aligned voxels that were a maximum of 2-voxels away. Less well aligned voxels could also join these clusters if they were within 1 voxel of a well aligned voxel, as inflow and

outflow to the placenta is likely divergent and convergent respectively, as inflow resembles 'fountains' and outflow resembles drains. Only clusters containing at least 3 voxels were considered further to try to limit the probability of a cluster being aligned purely due to chance. The mean number of clusters per slice in HP and CP, and the mean velocity of these clusters was used to provide quantitative information comparing inflow and outflow.

5.3.4 Statistical tests

Differences between the HP and CP group were measured using a Mann Whitney U test, where significance was defined as $p<0.05$. Within the HP and CP groups ROIs were only compared to the placental ROI, first differences within groups was tested with a Friedman test, and if that found a significant difference individual ROIs were compared to the placental ROI using a Wilcoxon signed rank test as a post-hoc test to determine which specific ROIs were different. When comparing the angle of travel of flow relative to the basal plate all HP angles were compared to all CP angles using a Mann Whitney U test, and flow travelling perpendicular (0-30° and 150-180°) was compared to flow travelling parallel to the basal plate (60-90° and 90-120°) for HP and CP using a Wilcoxon signed rank test.

5.4 Results

For one HP and CP the velocity from the three separate encoding directions are shown in **Figure 5.3**, with the speed calculated from the three encoding directions also shown. Mean speed from each participant, in each ROI calculated from the 3D velocity data is shown in **Figure 5.3**, where CP had significantly faster mean speed than HP in the placental and chorionic plate ROIs ($p<0.001$ & $p=0.003$ respectively). In CP the chorionic plate had significantly faster flow than the placenta ($p=0.004$), and in HP the uterine wall

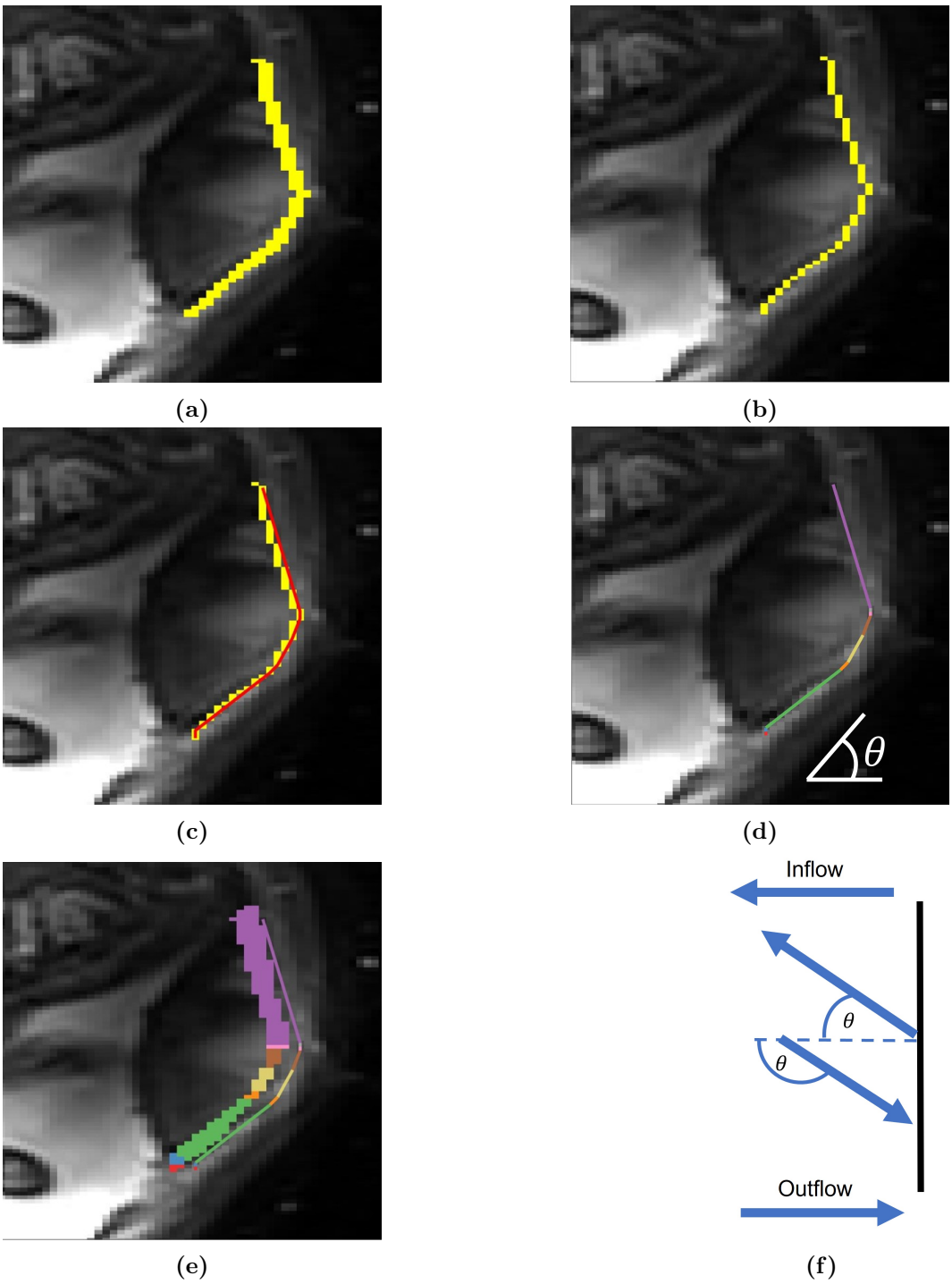


Figure 5.1: *Figure outlining the process of turning the 2D basal plate mask into a discrete series of convex hull edges. Starting with a) The basal plate mask (yellow) which was eroded to 1 pixel wide in b), and fit to a convex hull (corresponding to the red line) in c). As the convex hull consists of a series of edges, each edge is shown in a different colour in d) where the angle of each edge relative to the positive x-axis was computed. For voxels near to the basal plate the nearest convex hull edge was found in e), where placental voxels were colour coded to match the nearest convex hull edge. Voxels were then defined as inflow or outflow f) depending on the direction of travel of the 2D velocity vector compared with the normal to the basal plate.*

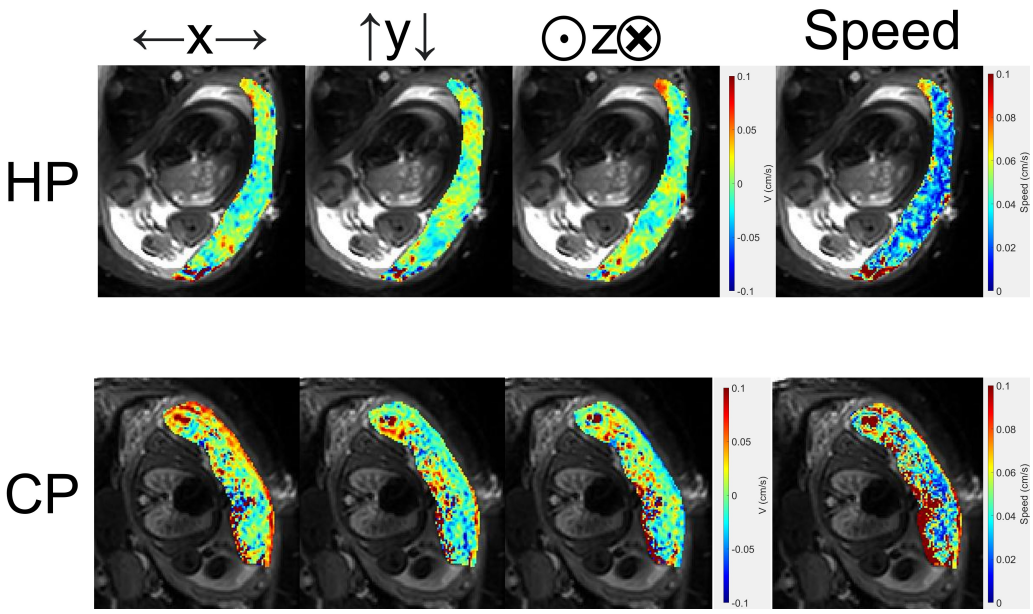
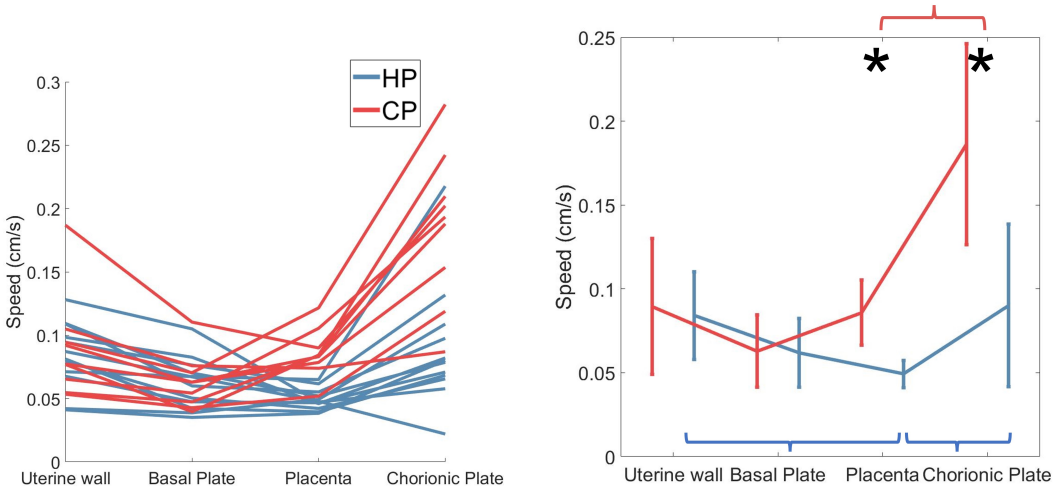


Figure 5.2: *Velocity maps produced by the three 1D encoding gradients from a single HP and CP, and the resulting speed map from combining the three directions.*

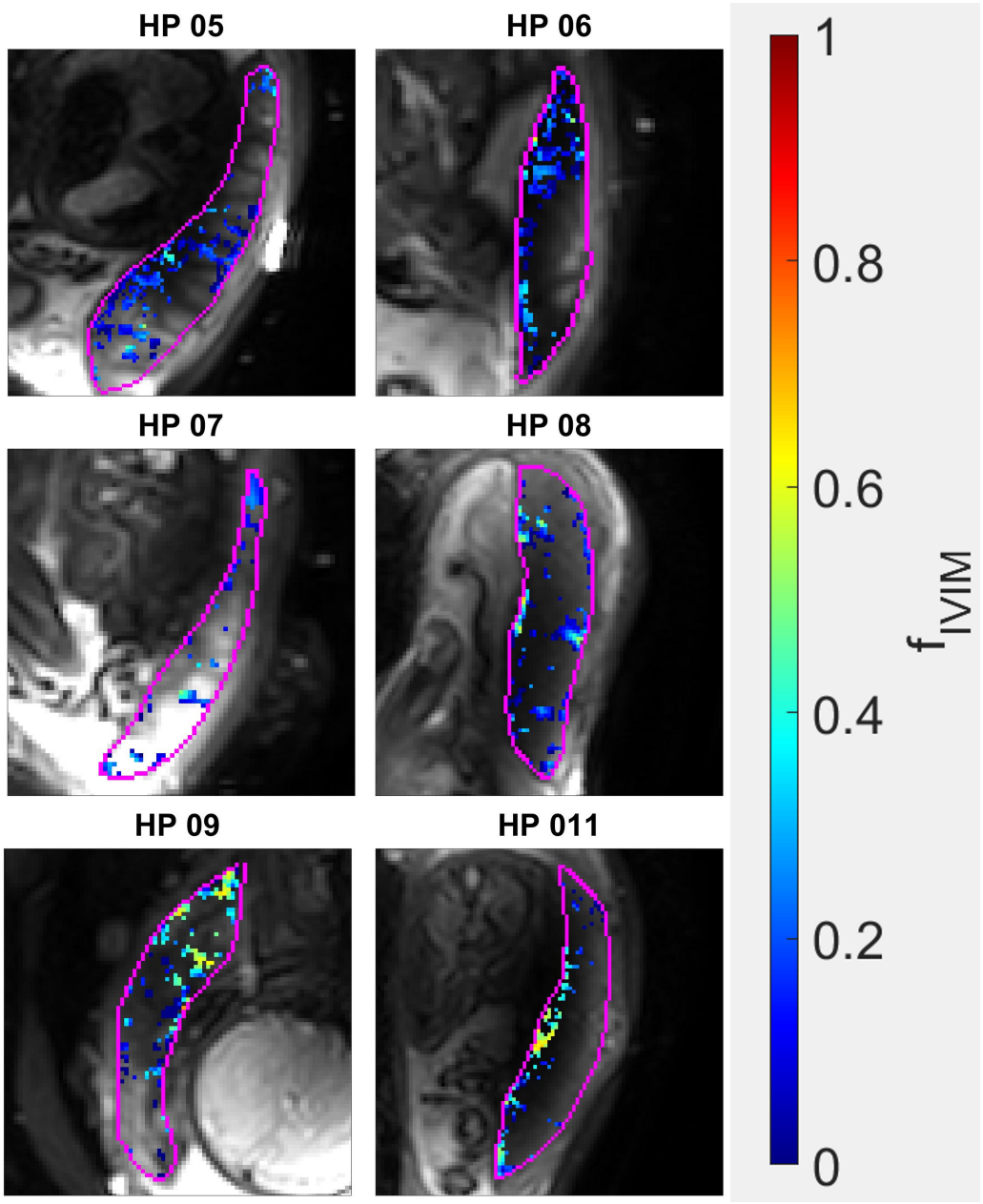
and chorionic plate had significantly faster flow than the placenta (p=0.002 & p<0.003 respectively).



(a) **(b)**

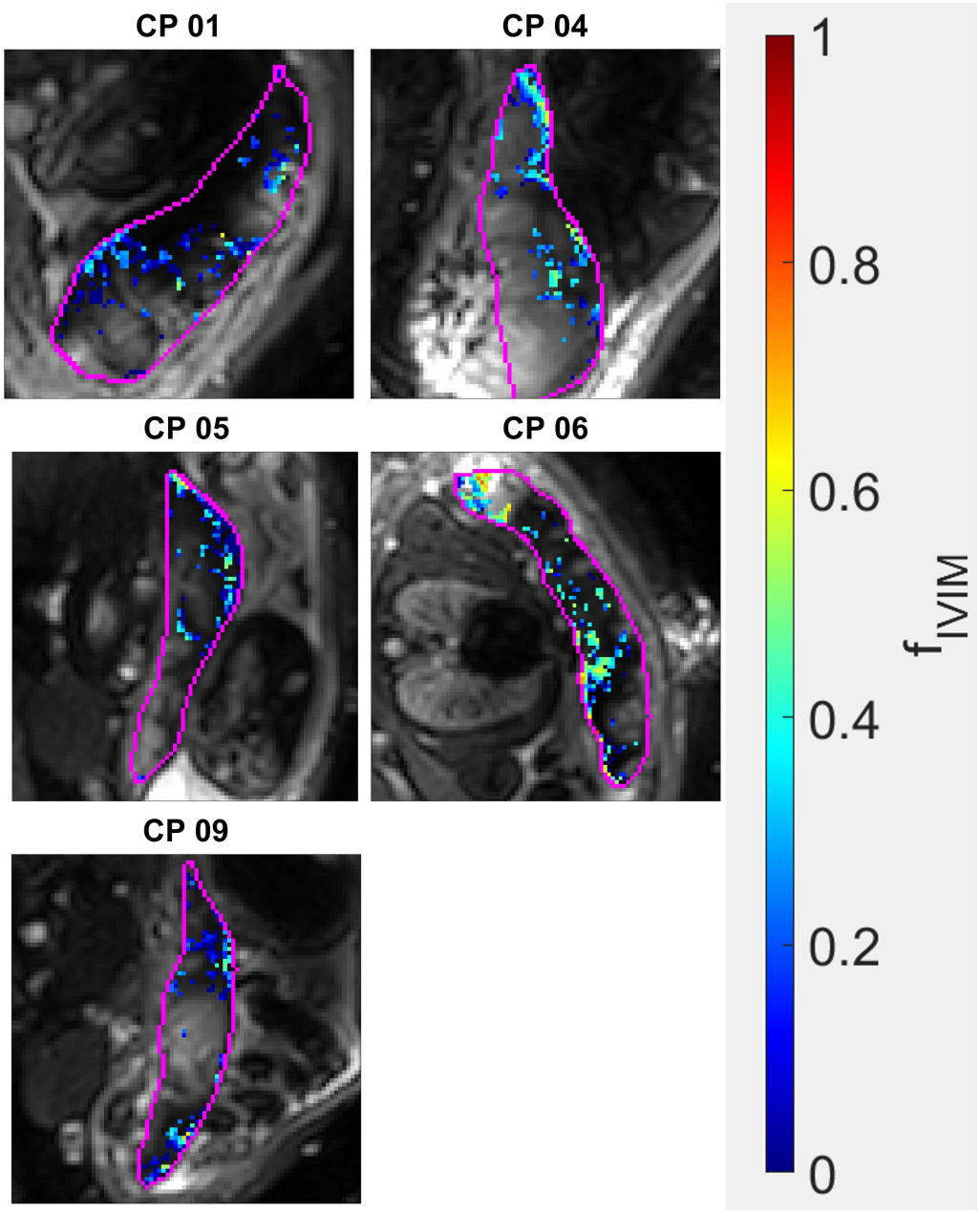
Figure 5.3: *Speed measured across the 4 placental ROIs where in a) each participant is represented by a line, with HP in blue and CP in red, and b) the means of the participant groups are plotted with errorbars denoting standard deviation. Significant differences between HP and CP are marked with an asterisk, and significant differences between the placental ROI and the remaining ROIs within groups are marked with a curly bracket.*

For placentas where there was good alignment between the placental ROI for both the PCA and DWI data sets a single slice through each participant is shown in **Figure 5.4**, where for the fastest 20% of voxels f_{IVIM} is overlaid onto a non-encoded slice. A bar chart is plotted in **Figure 5.5a** comparing how the f_{IVIM} of the fastest 20% voxels compares to the remaining 80%, where the fastest 20% had significantly higher f_{IVIM} than the slowest 80% (p=0.004, Wilcoxon signed rank test)



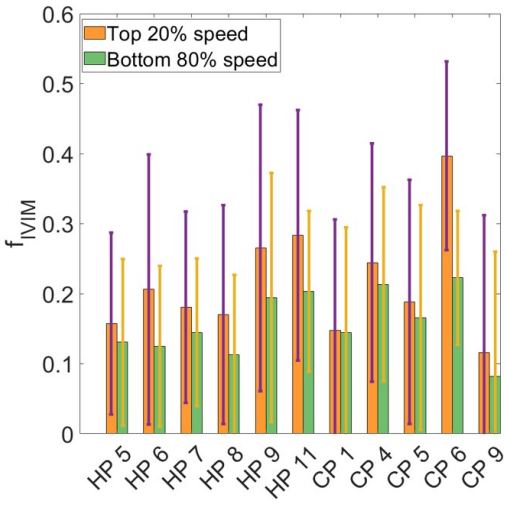
(a)

For the fastest 20% voxels (highlighted in **Figure 5.4**), within 4 voxels



(b)

Figure 5.4: *For the a) 6 HP and b) 5 CP which had good agreement between PCA and DWI masks the f_{ivim} is plotted for placental voxels which were in the fastest 20% of voxels.*



(a)

Figure 5.5: *Bar charts comparing placental voxels for a) mean f_{IVIM} for the fastest 20% voxels, compared to the slowest 80% for all participants with good agreement between the placental PCA and DWI masks, with errorbars showing standard deviation.*

(10mm) of the basal plate mask (as defined in **Section 5.3.3**), the mean speed over a range of acceptance angles was calculated and plotted in **Figure 5.6**. Over every angle range the CP had higher average speed than the HP group(maximum p = 0.03) , and for both HP and CP blood flowing perpendicular (both inflow at θ = 0-30°, and outflow at θ = 150-180°) was significantly faster than that flowing parallel to the basal plate (θ = 60-90° and 90-120°, maximum p = 0.04).

An example slice through a participant is shown in **Figure 5.7a**, where only the fastest 20% of voxels which were adjacent with the basal plate are shown. The mean speed of each voxel is shown, with voxels colour coded to define inflow vs outflow, and 2D velocity quivers also plotted to demonstrate the magnitude and direction of the in slice velocity components. These voxels were then clustered to try to group nearby regions of inflow and outflow together in **Figure 5.7b**, where each cluster is represented by a different colour. A histogram of cluster size was plotted in **Figure 5.8** for **b)** HP inflow, **c)** HP outflow, **d)** CP inflow, and **e)** CP outflow, which were normalised to count

clusters per slice (as more HP slices were present than CP). The mean speed of each cluster for both HP and CP was plotted for both inflow and outflow, where the size of each data point is relative to the size of the cluster. The mean speed of the clusters for HP inflow and outflow, and CP inflow and outflow are shown in **Table 5.1**.

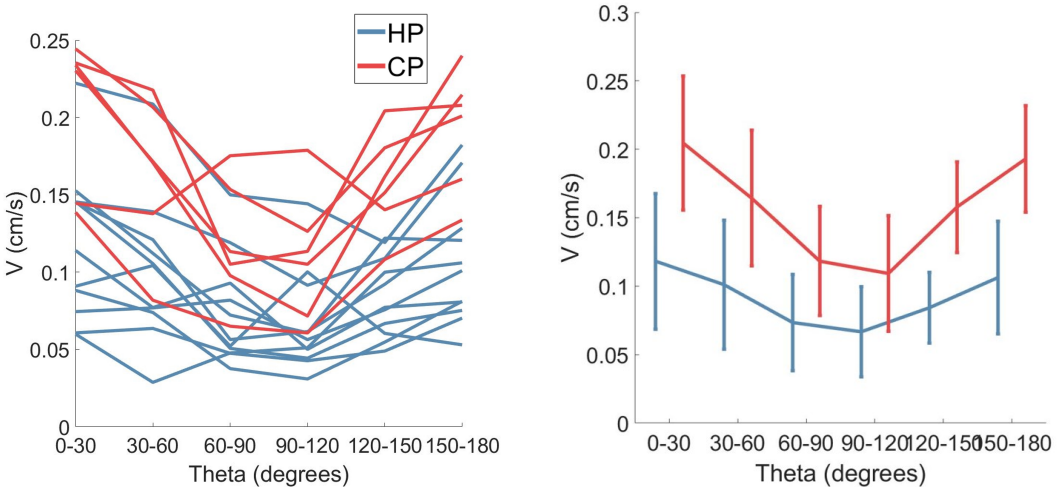


Figure 5.6: *Plot comparing the mean velocity of voxels, grouped by their angle of travel relative to the basal plate where participants are a) each represented by a single line (blue HP, orange CP), and b) the means of the participant groups are plotted with errorbars denoting standard deviation.*

	Inflow	Outflow	Participants
HP	0.08±0.05 cm/s	0.11±0.06 cm/s	n=12
CP	0.11±0.05 cm/s	0.12±0.08 cm/s	n=9

Table 5.1: Mean velocity of inflow and outflow clusters, for HP and CP.

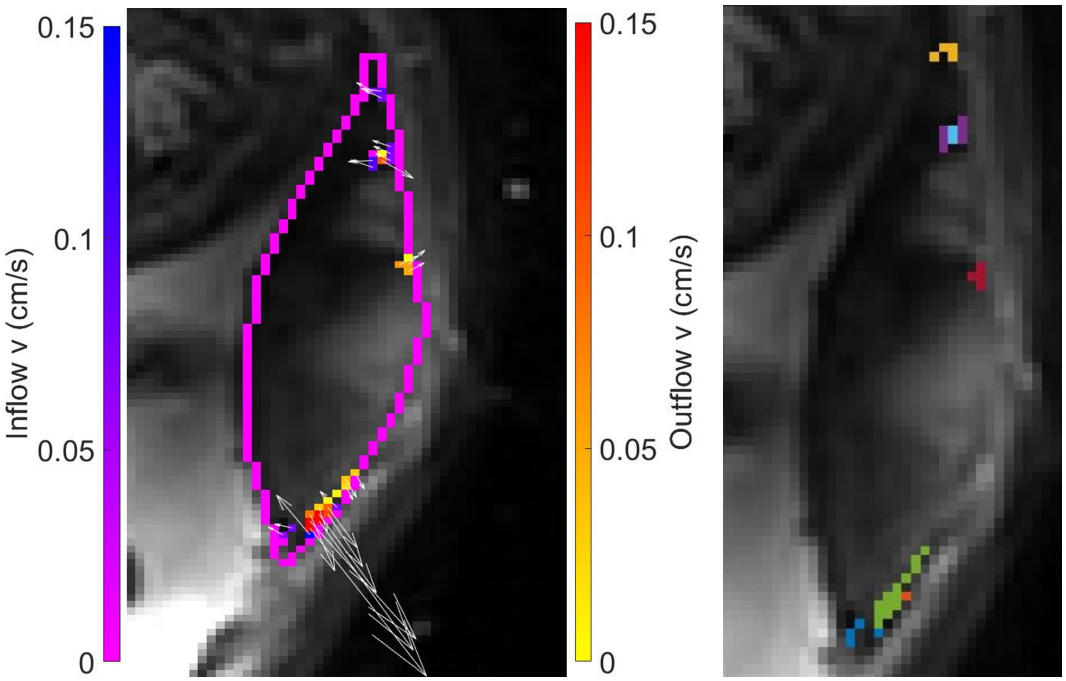
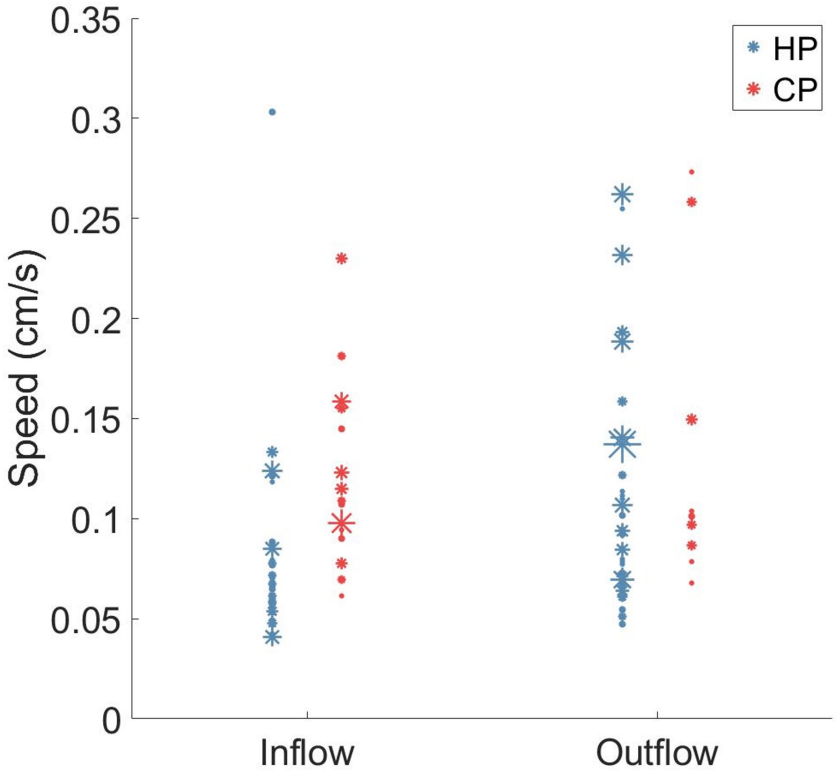
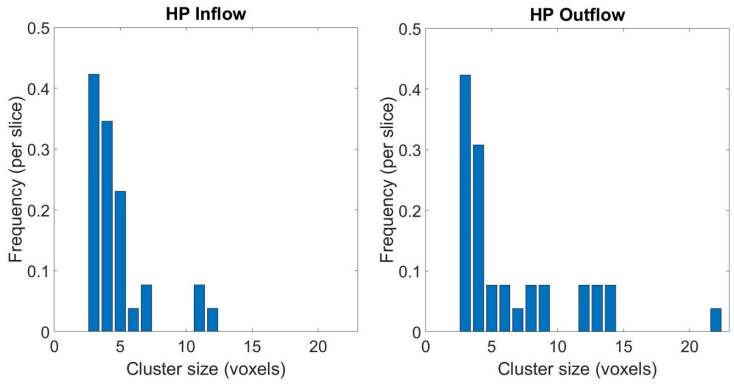


Figure 5.7: *a) A single slice through a participant, where the fastest 20% of voxels are shown, defined as inflow or outflow dependent on the angle of travel relative to the basal plate, with 2D velocity quivers plotted to show the direction of travel. Voxels are colour coded based on inflow/outflow and their velocity. b) The same placental slice, with neighbouring inflow and outflow regions clustered together, where each colour represents a different cluster.*

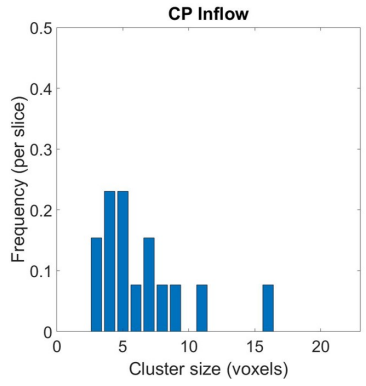


(a)

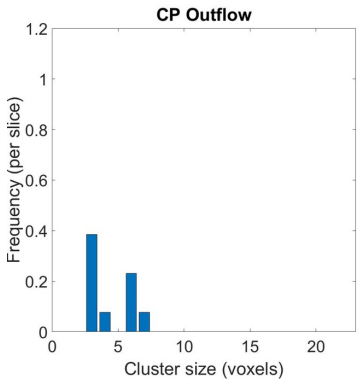


(b)

(c)



(d)



(e)

Figure 5.8: *Plot comparing the mean velocity for inflow and outflow clusters, for HP in blue and CP in red, and the size of each data point is proportional to cluster size. Histograms showing the number, and size of clusters per slice for a) HP inflow, b) HP outflow, c) CP inflow, and d) CP outflow.*

5.5 Discussion

Calculating the mean speed from the individual encoding directions (**Figure 5.3**) helps give a more detailed picture of placental haemodynamics. In HP the net speed of voxels in the uterine wall (**Figure 5.3**) was significantly faster than in the placenta, which was probably due to fast arterial input which was damped as it travels through the basal plate and into the placenta, supporting the theory that spiral artery erosion reduces resistance to flow and hence dampens the velocity of blood as it is supplied to the placenta.

In CP however I observed faster flow in the placental ROI, which was consistent with improper spiral artery remodelling which has been theorised to impair oxygen exchange [3, 4]. In both HP and CP, flows in the chorionic plate were significantly faster than those in the placenta, indicating the presence of fast flowing fetal blood which was significantly faster in CP than HP, which could indicate altered fetal cardiac output to account for the poor exchange[15]. These results were reported in [14] and were the first in vivo measurements of net flows in the placenta using PCA. The net speeds presented here are of a similar order to some mathematical simulations (0.6 cm/s [16]) but slower than others (5 cm/s [17]). These results do depend on the masking of data, similar to **Chapters 3 & 4** where it was observed that regions of basal plate may be extending into the placental ROI in some participants. Here that could cause increased variance of the speed of blood in the placental ROI of either HP or CP, but the exact effect on the difference in mean between the two groups is unclear. It would be expected that the velocity of blood flow drops as it travels from the uterine wall, through the basal plate and into the placenta. If in the placental ROI of CP there were more voxels which contained basal plate, this could cause an increase in velocity within the placental ROI. However here all CP but one have higher velocity in the placental ROI than the fastest HP, indicating that CP probably still contains faster flow within the placental ROI.

In both HP and CP fast voxels (top 20%) tended to be focused around the periphery of the placental ROI, and corresponded to higher f_{IVIM} values than the slower voxels (bottom 80%) in every participant (**Figure 5.4**). This indicated that faster voxels also showed a high degree of incoherent motion, possibly caused by blood that is either turbulent or percolating throughout the organ. It should however be noted that voxels with high speed could also have high f_{IVIM} due to additional dephasing caused by velocity components (discussed further in **Chapter 5**) and these results may need more investigation.

The method outlined in **Section 5.3.3** worked well to transform the basal plate mask into a series of straight lines around the maternal side of the placenta, which could then be used to investigate potential regions of inflow and outflow. Considering the fastest 20% of voxels, in close proximity to the basal plate, those travelling perpendicular to this mask (either inflow or outflow) had significantly faster speed than those travelling parallel (for both HP and CP) indicating that the fastest flowing blood in the placenta is travelling perpendicular to the basal plate, which is consistent for with inflow and outflow. These results outline the first MRI measurements of venous return in the placenta, and show it was occurring at a comparable rate to arterial input.

These results were used to try and investigate regions of inflow and outflow further, and find specific sites of arterial input and venous drainage. For both HP and CP a number of potential inflow and outflow sites were identified by clustering 'well aligned' and 'less well aligned' voxels (**Figure 5.7a**), with the average speed and size of every cluster shown in **Figure 5.8**. The mean values of inflow and outflow clusters (**Table 5.1**) were comparable, indicating the presence of fast venous drainage, occurring at a similar rate to arterial input. A limitation of this work is there was a small number of clusters, and

the exact results will be affected by the position of the slice relative to the placenta. While the odds of a cluster being aligned with the basal plate by chance I enforced a minimum cluster size of 3 voxels, there are still probably regions that were aligned by chance, meaning these results would provide an underestimate of the velocity.

5.6 Conclusion

In HP I observed faster flows in the uterine wall, which are dampened upon entry into the placenta, whereas in CP this dampening of flow was probably absent, causing placental blood flow to be significantly faster than in HP. Fast flow was also measured in the chorionic plate, which in CP is significantly faster than in HP. While these bulk flow measures can be used in conjunction with DWI to investigate the causes of incoherent motion there needs to be some caution, as fast flowing components can mimic f_{IVIM}. In the data presented here fast flowing voxels had higher f_{IVIM} than slower voxels, potentially indicating fast flowing blood percolating through the IVS. Finally I have also used MRI to try to detect and make quantitative estimates about arterial input, and venous drainage within the placenta, finding that the fastest flowing blood is perpendicular to the basal plate, which would be consistent with flow into and out of the placenta. By clustering regions of inflow and outflow together I found fast venous drainage, at a comparable rate to arterial input. These results highlight the usefulness of PCA for investigating the bulk flow of blood in HP and CP, and its potential to provide better understanding of flow environments present in the placenta.

5.7 Bibliography

[1] T. McNanley and J. Woods, "Placental physiology [internet]. glob libr women's med. 2008." :http://www.glowm.com/index.html?p=glowm.

cml/section_view&articleid=195, 2022.

[2] Y. Wang and S. Zhao, *Vascular Biology of the Placenta*. San Rafael (CA): Morgan Claypool Life Sciences, 2010.

[3] G. Burton, A. Woods, E. Jauniaux, and J. Kingdom, "Rheological and physiological consequences of conversion of the maternal spiral arteries for uteroplacental blood flow during human pregnancy," *Placenta*, vol. 30, no. 6, pp. 473–482, 2009.

[4] J. Kingdom, B. Huppertz, G. Seaward, and P. Kaufmann, "Development of the placental villous tree and its consequences for fetal growth," *Eur J Obstet Gynecol Reprod Biol*, vol. 92, no. 1, pp. 35–43, 2000.

[5] E. M. Ramsey, C. B. Martin, H. S. McGaughey, I. H. Kaiser, and M. W. Donner, "Venous drainage of the placenta in rhesus monkeys: Radiographic studies," *American Journal of Obstetrics and Gynecology*, vol. 95, no. 7, pp. 948–955, 1966.

[6] A. L. Karimu and G. J. Burton, "The effects of maternal vascular pressure on the dimensions of the placental capillaries," *Br J Obstet Gynaecol*, vol. 101, no. 1, pp. 57–63, 1994.

[7] R. Aughwane, E. Ingram, E. Johnstone, L. Salomon, A. David, and A. Melbourne, "Placental mri and its application to fetal intervention," *Prenatal Diagnosis*, vol. 40, pp. 38–48, 2020.

[8] J. Cnossen, R. Morris, R. G. ter, B. Mol, J. van der Post, A. Coomarasamy, A. Zwinderman, S. Robson, P. Bindels, J. Kleijnen, and K. Khan, "Use of uterine artery doppler ultrasonography to predict pre-eclampsia and intrauterine growth restriction: a systematic review and bivariable meta-analysis," *CMAJ*, vol. 178, no. 6, pp. 701–711, 2008.

[9] I. Derwig, D. Lythgoe, G. Barker, L. Poon, P. Gowland, and R. Yeung, "Association of placental perfusion, as assessed by magnetic resonance

imaging and uterine artery doppler ultrasound, and its relationship to pregnancy outcome," *Placenta*, vol. 34, no. 10, pp. 885–91, 2013.

[10] C. Guiot, P. Gaglioti, M. Oberto, E. Piccoli, R. Rosato, and T. Todros, "Is three-dimensional power doppler ultrasound useful in the assessment of placental perfusion in normal and growth-restricted pregnancies?," *Ultrasound Obstet Gynecol*, vol. 31, no. 2, pp. 171–6, 2008.

[11] K. Nayak, J. Nielsen, and Bernstein, "Cardiovascular magnetic resonance phase contrast imaging," *J Cardiovasc Magn Reson*, vol. 17, no. 71, 2015.

[12] T. David, P. Kunal, F. William, and K. Vinay, "Phase-contrast mri: Physics, techniques, and clinical applications," *RadioGraphics*, vol. 40, no. 1, pp. 122–140, 2020.

[13] J. Garcia, A. Barker, and M. Markl, "The role of imaging of flow patterns by 4d flow mri in aortic stenosis," *JACC Cardiovasc Imaging*, vol. 12, no. 2, pp. 252–266, 2019.

[14] N. Dellschaft, G. Hutchinson, S. Shah, N. Jones, C. Bradley, L. Leach, C. Platt, R. Bowtell, and P. Gowland, "The haemodynamics of the human placenta in utero," *PLOS Biology*, vol. 18(5), p. e3000676, 2020.

[15] F. Crispi, M. Comas, E. Hernández-Andrade, E. Eixarch, O. Gómez, F. Figueras, and E. Gratacós, "Does pre-eclampsia influence fetal cardiovascular function in early-onset intrauterine growth restriction?," *Ultrasound Obstet Gynecol*, vol. 34, pp. 660–665, 2009.

[16] A. S. Serov, C. M. Salafia, P. Brownbill, D. S. Grebenkov, and M. Filoche, "Optimal villi density for maximal oxygen uptake in the human placenta," *J Theor Biol*, vol. 364, pp. 383–396, 2014.

[17] E. Lecarpentier, M. Bhatt, G. I. Bertin, B. Deloison, L. J. Salomon, P. Deloron, T. Fournier, A. I. Barakat, and V. Tsatsaris, "Computational fluid dynamic simulations of maternal circulation: Wall shear stress in the

human placenta and its biological implications," *PLOS ONE*, vol. 11, pp. 1–18, 2016.

Chapter 6

Rebounding of PGSE data

6.1 Introduction

As discussed, PGSE sequences can provide insight into the motion of blood throughout the placenta and provide haemodynamic and structural information that differs in compromised placentas (CP) [1–4]. In the case of diffusion or incoherent motion in the placenta, for a PGSE of increasing sensitivity to motion (b-value), the magnitude signal is usually modelled as some combination of exponential decays. However in the data presented here, regions of voxels were observed that show either one or multiple instances where signal that initially decayed later recovers a portion of the initial signal, as in **Figures 6.1a & 6.1b**. In this chapter I refer to these as rebounds as it appears the signal decays until it hits some limit, where it 'bounces' back up before resuming decay. Similar to how if one plotted the trajectory of a ball dropped onto a hard surface, it would fall before rebounding of the surface, and bouncing to a new height where it would start to fall again. The concept of rebounding of signal by PGSE sequences is not novel[5] but is yet to be reported in experimental data [6], and the nature of these rebounds have been thought to rely on a combination of the PGSE gradient waveforms and the properties of the flow through the underlying microvasculature. It is unlikely the the rebounds shown here are caused by flow through microvasculature, as these

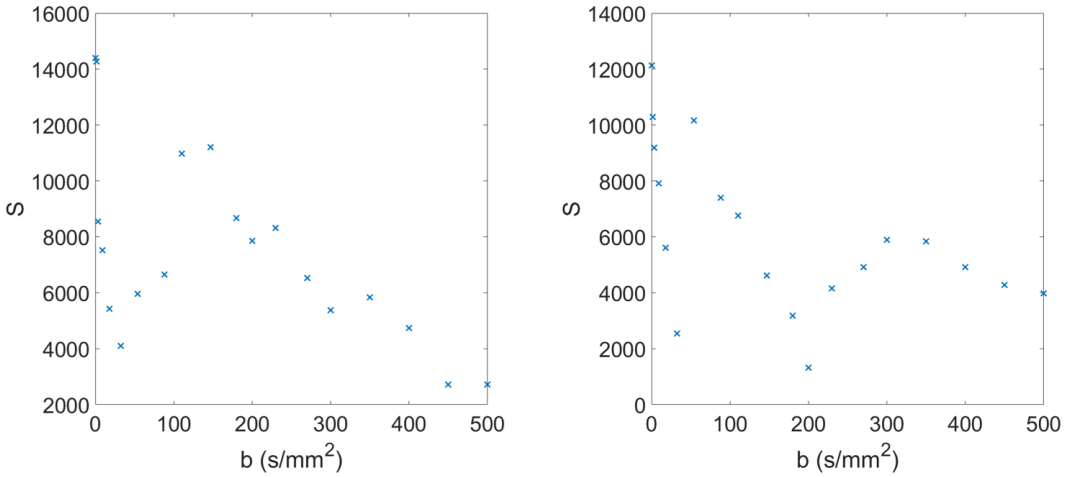


Figure 6.1: *Signal trace for voxels that show a) a single rebound b) multiple rebounds*

rely on isotropic distribution of capillary networks and blood velocities [5] but in the placenta blood flow propelled across the organ and back, causing net flows [7]. Instead I hypothesise that these rebounds are caused by sub-voxel flows within the organ, which means their exact shape and characteristics will be still be reliant on the sub-voxel movement of blood through the placenta, and the properties of the PGSE sequence.

Due to the complexity of the placenta there are a number of environments that give rise to different types of small scale motion such as capillary networks in the uterine wall, but also the movement of blood through the fetal villous tree network, the turbulent motion of blood as it enters the placenta, percolation throughout the InterVillous Space (IVS) and net flows across the organ[8]. If it were possible to better understand the observed rebounds they might be used to provide quantitative information about the underlying sub voxel circulations and provide new methods to understand placental structure and dynamics.

Here I demonstrate the observed rebounds, and proposed a novel quantitative model to describe the rebounds observed in placental PGSE data,

and proposed a fitting approach to differentiate rebounding voxels from those demonstrating Intra-Voxel Incoherent Motion (IVIM). I then applied this approach in both Healthy Placentas (HP) and Compromised Placentas (CP).

6.2 Theory

To characterise rebounds in placental PGSE data three models were used. First is the IVIM model, **Section 6.2.1**, which is commonly used in the placenta to fit diffusion data. Second is Le Bihan's sinc behaviour, **Section 6.2.2**, which has the potential to cause rebounds depending on the underlying microvasculature, and PGSE properties. Third I propose the rephased model, **Section 6.2.3**, which is a simplified approach to characterise the rebounds caused by net flow effects across a voxel.

6.2.1 The IVIM model

The IVIM model

$$S = S_0[(1 - f_{ivim})e^{-bD} + f_{ivim}e^{-bD^*}] \tag{6.1}$$

was outlined in **Chapter 1** and explains how DWI data can be fit to two components, a slow diffusive term (D), and a faster pseudodiffusive (D^*) term that is caused by the incoherent movement of blood. In classical diffusion terms

$$D^* = lv/6 \tag{6.2}$$

where l is the lengthscale of the incoherent motion, and v the velocity. A kurtosis term may be added due to non-Gaussian diffusion as discussed in **Chapter 4**, however this causes an increase it signal at high b-value, and would not explain the rebounds observed here.

6.2.2 The sinc model

In the sinc behaviour described by Le Bihan, rebounds are caused by flow through microvasculature (**Figure 6.2a**). This is because if the time blood

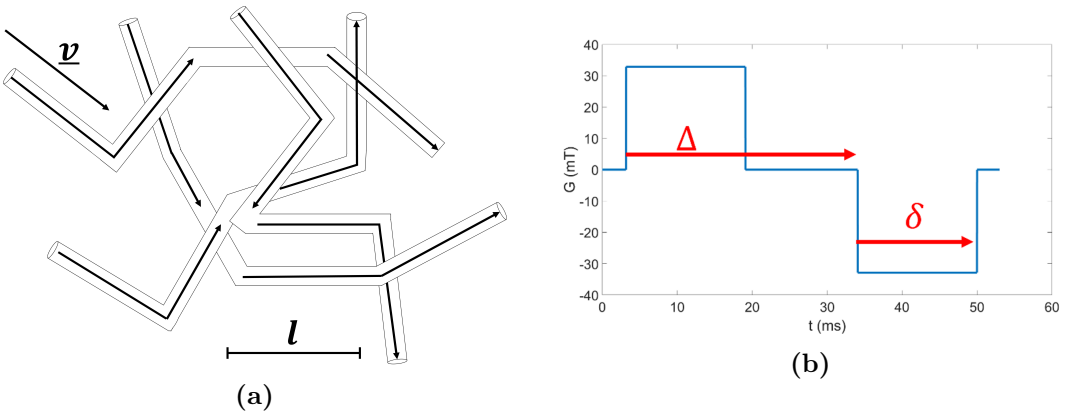


Figure 6.2: *a) Diagram of capillary network with velocity v and characteristic length (l) labelled. b) An example bipolar gradient lobe, with diffusion time (Δ) and lobe length (δ) labelled.*

spends in a capillary segment (τ) is shorter than, or approximately equal to the duration of the PGSE gradients (i.e. $\tau \leq \Delta + \delta$, for the gradients used here, shown in **Figure 6.2b**) then blood will approximately remain in a single capillary segment for the duration of the encoding gradients. From **Equation 1.41**, a spin travelling at a constant velocity during a PGSE encoding gradient will acquire a phase dependent on its velocity of

$$\phi = \gamma G_0 \Delta \delta v = cv \tag{6.3}$$

where

$$c = \gamma G_0 \Delta \delta \tag{6.4}$$

and v is the velocity of the isochromat, G is the maximum amplitude of the gradient lobes, Δ is the time between the gradients, and δ is the lobe length. The relationship between c and conventional b-value (as defined for diffusion imaging) is shown in **Figure 6.3**. To consider the angle of v relative to the

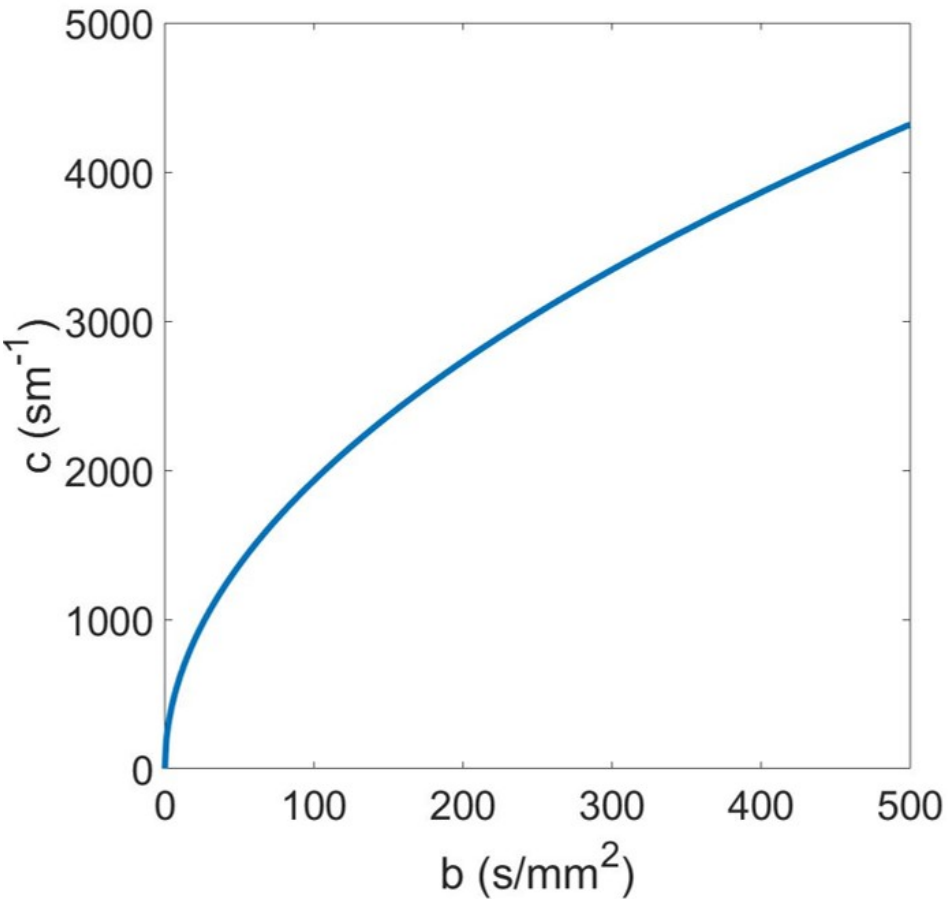


Figure 6.3: *Plot of how c varies with b-value for the gradient waveforms used in this experiment* ***Equation 6.4****.*

diffusion gradient **Equation 6.3** can be written

$$\phi(v,\theta) = cvcos(\theta) \tag{6.5}$$

where θ is the angle between the velocity of the isochromat, and the applied gradient. In Le Bihan's sinc behaviour it is assumed there is an isotropic distribution of capillary segments, and therefore an isotropic distribution of velocities, resembling the vectors in **Figure 6.4**. Considering only the phase change caused by this velocity, and summing over all spins (**Equation 1.47**) gives the attenuation factor

$$F = |\int_0^{\infty}\int_0^{2\pi}\int_0^{\pi} e^{icvcos\theta}\rho(\theta,\xi)p(v)sin\theta d\theta d\xi dv| \tag{6.6}$$

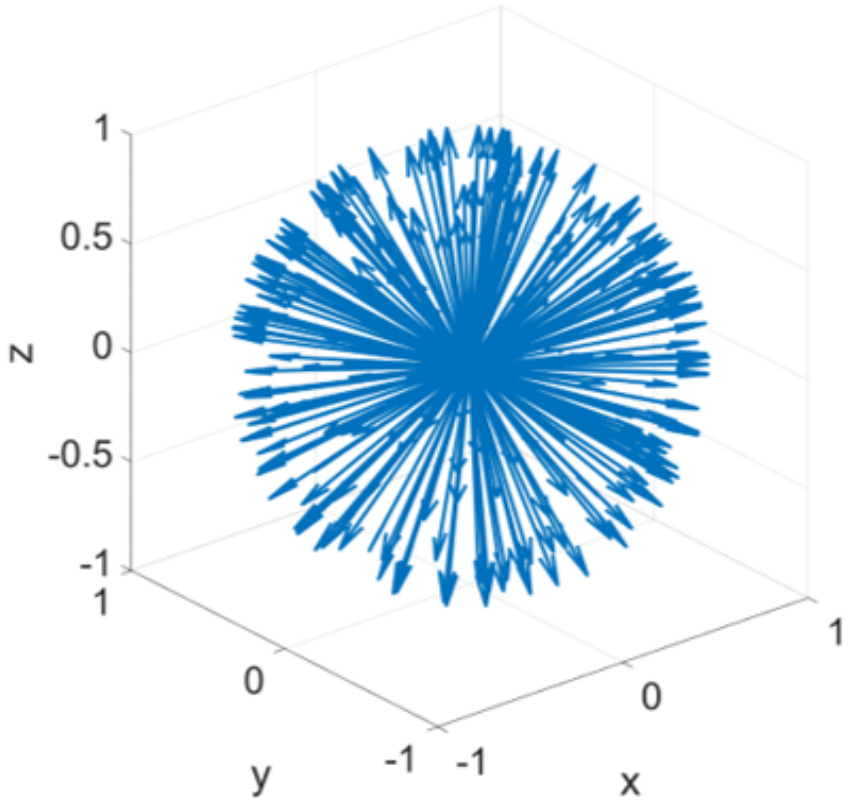


Figure 6.4: *A representation of isotropically distributed velocity vectors, at a constant speed* $|v|$.

where $\rho(\theta, \xi)$ describes the distribution of capillary orientations in 3D space, and $p(v)$ is the distribution of speeds within the capillaries[5]. Assuming a single speed, and isotropically distributed capillaries over 3D space gives

$$F = |\int_0^{\pi} \frac{1}{4\pi} e^{icvcos\theta} sin\theta d\theta| = |sinc(cv)|. \tag{6.7}$$

This behaviour occurs as field gradients only encode motion effects in one dimension, so the velocity vectors in **Figure 6.4** are only projected across one dimension. At low sensitivity to motion (b value) spins accumulate phase and fan out from zero phase, with faster spins acquiring more phase, and slower spins acquiring less phase. This causes dephasing and signal loss as shown in **1** in **Figure 6.5**. This continues until **2**, where the spins completely cancel out and the signal is nulled. As the sensitivity to motion increases further the fastest travelling spins begin to rephase with each other, which causes a

rebound in signal that peaks at **3**. However this only occurs provided the spins are approximately at constant velocity for the time scale of the PGSE encoding. The attenuation factor F can be added to the IVIM equation

$$S = S_0[(1 - f_{ivim})e^{-bD} + F f_{ivim} e^{-bD^*}] \tag{6.8}$$

which gives a modified IVIM expression, including the effect of Le Bihan's sinc rebounding in PGSE data (the Sinc model).

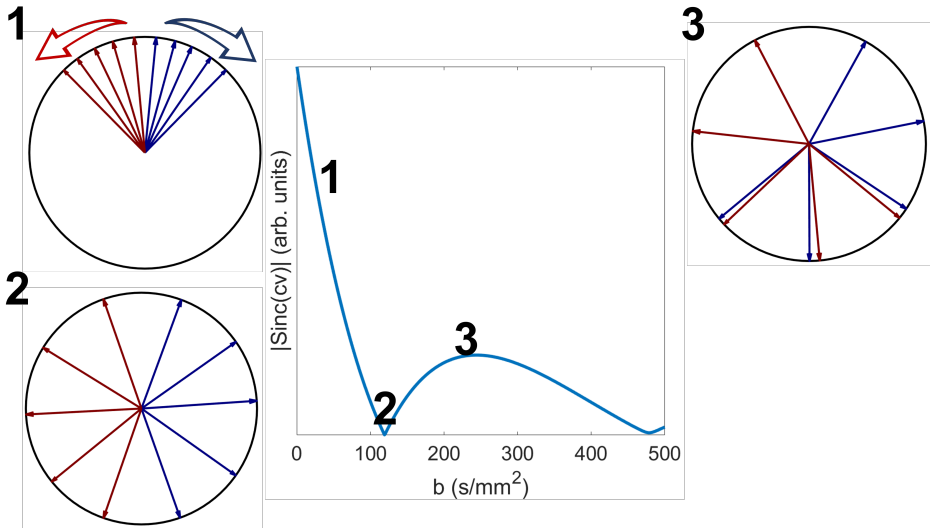


Figure 6.5: *Diagram showing how Le Bihan's sinc refocusing causes rebounds. Phase data was simulated using 10 000 isotropically distributed velocity vectors of constant magnitude $|v| = 1.5$mm/s. Phase was calculated using* ***Equation 6.3****, where c was set to match the gradient waveforms used in later experiments. Three points marked 1,2,3 are highlighted and the magnetisation vector of 10 individual spins at these points are projected onto a circle, where the corresponding signal is related to sum of the shown vectors. The selected spins are travelling at different velocities, with those marked blue moving in a positive direction relative to the applied field gradient, and those in red a negative direction.*

6.2.3 Rephased model

In the placental data I observed, Le Bihan's sinc behaviour does not accurately characterise the rebounds as in the sinc behaviour signal can not rebound high enough to describe the placental data presented here. Other explanations for the rebounds were investigated, including accelerations and circular motion, but the simplest and most physically plausible was that within a voxel there are two pools of spins, where pool 1 is diffusing but has (for instance) no net velocity, and pool 2 is also diffusing but has net velocity across the voxel. For

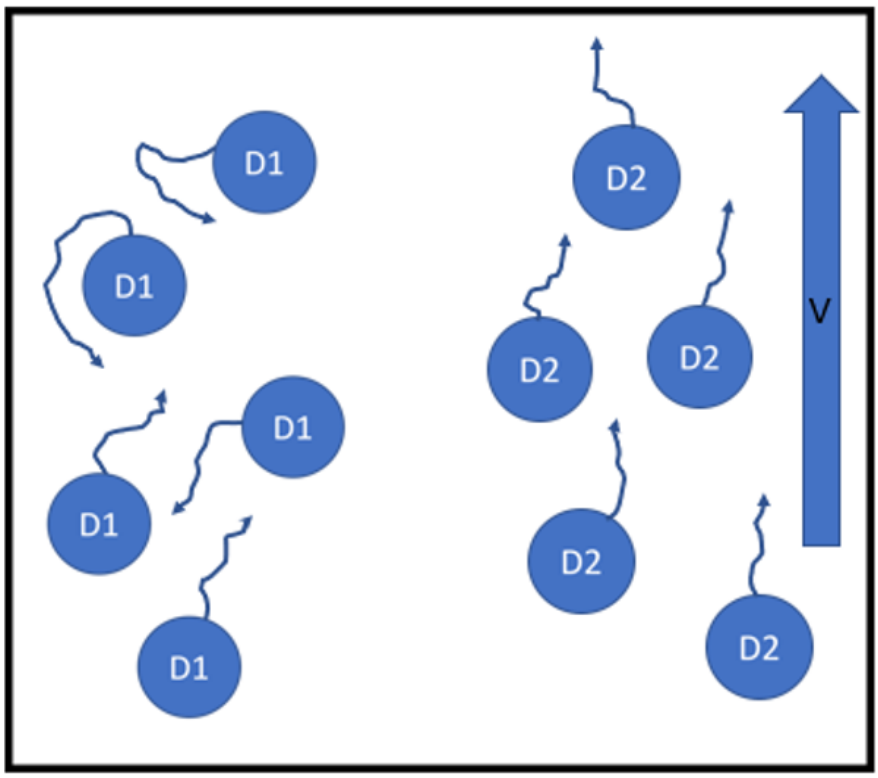


Figure 6.6: *Diagram of two isochromat pools, with diffusion coefficients D_1 and D_2. Pool 2 has a net velocity causing it to move across the voxel.*

example in **Figure 6.6**, pool 2 will have a net velocity, in the direction of the applied field gradient of

$$v_2 = vcos\theta \tag{6.9}$$

where θ is the angle between the initial velocity of an isochromat v and the field gradient. The phase caused by a velocity v_2 in the direction of the applied

field gradient is

$$\phi = cv_2. \tag{6.10}$$

Therefore for two pools of spins, where Pool 1 is stationary, and Pool 2 has a net velocity across the voxel, Pool 1 will have no phase change due to its velocity (as there is no net velocity) but Pool 2 will accumulate a phase dependent on the velocity v_2. At low sensitivity to motion pool 2 will dephase from Pool 1, shown in **1** in **Figure 6.7**, which continues until **2** where the spins cancel out and the signal is nulled. As the sensitivity to motion increases further Pool 2 begins to rephase with Pool 1, causing signal to recover and form a rebound, which peaks at **3** where the spins completely rephase. Mathematically the

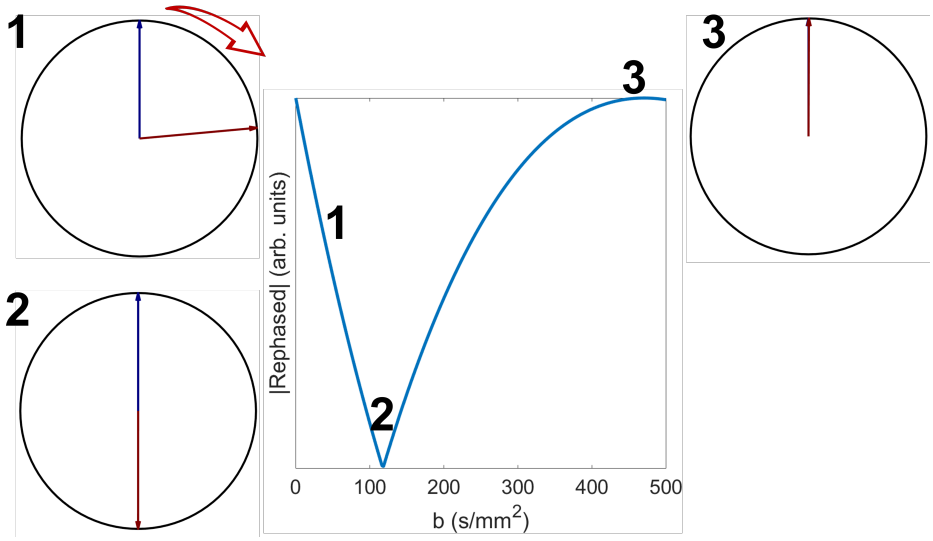


Figure 6.7: *Diagram showing how the rephased model can produce rebounds. Phase data was simulated using two spins, one stationary and one with constant velocity v = 1.5 mm/s in the direction of the simulated gradient. Phase was calculated using* ***Equation 6.3****, where c was set to match the gradient waveforms used in later experiments. Three points marked 1,2,3 are highlighted and the magnetisation vector of the two spins at these points are projected onto a circle, where the corresponding signal is related to the sum of the shown vectors. The blue vector corresponds to the stationary spin, and the red vector the moving spin.*

signal from the two pool system can be written starting from **Equation 1.47**, and including apparent diffusion, as

$$S = \sum_{n=1}^{N_1} e^{-bD_1} + \sum_{n=1}^{N_2} e^{icv_2} e^{-bD_2} \tag{6.11}$$

resulting in a magnitude signal of

$$|S| = |N_1 e^{-bD_1} + N_2 cos(cv_2) e^{-bD_2} + iN_2 sin(cv_2) e^{-bD_2}|. \tag{6.12}$$

This is plotted in **Figure 6.8**, along with a standard IVIM trace, and Le Bihan sinc trace, where all 3 fits have identical parameters (except the IVIM is lacking a velocity term). The key differences between **Equation 6.12** and

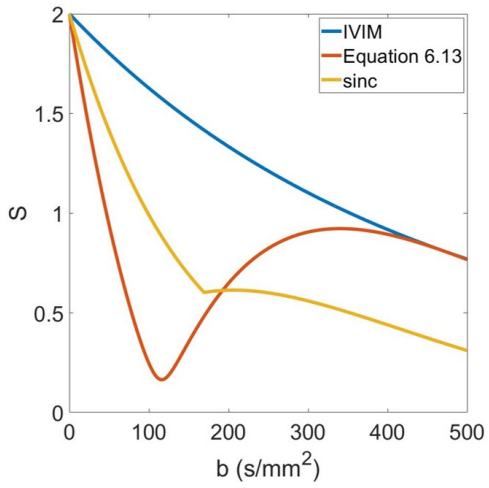


Figure 6.8: *Plot comparing a standard IVIM fit with* ***Equation 6.12****, and the sinc behaviour, where all have* $N_1 = 1$, $N_2 = 1$ *(corresponding to* $f_{IVIM} = f = 0.5$, $D_1 = D = 3 \times 10^{-3}$ *mm*^{2}*/s,* $D_2 = D^* = 1 \times 10^{-3}$ *mm*^{2}*/s, and* $v = v_2 = 1.5$ *mm/s.*

the sinc behaviour is that **Equation 6.12** allows for recovery of the signal, back to the IVIM trace, which is necessary to describe the large rephasing in the placental data acquired here. As it proved too difficult to reliably fit **Equation 6.12** to real placental data instead I propose a simplification of **Equation 6.12** which I define as the rephased model where

$$S = S_0[(1-f)e^{-bD_1} + f|cos(cv')|e^{-bD_2}]. \tag{6.13}$$

This is an empirical approach to fit the data, and the quantities f, D_1, D_2, and v' do not match those in **Equation 6.12**. It does however offer a mathematical model which can provide quantitative information about the frequency of the rebounds, and therefore the velocity of underlying flowing components within

a voxel, while allowing for signal decay from two diffusive components. A comparison between **Equation 6.12** and **Equation 6.13** is shown in **Figure 6.9**. While the model does not perfectly fit the underlying data, the simplified

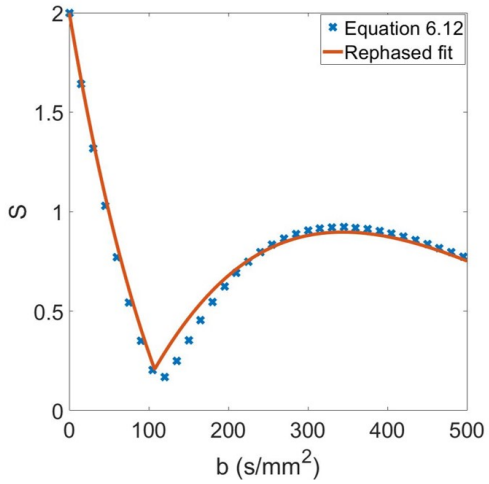


Figure 6.9: *Data simulated using **Equation 6.12**, which is fitted to using the rephased model.*

equation is still periodic with c, allows for full recovery of the signal to the same level as **Equation 6.12**, and provides quantitative information about the rebounds through v'.

6.3 Methods

6.3.1 Isochromat simulations

Initially simulations were used to confirm that **Equation 6.12** properly described the environment outlined in **Figure 6.6**. Simulations were carried out by simulating two pools of isochromats, and tracking the phase change of individual spins as their position changed within simulated encoded gradients, similar to [9]. The encoding gradients were 1D bi-polar gradients of constant $\delta = 15.9$ms and $\Delta = 30.9$ms, which match those used in the participants, and 80 b-values were simulated linearly spaced between 0-500 s/mm^2 changed only

by increasing the gradient strength. Spins could take a step

$$\Delta r_d = \pm\sqrt{2D\Delta t} \tag{6.14}$$

in either the positive or negative direction randomly, where D is the diffusion coefficient of the spin, and Δt is the time between steps in the simulation. Over the entire encoding gradient (total length 53ms) 10 000 samples were taken, corresponding to a step size of Δt = 0.0011ms. Additionally spins could have a velocity v (like in **Figure 6.6**) causing them to travel across the voxel, so the step size including velocity was

$$\Delta r = \pm\sqrt{2D\Delta t} + v\Delta t. \tag{6.15}$$

Simulations contained N total spins, each capable of having a unique diffusion coefficient D, and velocity v. Phase accumulation of a spin at position $r(t)$ experiencing a gradient of $G(t)$ for a single timestep Δt

$$\Delta\phi = \mathbf{r}(t)\mathbf{G}(t)\Delta t \tag{6.16}$$

was added to the phase every Δt. Final signal was calculated by vectorially summing the signals

$$S = \sum_{n=1}^{N} e^{i\phi_n} \tag{6.17}$$

over all spins. In practice simulations contained two pools of spins which were defined by their diffusion coefficient and velocities. Pool 1 contained N_1 spins, diffusing at a rate D_1 and travelling with zero velocity, and pool 2 contained N_2 spins, diffusing at a rate D_2 and travelling with added velocity v_2. These simulations were then used to validate **Equation 6.12** by comparing the theoretical fit to the simulated signal and phase histograms.

6.3.2 Synthetic data

Due to the high computational cost of running the isochromat simulations from **Section 6.3.1** they were only used to verify that **Equation 6.12** fits the simulated data. After this synthetic data was used by simulating data using **Equation 6.12**, and adding Gaussian distributed noise of mean $\mu = 0$ and standard deviation $\sigma = 10\%$ of S_0. The synthetic data was then used to investigate the relationship between v' and v_2, and to investigate how best to identify rebounding voxels.

To investigate how well the rephased model performed on the synthetic data the fits were compared against the standard IVIM fit (**Equation 6.1**) using an F-test to measure when the rephased model provided a significantly better fit than the IVIM model. It was important to select voxels only where the fit provided a significant improvement as at low velocity the two models are indistinguishable, and I only wanted to capture voxels which had a high probability of containing a rebound, and therefore have a more reliable measure of v'. This approach was tested using synthetic data which was created over 80 velocities, v_2, linearly spaced from 0-3.5mm/s, with each data set created for 40 b-values linearly spaced from 0-500 s/mm^2. N_1 was set to 10 000 spins diffusing at $D_1 = 8 \times 10^{-3}$ mm^2/s, and N_2 was 10 000 spins diffusing at $D_2 = 2 \times 10^{-3}$ mm^2/s. These values are within the ranges typically seen within the placenta, and the ratio of spins would provide a fraction f of 0.50. As the rephased model is not measuring v_2 directly the relationship between v_2 and v' was investigated further. This was done by creating 9 synthetic data sets over a range of N_1 and N_2 from 2500-4500 (resulting in a fraction f of 0.36 to 0.64), D_1 and D_2 from 2-20 $\times 10^{-3}$ mm^2/s, and v_2 from 0-3.5 mm/s, which were all fitted to the rephased model to investigate the relationship between v_2 and v'.

Data was fitted to an IVIM model using the same approach as in **Chapter 4** by first fitting higher b-values (200-500 s/mm^2) to a mono-exponential decay to characterise the slow diffusive component D, and low b-values (0-110 s/mm^2) to a mono-exponential decay to characterise the fast component D^*, which were supplied as initial guesses to the full IVIM fit. To fit to the rephased model the slow D component was used as an initial guess for both D_1 and D_2 as this proved more reliable for fitting rebounding voxels (noting that D_1 and D_2 do not exactly represent the underlying diffusion).

6.3.3 Placental data

The DWI data presented here is the same as from **Chapters 3 & 4**, and data collection steps and preprocessing is outlined in **Chapter 2**.

During the investigation it was observed that a significant number of placental voxels showed increasing initial signal over low b-values (18-148 s/mm^2), increasing far higher than the intensity over 0-18 s/mm^2 (for example **Figure 6.10**), which is in violation of standard diffusion models. To detect these voxels, data was smoothed voxel-wise using a moving mean function of kernel size 5 to reduce the effect of noise at low b-values. If the maximum signal intensity of this smoothed data occurred within a b value range of 18-148 s/mm^2 the voxel would be considered as increasing initial signal and removed from the fitting.

The remaining voxels were fitted voxel-wise to the IVIM model **Equation 6.2**, sinc model **Equation 6.8**, and Rephased model **Equation 6.13** as outlined in **Section 6.3.2**. For the sinc model initial guesses from the mono-exponential high b-value fit (b = 200-500 s/mm^2) were used to inform the sinc fit. Voxels were all considered to exhibit IVIM unless either the rephased and/or sinc models separately provided a significantly better fit (for $p< 0.05$, F-test). This meant voxels could fit into 4 categories , 1) IVIM, 2) sinc, 3)

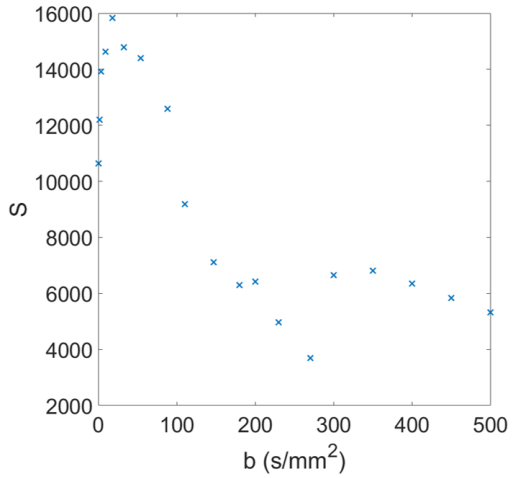


Figure 6.10: *Raw data from a single voxel which has increasing initial signal.*

Rephased, or 4) Both rephased and sinc.

6.4 Results

6.4.1 Isochromat simulations

Data produced using the isochromat simulations from **Section 6.3.1** are shown in **Figure 6.11**, where the simulated data was plotted against the expected values from the Rephased model **Equation 6.12** for a range of velocities. Phase data from these simulations was used to produce phase histograms (**Figure 6.12**) to demonstrate how the scenario outlined in **Figure 6.6** produces rebounds.

6.4.2 Synthetic data

Data was also simulated as outlined in **Section 6.3.2**, by using **Equation 6.12** and adding a small amount of Gaussian distributed noise. Simulations were repeated over a range of velocities and the sum of square errors from both the IVIM and Rephased fit to the simulated data are shown in **Figure 6.13a**. A comparison between the IVIM fit and Rephased fit at $v_2 = 0$ mm/s and $v_2 = 3$ mm/s are shown in **Figure 6.13b & 6.13c**. These simulations were also used to investigate the relationship between v' and simulated v_2, and an ex-

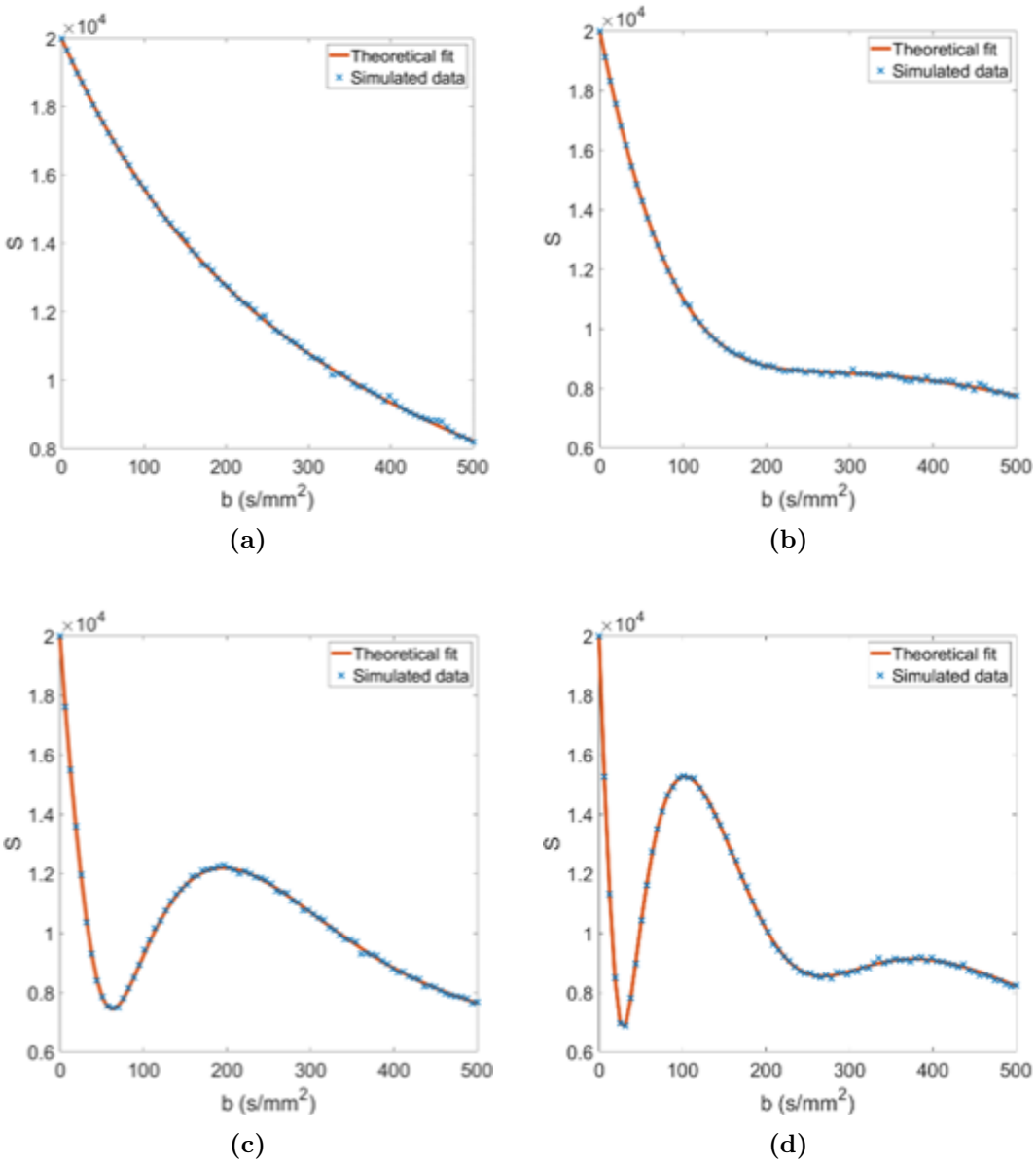


Figure 6.11: *Data was simulated as in* ***Section 6.3.1*** *where two pools of isochromats were simulated. Pool 1 contained N_1 = 10000 spins, diffusing at a rate D_1 = 8 $\times 10^{-3}$ mm^2/s. Pool 2 contained N_2 = 10000 spins, diffusing at a rate D_2 = 2 $\times 10^{-3}$ mm^2/s, with increasing velocities a) v_2 = 0 mms^{-1}, b) v_2 = 1 mms^{-1}, c) v_2 = 2 mms^{-1}, and d) v_2 = 3 mms^{-1}.*

ample plot of v' (from the Rephased model **Equation 6.13**) vs v_2 (simulated velocity, as in **Equation 6.9**) is shown in **Figure 6.14a**. These simulations were repeated for a range of N_1 and N_2 (between 4500 and 2500, resulting in a range of fractions f from 0.36-0.64) and a range of D_1 and D_2 (from 2-20 $\times 10^{-3}$mm^2/s) and a plot of v' vs v_2 for all of these simulations is shown in **Figure 6.14b**.

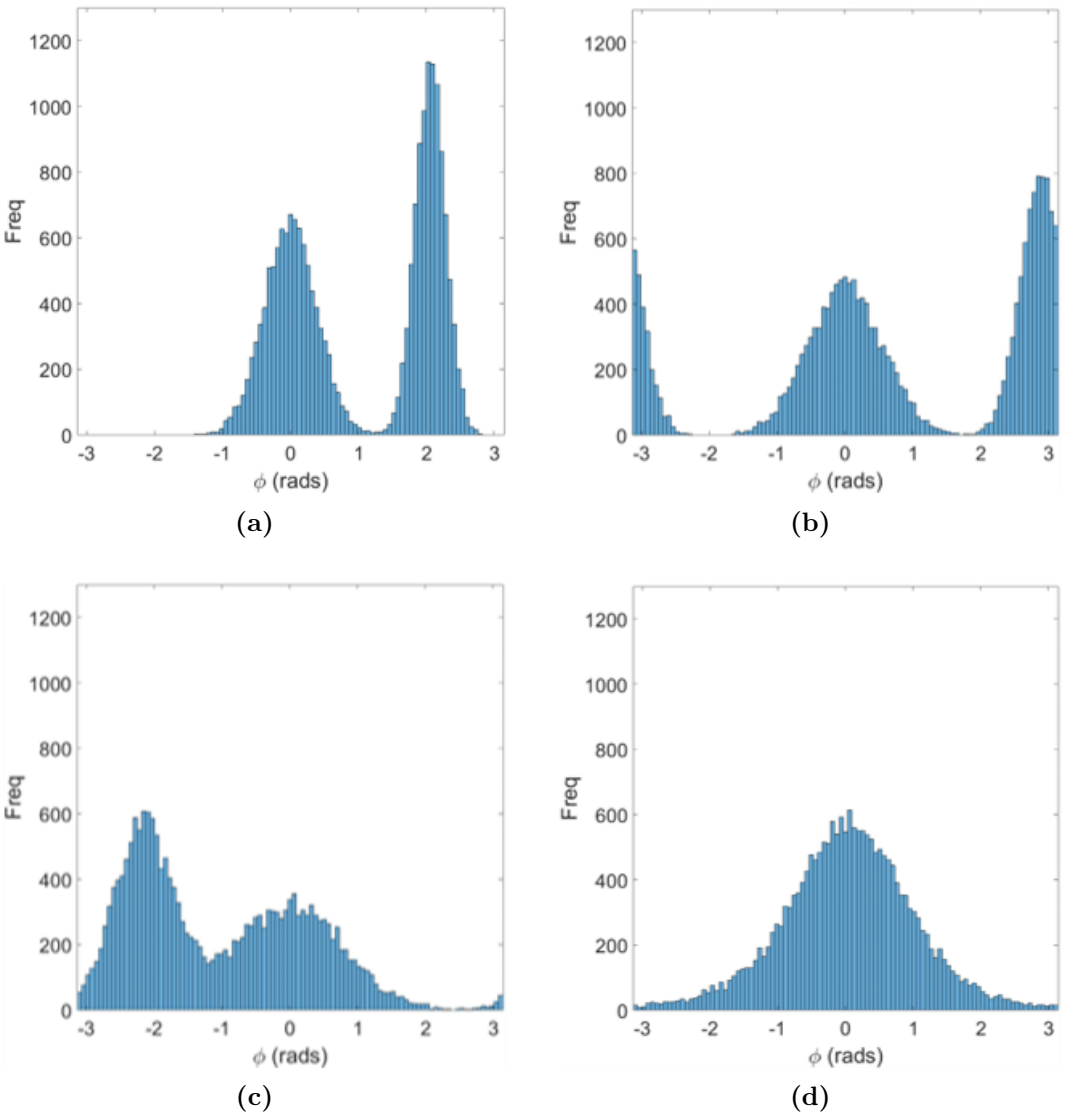


Figure 6.12: *Phase histograms from the simulation in* ***Figure 6.11d*** *at a) b = 13 s/mm^2, b) b = 25 s/mm^2, c) b = 50 s/mm^2, and d) b = 120 s/mm^2. At each b-value the phase of every spin was stored and fitted into bins from -π to π.*

6.4.3 Placental results

All placentas were then fitted to the IVIM, rephased, and sinc models. For the rephased fit the v' for a slice through a participant is shown in **Figure 6.15**, for voxels where the rephased fit significantly outperformed the IVIM fit. Four voxels were selected and the raw data from these voxels is shown, with the rephased fit also plotted. For each participant a single central slice is shown for all HP (**Figure 6.16a**) and CP (**Figure 6.16b**) with the v' overlaid for voxels where the rephased model significantly outperformed the IVIM model. For every participant the fraction of voxels that were best described by either

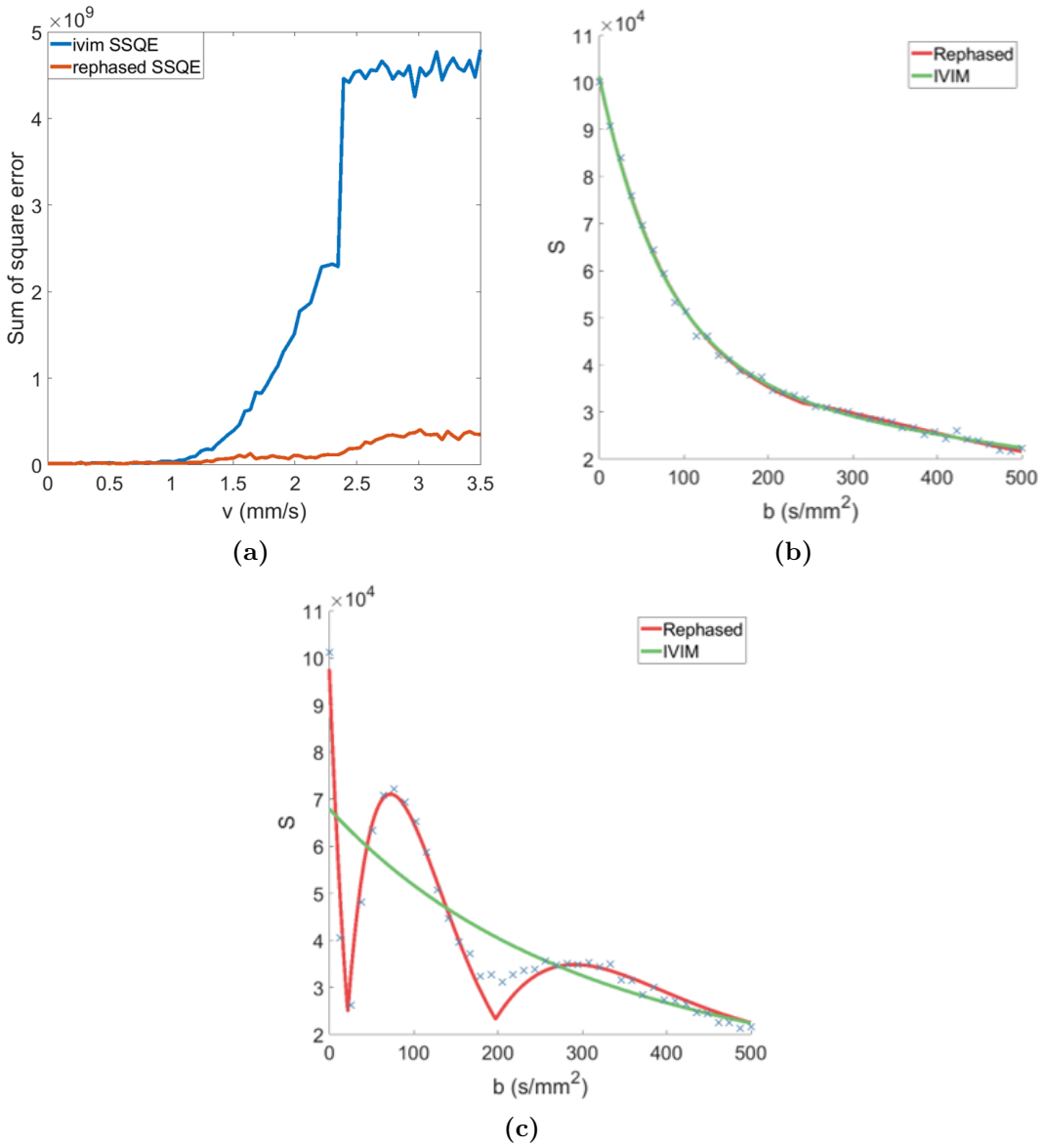


Figure 6.13: *a) A comparison of SSQE for IVIM fit and rephased fit to synthetic data, created by adding Gaussian noise to* ***Equation 6.12*** *using N_1 = 5000, N_2 = 5000, D_1 = 8 ×10^{-3} mm^2/s, D_2 = 2 ×10^{-3} mm^2/s and v_2 = 0-3.5 mm/s. The IVIM (green) and rephased (red) fits to the synthetic data at b) v_2 = 0 mm/s and c) v_2 = 3 mm/s are shown.*

the rephased, sinc, or both models was calculated and plotted in a bar chart in **Figure 6.17**.

Increasing initial intensity voxels were detected in all placentas, and the example signal from a single voxel is shown in **Figure 6.10**. For a single central slice through all HP and CP maps were produced to show the location of increasing initial signal voxels in **Figure 6.18**.

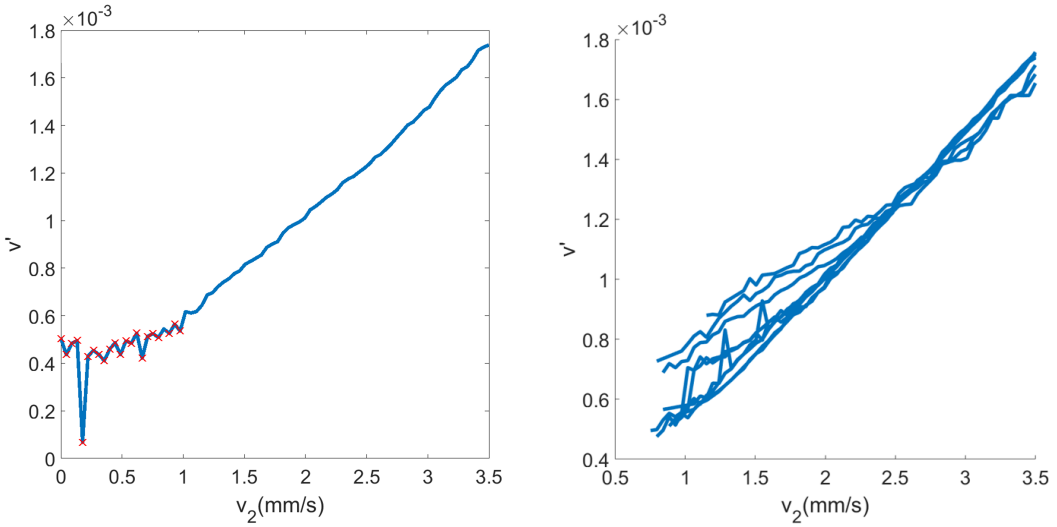


Figure 6.14: *a) Plot showing v' from the rephased fit against simulated v_2, plots where the rephased model was not a significant improvement against the IVIM model are marked with a red x. b) Plot showing v' against v_2 for a range of N_1, N_2, D_1, and D_2.*

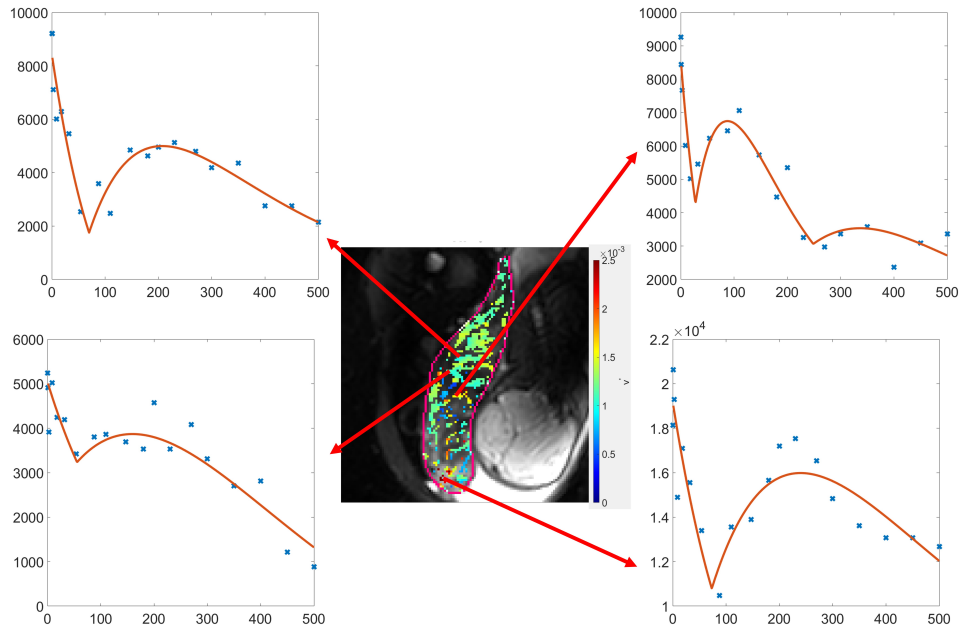
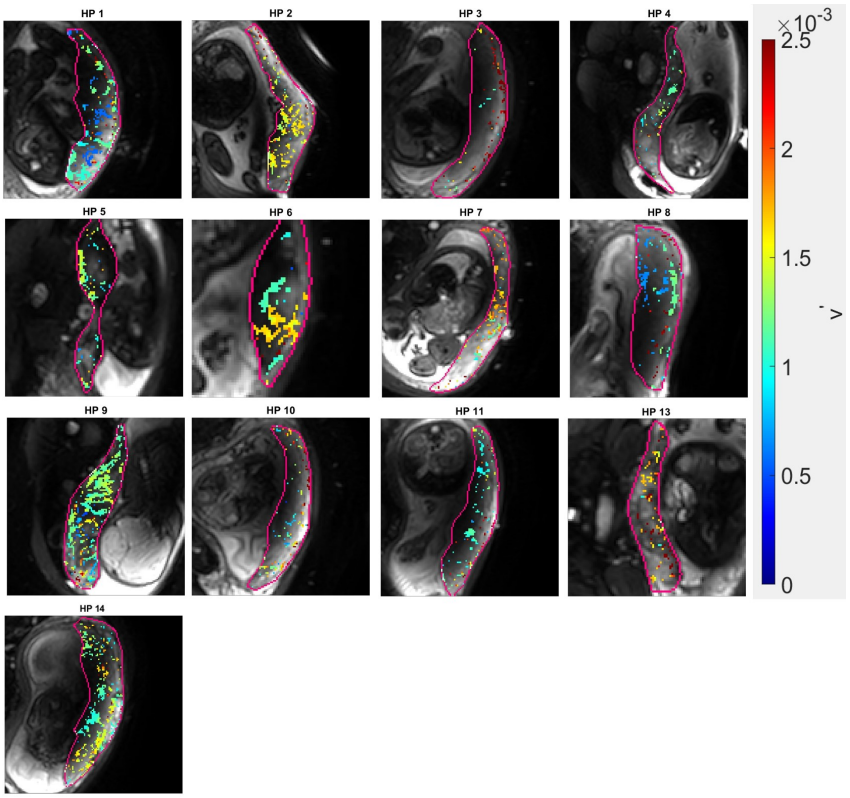
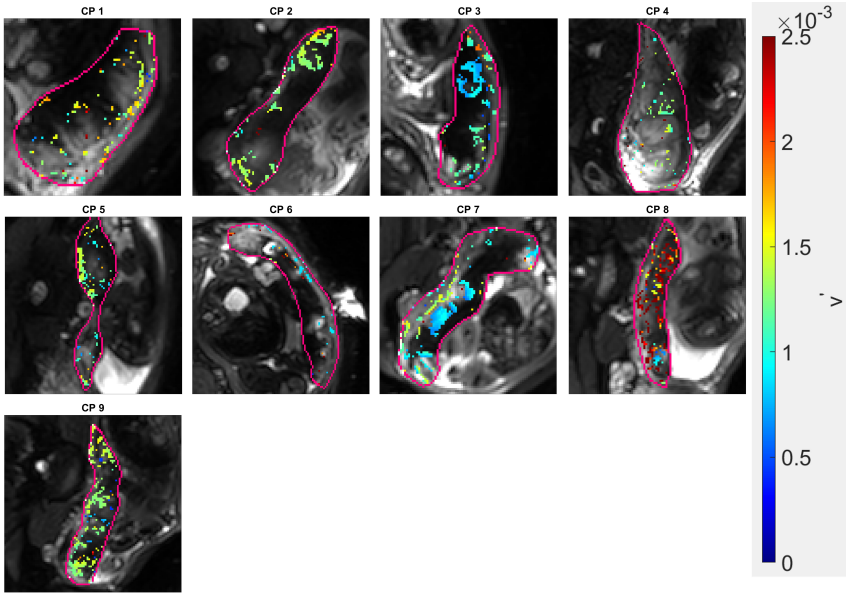


Figure 6.15: *An example slice through a placenta, with the v' map overlaid for voxels where the rephased model significantly outperforms the IVIM model, with the signal traces from 4 voxels plotted and labelled.*



(a)



(b)

Figure 6.16: *A single central slice from each participant, with the v' value overlaid for voxels where the rephased model was a significant improvement to the IVIM model for a) HP and b) CP. The boundary of the placental ROI is marked in magenta.*

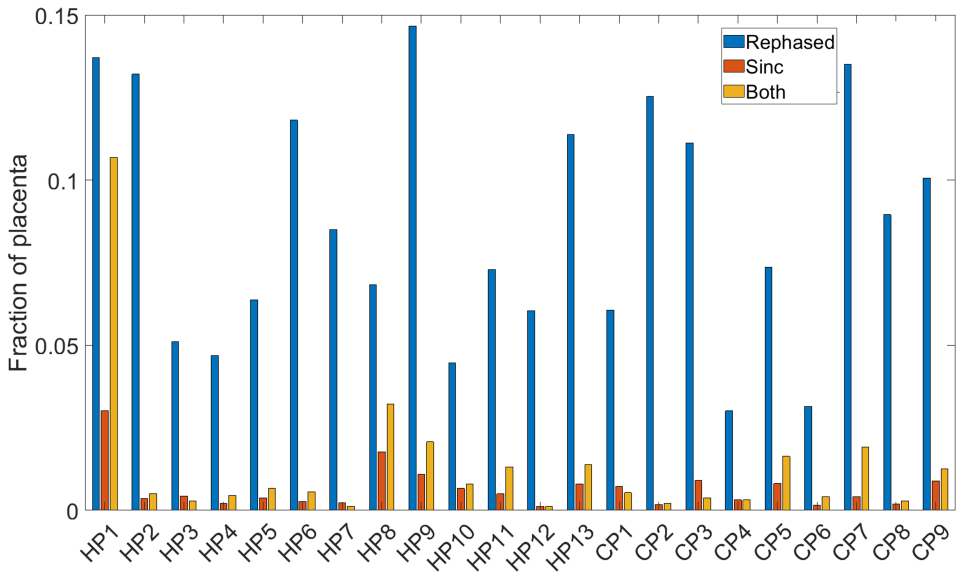
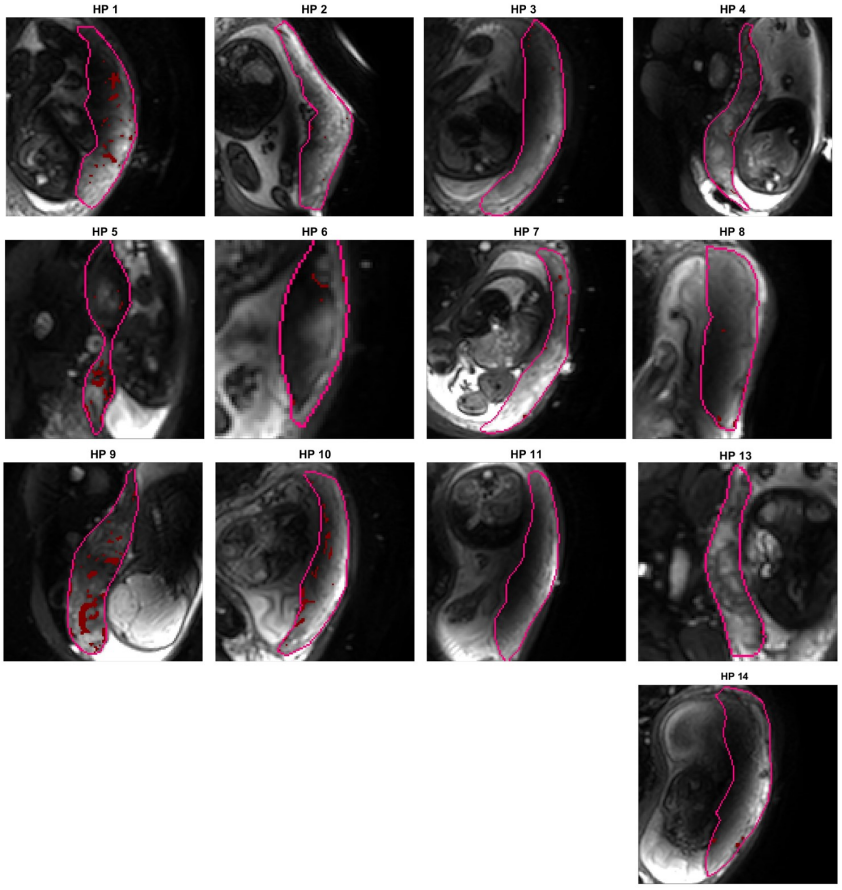
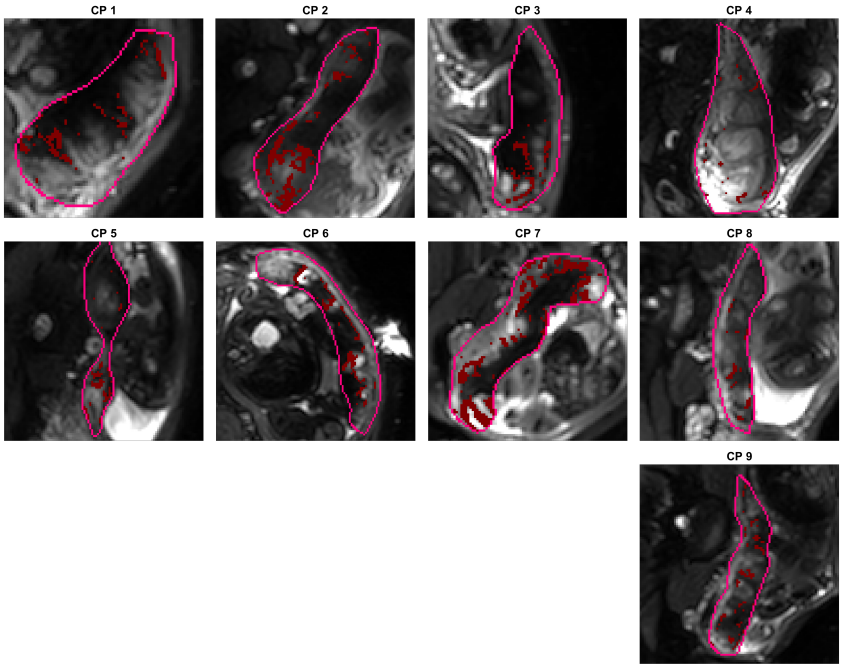


Figure 6.17: *Bar chart of the fraction of voxels from each participant where either the rephased model (blue), the sinc model (orange), or both models (yellow) provide significantly better fits than the IVIM model.*



(a)



(b)

Figure 6.18: *For a single central slice through all a) HP and b) CP increasing initial intensity voxels are plotted in red, with the placental ROI outlined in magenta.*

6.5 Discussion

As the simulated velocity increased in **Figure 6.11** the rate of signal decay over low b-value increases, and a rebound begins to form which recovered a significant proportion of the b = 0 s/mm^2 signal intensity in **Figure 6.11c & 6.11d**. The reason a rebound formed can be seen by investigating the phase histogram in **Figure 6.12** which is taken from the v = 3 mm/s simulation (**Figure 6.11d**). Initially all spins started with zero phase, but over low b-values there was additional dephasing as the peak corresponding to the moving pool of spins (at approximately $\phi = 2\ \pi$ rads in **Figure 6.12a**, and $\phi = 3\ \pi$ rads in **Figure 6.12b**) moved away from $\phi = 0$ rads. This continued until around b = 50 s/mm^2 (**Figure 6.12b**) where the phase wraps back around, and the extra dephasing caused by the moving pool begins to reduce, corresponding to the minimum at b = 50 s/mm^2 in **Figure 6.11d**. As the two peaks continued to rephase the signal increased until they completely rephased at approximately b = 120 s/mm^2 (**Figure 6.12d**) where the two pools became recoherent, and there was a maximum in signal.

At low velocity the IVIM and rephased models were indistinguishable, so provided very similar sum of square fits (**Figure 6.13a**). As the simulated velocity v_2 increased the rebounds became more pronounced, the rephased model provided a better sum of squares fit. Over low velocities simulations did not provide a significantly better sum of squares fit (through use of an F-test) to the underlying data (**Figure 6.14a**) and there was no clear relationship between v' and v_2. As v_2 increased the rephased model fitted the data significantly better, and a linear relationship was evident with v', which was consistent across a range of simulated coefficients (**Figure 6.14b**), supporting the use of the F-test to identify voxels with significant rebounds. Even though the rephased model did not provide a perfect fit to the data (**Figure 6.13c**) it was designed as an empirical approach to detect the rebounds, and charac-

terise the frequency and position of the rebounds which it managed well. v' should therefore contain quantitative information about the relative velocity of coherent flows within a voxel.

In placental data the rephased model was generally good at fitting rebounding voxels, as shown in **Figure 6.15**, where four example voxels have been highlighted from a single slice. In general these voxels showed very fast decay over low b values, after which signal began to recover and consistently increased with b value, before beginning to decay again. From the v' maps (**Figure 6.16**) and the fraction of voxels that were best described by each model (**Figure 6.17**) it can be seen that while most placentas contained a significant amount of rebounding voxels, the majority of voxels were still described by IVIM. Rebounding voxels tended to be clustered together, of similar v' indicating these were distinct regions that were exhibiting similar behaviour, and was unlikely to be just due to noise. Other non-physiological reasons for the rebounds were considered, such as fetal and maternal motion, which could have caused a rebound if regions of longer T_2 moved into an area of shorter T_2 during scanning. However the rebounds tend to be localised and not global across the image, and there was no link between the number of voxels discarded due to motion and the proportion of rebounds. The rephased model also fit a higher proportion of voxels than the sinc behaviour in all participants, indicating that the rebounds observed here are not of the same form as those described by Le Bihan.

During the investigation voxels were observed that showed increasing initial intensity over the low b-values (**Figure 6.10**). Due to the way these voxels were identified (by smoothing data over b = 18-148 s/mm^2), that they tended to be clustered together (**Figure 6.18**), and that they resumed normal decay after increasing in signal (**Figure 6.10**), it was unlikely these were just due to random noise. The exact cause of these voxels was unclear, but I theorised

that these were voxels that experience some local field offset during the encoding gradients. This was supported by these voxels having significantly lower mean signal intensity at b = 0 s/mm^2 than the rest of the placenta in every participant (t-test, highest p = 0.02, **Figure 6.19a**) implying there was been some additional signal decay in these voxels (example histogram from a single participant is shown in **Figure 6.19a**). Any field offset applied during the DWI encoding gradients would cause a mismatch between the theoretically applied b-value and the actually applied b-value. If this field offset was in the opposite direction to the encoding gradients this would cause the scan to start at a higher b-value than planned (**Figure 6.19d**), causing signal to increase as the encoding gradient overcomes the field offset before decay resumes again. If the voxel contained a rebound, and the local field offset was in the same direction to the applied field gradients, this could also cause increasing initial intensity as shown by the simulations in **Figure 6.19b**, where the methodology for the simulations was the same as outlined in **Section 6.3.1**. This caused a translation of the decay curve across b, as the field offset meant the applied b-values are higher than expected, skipping part of the decay curve. If the voxel contained a rebound then this translation could skip the initial decay from a signal decay, as in **Figure 6.19c** were a placental voxel was manually fitted to the rephased model, but the b-value was shifted to reproduce the lost initial decay (dashed line). To investigate the exact cause the maximum signal intensity of these increasing initial intensity voxels should be investigated further, an offset in the opposite direction to the applied gradients should recover the signal back to a signal comparable with the b = 0 s/mm^2 intensity of normal placental voxels, wheras an offset in the same direction as the gradients, combined with a rebound, would not recover signal to this b = 0 s/mm^2 intensity.

Increasing initial intensity voxels made up a larger fraction of compromised placentas **Figure 6.19e** (p=0.005, Mann Whitney U test) than healthy pla-

centas, which could be caused by inhomogenous distribution of de-oxygenated blood in those placentas[1], giving rise to larger regions with local magnetic fields causing more increasing initial intensity voxels.

More work is needed to investigate these rebounds, which should include checking other placental data sets to check whether these rebounds are occurring in data acquired in other studies. While the rebounds presented here are assumed to be caused by one stationary pool, and one moving pool of spins in practice the environment is probably more complicated, with flows and counter flows, or divergent or convergent flows. To better understand the causes of these rebounds their relationship to PGSE properties (c) should be investigated further, for example by repeating two gradients sets where the diffusion time (Δ) is altered and checking that the rebounds are present, and respond as expected to the altered PGSE properties c.

6.6 Conclusion

Rebounds in PGSE data have been proved to be theoretically possible but had not previously been reported in experimental data, indicating the rebounds presented here are likely to be due to the complex system of blood flow unique to the placenta, and could be easy to overlook. Due to the shape of these rebounds they are probably not the same as those proposed by Le Bihan, and are better characterised by a new model I propose which was due to the rephasing of spins travelling at constant velocity during the PGSE sequence. While this may not be a perfect quantitative model it was still able to prove the existence of these rebounds, that they make up a significant number of placental voxels, and provide some quantitative information about the frequency of the rebounds. If these rebounds are caused by flow across a voxel, then by altering the PGSE properties (c) scans could be optimised to provide both diffusion and flow information from a single set of gradients, allowing for better un-

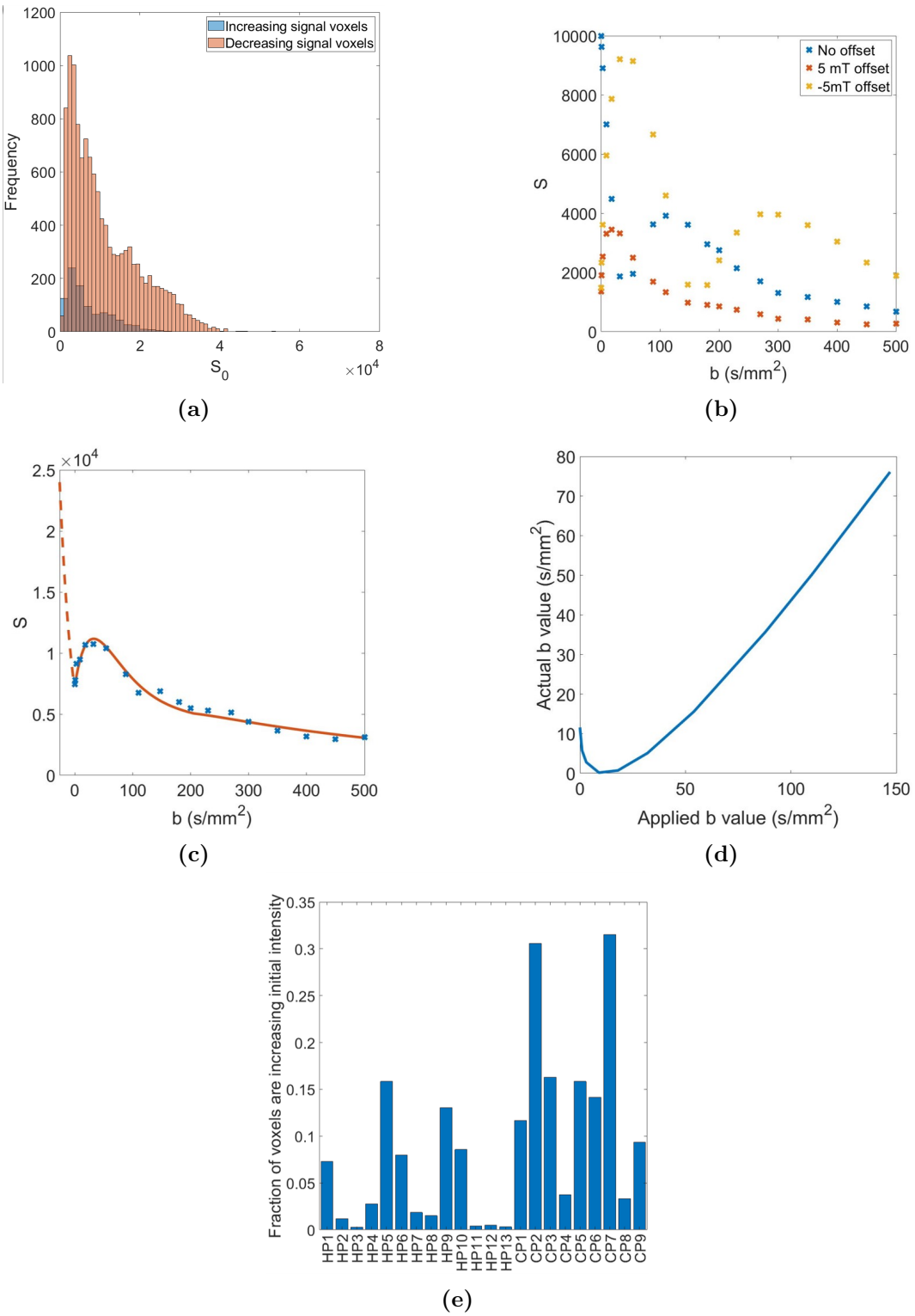


Figure 6.19: *a) Histogram showing the b=0 s/mm^2 intensity from a single participant. b) Simulated data showing how a field offset in the direction of (orange), or opposing (yellow) the applied DWI gradients can create a voxel of increasing initial intensity. c) Increasing initial intensity voxel fit to the rephased model. d) Plot showing applied b-value vs actual b value for a constant field offset in the opposite direction to the applied DWI gradients. e) Bar chart showing the fraction of voxels which are increasing initial intensity in each participant*

derstanding of placental haemodynamics, and potentially could be used as a marker of placental dysfunction.

6.7 Bibliography

[1] N. S. Dellschaft, G. Hutchinson, S. Shah, N. W. Jones, C. Bradley, L. Leach, R. B. C. Platt, and P. A. Gowland, "The haemodynamics of the human placenta in utero," *PLOS Biology*, vol. 18(5), p. e3000676, 2020.

[2] P. J. Slator, J. Hutter, L. McCabe, A. D. S. Gomes, A. N. Price, E. Panagiotaki, M. A. Rutherford, J. V. Hajnal, and D. C. Alexander, "Placenta microstructure and microcirculation imaging with diffusion mri," *Magnetic Resonance in Medicine*, vol. 80, no. 2, pp. 756–766, 2018.

[3] R. J. Moore, B. K. Strachan, D. J. Tyler, K. R. Duncan, P. N. Baker, B. S. Worthington, I. R. Johnson, and P. A. Gowland, "In utero perfusing fraction maps in normal and growth restricted pregnancy measured using ivim echo-planar mri," *Placenta*, vol. 21, no. 7, pp. 726–32, 2000.

[4] A. Jakab, R. L. Tuura, R. Kottke, N. Ochsenbein-Kölble, G. Natalucci, T. D. Nguyen, C. Kellenberger, and I. Scheer, "Microvascular perfusion of the placenta, developing fetal liver, and lungs assessed with intravoxel incoherent motion imaging," *Journal of Magnetic Resonance Imaging*, vol. 48, no. 1, pp. 214–225, 2018.

[5] D. Le Bihan, E. Breton, D. Lallemand, M. Aubin, J. Vignaud, and M. Laval-Jeantet, "Separation of diffusion and perfusion in intravoxel incoherent motion mr imaging," *Radiology*, vol. 168, no. 2, pp. 497–505, 1988.

[6] D. L. Bihan, "What can we see with ivim mri?," *Neuroimage*, vol. 187, pp. 56–67, 2019.

[7] Y. Wang and S. Zhao, *Vascular Biology of the Placenta*. San Rafael (CA): Morgan Claypool Life Sciences, 2010.

[8] L. K. Harris and J. D. Aplin, "Vascular remodeling and extracellular matrix breakdown in the uterine spiral arteries during pregnancy," *Reproductive Sciences*, vol. 14, no. $8_s uppl), pp.\ 28 - -34, 2007$.

[9] J. Rafael-Patino, D. Romascano, A. Ramirez-Manzanares, E. J. Canales-Rodríguez, G. Girard, and J. P. Thiran, "Robust monte-carlo simulations in diffusion-mri: Effect of the substrate complexity and parameter choice on the reproducibility of results," *Frontiers in Neuroinformatics*, vol. 14, 2020.

Chapter 7

Effects of PGSE sequence on DWI data

7.1 Introduction

It is expected that the diffusion weighting imaging (DWI) results could vary depending on the exact sequence or sequence parameters used to encode for diffusion. For an intra-voxel incoherent motion (IVIM) fit (as shown in **Chapter 3**) it has been shown that the exact values of f_{IVIM}, D, and D^* vary depending on the sequences or timings used in rat brain [1, 2] and the human liver [3]. Using pulse gradient spin echo (PGSE) sequences IVIM parameters have been shown to vary with diffusion time (Δ) in breast cancer tumours [4] and in rat brain [5], where the studies report contrasting results implying that the effect of Δ on IVIM parameters could vary depending on the environment being imaged. In [4] f_{IVIM} was found to increase with Δ, while D^* remained the same, and D decreased. In [5] however f_{IVIM} remained the same, while D^* decreased at low Δ, and D increased, despite both studies using similar values of Δ (9.6 and 27.6 ms in [4], and 14, 24, and 36 ms in [5]). This work is yet to be carried out in the placenta, where the exact system of flows and turbulent motion are unique, so needs to be investigated.

Here I aimed to use a phantom to simulate the placental environment and investigate the effects of how *Delta* influences IVIM in the placenta for a PGSE sequence. Additionally as the phase data of PGSE data are sensitive to velocity depending on c

$$c = \gamma G \Delta \delta \tag{7.1}$$

for a PGSE. I also investigated whether there was sensitivity to flow that could be measured with varying Δ. While the ultimate aim of this work was to develop and apply the sequences in human placentas in utero this was not possible due to the COVID-19 pandemic.

7.2 Methods

7.2.1 Phantom

A schematic of the phantom is shown in **Figure 7.1b**. Water was pumped into the phantom using a Tamson instruments TLC-15 heatbath/pump combination unit that provided approximately 2 litres of water per minute into the phantom. The phantom contained two cylindrical chambers, where water was pumped into the first chamber (of diameter 70mm and length 160mm) which was packed with four cellulose sponges to fill the cross section of the chamber. Cellulose sponges have previously been shown to be an effective method to simulate an IVIM effect [6], and here the water would flow through these sponges and combine bulk flow effects with percolation through the pores of the sponges to simulate the placental environment. All four sponges had the same pore size of approximately 2-3mm, but the exact properties of each sponge was unknown, procurement of sponges of different pore sizes or consistent pore sizes was difficult due to the COVID-19 pandemic. Initially this work was supposed to be carried out with porous plastics, which would have been manufactured with known, consistent pore sizes but this work had to be halted due to the COVID-19 pandemic. Sponges 1 and 2 were imaged in this

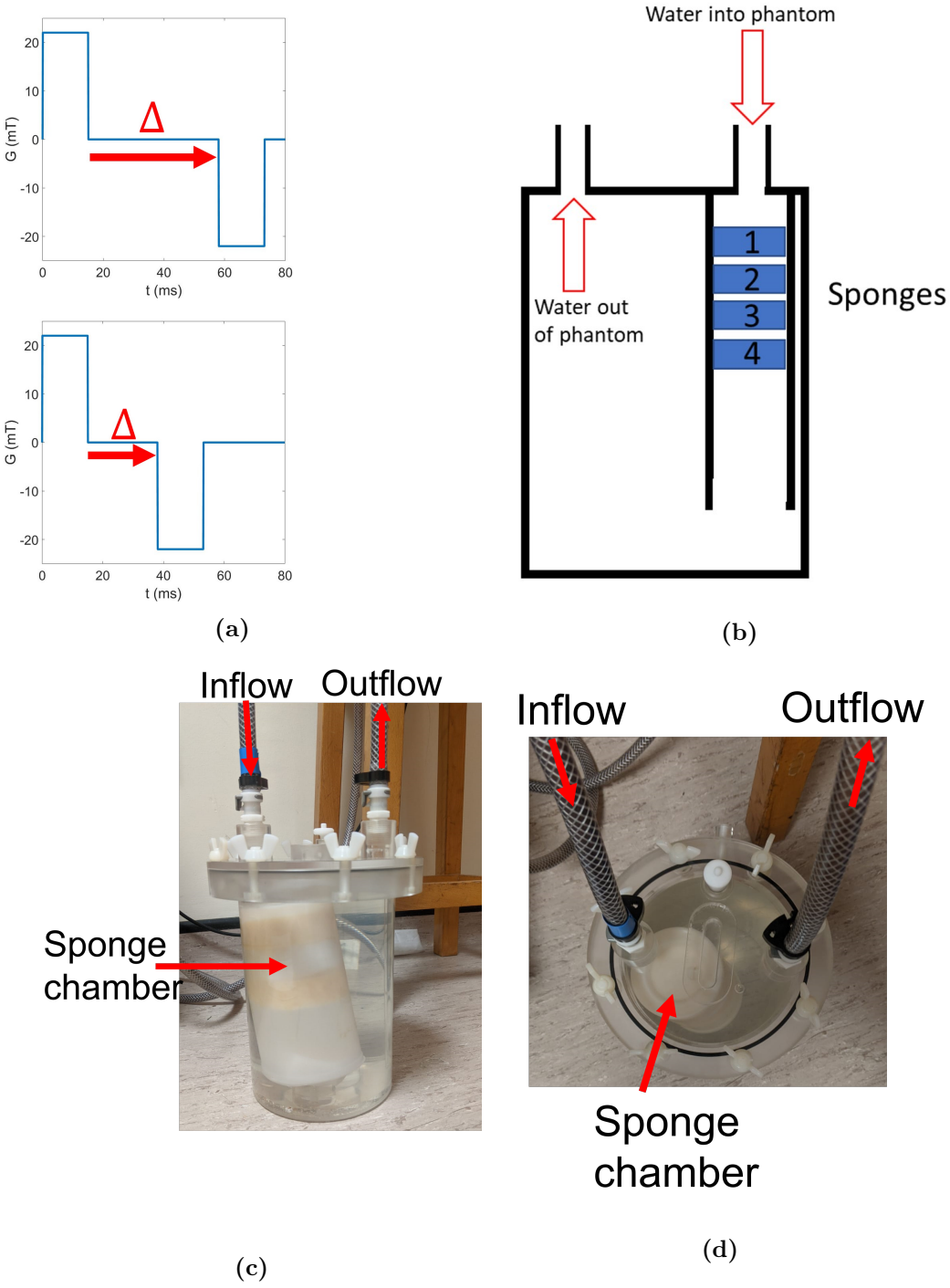


Figure 7.1: *a) Two example PGSE gradients of varying diffusion time (Δ). b) Scehmatic of the flow phantom with c) a side on and d) a top down picture of the phantom, with sponge chamber, inflow and outflow directions labelled.*

experiment, but sponges 3 and 4 were not. Water would then flow out of the first chamber, into the second where it would return to the pump via an outlet. Labelled photographs from side on, and top down views are shown in **Figure 7.1c & 7.1d**. As the pump unit used was also a water bath and there was large gaps between imaging sessions due to COVID-19 the phantom had to be

taken apart and water flushed out at the end of each imaging session due to concerns around Legionella.

7.2.2 Imaging

Imaging was carried out on a Phillips 3T Achieva scanner where the phantom was placed in a 32 channel head coil for imaging. A PGSE with an echo time (TE) of 90ms was used, with voxel size 1.08x1.08x4mm^3 with an FOV of 138x138mm. Two slices were collected, one through the first sponge and one through the second sponge as labelled in **Figure 7.1b**. To image the phantom two sets of gradients were used of varying diffusion time Δ (for example **Figure 7.2b**) where one set encoded for diffusion through the conventional b-value, and another encoded for flow through c value.

7.2.2.1 Diffusion Encoding

The diffusion encoded gradients used 14 b-values between 0-219 s/mm^2, where the b-value was changed by only altering the gradient amplitude. These scans were repeated for 5 different Δ from 23-44 ms, for a constant lobe length of δ = 15ms, which meant the flow encoding c would vary between scans but the b-values would remain constant (**Figure 7.2a**). Scans were repeated in three separate scanning sessions, which required the phantom to be reconstructed and the sponges repacked. Diffusion encoded data was fitted to an IVIM model, by fitting low b-value data (0-120 s/mm^2), and high b-value (120-219 s/mm^2) data to a mono-exponential decay to provide initial estimates of D^* and D respectively. These initial estimates were used as estimates for the final IVIM fit, where f_{IVIM}, D, and D^* were constrained between 0-1, 0-10$\times10^{-3}$mm^2/s, and 10-1000$\times10^{-3}$mm^2/s. The sponges were masked by hand on the b = 0 s/mm^2 slice, where dark regions corresponding to low signal in the b = 0 s/mm^2 were not included in the mask.

7.2.3 Flow Encoding

The flow encoded gradients used 3 c values (c_1,c_2 and c_3 which were kept constant across the same 5 Δ (**Figure 7.2b**)). The data were phase corrected by repeating these gradients twice, once for the phantom with the pump turned off, and again with the pump-on causing water to flow through the phantom. The pump-off phase image was then subtracted from the pump-on phase image, to correct for background variations in phase not caused by flow through the system. Phase data was only considered for the through slice component, and the phase corrected data were masked using the same sponge mask as for the diffusion encoding experiment, which were used to produce phase histograms. During the investigation the phase histograms were found to contain two peaks, which were identified by fitting the histograms to the sum of two Gaussian functions, where the peak position for each Gaussian indicated the location of the peak, which was divided by c to provide a measure of the apparent velocity.

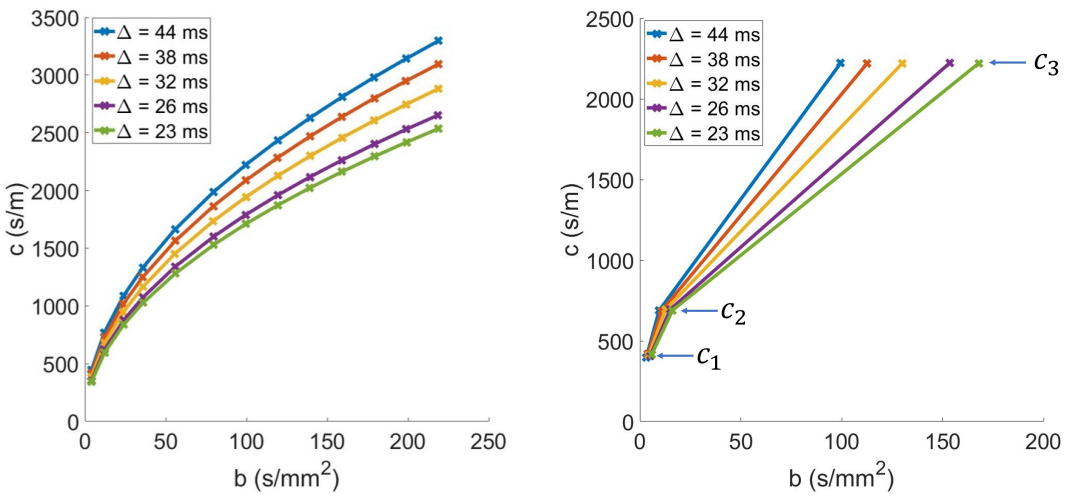


Figure 7.2: *A) c against b-value for the first set of gradients. b) c against b-value for the second set of gradients, where the points of constant c are labelled.*

7.2.4 Results

Figure 7.3 shows the magnitude image of the phantom across all b-values for $\Delta = 23$ms from session 1, and an example of the raw data and subsequent IVIM fit from a single voxel in sponge 1 and 2 are shown in **Figure 7.4**.

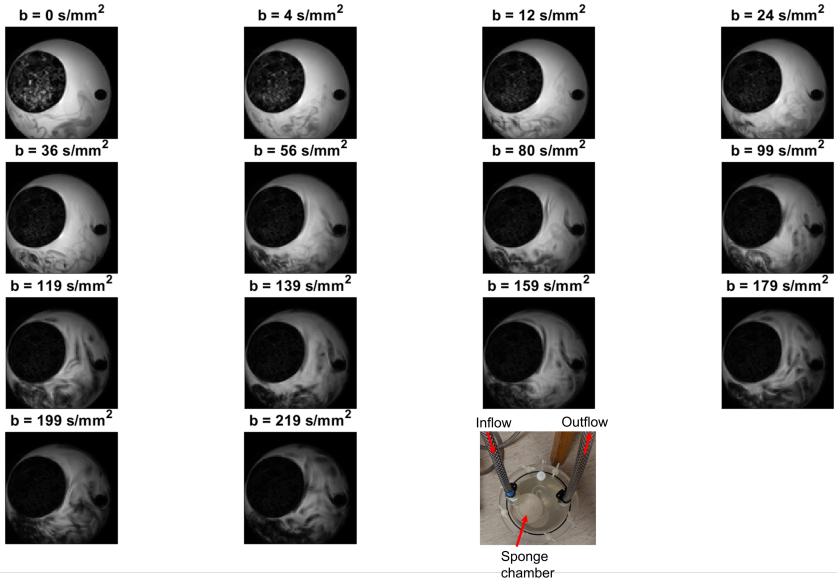


Figure 7.3: *Magnitude images through the first sponge for $\Delta = 23ms$, with an image of the phantom to show the location of the sponge and outflow pipe.*

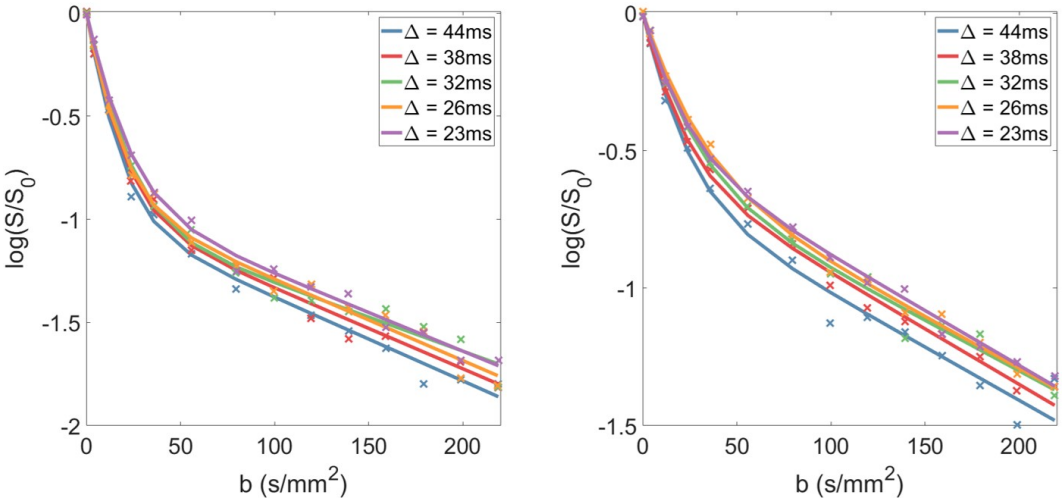


Figure 7.4: *Underlying data and IVIM fit for a single voxel from a) sponge 1, and b) sponge 2*

Mean f_{IVIM}, D, and D^* across each of the sponges was then also calculated from all three sessions, and plotted against Δ in **Figure 7.5a**. Phase

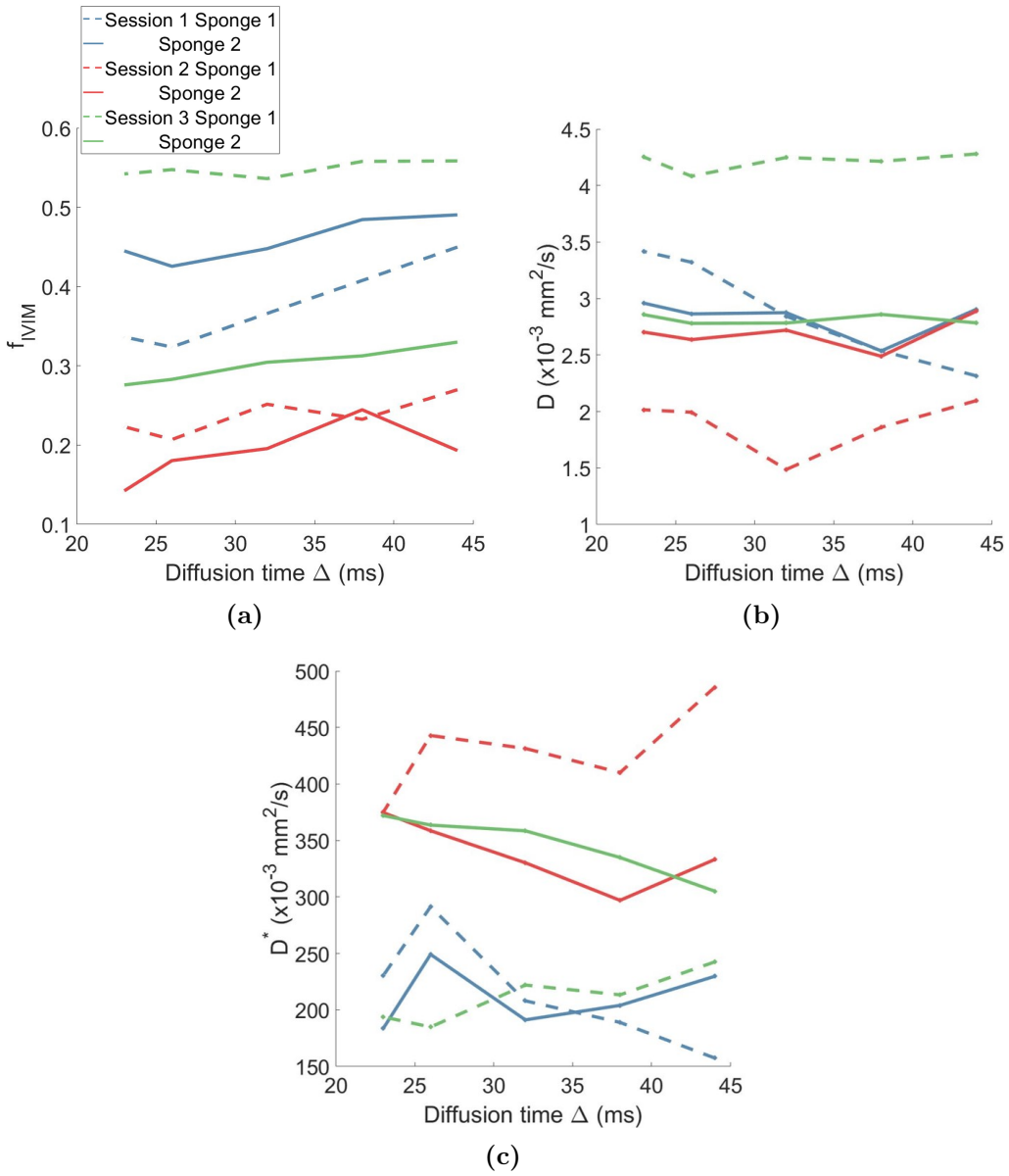


Figure 7.5: *a) Mean f_{IVIM}, b) D, c) D* data from the three scanning sessions.*

histograms, only considering the encoded flow through the imaging slice from the first scanning session are shown in **Figure 7.6**, for 3 Δ values, and the corresponding flow encoding c_1, c_2, and c_3. The histograms were fitted to the sum of two Gaussian functions, where the position of the peak of each Gaussian was used to calculate the apparent velocity of the two peaks, which are labelled. The apparent velocities measured from these histograms were plotted in **Figure 7.7** against Δ.

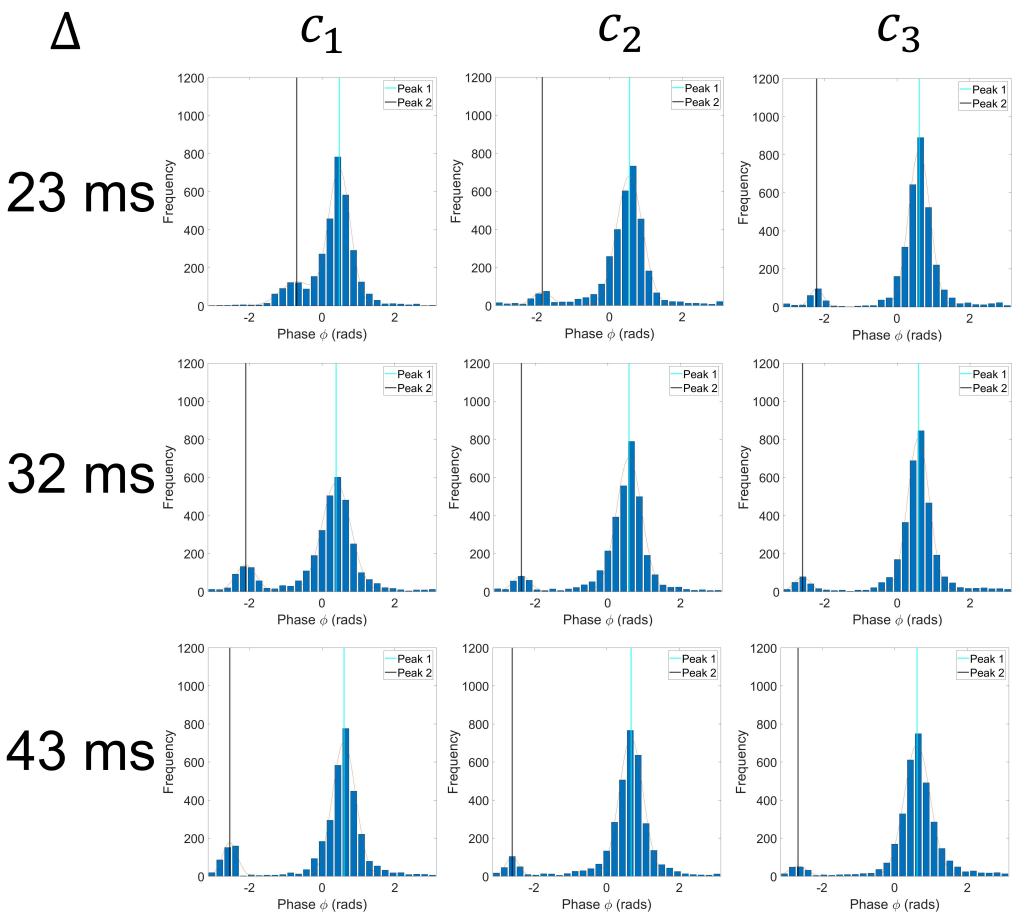


Figure 7.6: *Phase histograms across the 3 c values imaged, for 3 Δ values where the locations of the peaks measured by fitting the histogram to the sum of two Gaussian functions, where the mean of each Gaussian was taken as the peak location.*

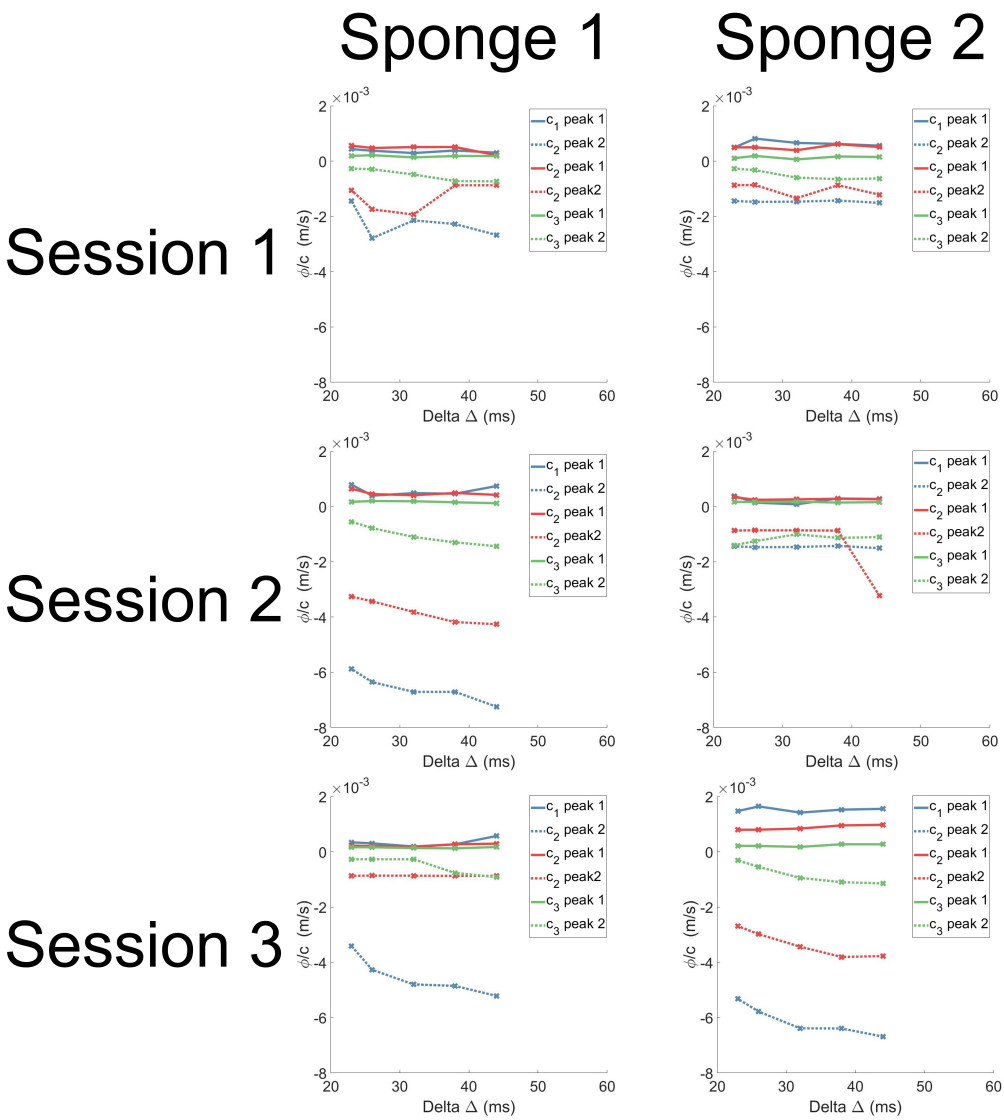


Figure 7.7: *The apparent velocity for peak 1 and 2 plotted against diffusion time* Δ*, for all three c values recorded. This is repeated for both sponges, for all three scanning sessions.*

7.3 Discussion

The example voxels in **Figure 7.4** show the underlying data and IVIM fit and highlight the changes seen in the signal as Δ changes. As Δ increases so did mean f_{IVIM} (**Figure 7.5a**) in both sponges, similar to [4] but different to [5].

While D did not show any clear variation with Δ it is possible that either: the b values here were not high enough to properly investigate the relationship, the shortest diffusion time was too long, or the pore sizes in the sponge were much higher than in previous work [4, 5]. The relationship between Δ and D is thought to relate to the amount of kurtosis (K), as in breast cancer tumours there is a high degree of kurtosis, so at longer Δ there is more time for spins to reach the restrictive limit of the system, which decreases D. In rat brain however there was no change in kurtosis at longer diffusion times, which would allow spins to fully diffuse during the imaging gradient, causing D to increase with Δ up to a point, where it would plateau. From **Chapter 3** however I saw regions of high and low kurtosis in the placenta, implying there may be a mixture of increasing and decreasing D with increasing Δ, which could be investigated in future work. D^* also showed no relationship with Δ (**Figure 7.5c**), which is the same as both [4] and [5].

The results of f_{IVIM}, D and D^* did vary heavily between session and sponge, but are reasonably consistent within a single sponge for a single session. The variance is probably because the phantom was reconstructed before each scanning session, meaning the sponges had to be re-packed into the cylindrical chamber and differences in compression would affect the structure of the sponge and the IVIM parameters. If a sponge was more compressed this would have shrunk the pore sizes, and caused a reduction in f_{IVIM} as within any voxel there would be less water percolating throughout the structure. This would also have affected D, as with smaller pore sizes there would have been

more chance that spins reach the boundary of the pore, reducing D. D^* would have increased, as $D^* = l/v$ depends on the velocity of flow (which was constant) and the lengthscale of the incoherent motion l. If the sponge was more compressed l would be reduced, causing D^* to increase.

In the phase data for the through slice component there were two peaks which varied with both Δ and c (**Figure 7.6**). The first peak contained the largest number of voxels, probably indicating the slow motion of water through the sponges, with the location of the peak independent of diffusion time or flow encoding (**Figure 7.7**). The second peak did however vary with encoding time, and is probably related to the preferred pathway through the porous sponge as these voxels tended to be clustered together, and response to Δ would rely on the exact structure of the porous media, indicating this could be a useful placental measure in the future.

Ultimately the flow phantom used here can only simulate the placental environment so well, and while it does provide a net flow across a porous media it is lacking a number of features of the placental environment, such as counter flows, fetal circulation, and exchange across the fetal/maternal barrier. These could all have effects on both the diffusion encoded and flow encoded data and the effects cannot be properly investigated without applying the technique in utero, which was unfortunatley not possible due to the COVID-19 pandemic.

7.3.1 Conclusion

Here I aimed to demonstrate the potential effects of altering the diffusion time (Δ) on the placental DWI by use of a porous flow phantom. I found that f_{IVIM} would be expected to increase at longer Δ, similar to work in other organs and demonstrating that the results from any placental DWI experiment will probably depend on the exact sequence timings used. I found that D and

D^* did not change with Δ, but the maximum b value used here was probably too short for the size of pores in this phantom. Additionally I showed that the phase data from varying Δ imaging could provide useful information about flow and pores, indicating that by combining the diffusion encoding and flow encoding gradients into a single set of imaging gradients could be advantageous in future work by providing simultaneous diffusion and flow information.

7.4 Bibliography

[1] M. Iima, T. Nobashi, H. Imai, S. Koyasu, T. Saga, Y. Nakamoto, M. Kataoka, A. Yamamoto, T. Matsuda, and K. Togashi, "Evidence of the diffusion time dependence of intravoxel incoherent motion in the brain," *Radiol Open*, vol. 7, no. 1, pp. 1–8, 2018.

[2] N. Pyatigorskaya, D. Le Bihan, O. Reynaud, and L. Ciobanu, "Relationship between the diffusion time and the diffusion mri signal observed at 17.2 tesla in thehealthy rat brain cortex," *Magnetic Resonance in Medicine*, vol. 72, no. 2, pp. 492–500, 2014.

[3] A. Wetscherek, B. Stieltjes, and F. B. Laun, "Flow-compensated intravoxel incoherent motion diffusion imaging," *Magnetic Resonance in Medicine*, vol. 74, no. 2, pp. 410–419, 2015.

[4] M. Iima, T. Nobashi, H. Imai, S. Koyasu, T. Saga, Y. Nakamoto, M. Kataoka, A. Yamamoto, T. Matsuda, and K. Togashi, "Effects of diffusion time on non-gaussian diffusion and intravoxel incoherent motion (ivim) mri parameters in breast cancer and hepatocellular carcinoma xenograft models," *Acta Radiol Open*, vol. 7, no. 1, 2018.

[5] G. Fournet, J. Li, A. Cerjanic, B. Sutton, L. Ciobanu, and D. Le Bihan, "A two-pool model to describe the ivim cerebral perfusion," *J Cereb Blood Flow Metab.*, vol. 37, no. 8, pp. 2987–3000, 2016.

[6] G. Y. Cho, S. Kim, J. H. Jensen, P. Storey, D. K. Sodickson, and E. E. Sigmund, "A versatile flow phantom for intravoxel incoherent motion mri," *Magnetic Resonance in Medicine*, vol. 67, no. 6, pp. 1710–1720, 2012.

Chapter 8

Summary and conclusions

In this thesis I used Magnetic Resonance Imaging (MRI) to investigate and provide better understanding of placental haemodynamics and structure, and how these differ in placental dysfunction, namely Fetal Growth Restriction (FGR) and Pre-Eclampsia (PE).

In **Chapter 1** I introduced the biology of the human placenta, providing information about key structures and flows with particular attention to those relevant to the scales and sensitivities provided by MRI, and how these are thought to be altered in disease. I then outlined MRI theory, including techniques which are of interest for measuring placental haemodynamics in utero, and consider the safety concerns present when using MRI on a pregnant participant.

In **Chapter 2** I outlined the criteria for defining both HP and CP, and provided a summary of the participant groups in this thesis, including which participants had complete Diffusion Weighted Imaging (DWI) or Phase Contrast Angiography (PCA) data. I also outlined the data collection and preprocessing steps for the human DWI and PCA data used in this thesis.

In **Chapter 3** I fitted placental Diffusion Weighted Imaging (DWI) data

using an Inverse Laplace Transform (ILT) based technique to provide better understanding of the underlying signal. I showed that the signal is dominated by slow water diffusion, with multiple faster incoherent components which the ILT fit was able to detect. These results help provide information about placental haemodynamics, and it was found that these faster incoherent components were altered in placental dysfunction, highlighting the ability of the technique to investigate structural or haemodynamic changes in disease.

In **Chapter 4** I fitted the same data as **Chapter 3** to a more commonly used Intra-Voxel Incoherent Motion (IVIM) model, and provided more insight about the pseudodiffusive term D^*. The results from the IVIM fit agreed with previous literature, and showed that the technique is sensitive to changes in placental dysfunction, and provided information about placental haemodynamics. While a limitation of the IVIM model is that the placenta is always assumed to be made of two components, I showed by a direct comparison between the IVIM and ILT methods that there was still good agreement between the IVIM and ILT results, with most key metrics from the ILT fits having an IVIM analogue.

In **Chapter 5** I used the sensitivity of phase data from PGSE gradients to motion using Phase Contrast Angiography (PCA) to measure the velocity of blood in the placenta. These results were used to both investigate how the speed of blood differs as it traverses the placenta, and provide more context to the sub-voxel motion of blood measured with the IVIM approach. I then used the velocity information that PCA provided to better understand arterial input to, and venous return from the placenta, the latter of which is poorly understood in human placentas.

In **Chapter 6** I investigated the presence of rebounds which I observed in placental PGSE data, which have been theoretically proven to be possible, but

not reported in PGSE data before. Due to the shape of these rebounds I believe they were different to those theorised before, and were instead caused by flow effects within a voxel. Then I outlined a method to identify these voxels, using an empirical model which provided information about the underlying flow effects, and I found that while the majority of voxels were described by IVIM, a significant proportion contained these rebounds.

In **Chapter 7** I used an imaging phantom to demonstrate that the exact ILT and IVIM values presented here may vary depending on the exact sequence timings used. However these timings could potentially be exploited, and combined with phase measurements to measure simultaneous diffusion and velocity which may be of use in future placental research but need be investigated in utero first.

In all this thesis used MRI to help illustrate the path of blood, especially the maternal circulation as it enters and travels through the placenta, how this differs in disease, and could lead to placental insufficiency. Using PCA I showed in the healthy placenta fast flowing blood is dampened as it travels through the uterine wall, basal plate and into the placenta losing speed to provide a slower flow of blood throughout the intervillous space. This is thought to be driven by spiral artery remodelling, which slows the fast flowing arterial blood to provide a high volume, slow, continuous stream of blood into the placenta. The transformation of this blood can also be seen through DWI measures, where both the ILT and IVIM model showed a higher proportion of faster incoherent blood within the uterine wall and basal plate, which is reduced upon entry to the placenta. Using PCA I also showed that the fastest travelling blood in the placenta is travelling perpendicular to the basal plate, which is consistent with arterial input, and venous return from the placenta, where I measured that the two were occurring at comparable rates. While it may seem obvious to state that what enters the placenta must also leave

again, unimpeded venous drainage must be important for sustaining the placental environment, and such measurements have not been made before using MRI.

In placental dysfunction however a number of these features are altered. Blood travelling in the uterine wall was moving at a comparable speed to HP, however upon entry to the placenta I did not observe the same reduction in speed. When comparing the direction of travel of the fastest flowing blood within the placenta the CP had significantly faster flowing blood in all directions, and was fastest perpendicular to the basal plate. This combined with the reduction in incoherent motion of blood in the uterine wall were consistent with improper spiral artery remodelling, causing faster flowing jets of blood to enter the placenta, instead of the long, slow, continuous flow of blood spiral artery remodelling is thought to provide. These faster flows are thought to impair exchange between the maternal and fetal blood pools by causing hypoxia, oxidative stress, inflammation, and the velocity of these flows could damage the villous trees that are anchored to the basal plate as outlined in **Chapter 1**. Through the IVIM model I saw a reduction in the slow self diffusion of water within the placental ROI, which could be indicative of altered exchange between the maternal and fetal blood pools, and while I did not observe any change in f_{IVIM} within the placental ROI of CP I did observe a reduction in medium section motion through use of the ILT, which could indicate changes in placental structure but requires more investigation. As well as faster blood within the placental ROI I also observed faster blood within the chorionc plate of CP, which may indicate increased fetal cardiac response, which could be a response to placental insufficiency.

It has also paved the way for future research, where by observing rebounds in the placental PGSE data I demonstrated that these could be related to the flow within a voxel but require further investigation. If these rebounds are in

fact linked to flow, they could be valuable for understanding the haemodynamics of the placenta, as these flow networks are vital for placental function.

While the PGSE data presented here are likely to depend on the exact PGSE properties, I also showed that by altering the diffusion time Δ of the PGSE gradients it could be possible to better understand IVIM parameters. This could be combined with measures of flow encoding to provide simultaneous flow and diffusion information from a single set of scans, providing more information about both the sub-voxel motion of blood throughout the organ, as well as larger scale flows.

Future work should include investigating the effects of PGSE properties on DWI data, this would not only help in comparisons between different studies but could prove useful for further investigating changes in placental structure through altered f_{IVIM} parameters. This would also be useful for identifying regions of rebounds, which should respond to changes in diffusion time or lobe length which could be a marker of flow in future placental DWI experiments. Future work could also include more analysis of the venous drainage system using measurements such as PCA, or through the use of contrast agents in extracorporeally perfused placentas which could be used to track how blood exits the placenta. This information cannot be achieved by dissection alone, as after delivery these flow networks collapse as the blood drains from the organ making it unclear what path blood would actually take to exit the placenta, making MRI well suited to this task as we can image the interal flow networks within the organ.

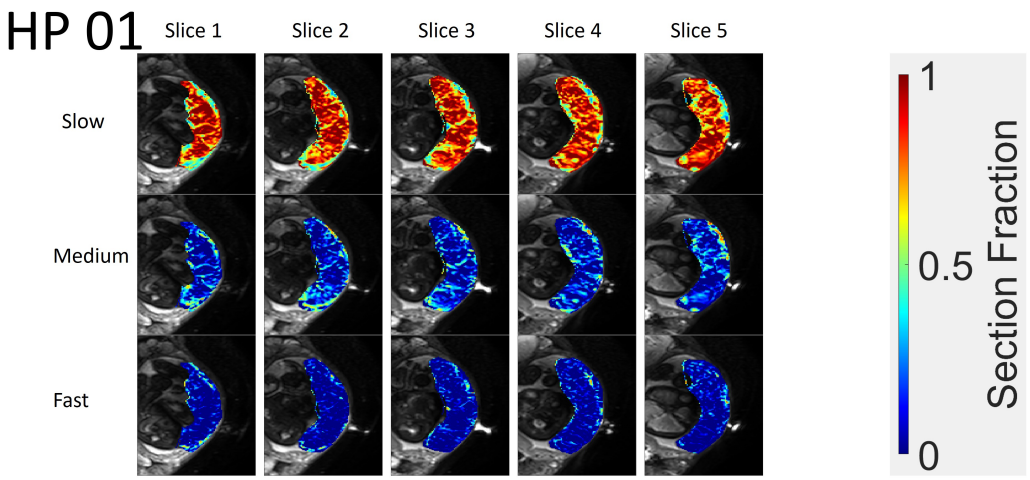
Appendix A

List of Abbreviations

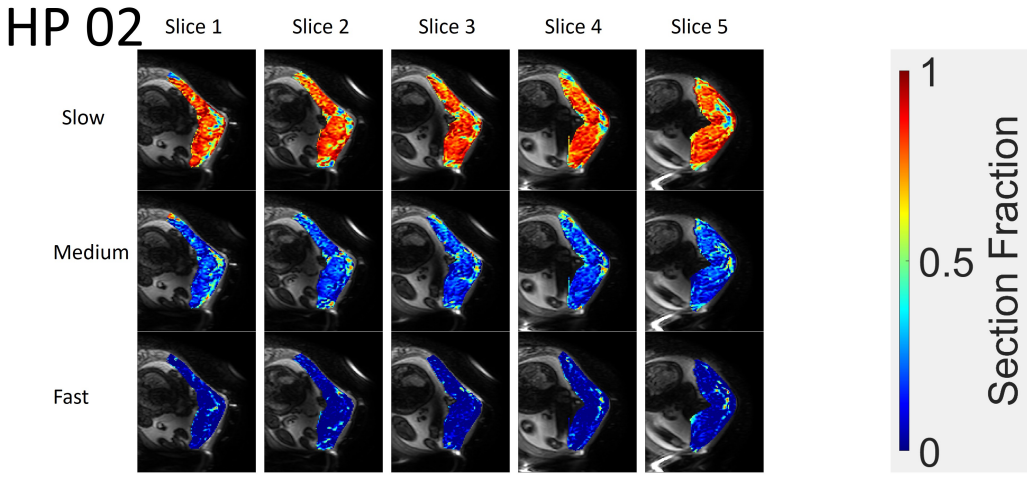
MRI	Magnetic Resonance Imaging
FGR	Fetal Growth Restriction
PE	Pre Eclampsia
IVS	Inter Villous Space
DWI	Diffusion Weighted Imaging
PCA	Phase Contrast Angiography
NMR	Nuclear Magnetic Resonance
EPI	Echo Planar Imaging
SENSE	Sensitivity Encoding
PGSE	Pulse Gradient Spin Echo
IVIM	Intra-Voxel Incoherent Motion
MTT	Mean Transit Time
SGA	Small for Gestational Age
VI	Vascuraisation Index
VFI	Vascular Flow Index
FI	Flow Index
SAR	Specific Absorption Rate
ASL	Arterial Spin Labelling
DCE	Dynamic Contrast Enhancement
HASTE	Half-Fourier Acquisition Single-shot Turbo Spin-Echo
RF	Radio Frequency
ILT	Inverse Laplace Transform
HP	Healthy Placenta
CP	Compromised Placenta
ROI	Region of Interest
GA	Gestational Age
VENC	Velocity Encoding

Appendix B

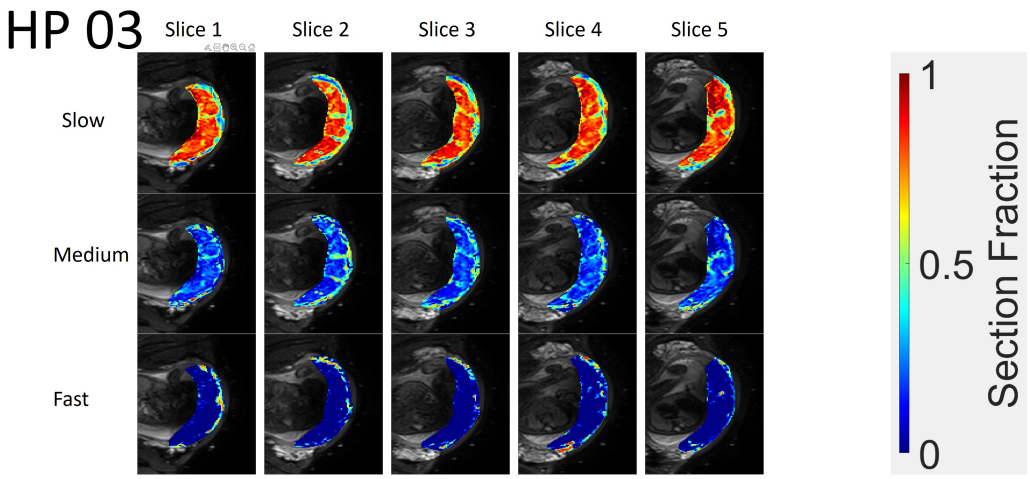
ILT of all participants



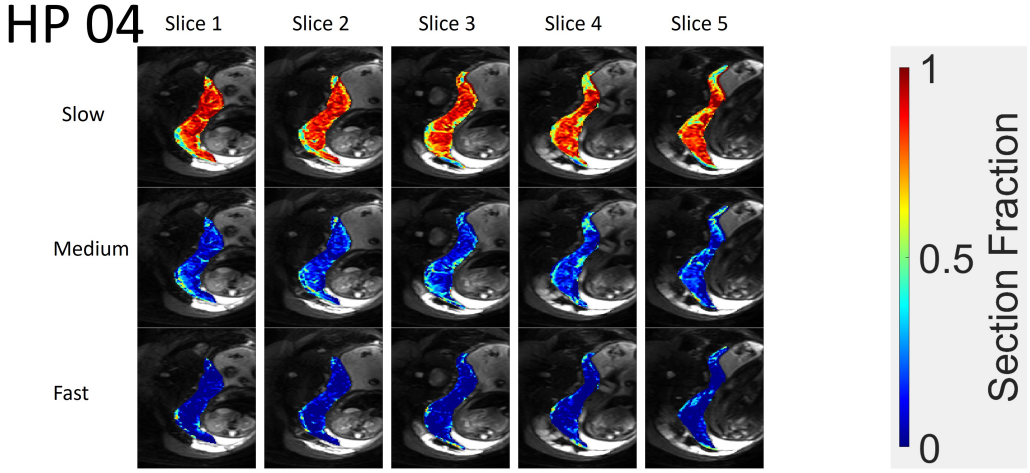
(a)



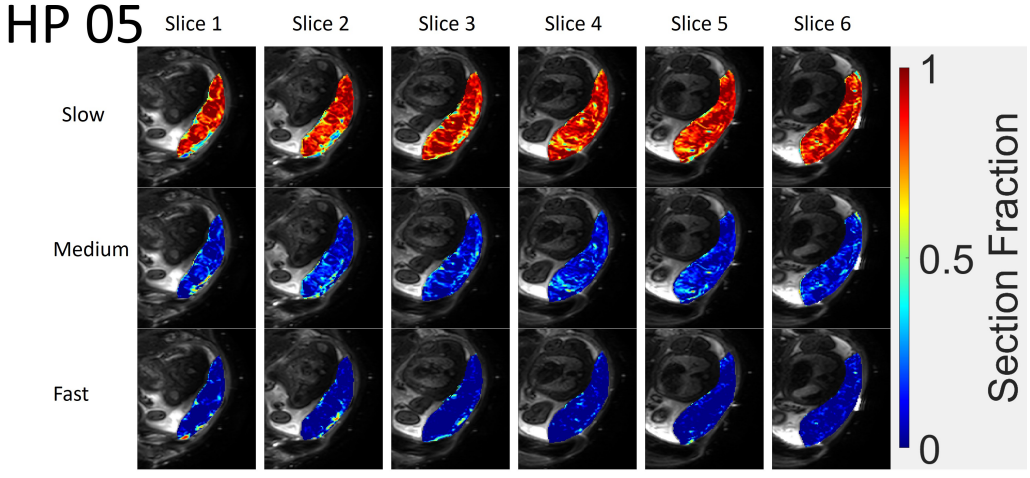
(b)


HP 03
Slice 1
Slice 2
Slice 3
Slice 4
Slice 5
Slow
Medium
Fast
1
0.5
0
Section Fraction

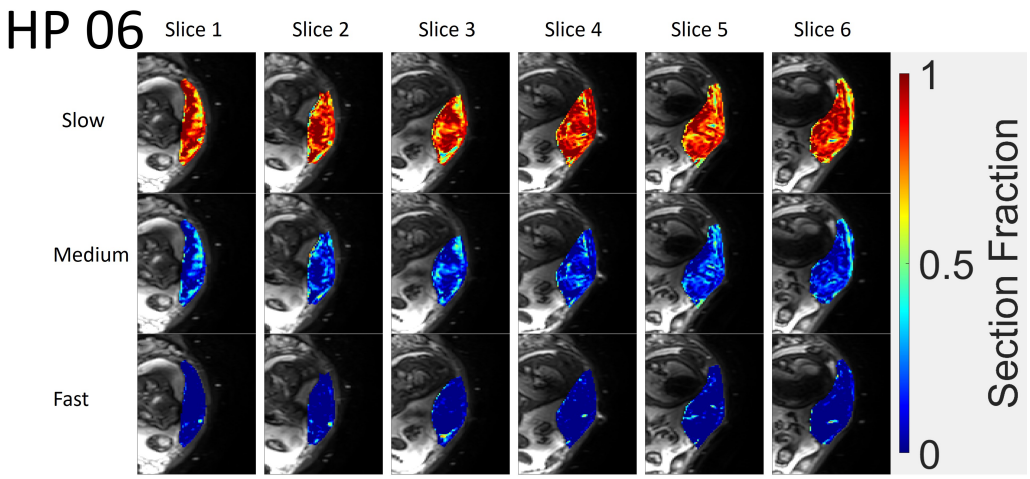
(c)


HP 04
Slice 1
Slice 2
Slice 3
Slice 4
Slice 5
Slow
Medium
Fast
1
0.5
0
Section Fraction

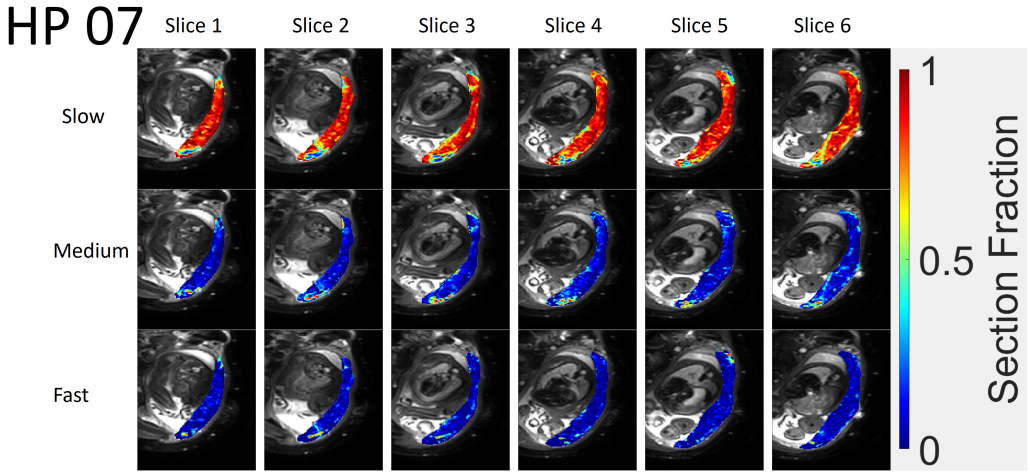
(d)


HP 05
Slice 1
Slice 2
Slice 3
Slice 4
Slice 5
Slice 6
Slow
Medium
Fast
1
0.5
0
Section Fraction

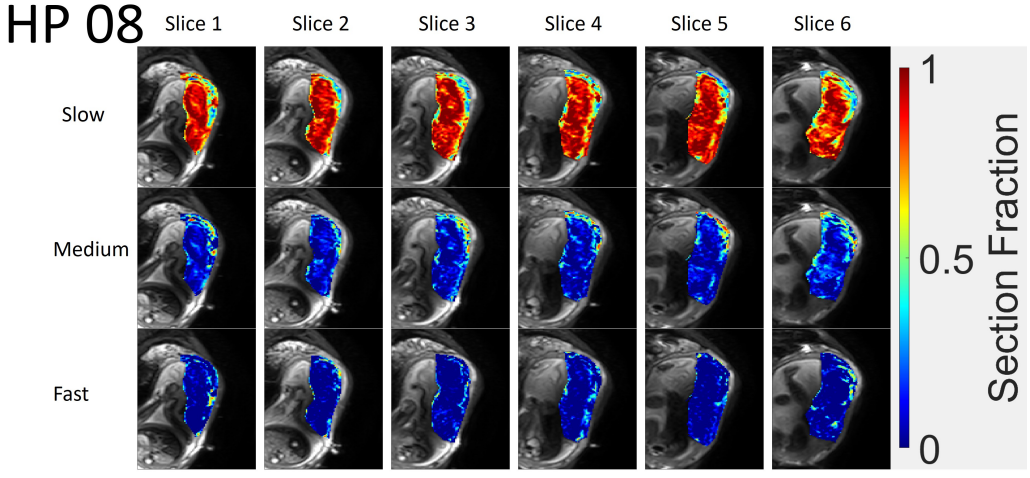
(e)


HP 06
Slice 1
Slice 2
Slice 3
Slice 4
Slice 5
Slice 6
Slow
Medium
Fast
1
0.5
0
Section Fraction

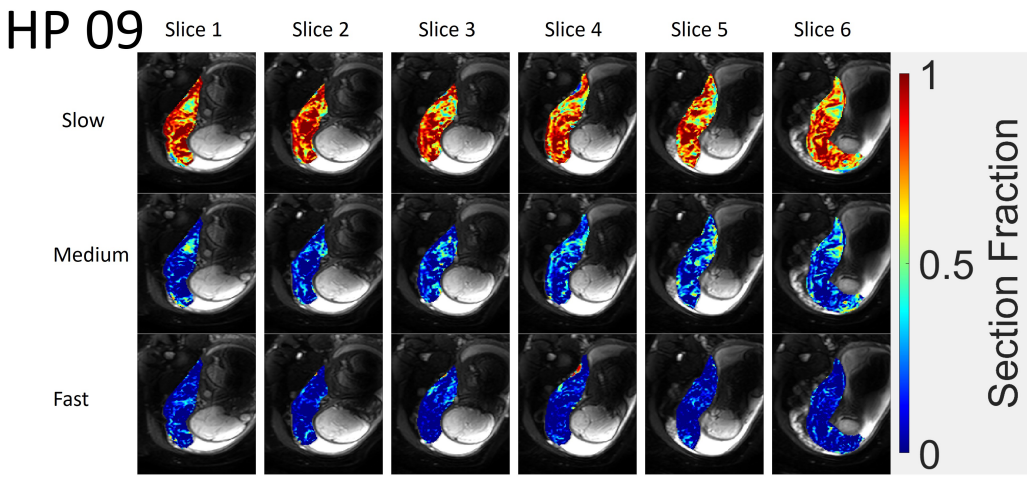
(f)


HP 07
Slice 1
Slice 2
Slice 3
Slice 4
Slice 5
Slice 6
Slow
Medium
Fast
1
0.5
0
Section Fraction

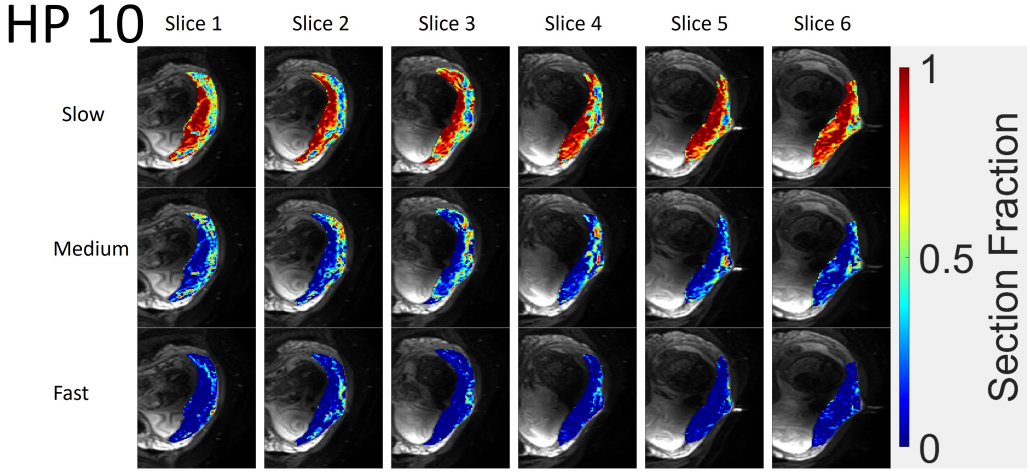
(g)


HP 08
Slice 1
Slice 2
Slice 3
Slice 4
Slice 5
Slice 6
Slow
Medium
Fast
1
0.5
0
Section Fraction

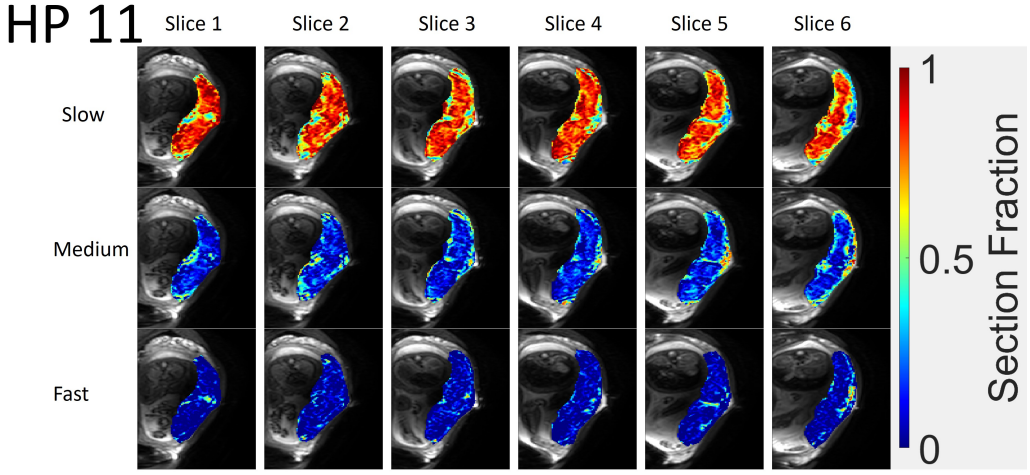
(h)


HP 09
Slice 1
Slice 2
Slice 3
Slice 4
Slice 5
Slice 6
Slow
Medium
Fast
1
0.5
0
Section Fraction

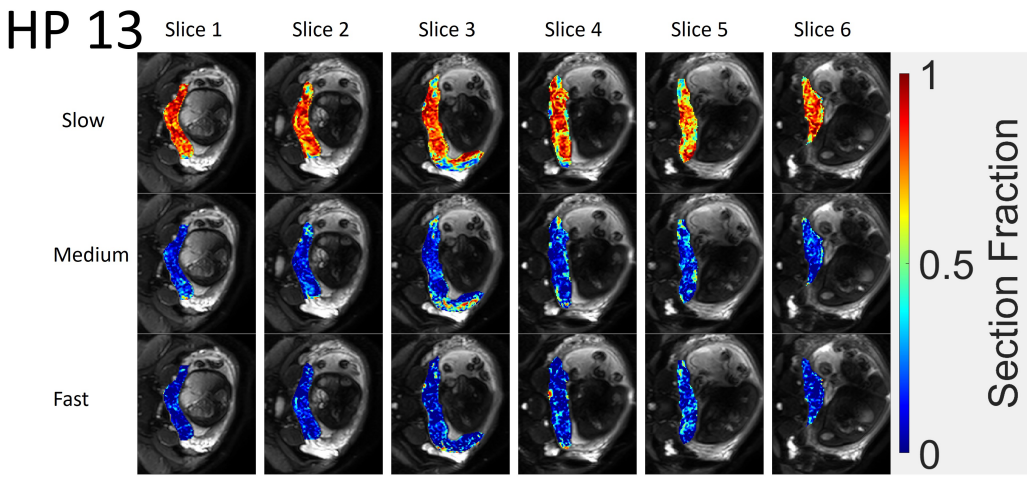
(i)


HP 10
Slice 1
Slice 2
Slice 3
Slice 4
Slice 5
Slice 6
Slow
Medium
Fast
1
0.5
0
Section Fraction

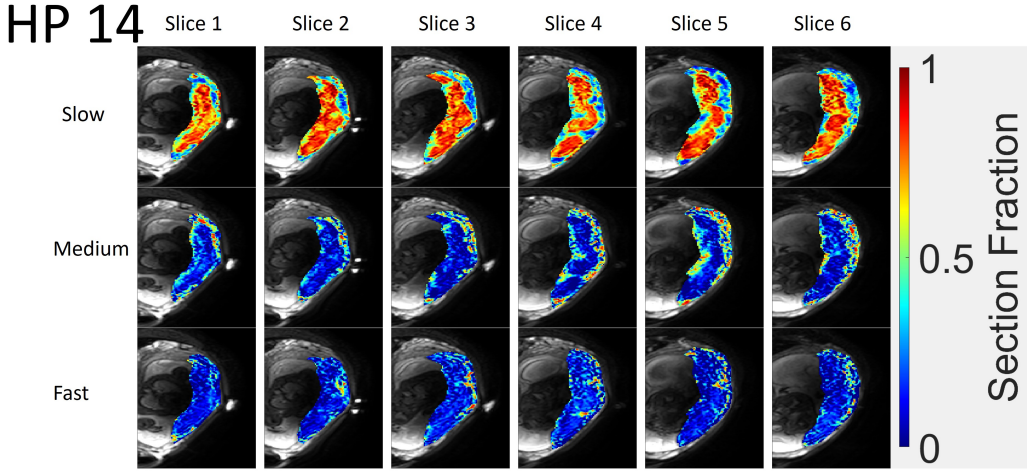
(j)


HP 11
Slice 1
Slice 2
Slice 3
Slice 4
Slice 5
Slice 6
Slow
Medium
Fast
1
0.5
0
Section Fraction

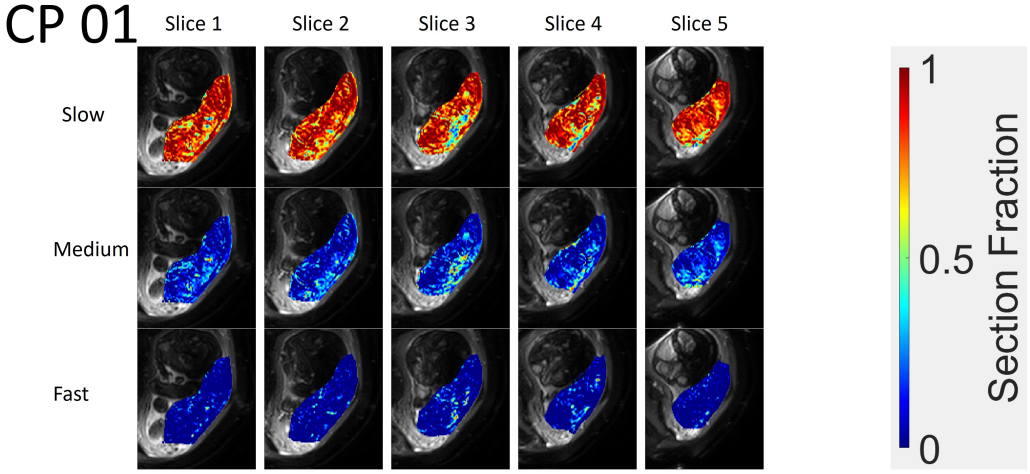
(k)


HP 13
Slice 1
Slice 2
Slice 3
Slice 4
Slice 5
Slice 6
Slow
Medium
Fast
1
0.5
0
Section Fraction

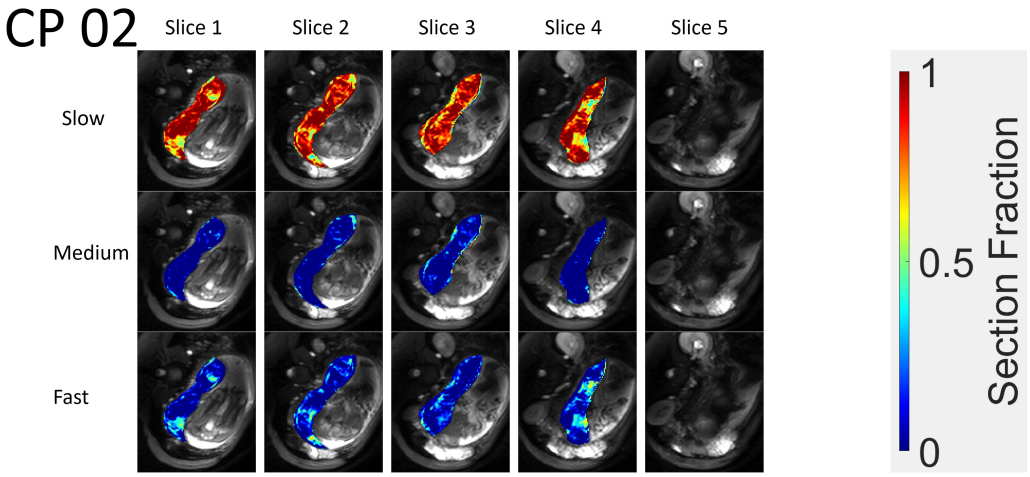
(l)


HP 14
Slice 1
Slice 2
Slice 3
Slice 4
Slice 5
Slice 6
Slow
Medium
Fast
1
0.5
0
Section Fraction

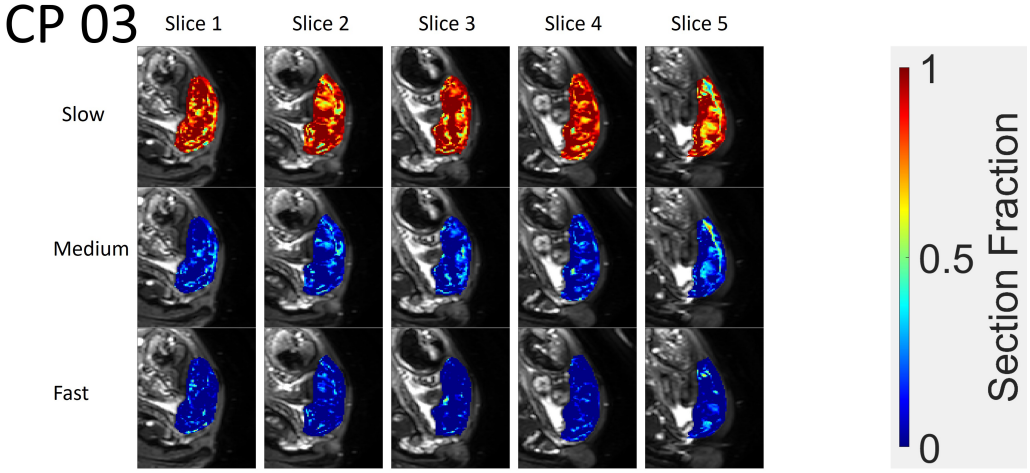
(m)


CP 01
Slice 1
Slice 2
Slice 3
Slice 4
Slice 5
Slow
Medium
Fast
1
0.5
0
Section Fraction

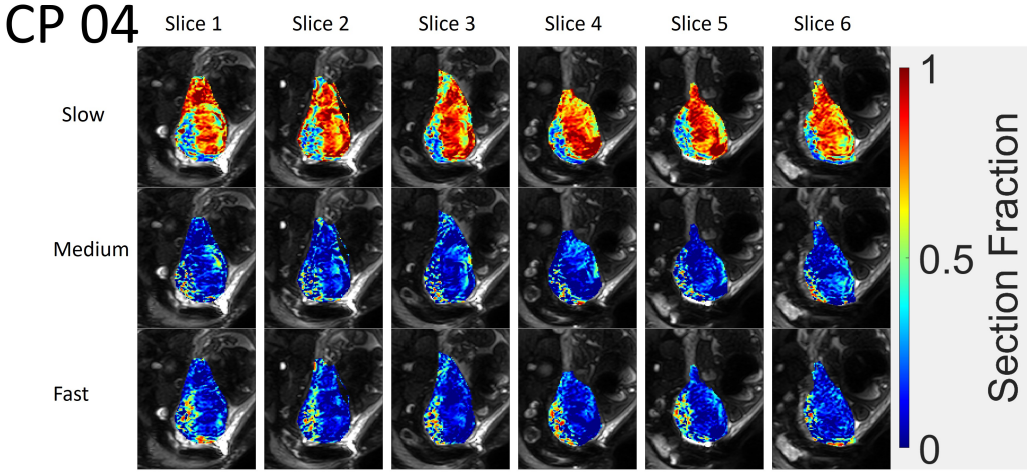
(n)


CP 02
Slice 1
Slice 2
Slice 3
Slice 4
Slice 5
Slow
Medium
Fast
1
0.5
0
Section Fraction

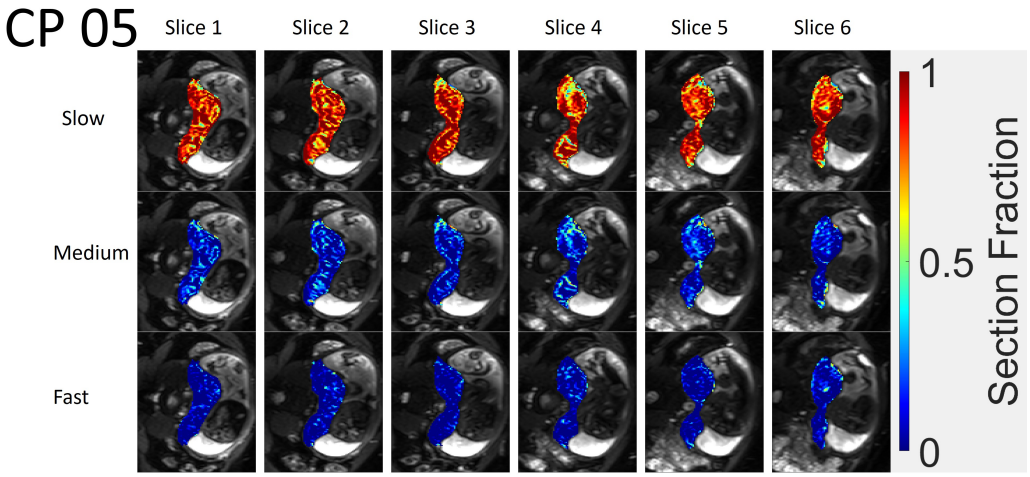
(o)


CP 03
Slice 1
Slice 2
Slice 3
Slice 4
Slice 5
Slow
Medium
Fast
1
0.5
0
Section Fraction

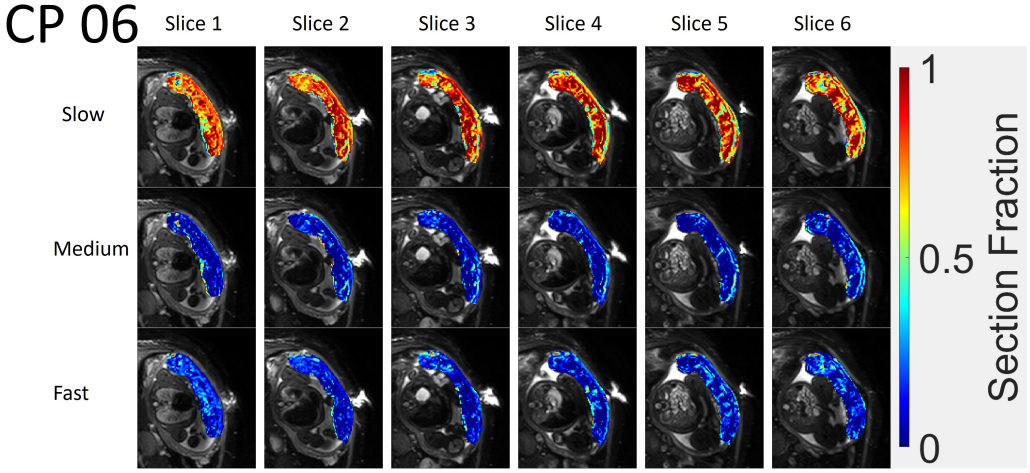
(p)


CP 04
Slice 1
Slice 2
Slice 3
Slice 4
Slice 5
Slice 6
Slow
Medium
Fast
1
0.5
0
Section Fraction

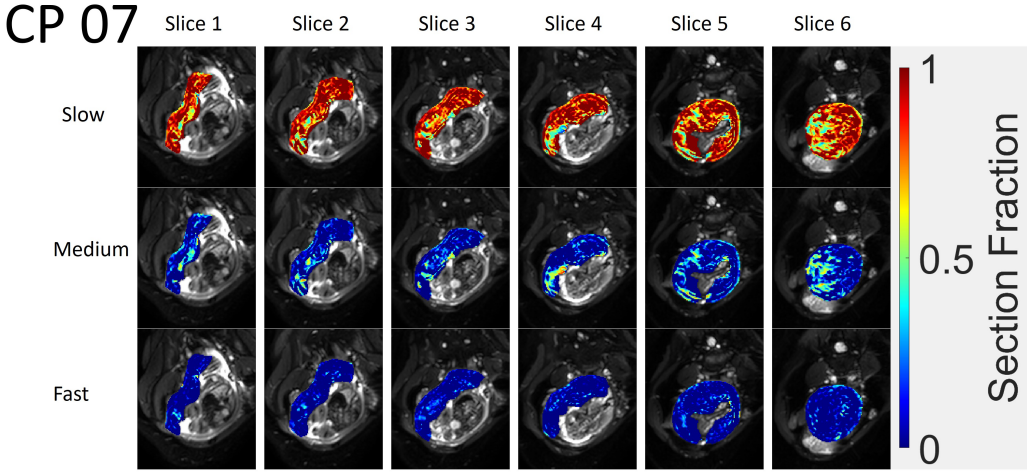
(q)


CP 05
Slice 1
Slice 2
Slice 3
Slice 4
Slice 5
Slice 6
Slow
Medium
Fast
1
0.5
0
Section Fraction

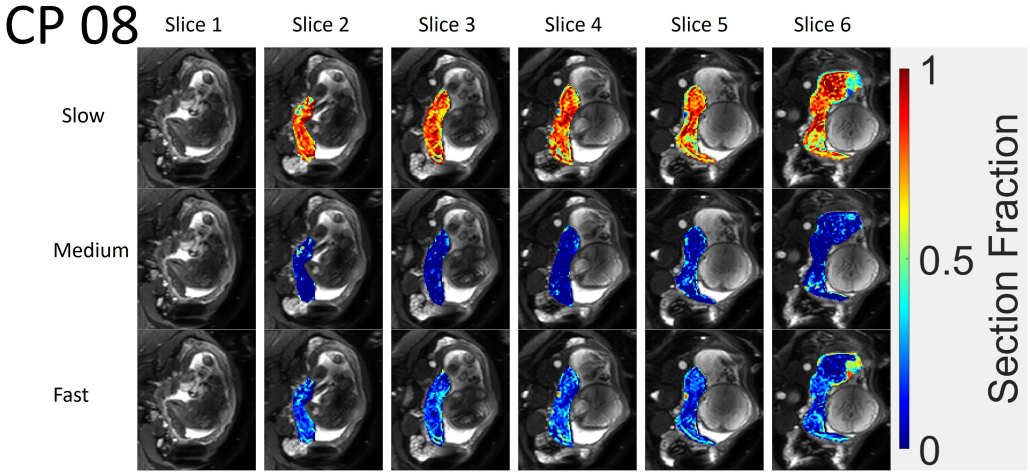
(r)


CP 06
Slice 1
Slice 2
Slice 3
Slice 4
Slice 5
Slice 6
Slow
Medium
Fast
1
0.5
0
Section Fraction

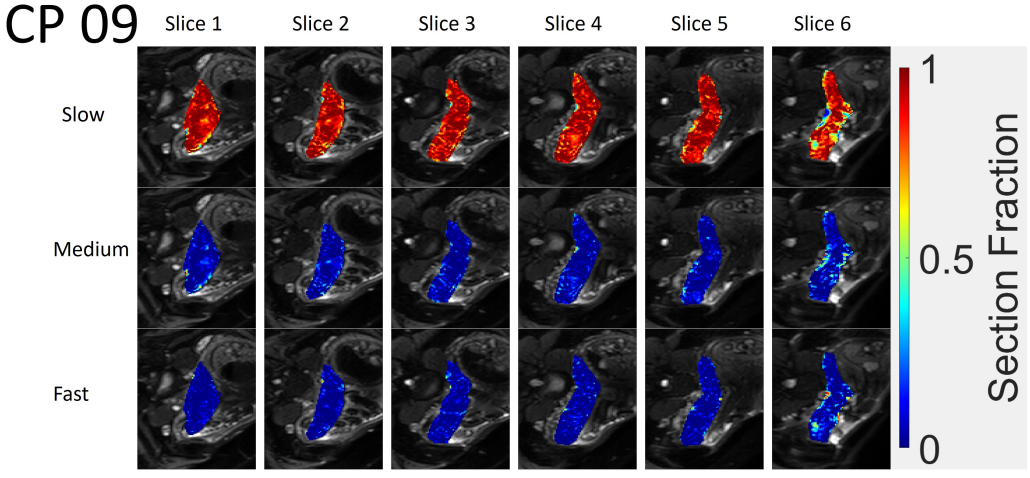
(s)


CP 07
Slice 1
Slice 2
Slice 3
Slice 4
Slice 5
Slice 6
Slow
Medium
Fast
1
0.5
0
Section Fraction

(t)


CP 08
Slice 1
Slice 2
Slice 3
Slice 4
Slice 5
Slice 6
Slow
Medium
Fast
1
0.5
0
Section Fraction

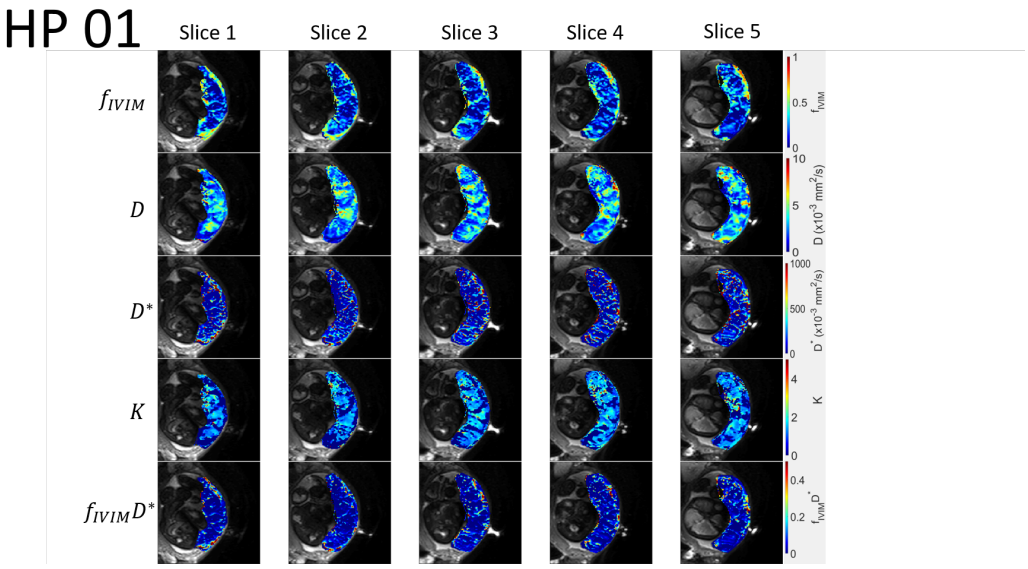
(u)


CP 09
Slice 1
Slice 2
Slice 3
Slice 4
Slice 5
Slice 6
Slow
Medium
Fast
1
0.5
0
Section Fraction

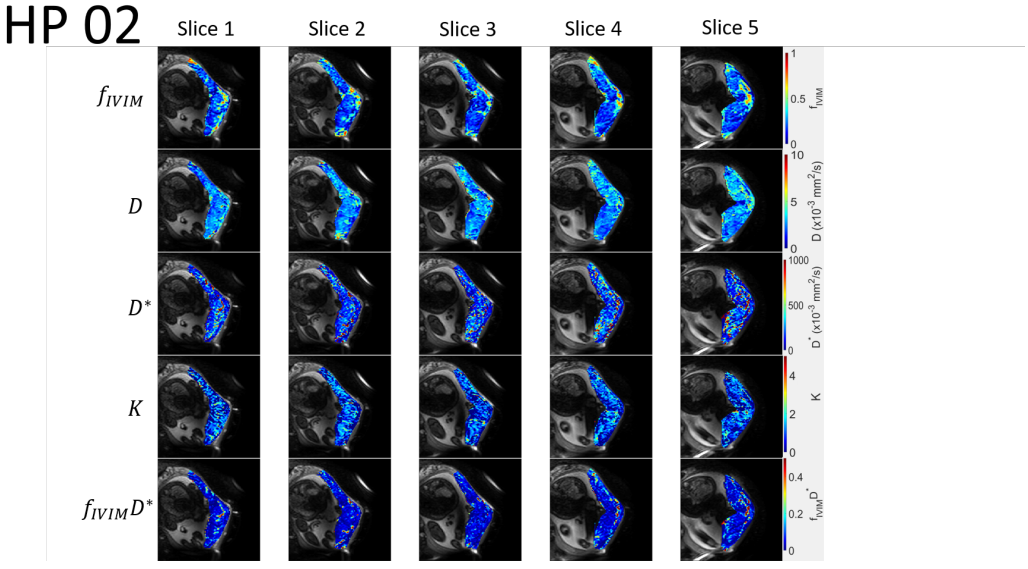
(v)

Appendix C

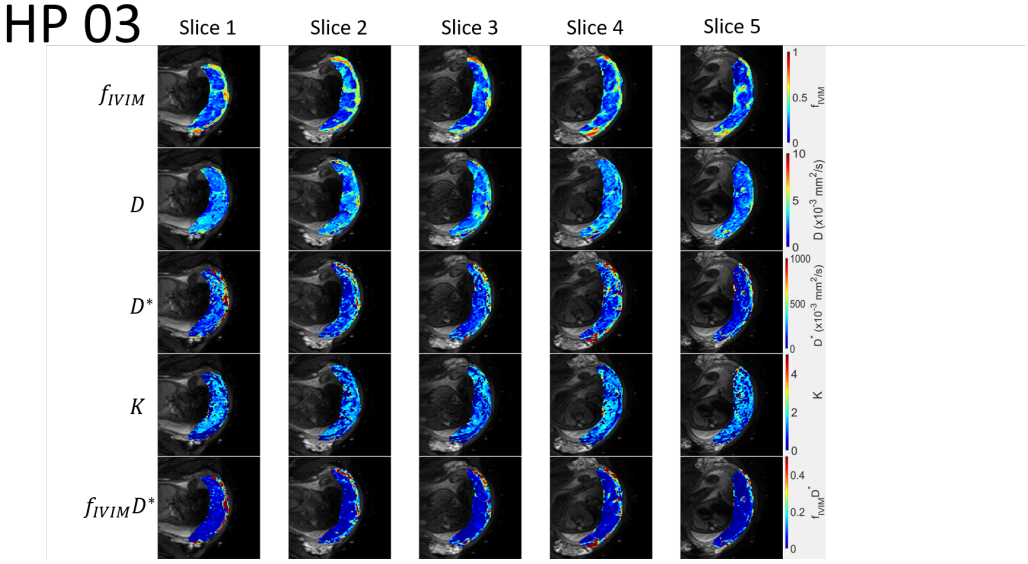
IVIM maps of all participants



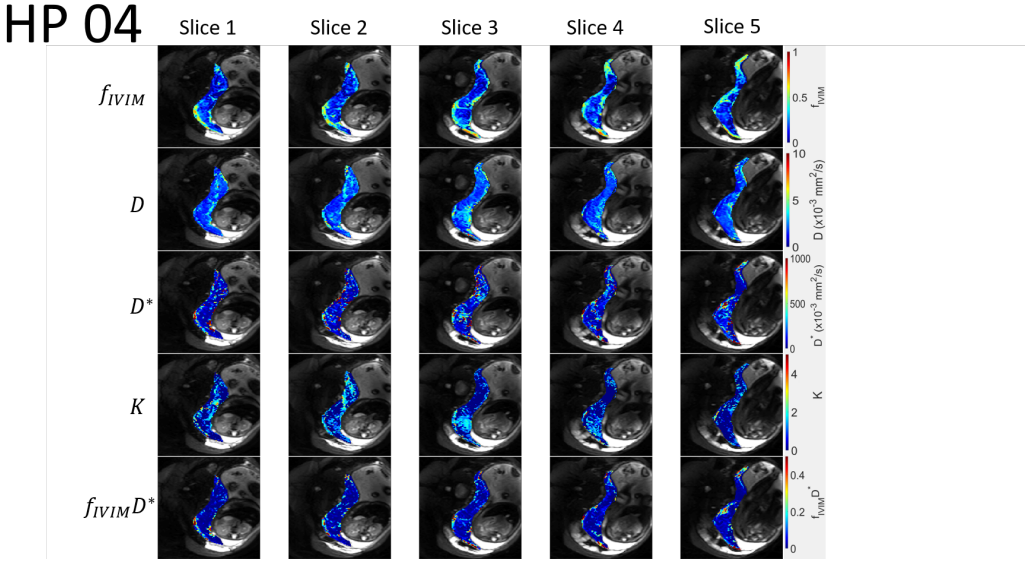
(a)



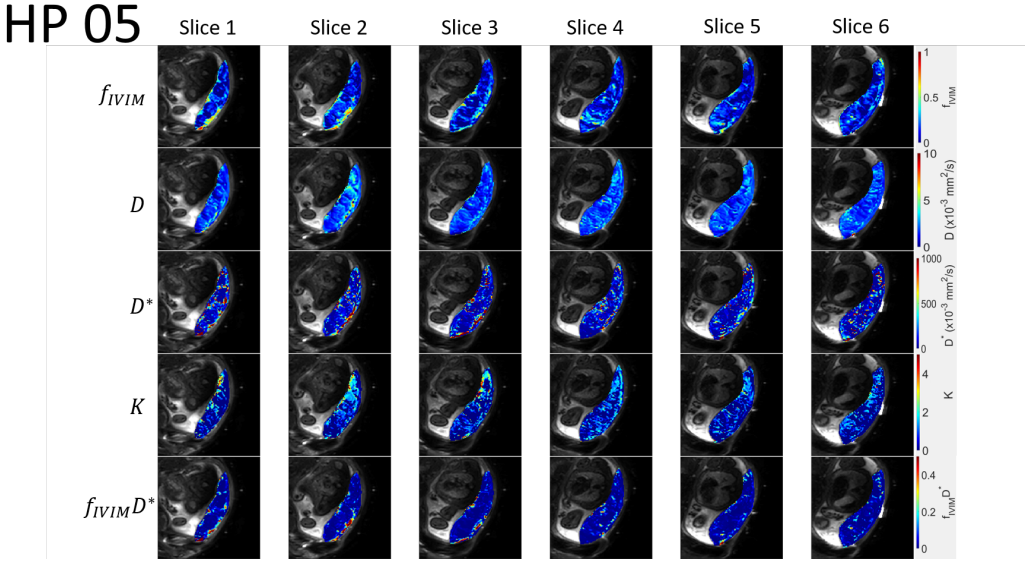
(b)


HP 03
Slice 1
Slice 2
Slice 3
Slice 4
Slice 5
f_{IVIM}
D
D^*
K
$f_{IVIM}D^*$

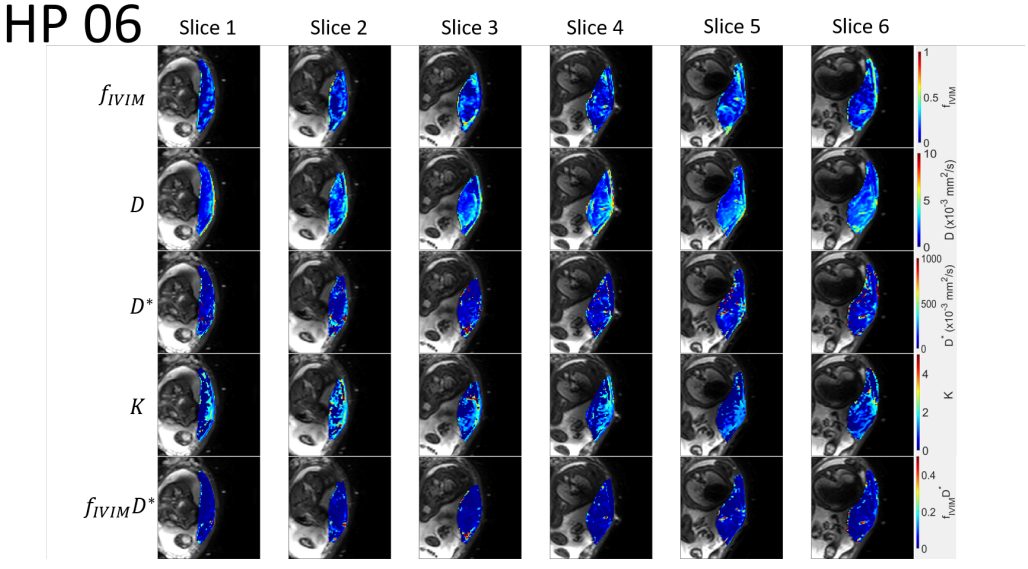
(c)


HP 04
Slice 1
Slice 2
Slice 3
Slice 4
Slice 5
f_{IVIM}
D
D^*
K
$f_{IVIM}D^*$

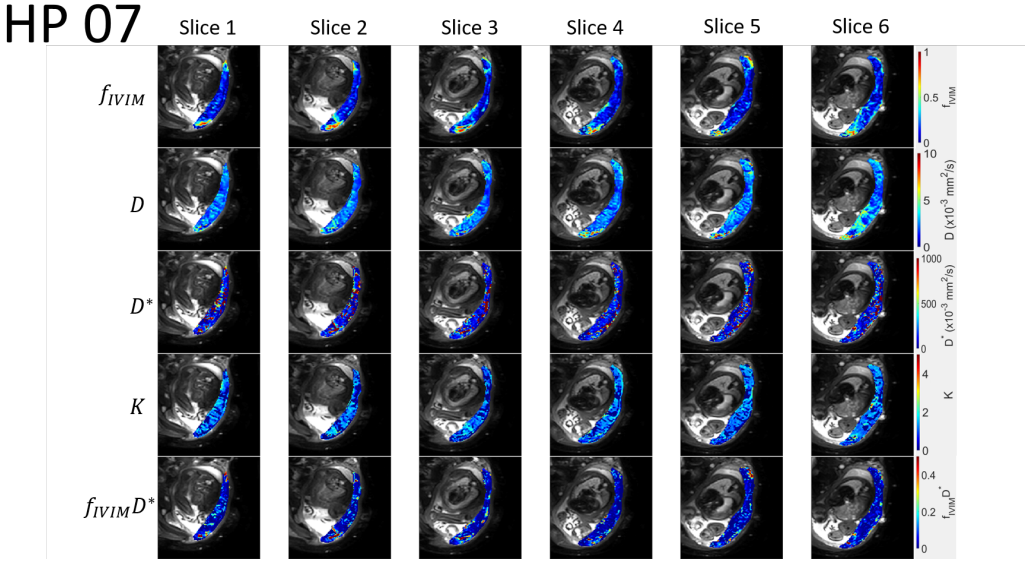
(d)


HP 05
Slice 1
Slice 2
Slice 3
Slice 4
Slice 5
Slice 6
f_{IVIM}
D
D^*
K
$f_{IVIM}D^*$

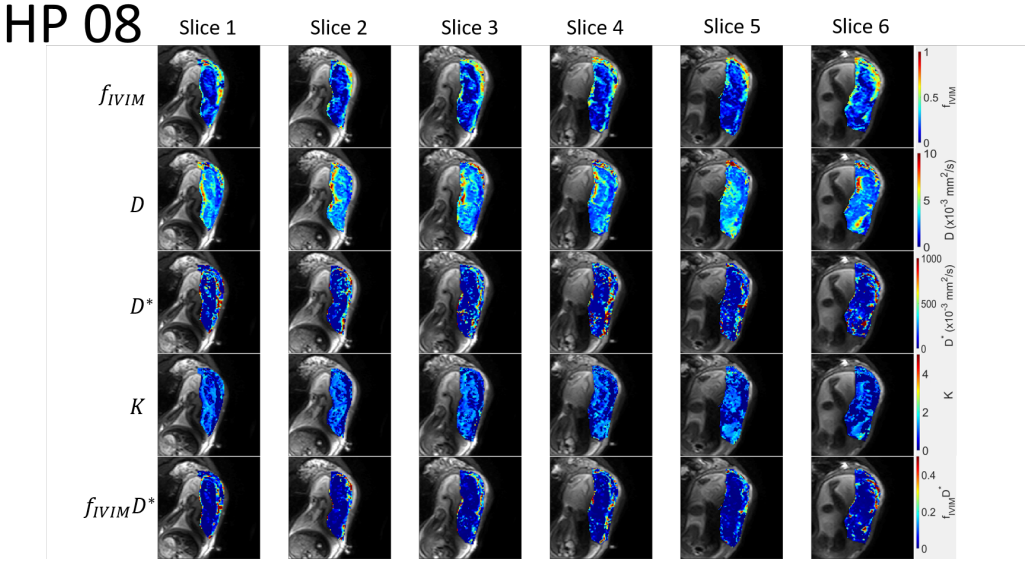
(e)


HP 06
Slice 1
Slice 2
Slice 3
Slice 4
Slice 5
Slice 6
f_{IVIM}
D
D^*
K
$f_{IVIM}D^*$

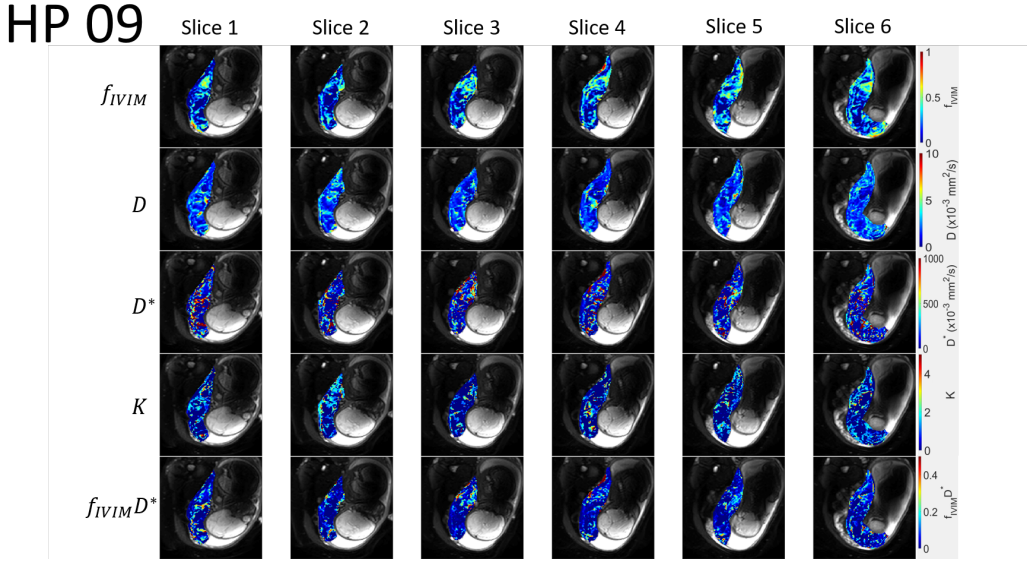
(f)


HP 07
Slice 1
Slice 2
Slice 3
Slice 4
Slice 5
Slice 6
f_{IVIM}
D
D^*
K
$f_{IVIM}D^*$

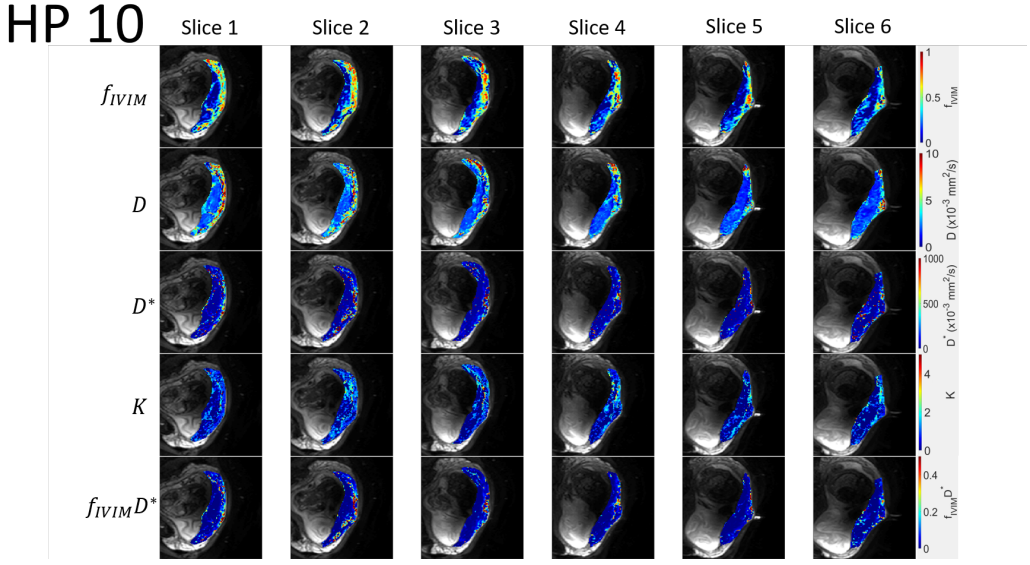
(g)


HP 08
Slice 1
Slice 2
Slice 3
Slice 4
Slice 5
Slice 6
f_{IVIM}
D
D^*
K
$f_{IVIM}D^*$

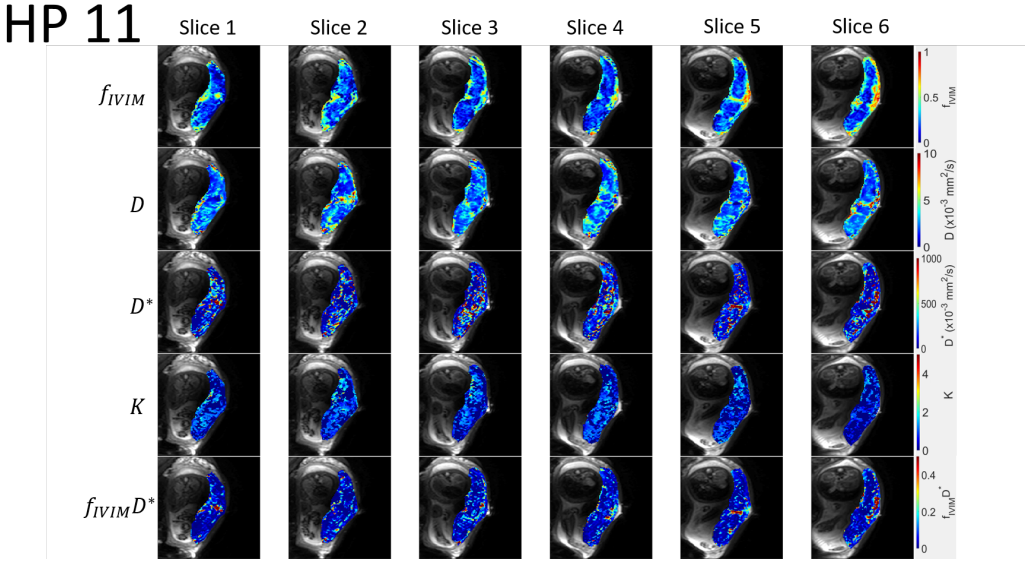
(h)


HP 09
Slice 1
Slice 2
Slice 3
Slice 4
Slice 5
Slice 6
f_{IVIM}
D
D^*
K
$f_{IVIM}D^*$

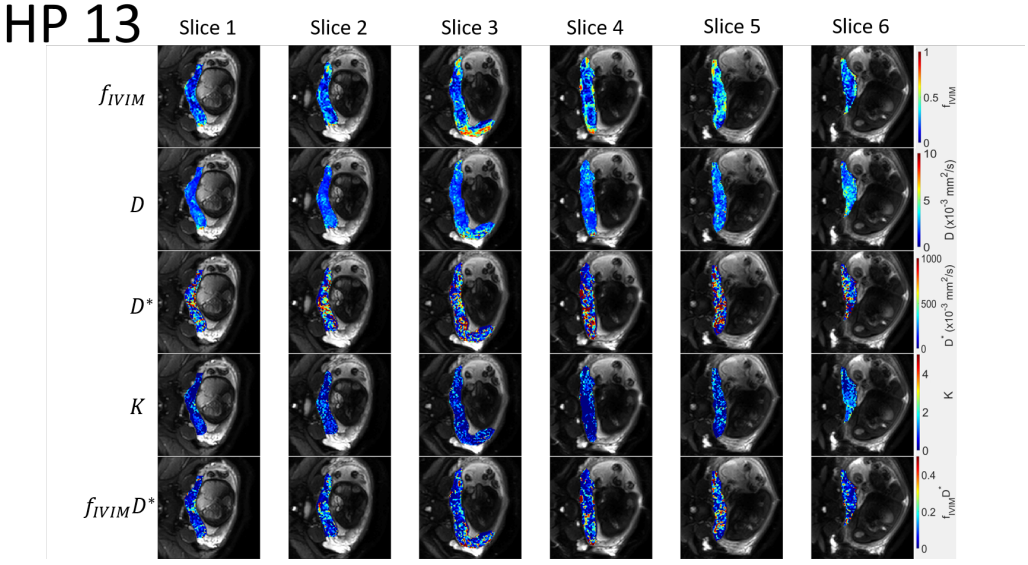
(i)


HP 10
Slice 1
Slice 2
Slice 3
Slice 4
Slice 5
Slice 6
f_{IVIM}
D
D^*
K
$f_{IVIM}D^*$

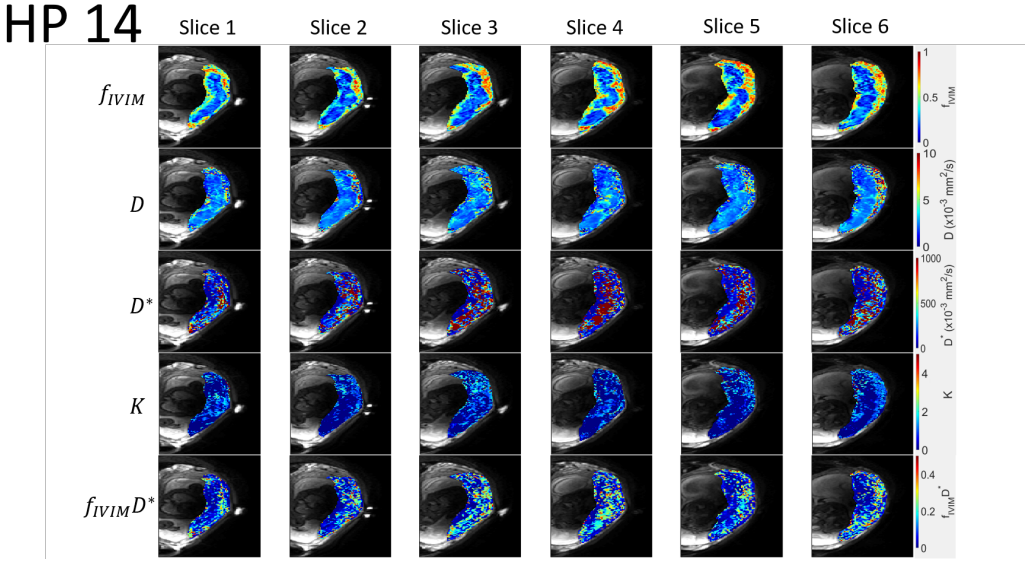
(j)


HP 11
Slice 1
Slice 2
Slice 3
Slice 4
Slice 5
Slice 6
f_{IVIM}
D
D^*
K
$f_{IVIM}D^*$

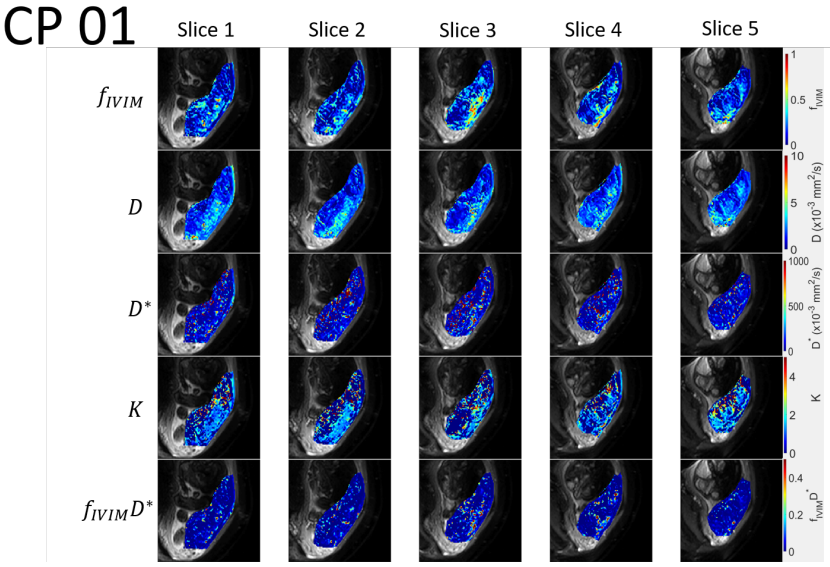
(k)


HP 13
Slice 1
Slice 2
Slice 3
Slice 4
Slice 5
Slice 6
f_{IVIM}
D
D^*
K
$f_{IVIM}D^*$

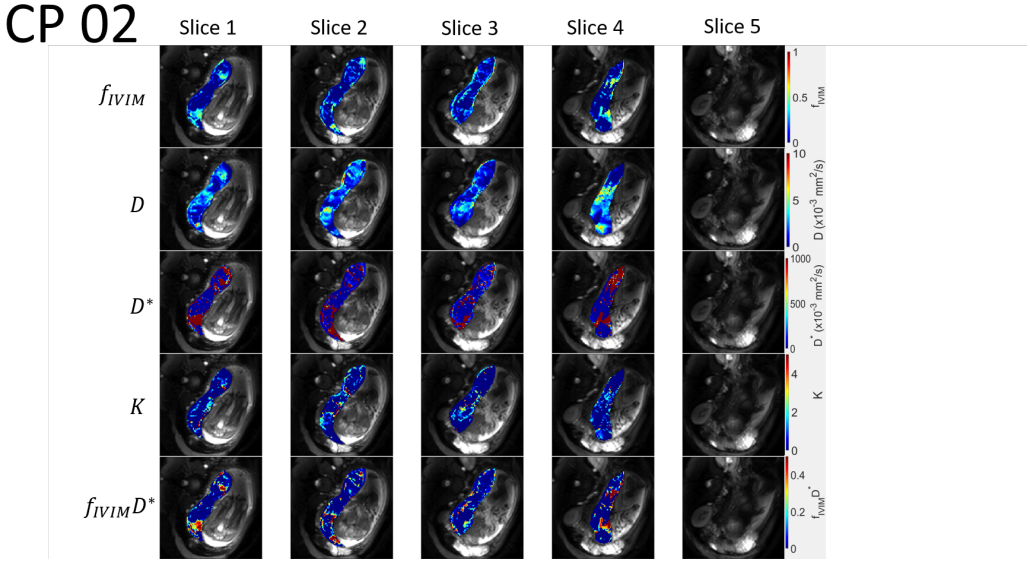
(l)


HP 14
Slice 1
Slice 2
Slice 3
Slice 4
Slice 5
Slice 6
f_{IVIM}
D
D^*
K
$f_{IVIM}D^*$

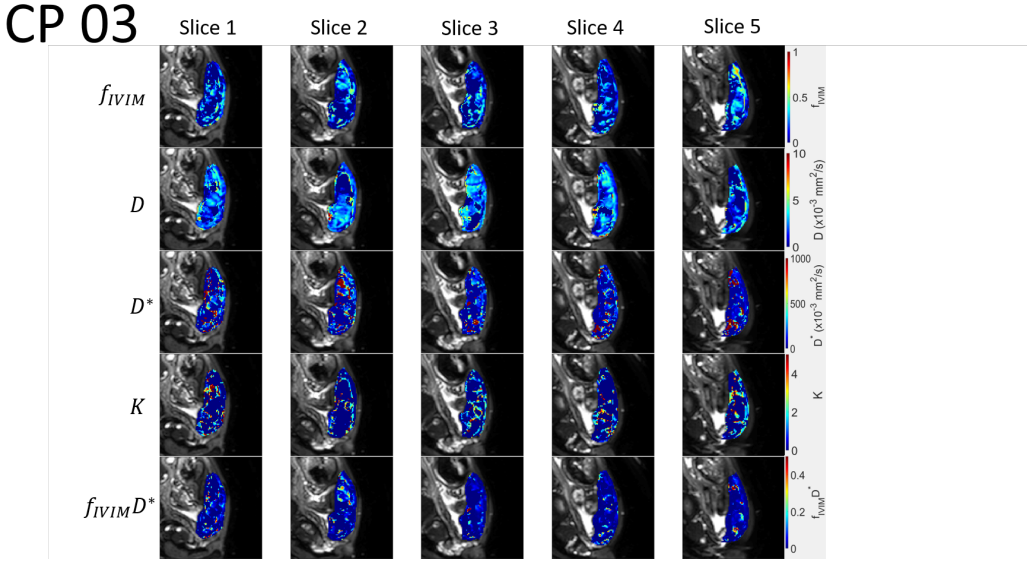
(m)


CP 01
Slice 1
Slice 2
Slice 3
Slice 4
Slice 5
f_{IVIM}
D
D^*
K
$f_{IVIM}D^*$

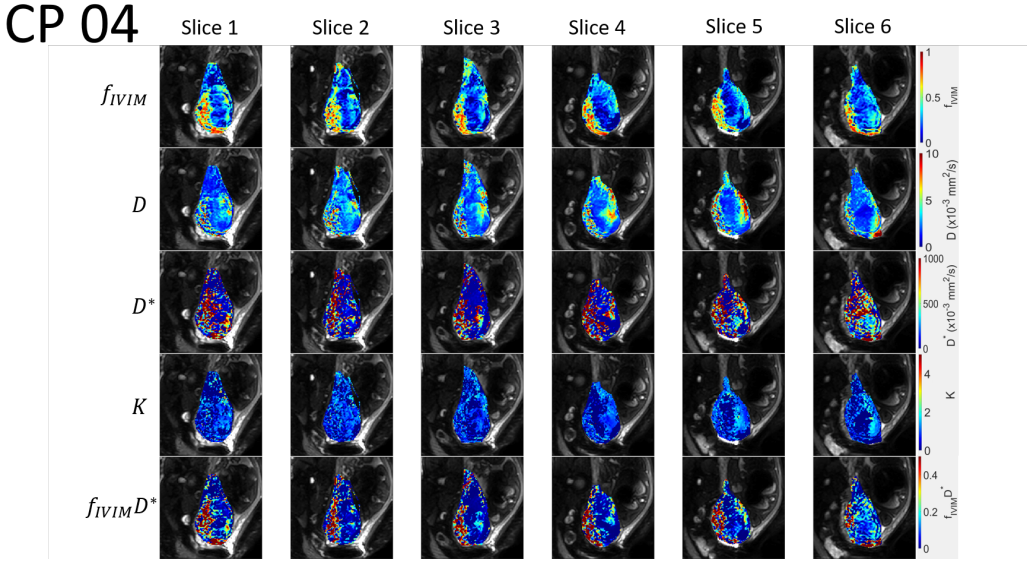
(n)


CP 02
Slice 1
Slice 2
Slice 3
Slice 4
Slice 5
f_{IVIM}
D
D^*
K
$f_{IVIM}D^*$

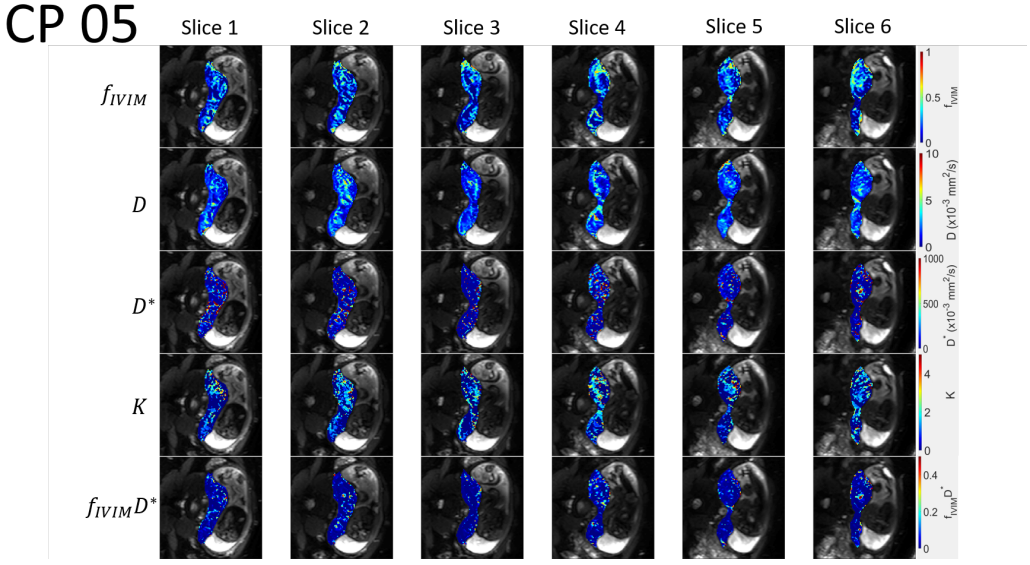
(o)


CP 03
Slice 1
Slice 2
Slice 3
Slice 4
Slice 5
f_{IVIM}
D
D^*
K
$f_{IVIM}D^*$

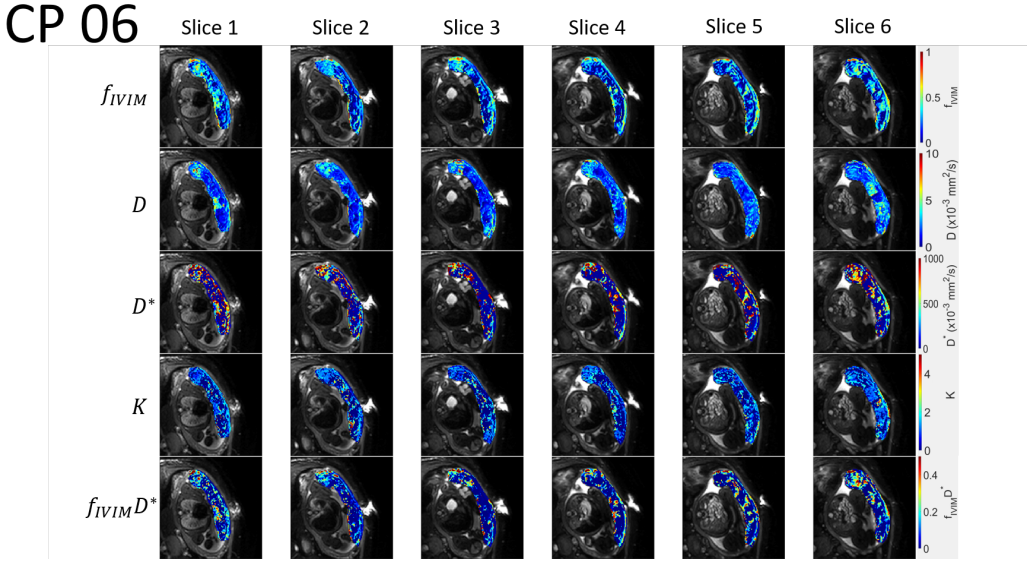
(p)


CP 04
Slice 1
Slice 2
Slice 3
Slice 4
Slice 5
Slice 6
f_{IVIM}
D
D^*
K
$f_{IVIM}D^*$

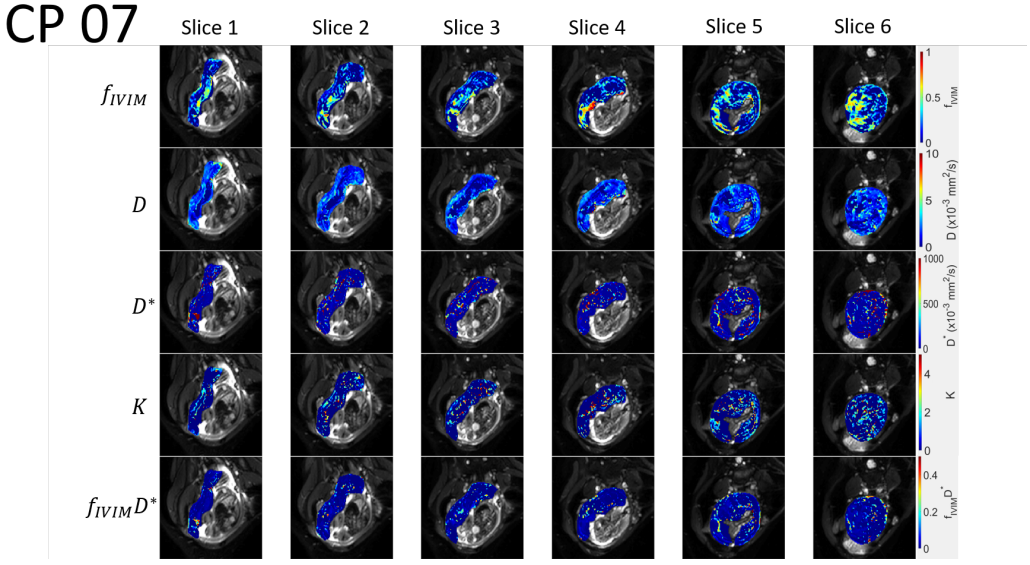
(q)


CP 05
Slice 1
Slice 2
Slice 3
Slice 4
Slice 5
Slice 6
f_{IVIM}
D
D^*
K
$f_{IVIM}D^*$

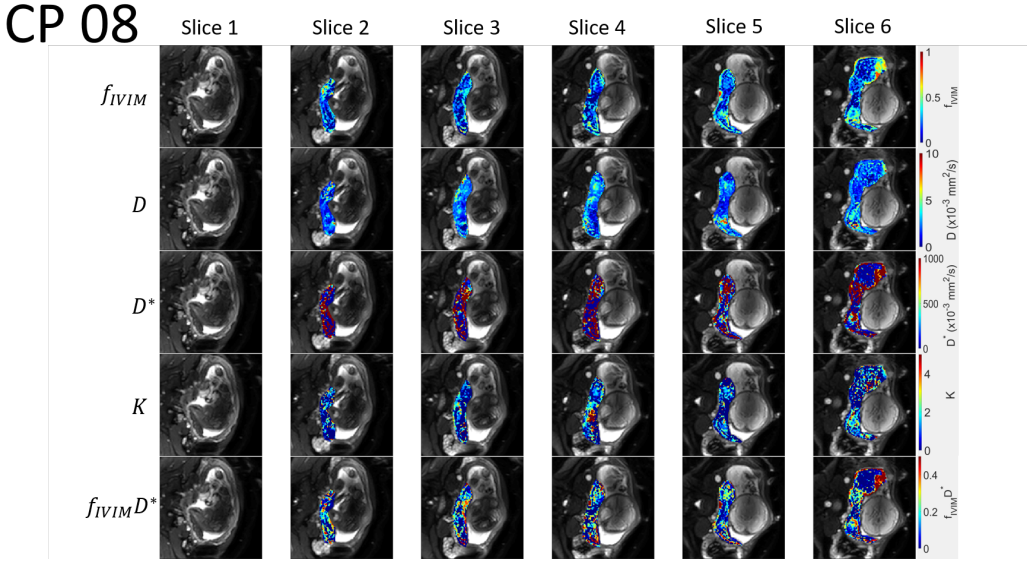
(r)


CP 06
Slice 1
Slice 2
Slice 3
Slice 4
Slice 5
Slice 6
f_{IVIM}
D
D^*
K
$f_{IVIM}D^*$

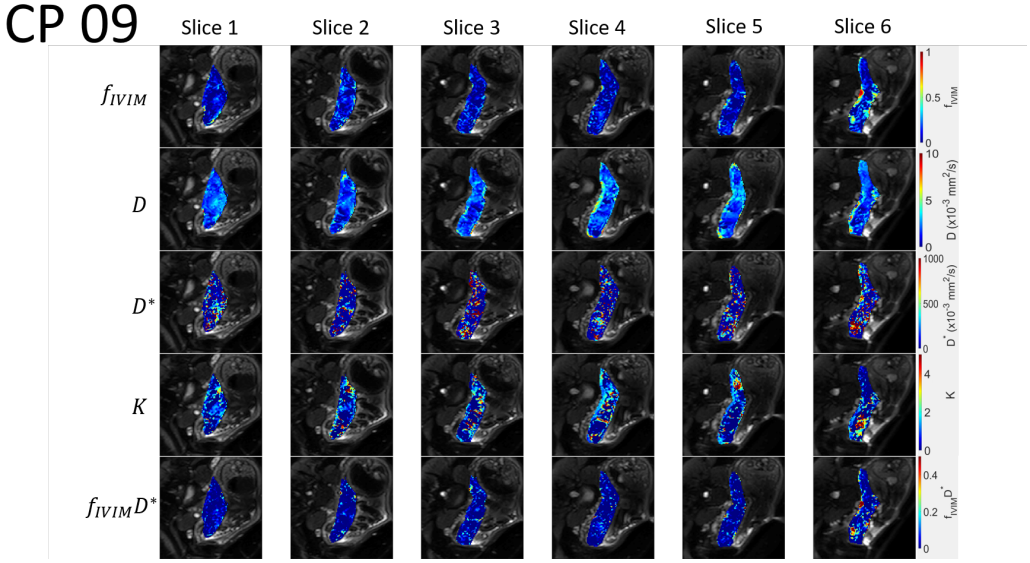
(s)


CP 07
Slice 1
Slice 2
Slice 3
Slice 4
Slice 5
Slice 6
f_{IVIM}
D
D^*
K
$f_{IVIM}D^*$

(t)


CP 08
Slice 1
Slice 2
Slice 3
Slice 4
Slice 5
Slice 6
f_{IVIM}
D
D^*
K
$f_{IVIM}D^*$

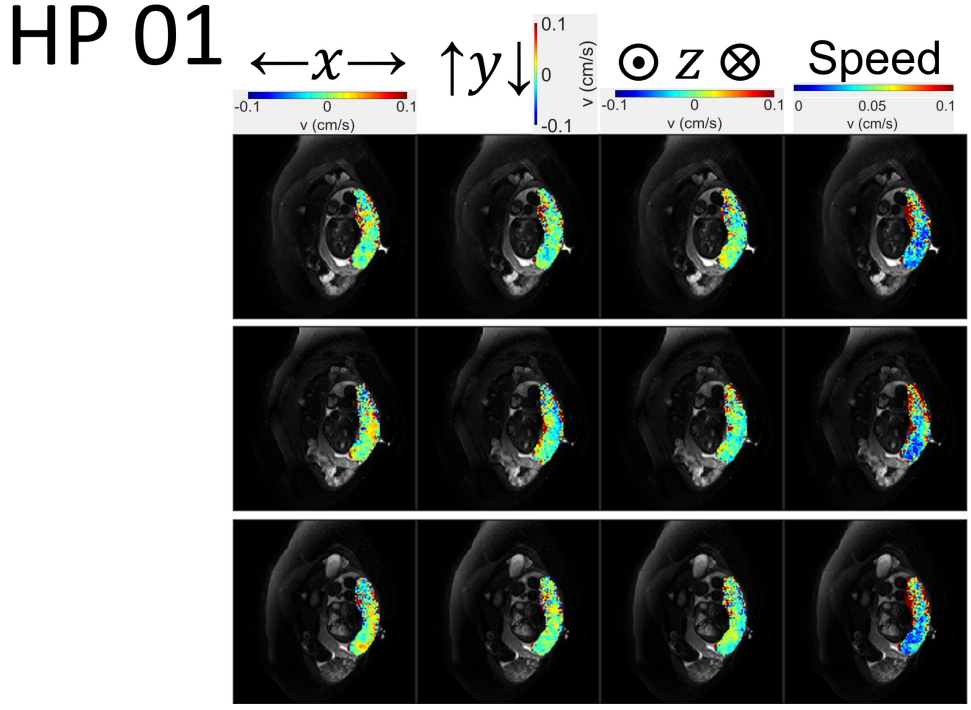
(u)


CP 09
Slice 1
Slice 2
Slice 3
Slice 4
Slice 5
Slice 6
f_{IVIM}
D
D^*
K
$f_{IVIM}D^*$

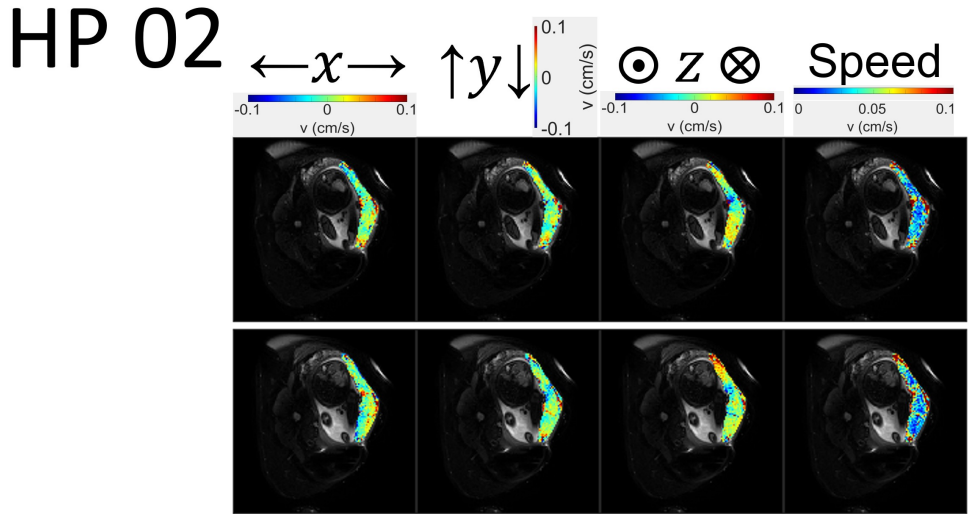
(v)

Appendix D

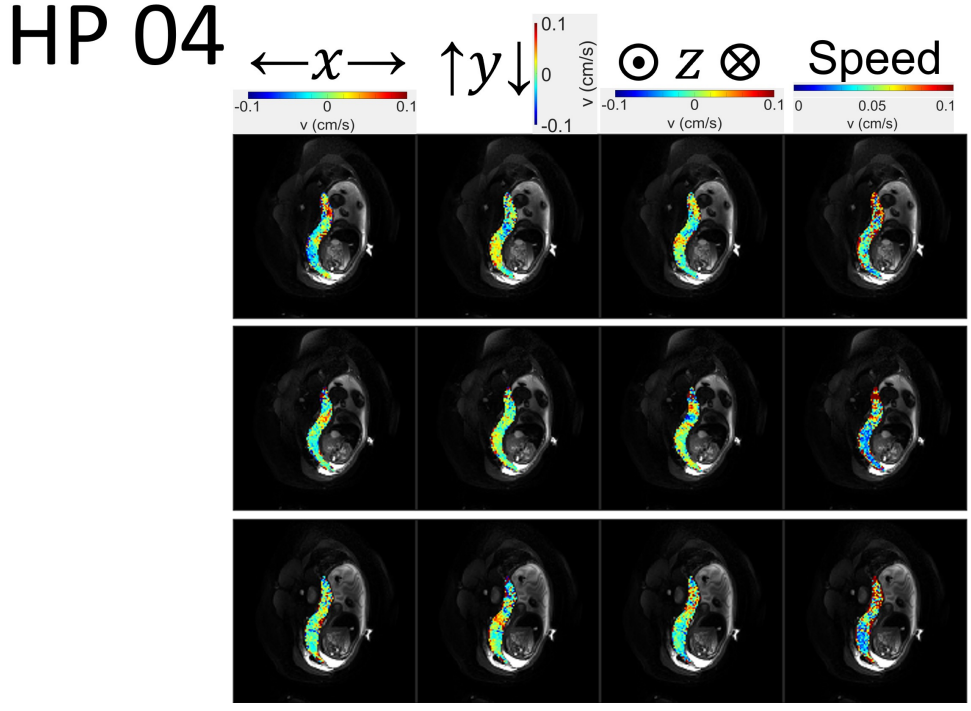
PCA results from all participants



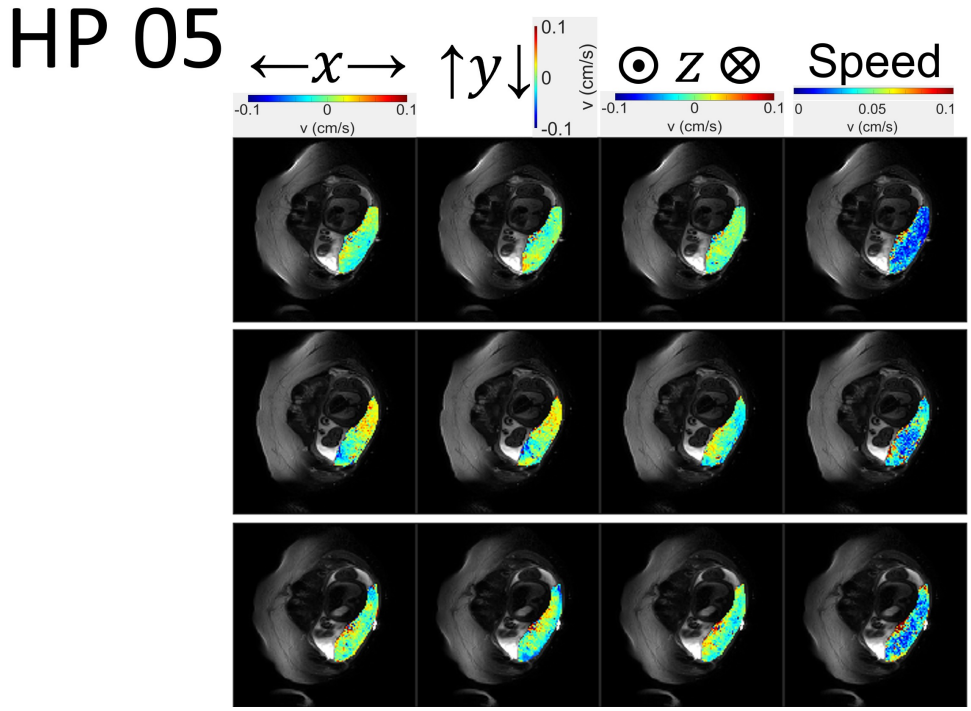
(a)


HP 02
←x→
↑y↓
⊙ z ⊗
Speed
-0.1
0
0.1
v (cm/s)
0.1
0
-0.1
v (cm/s)
0
0.05
0.1

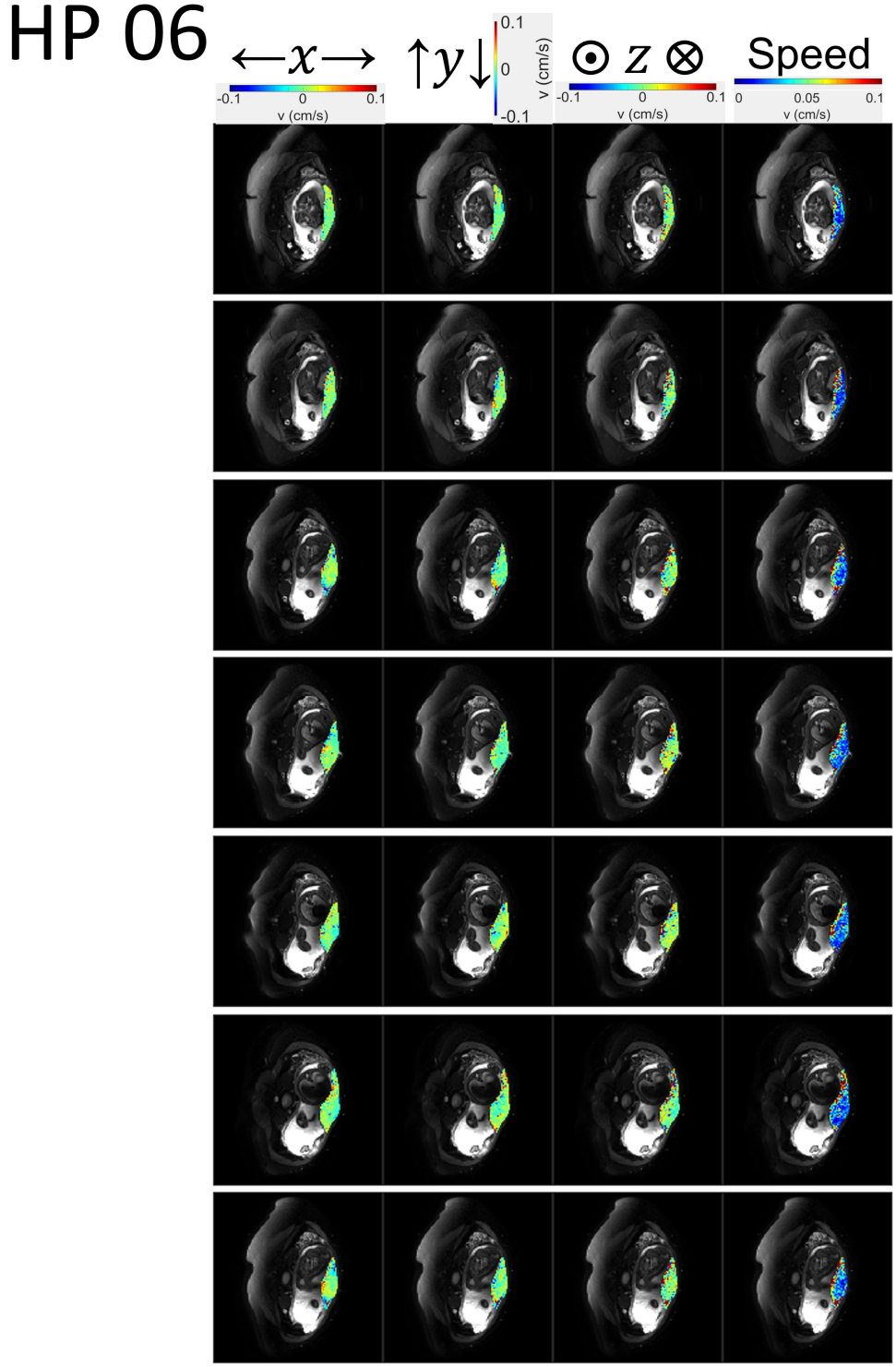
(b)


HP 04
←x→
↑y↓
⊙ z ⊗
Speed
-0.1
0
0.1
v (cm/s)
0.1
0
-0.1
v (cm/s)
0
0.05
0.1

(c)

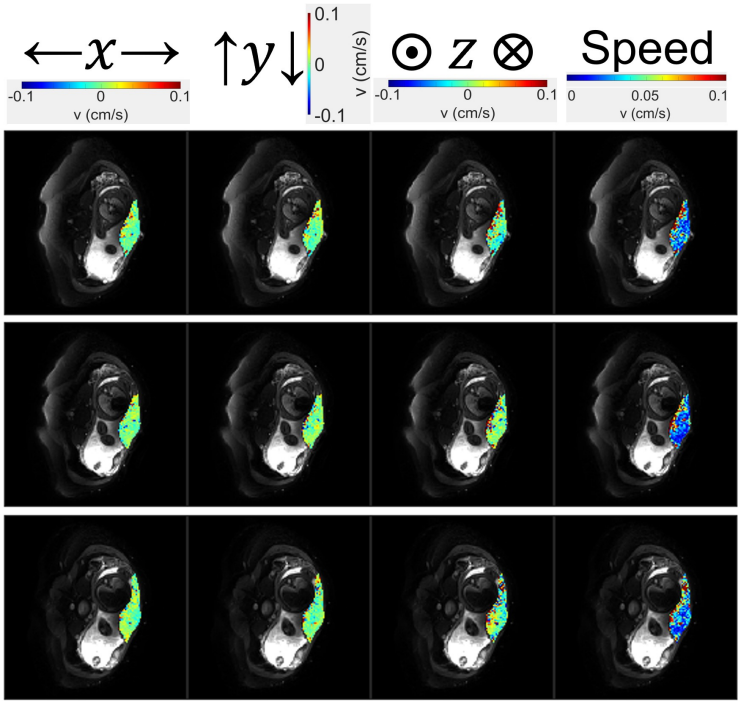


(d)

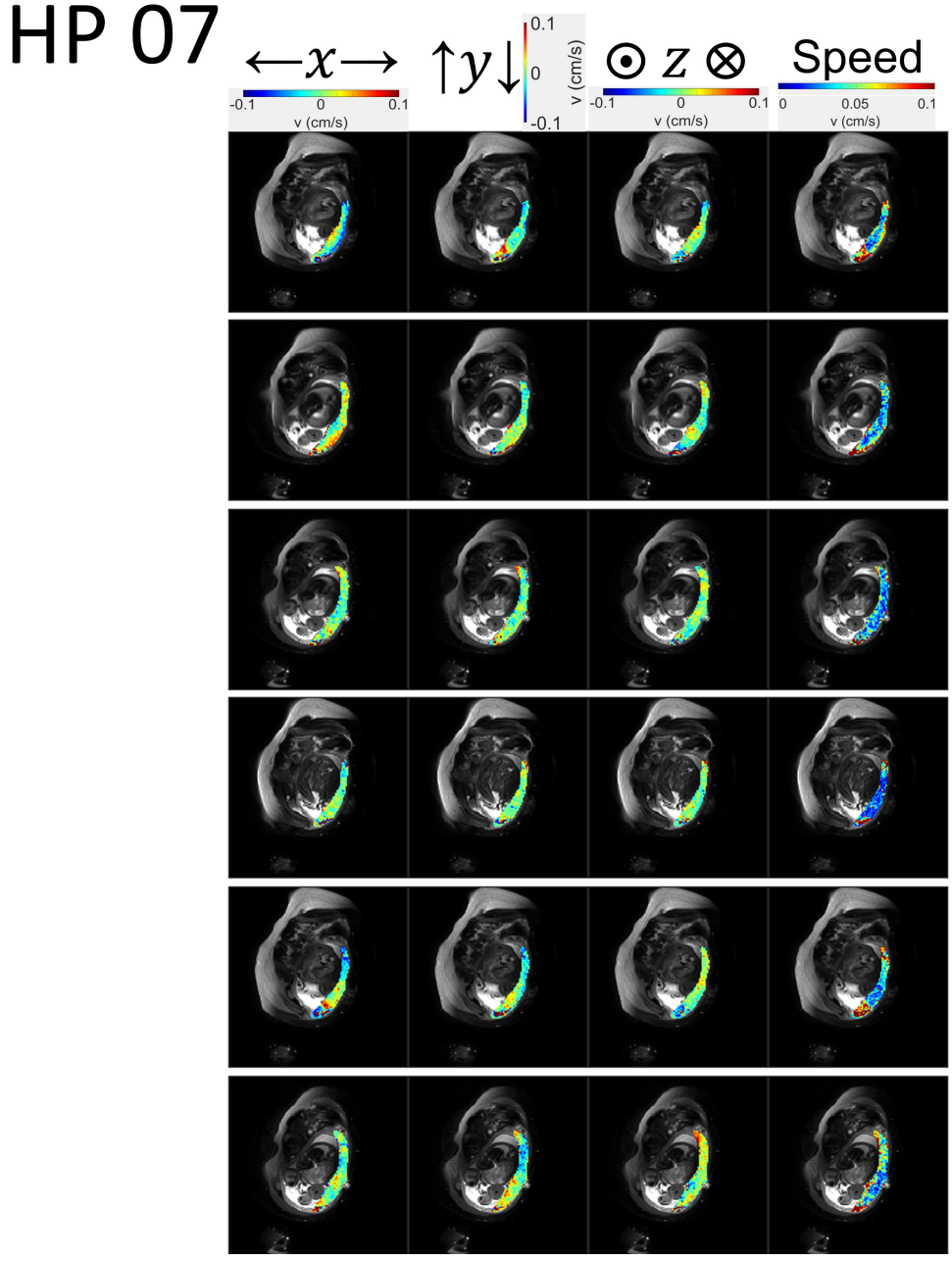


(e)

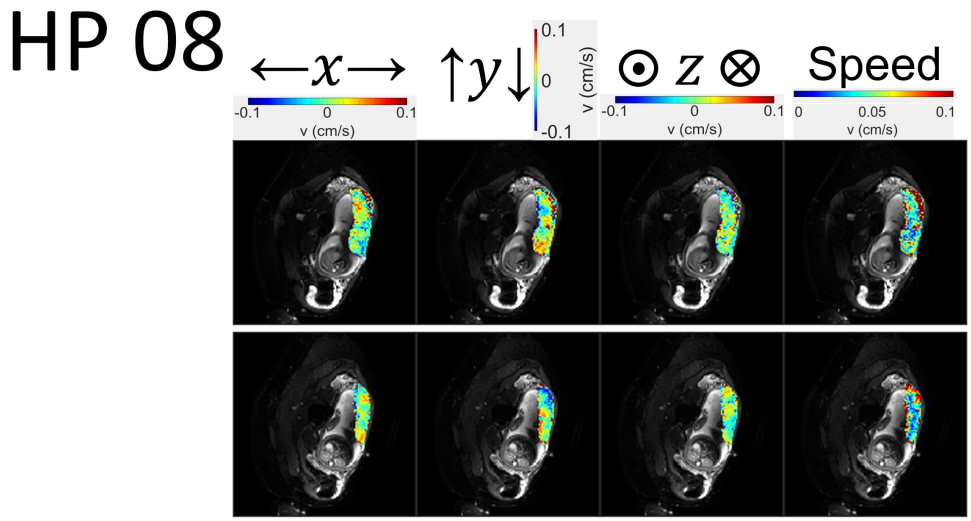
HP 06 cont.



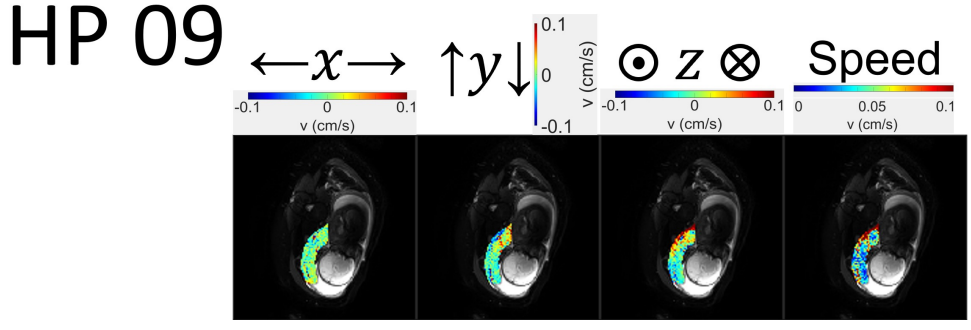
(f)



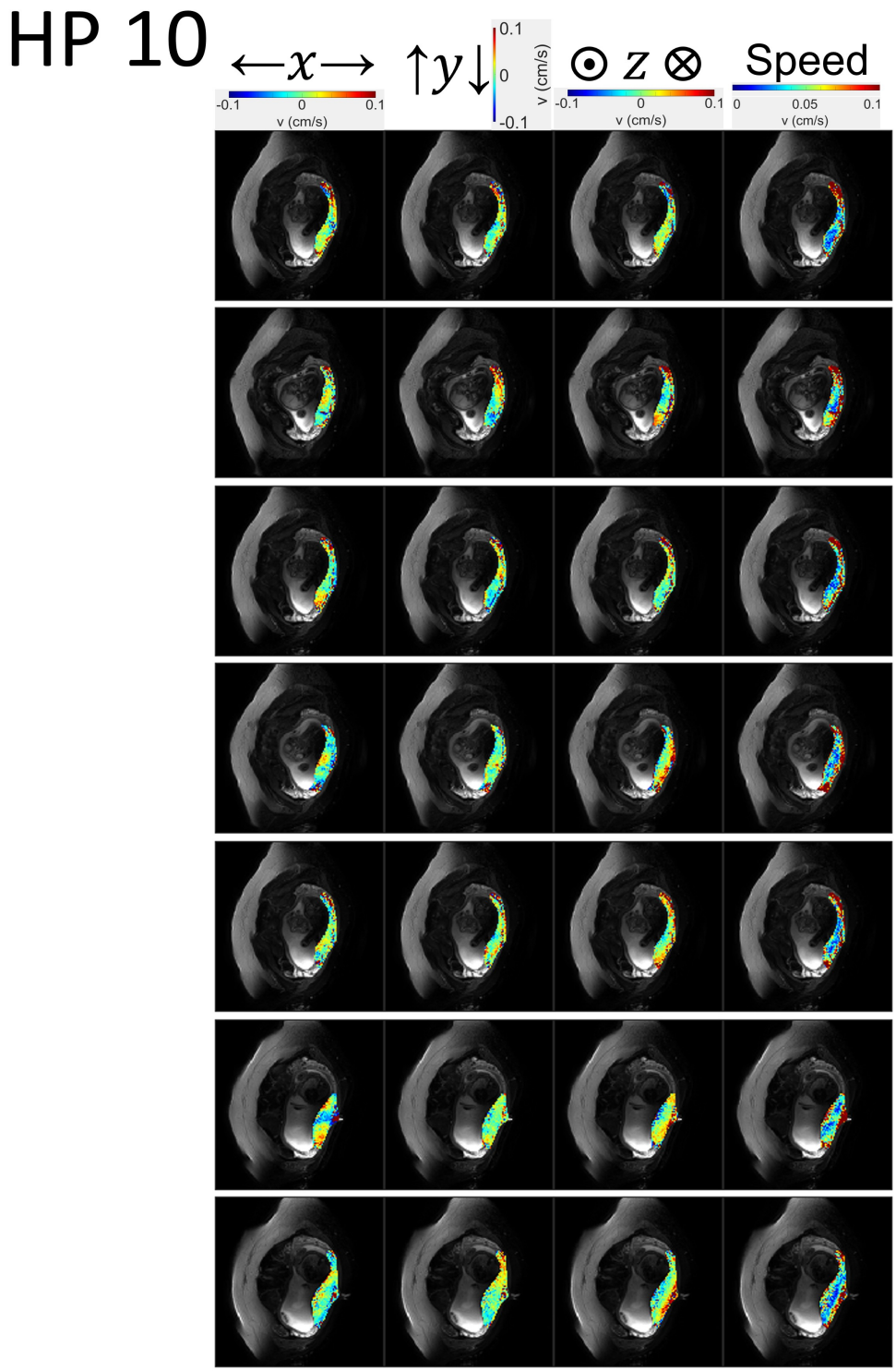
(g)


HP 08
←x→
↑y↓
⊙ z ⊗
Speed
-0.1
0
0.1
v (cm/s)
0.1
0
-0.1
v (cm/s)
0
0.05
0.1

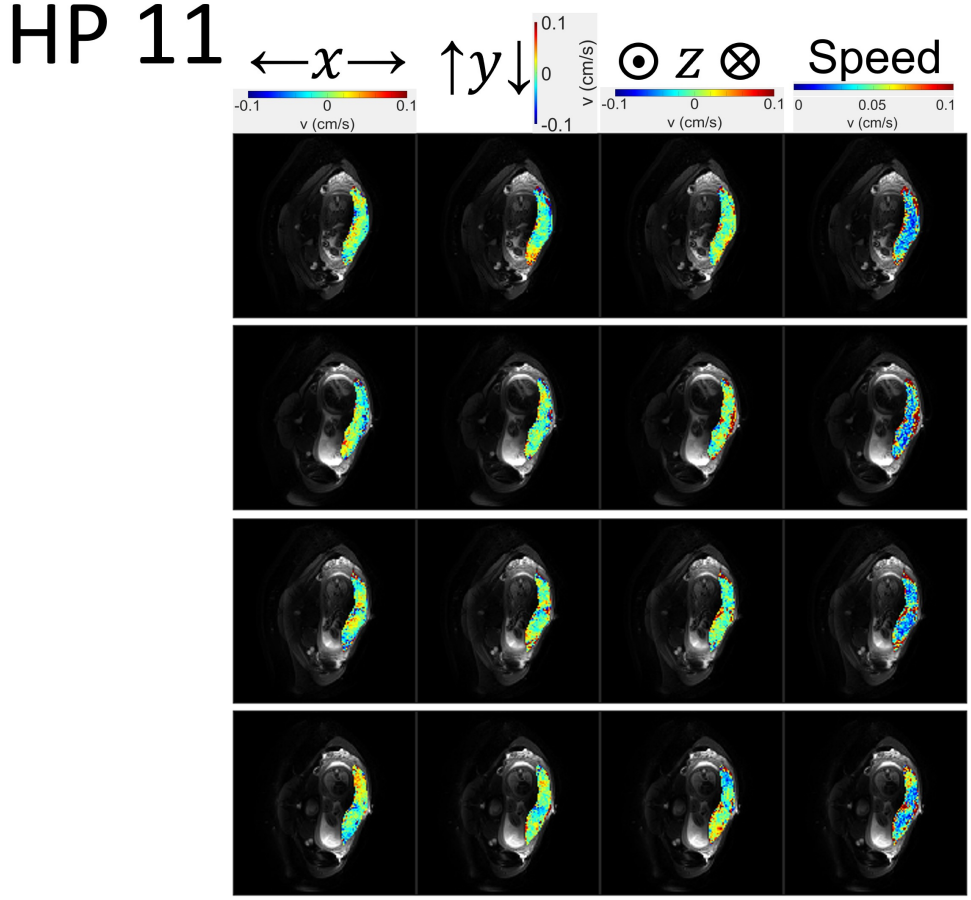
(h)


HP 09
←x→
↑y↓
⊙ z ⊗
Speed
-0.1
0
0.1
v (cm/s)
0.1
0
-0.1
v (cm/s)
0
0.05
0.1

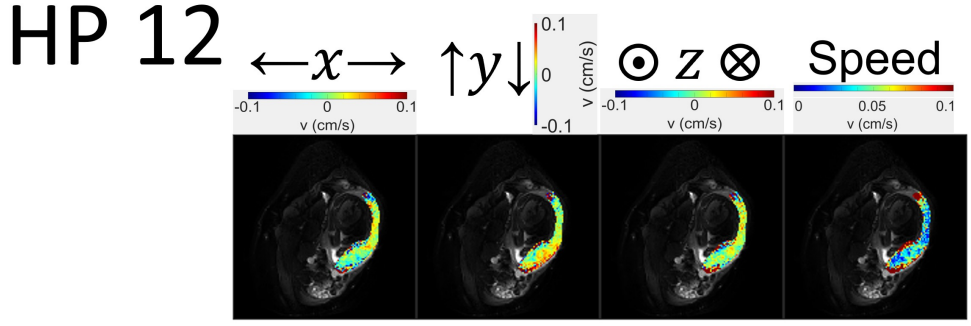
(i)



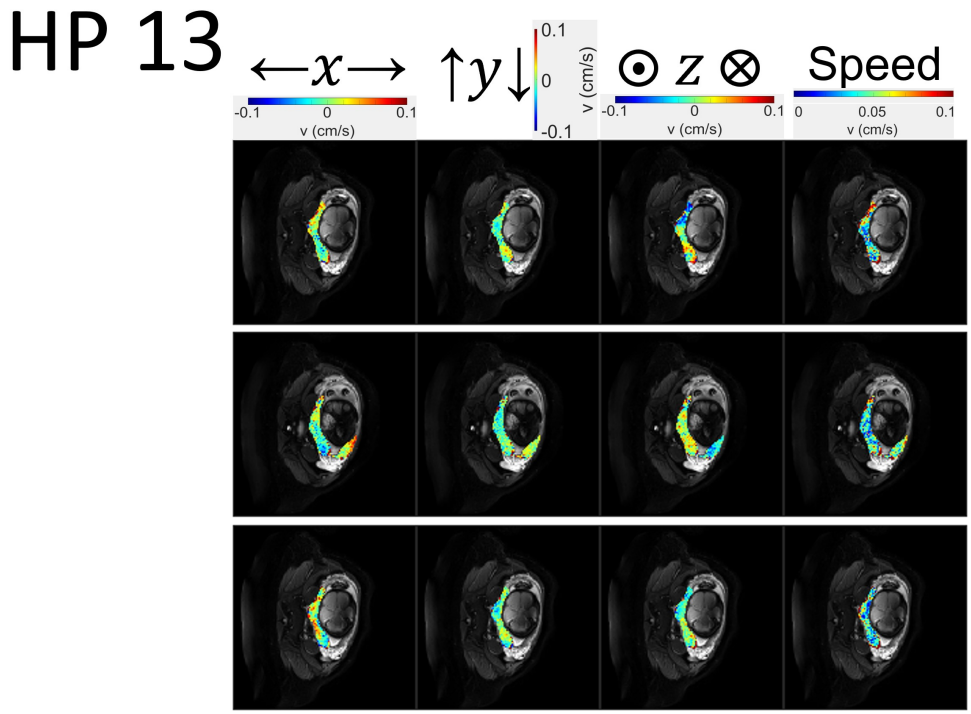
(j)


HP 11
←x→
↑y↓
⊙ z ⊗
Speed
-0.1
0
0.1
v (cm/s)
0.1
0
-0.1
v (cm/s)
0
0.05
0.1

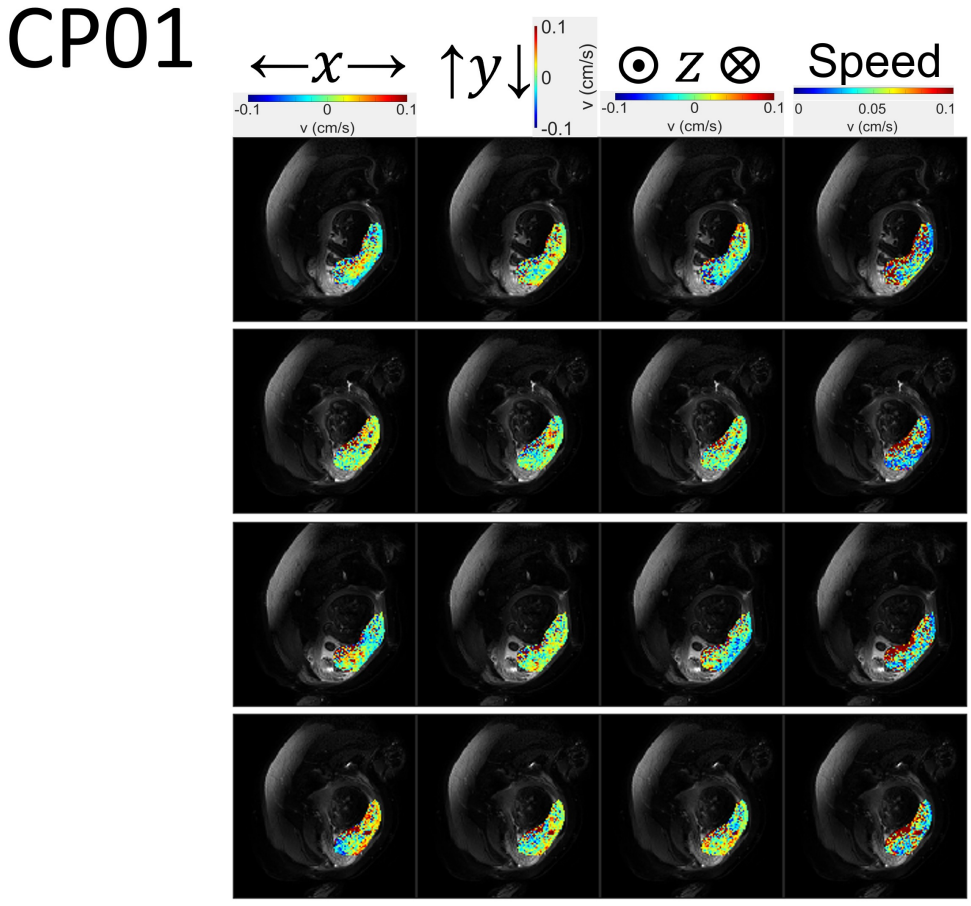
(k)


HP 12
←x→
↑y↓
⊙ z ⊗
Speed
-0.1
0
0.1
v (cm/s)
0.1
0
-0.1
v (cm/s)
0
0.05
0.1

(l)

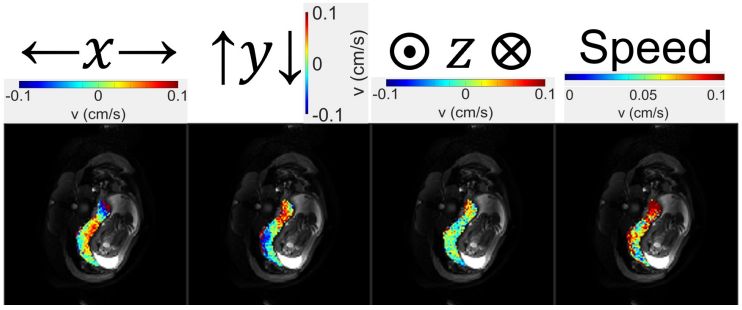

HP 13
←x→
↑y↓
⊙ z ⊗
Speed
-0.1
0
0.1
v (cm/s)
0.1
0
-0.1
v (cm/s)
0
0.05
0.1

(m)


CP01
←x→
↑y↓
⊙ z ⊗
Speed
-0.1
0
0.1
v (cm/s)
0.1
0
-0.1
v (cm/s)
0
0.05
0.1

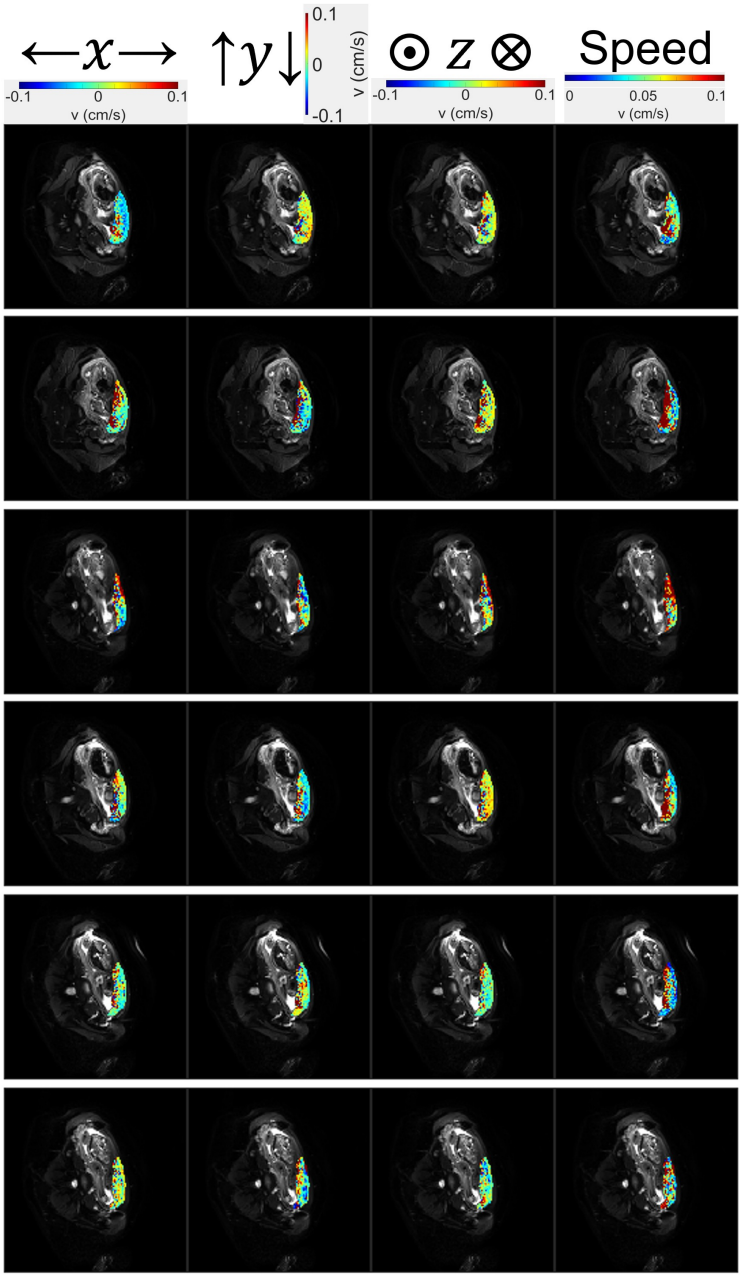
(n)

CP02

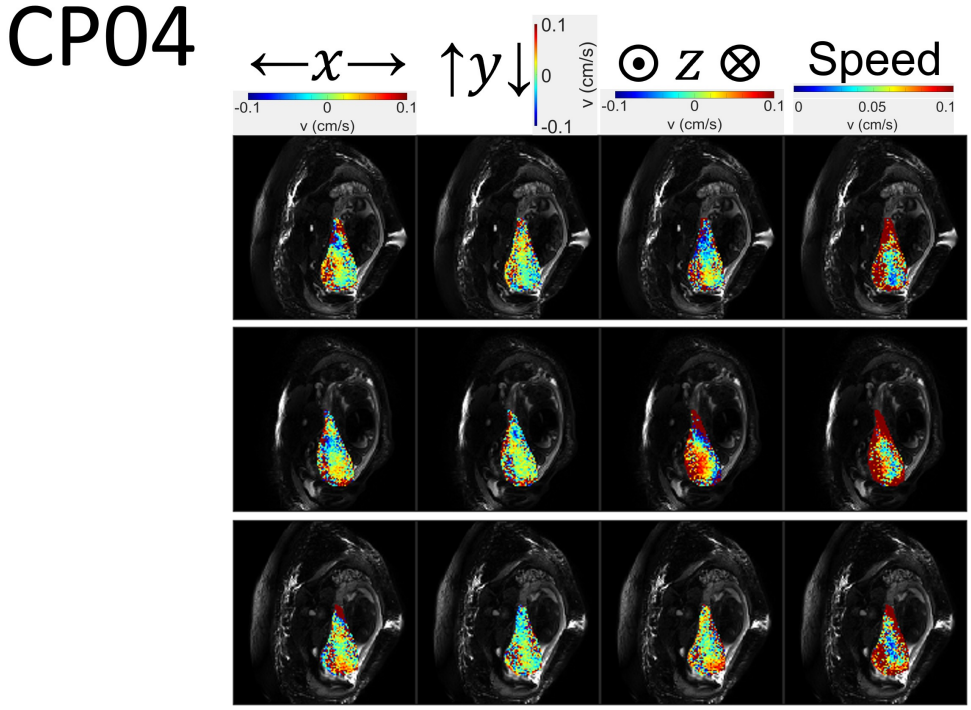

←x→
↑y↓
⊙ z ⊗
Speed
-0.1
0
0.1
v (cm/s)
0.1
0
-0.1
0
0.05
0.1

(o)

CP03

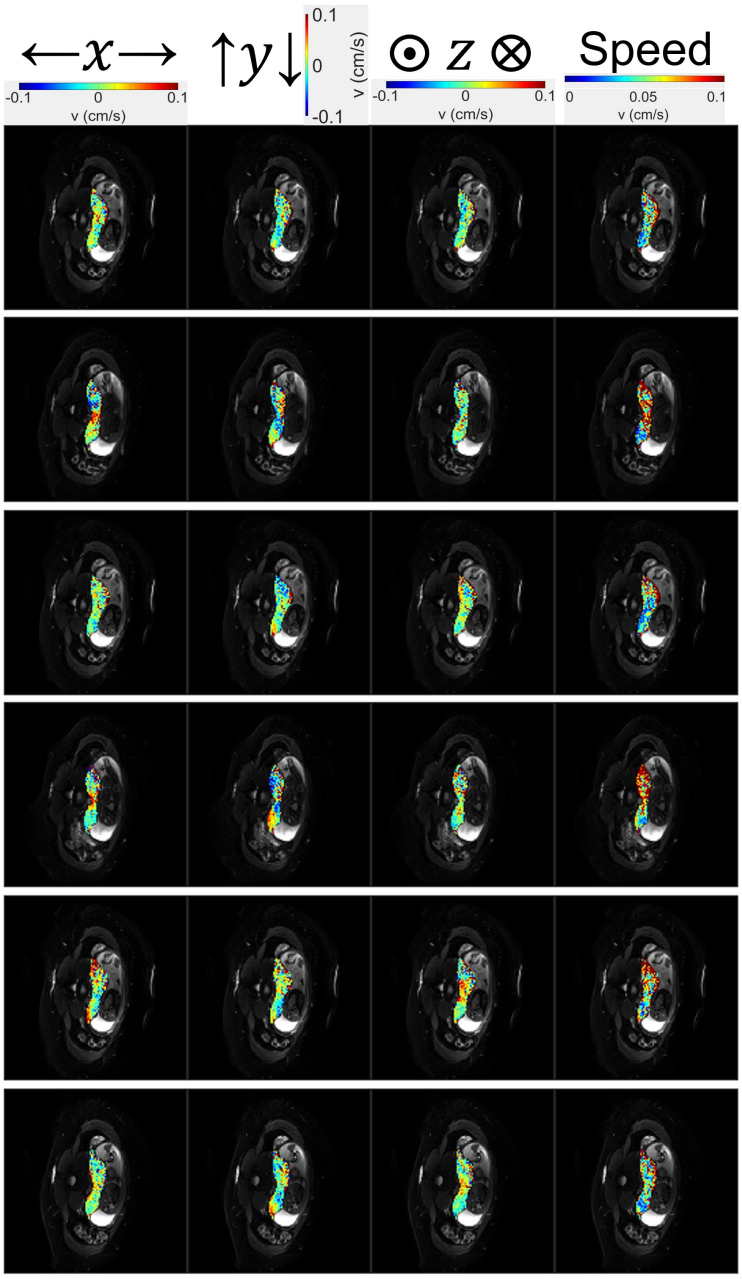

←x→
↑y↓
⊙ z ⊗
Speed
-0.1
0
0.1
v (cm/s)
0.1
0
-0.1
0
0.05
0.1

(p)



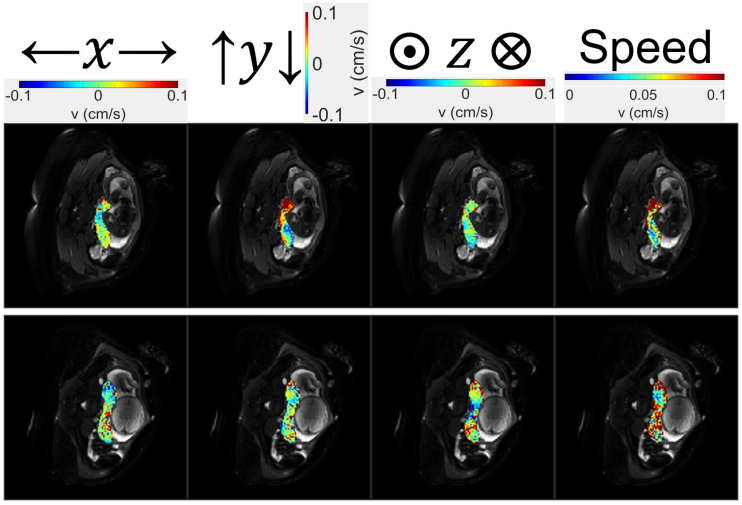
(q)

CP05



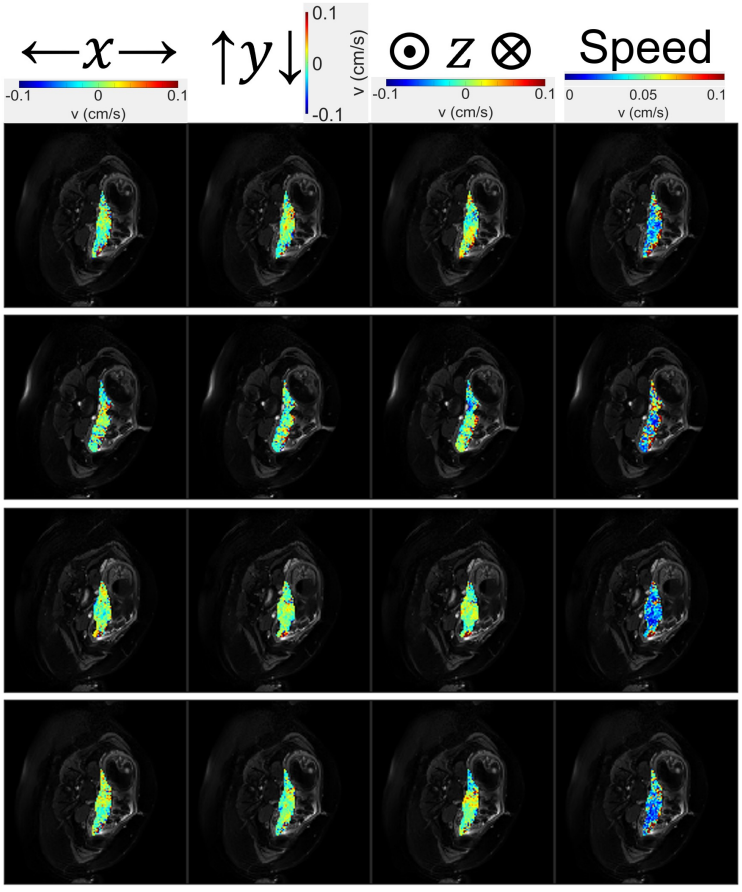
(r)

CP06


←x→
↑y↓
⊙ z ⊗
Speed
-0.1 0 0.1
v (cm/s)
0.1
0
-0.1
v (cm/s)
0 0.05 0.1

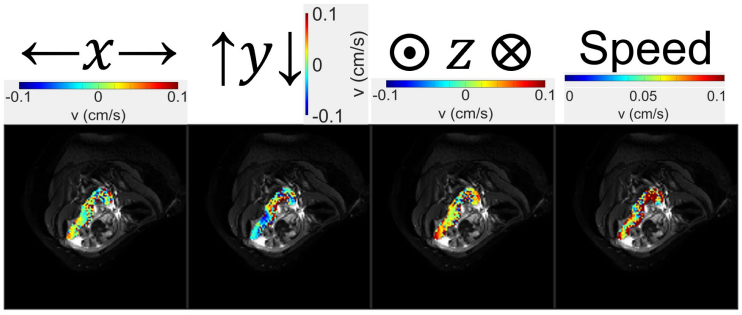
(s)

CP07


←x→
↑y↓
⊙ z ⊗
Speed
-0.1 0 0.1
v (cm/s)
0.1
0
-0.1
v (cm/s)
0 0.05 0.1

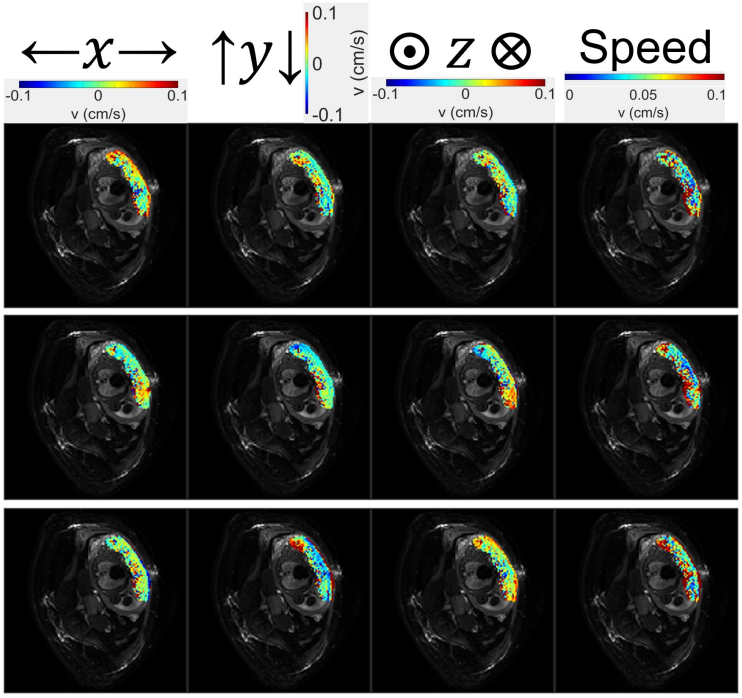
(t)

CP08


←x→
↑y↓
⊙ z ⊗
Speed
-0.1
0
0.1
v (cm/s)
0.1
0
-0.1
v (cm/s)
0
0.05
0.1

(u)

CP09


←x→
↑y↓
⊙ z ⊗
Speed
-0.1
0
0.1
v (cm/s)
0.1
0
-0.1
v (cm/s)
0
0.05
0.1

(v)